



# Analyse multifractale utilisant le taux de précipitations dans cas de typhon en 2012, Corée

Jisun Lee

## ► To cite this version:

Jisun Lee. Analyse multifractale utilisant le taux de précipitations dans cas de typhon en 2012, Corée. Ingénierie de l'environnement. Université Paris-Est; Institute of Fisheries Science (Corée (République)), 2020. Français. NNT : 2020PESC1007 . tel-03136520

HAL Id: tel-03136520

<https://pastel.hal.science/tel-03136520>

Submitted on 9 Feb 2021

**HAL** is a multi-disciplinary open access archive for the deposit and dissemination of scientific research documents, whether they are published or not. The documents may come from teaching and research institutions in France or abroad, or from public or private research centers.

L'archive ouverte pluridisciplinaire **HAL**, est destinée au dépôt et à la diffusion de documents scientifiques de niveau recherche, publiés ou non, émanant des établissements d'enseignement et de recherche français ou étrangers, des laboratoires publics ou privés.

Thése présentée pour obtenir le grade de  
Docteur de l'Université Paris-Est  
Spécialité: Sciences et Techniques de Meteorologie et l'Environnement  
par  
Jisun Lee

Ecole Doctorale : Sciences, Ingénierie et Environnement

*Multifractal Analysis on the Rainfall Rate  
in Typhoon Cases in 2012, Korea*

Thése soutenue le 15 Janvier 2020 devant le jury composé de :

Klaus Fraedrich *Rapporteur*

Cheol-Hwan You *Rapporteur*

Mi-Young Kang *Examinateur*

Auguste Gires *Examinateur*

Kyung-Sik Kim *Examinateur*

Ioulia Tchiguirinskaia *co-superviseur*

Dong-In Lee *Directeur de thése*

Daniel Schertzer *Directeur de thése*

# Analyse multifractale utilisant le taux de précipitations dans cas de typhon en 2012, Corée

Jisun Lee

HM&Co, École des ponts, Sciences, Ingénierie et Environnement, École doctoral, Université Paris-Est

Department of Environmental Atmospheric Science, The Graduate School, Pukyong National University

## Résumé

L'approche multifractale a été utilisée pour analyser le taux de précipitations de trois typhons (Khanun, Bolaven et Sanba) qui ont frappé la Corée du Sud en passant par l'île de Jeju vers la péninsule coréenne en 2012. Les données sur le taux de précipitations sont obtenues à partir d'un radar en bande S exploité par la Corée Administration météorologique (KMA) et la simulation de modèle CReSS.

L'analyse multifractale a été réalisée à l'aide de l'analyse Trace Moment (Schertzer et Lovejoy, 1987) et de l'analyse Double Trace Moment (Lavallée et al., 1992) pour quantifier l'intermittence moyenne à l'aide de sa co-dimension fractale  $C_1$  et de sa multifractalité. index  $\alpha$ , qui mesure la rapidité avec laquelle évolue l'intermittence pour l'ordre statistique supérieur avec une grande quantité de données spatio-temporelles.

Premièrement, avec les données radar, l'analyse spectrale a été réalisée pour vérifier la prudence du champ. Dans le cas des typhons Khanun, Bolaven et Sanba, les valeurs moyennes de l'exposant d'échelle  $\beta$  pour l'analyse spectrale sont respectivement de 1,92 (Khanun), 1,710 (Bolaven) et 2,233 (Sanba), toutes

hauteurs des domaines de 256 km.  $\times$  256 km. Alors que 2.515 (Khanun), 2.553 (Bolaven) et 2.513 (Sanba) dans la taille du domaine 64 km  $\times$  64 km. Tous les champs de différentes tailles de domaines à différentes altitudes étaient conservateurs.

En analyse TM et DTM, avec l'ordre des moments  $q$  et  $(q, \eta)$ , il est montré que  $K(q)$  et  $K(q, \eta)$  satisfont à la forme universelle présentant les paramètres de messagerie unifiée  $\alpha$  et  $C_1$ . Chaque paramètre indique le degré de multifractalité du processus ( $\alpha$ ) et la codimension de la singularité moyenne du champ ( $C_1$ ). Dans tous les cas, les champs pluviométriques étaient constants en basse altitude (1, 2 km), alors que les fluctuations étaient plus marquées en haute altitude.

Pour vérifier le résultat de l'observation radar, nous avons également utilisé le taux de précipitation obtenu par simulation du modèle CReSS. En conséquence des paramètres de messagerie unifiée de tous les cas du modèle CReSS, uniquement dans le cas de Khanun,  $\alpha$  est inférieur à 1 dans les deux domaines. D'autre part,  $\alpha$  est supérieur à 1 avec Bolaven et Sanba dans les deux domaines.

Avec le résultat, il est montré qu'il existe une dépendance de  $\alpha$  avec l'altitude qui montre la déduction de la configuration du champ de précipitations dans chaque altitude avec les paramètres UM. Cela permet de voir l'évolution du champ de précipitations. Lorsque le typhon a traversé l'île de Jeju, où se trouve le mont Halla, il a commencé à diminuer les cyclones, libérant ainsi son humidité sous forme de pluie torrentielle sur l'île. Étant donné que le stade de tous les typhons était en phase d'affaiblissement ou de dissipation, les paramètres UM montrent que le cisaillement du vent a incliné le vortex pour obtenir les différentes configurations des champs de précipitations à chaque altitude.

# Multifractal Analysis on the Rainfall Rate in Three Typhoon Cases, Korea

Jisun Lee

HM&Co, École des ponts, Sciences, Ingénierie et Environnement, École doctoral,  
Université Paris-Est

Department of Environmental Atmospheric Science, The Graduate School, Pukyong National  
University

## Abstract

The multifractal approach was used to analyze the rainfall rate of three typhoons (Khanun, Bolaven, Sanba) that struck South Korea passing through Jeju Island to the Korean peninsula in 2012. The rainfall rate data are obtained from S-band radar operated by the Korea Meteorological Administration (KMA) and the model simulation CReSS.

The multifractal analysis was performed with the help of Trace Moment analysis (Schertzer and Lovejoy, 1987) and Double Trace Moment analysis (Lavallée et al., 1992) to quantify the mean intermittency with the help of its fractal co-dimension  $C_1$  and its multifractality index  $\alpha$ , which measures how fast the intermittency evolves for the higher order of statistics with a large amount of space-time data.

Firstly, with the radar data, the spectral analysis was done to check the conservativeness of the field. In the case of Typhoon Khanun, Bolaven, and Sanba, the average values of scaling exponent  $\beta$  for spectral analysis are, respectively, 1.92 (Khanun), 1.710 (Bolaven), and 2.233 (Sanba) in all heights of the domain sizes  $256 \text{ km} \times 256 \text{ km}$ . While 2.515 (Khanun), 2.553 (Bolaven),

and 2.513 (Sanba) in the domain size  $64 \text{ km} \times 64 \text{ km}$ . All the fields of different sizes of domains at different altitudes were conservative.

In TM and DTM analysis, along with the moment order  $q$ , and  $(q,\eta)$ , it is shown that  $K(q)$  and  $K(q,\eta)$  satisfies the universal form presenting the UM parameters  $\alpha$  and  $C_1$ . Each parameter shows the degree of multifractality of the process ( $\alpha$ ) and the codimension of the mean singularity of the field ( $C_1$ ). In all the cases, the rainfall fields were constant in low altitudes (1, 2 km) while it shows more fluctuation in higher altitudes.

To compare the result of the radar observation, the rainfall rate obtained by CReSS model simulation was also used. As a result of the UM parameters of all cases from CReSS model, only with the Khanun case,  $\alpha$  is less than 1 in both domains. On the other hand,  $\alpha$  is larger than 1 with Bolaven and Sanba in both domains.

With the result, it is shown that there is a dependence of  $\alpha$  along with the altitude which shows the deduction of the pattern of the rainfall field in each altitude with the UM parameters. This enables to see the development of the rainfall field. As the typhoon passes through the Jeju Island, where there is Halla Mountain, it started to diminishing cyclones unleashing their moisture as torrential rainfall on the island. Since the stage of all the typhoons was in weakening or dissipating stage, the UM parameters show that the wind shear tilted the vortex to have the different patterns of the rainfall fields in each altitude.

# CONTENTS

Abstracts	i
<hr/>	
I. French .....	i
II. English .....	iii
Contents .....	v
List of Tables .....	viii
List of Figures .....	ix
1. Introduction	1
<hr/>	
2. Data	5
<hr/>	
2.1. Typhoon track data .....	5
2.2. Automatic weather station (AWS) .....	5
2.3. NCEP/NCAR reanalysis data .....	6
2.4. Doppler radar data .....	6
2.5. Cloud Resolving Storm Simulator .....	7

3. Data Processing	9
3.1. Rainfall rate retrieval	9
3.2. Wind field retrieval	9
3.3. CReSS rainfall rate retrieval	14
4. Multifractal	15
4.1. Fractal dimensions	15
4.2. The Universal Multifractal (UM)	22
4.2.1. Discrete Cascade	22
4.2.2. Universal Multifractal Framework	23
4.2.3. UM Parameters	25
4.2.4. Critical values of moment order ( $q_s$ and $q_D$ )	26
4.3. Universal Multifractal data analysis techniques	27
4.3.1. Spectral Analysis	27
4.3.2. Trace Moment Analysis (TM)	28
4.3.3. Double Trace Moment Analysis (DTM)	29

5. The results of three typhoon cases in 2012	31
5.1. Typhoon Khanun .....	31
5.1.1. Environmental description .....	31
5.1.2. Observational results .....	35
5.1.3. Multifractal analysis .....	44
5.2. Typhoon Bolaven .....	69
5.2.1. Environmental description .....	69
5.2.2. Observational results .....	73
5.2.3. Multifractal analysis .....	82
5.3. Typhoon Sanba .....	110
5.3.1. Environmental description .....	110
5.3.2. Observational results .....	114
5.3.3. Multifractal analysis .....	123
6. Summary and Conclusion	151
References .....	155
Appendix A .....	169

## List of Tables

Table 5.1.1.	The values of $\beta$ and $R^2$ after spectral analysis in the domain size 256 km $\times$ 256 km with the case of Typhoon Khanun.	45
Table 5.1.2.	The estimated UM parameters from TM and DTM in the domain size 256 km $\times$ 256 km.	52
Table 5.1.3.	The values of $\beta$ and $R^2$ after spectral analysis in the domain size 64 km $\times$ 64 km with the case of Typhoon Khanun.	54
Table 5.1.4.	The estimated UM parameters from TM and DTM in the domain size 64 km $\times$ 64 km.	58
Table 5.1.5.	The estimated UM parameters from TM and DTM analysis with the dataset of CReSS in the domain 256 km $\times$ 256 km and 64 km $\times$ 64 km.	65
Table 5.2.1.	The same as Table 5.1.1 but with Typhoon Bolaven.	83
Table 5.2.2.	The same as Table 5.1.2 but with Typhoon Bolaven.	90
Table 5.2.3.	The same as Table 5.1.3 but with Typhoon Bolaven.	92
Table 5.2.4.	The same as Table 5.1.4 but with Typhoon Bolaven.	99
Table 5.2.5.	The same as Table 5.1.5 but with Typhoon Bolaven.	106
Table 5.3.1.	The same as Table 5.1.1 but with Typhoon Samba.	124
Table 5.3.2.	The same as Table 5.1.2 but with Typhoon Samba.	131
Table 5.3.3.	The same as Table 5.1.3 but with Typhoon Samba.	133
Table 5.3.4.	The same as Table 5.1.4 but with Typhoon Samba.	140
Table 5.3.5.	The same as Table 5.1.5 but with Typhoon Samba.	147

## List of Figures

---

Fig. 2.1. The map of the selected area for this study indicated with the red box and the radar observation sites shown with the red dots (Gosan and Seongsanpo) in Jeju Island, Korea. 6

---

Fig. 2.2. The schematic diagram of microphysical process used in the model calculation. 7

---

Fig. 3.1. The map of the selected domain when using the numerical model CReSS. 14

---

Fig. 4.1. The schematic diagram of the rainfall intensity on the selected domain of typhoon. 16

---

Fig. 4.2. The fractal dimension calculated at 1940 LST 18 July 2012 with (a) radar at 5 km with the domain size 265 km × 265 km, (c) in the domain size 64 km × 64 km with the threshold 1 mm/hr (black), 3 mm/hr (blue) and 5 mm hr (red). (b) and (d) indicates the area with the rainfall field with the black shaded area along with the different thresholds. 19

---

---

The fractal dimension calculated at 2330 LST 27 August 2012. (a) radar at 5 km with the domain size of  $265 \times 265$  with the threshold 1 mm/hr (black), 5 mm/hr (blue) and 10 mm/hr (red), (c) in the domain size of  $64 \text{ km} \times 64 \text{ km}$  with the threshold 1 mm/hr (black), 3 mm/hr (blue) and 5 mm/hr (red). (b) and (d) indicates the area with the rainfall field with the black shaded area along with the different thresholds.

Fig. 4.3.

20

Fig. 4.4.

21

The fractal dimension calculated at 1940 LST 18 September 2012 with (a) radar at 5 km with the domain size  $265 \text{ km} \times 265 \text{ km}$ , (c) in the domain size  $64 \text{ km} \times 64 \text{ km}$  with the threshold 1 mm/hr (black), 3 mm/hr (blue) and 5 mm hr (red). (b) and (d) indicates the area with the rainfall field with the black shaded area along with the different thresholds.

Fig. 4.5.

Diagram of cascade phenomenon for (a) 1-dimension and (b) 2-dimension.

23

Fig. 5.1.1.

The track of typhoon Khanun. The red dots indicate the location of the typhoon center.

32

Fig. 5.1.2.

The daily accumulated rainfall on 18 July 2012 in Korea.

32

Fig. 5.1.3.

The graph of typhoon center pressure (hPa) in red and the maximum wind speed (m/s) in blue.

33

---

	The synoptic flow at 1200 UTC on 18 July 2012.	
Fig. 5.1.4.	(a) at the surface showing the pressure (sea level pressure, hPa), (b) at 850 hPa showing the equivalent potential temperature (K), (c) at 500 hPa showing the relative vorticity ( $10^{-5}s^{-1}$ ), and (d) at 300 hPa showing the geopotential height (m) with wind vector.	34
	The wind field superimposed on the radar reflectivity (dBZ) on each altitude (1, 2, 4, 5, 6, 8 km) at 1730 LST, 1930 LST, 2030 LST and 2130 LST during Typhoon Khanun.	36
Fig. 5.1.6.	The vertical wind field superimposed on the radar reflectivity (dBZ) on each time step. Vertical cross section is indicated with the red line (A-B).	39
Fig. 5.1.7.	The horizontal distribution of wind field of divergence (red) and convergence (blue) with the radar reflectivity (contour).	41
Fig. 5.1.8.	The result of spectral analysis, $\ln E(k)$ as a function of $\ln k$ with the rainfall rate retrieved from radar data on every height (a) 1 km, (b) 2 km, (c) 4 km, (d) 5 km, (e) 6 km and (f) 8 km in 256 km $\times$ 256 km size of the domain.	45
Fig. 5.1.9.		47

---

---

The result of TM analysis obtained from the radar dataset in the  $256 \text{ km} \times 256 \text{ km}$  sizes of the domain. The scaling behavior with the value of different  $q$  from 0.1 to 7.0 at 1 km, 2 km, 4 km, 5 km, 6 km and 8 km (a, b, c, d, e, f).  $K(q)$  (black) is obtained in the graph (g, h, i, j, k, l) and the multifractal parameters retrieved from TM analysis are shown on the left top corner.

---

Fig. 5.1.10. The scaling moment function  $K(q)$  obtained from the empirical dataset (black), from using UM parameters obtained from TM (red), from using UM parameters obtained from DTM (green).

49

Fig. 5.1.11. The result of DTM analysis obtained from the radar dataset in the  $256 \text{ km} \times 256 \text{ km}$  sizes of the domain. The scaling behavior with the value of different  $\eta$  from 0.1 to 2.5 at 1 km, 2 km, 4 km, 5 km, 6 km and 8 km (a, b, c, d, e, f) at fixed  $q = 1.5$ . DTM curve is shown in (g, h, I, j, k, l).

50

Fig. 5.1.12. The UM parameters obtained from TM and DTM.

52

Fig. 5.1.13. The same as Fig. 5.1.8 but in the altitudes of (a) 4 km, (b) 5 km, (c) 6 km, and (d) 8 km in the domain size  $64 \text{ km} \times 64 \text{ km}$ .

53

Fig. 5.1.14. The same as Fig. 5.1.9 but in the altitudes of (a,e)

55

---

4 km, (b,f) 5 km, (c,g) 6 km, and (d,h) 8 km in the domain size  $64 \text{ km} \times 64 \text{ km}$ .

---

Fig. 5.1.15. The same as Fig. 5.1.10 but in the altitudes of (a)  
4 km, (b) 5 km, (c) 6 km, and (d) 8 km in the 56  
domain size  $64 \text{ km} \times 64 \text{ km}$ .

---

Fig. 5.1.16. The same as Fig. 5.1.11 but in the altitudes of (a,e)  
4 km, (b,f) 5 km, (c,g) 6 km, and (d,h) 8 km in the 57  
domain size  $64 \text{ km} \times 64 \text{ km}$ .

---

Fig. 5.1.17. The same as Fig. 5.1.12 but in domain  $64 \text{ km} \times$   
64 km. 58

---

Fig. 5.1.18. The accumulated rainfall field on each altitudes  
of typhoon Khanun. 59

---

Fig. 5.1.19. The result of spectral analysis from CReSS model  
dataset. 60

---

Fig. 5.1.20. The result of TM analysis obtained from CReSS  
model dataset in domain  $256 \text{ km} \times 256 \text{ km}$ . (a) 61

---

---

The scaling behavior with the value of different  $q$  from 0.1 to 7.0 and (b) the graph of  $K(q)$  with the values of multifractal parameters indicated which were obtained from TM analysis. (c) The scaling moment function  $K(q)$  obtained from the empirical dataset (black), from using UM parameters obtained from TM (red), from using UM parameters obtained from DTM (green).

---

- Fig. 5.1.21. The result of DTM analysis with CReSS model dataset in domain 256 km  $\times$  256 km. (a) The scaling behavior with the value of different  $\eta$  from 0.1 to 2.5 at fixed  $q=1.5$ . (b) DTM curve with multifractal parameters. 62

- 
- Fig. 5.1.22. The same as Fig. 5.1.19 but in the domain 64 km  $\times$  64 km. 63

- 
- Fig. 5.1.23. The same as Fig. 5.1.20 but in the domain 64 km  $\times$  64 km. 64

- 
- Fig. 5.1.24. The same as Fig. 5.1.21 but in domain 64 km  $\times$  64 km. 65

- 
- Fig. 5.1.25. Comparison between the empirical  $K(q)$  for each height of the radar data and the CReSS model in the domain size of 256 km  $\times$  256 km of typhoon Khanun. The blue dots correspond to the  $K(q)$  67

---

values for each  $q$  value; the black lines are the linear regression fits.

---

Fig. 5.1.26.	The same as Fig. 5.1.25 but with the domain 64 km $\times$ 64 km.	68
--------------	---	----

---

Fig. 5.2.1.	The track of Typhoon Bolaven. The red dots indicate the location of the typhoon center.	70
-------------	---	----

---

Fig. 5.2.2.	The daily accumulated rainfall on 27 August 2012 in Korea.	70
-------------	--	----

---

Fig. 5.2.3.	The graph of typhoon center pressure (hPa) in red and the maximum wind speed (m/s) in blue.	71
-------------	---	----

---

Fig. 5.2.4.	The synoptic flow at 1200 UTC on 27 August 2012. (a) at the surface showing the pressure (sea level pressure, hPa), (b) at 850 hPa showing the equivalent potential temperature (K), (c) at 500 hPa showing the relative vorticity ( $10^{-5} s^{-1}$ ), and (d) at 300 hPa showing the geopotential height (m) with wind vector.	72
-------------	---	----

---

Fig. 5.2.5.	The same as Fig. 5.1.5 but with Bolaven case.	74
-------------	---	----

---

Fig. 5.2.6.		77
-------------	--	----

---

---

	The same as Fig. 5.1.6 but with Bolaven case.	
Fig. 5.2.7.	The same as Fig. 5.1.7 but with case of typhoon Bolaven.	79
Fig. 5.2.8.	The same as Fig. 5.1.8 but with Bolaven case.	83
Fig. 5.2.9.	The same as Fig. 5.1.9 but with Bolaven case.	85
Fig. 5.2.10.	The same as Fig. 5.1.10 but with Bolaven case.	87
Fig. 5.2.11.	The same as Fig. 5.1.11 but with Bolaven case.	88
Fig. 5.2.12.	The UM parameters obtained from TM and DTM.	90
Fig. 5.2.13.	The same as Fig. 5.2.8 but in the domain size 64 km × 64 km.	92
Fig. 5.2.14.	The same as Fig. 5.2.9 but in the domain size 64 km × 64 km.	94
Fig. 5.2.15.	The same as Fig. 5.2.10 but in the domain size 64 km × 64 km.	96
Fig. 5.2.16.	The same as Fig. 5.2.11 but in the domain size 64	97

---

---

km  $\times$  64 km.

---

Fig. 5.2.17. The same as Fig. 5.2.12 but in domain 64 km  $\times$  64 km. 99

---

Fig. 5.2.18. The same as Fig. 5.1.18 but with the case of typhoon Bolaven. 100

---

Fig. 5.2.19. The result of spectral analysis from CReSS model dataset with domain 256 km  $\times$  256 km. 101

---

Fig. 5.2.20. The same as Fig. 5.1.20 but with Bolaven case. 102

---

Fig. 5.2.21. The same as Fig. 5.1.21 but with Bolaven case. 103

---

Fig. 5.2.22. The result of spectral analysis by CReSS model dataset in domain 64 km  $\times$  64 km. 104

---

Fig. 5.2.23. The same as Fig. 5.2.20 but in domain 64 km  $\times$  105

---

---

64 km.

---

Fig. 5.2.24.	The same as Fig. 5.2.21 but in domain 64 km × 64 km.	106
--------------	--	-----

---

Fig. 5.2.25.	The same as Fig. 5.1.25 but with the case of Typhoon Bolaven.	108
--------------	---	-----

---

Fig. 5.2.26.	The same as Fig. 5.2.25 but in the domain size of 64 km × 64 km.	109
--------------	--	-----

---

Fig. 5.3.1.	The track of Typhoon Sanba. The red dots indicate the location of the typhoon center.	111
-------------	---	-----

---

Fig. 5.3.2.	The daily accumulated rainfall on 17 September 2012 in Korea.	111
-------------	---	-----

---

Fig. 5.3.3.	The graph of typhoon center pressure (hPa) in red and the maximum wind speed (m/s) in blue.	112
-------------	---	-----

---

Fig. 5.3.4.	The synoptic flow at 1800 UTC on 16 September 2012. (a) at the surface showing the pressure (sea	113
-------------	--	-----

---

---

level pressure, hPa) and wind vector, (b) at 850 hPa showing the equivalent potential temperature (K) and wind vector, (c) at 500 hPa showing the relative vorticity ( $10^{-5}s^{-1}$ ) and wind vector, and (d) at 300 hPa showing the geopotential height (m) and wind vector.

---

Fig. 5.3.5.	The same as Fig. 5.1.5 but with Typhoon Sanba case.	115
-------------	---	-----

---

Fig. 5.3.6.	The same as Fig. 5.1.6 but with Sanba case.	118
-------------	---	-----

---

Fig. 5.3.7.	The same as Fig. 5.1.7 but with typhoon Sanba.	120
-------------	--	-----

---

Fig. 5.3.8.	The same as Fig. 5.1.8 but with Sanba case.	124
-------------	---	-----

---

Fig. 5.3.9.	The same as Fig. 5.1.9 but with Sanba case.	126
-------------	---	-----

---

Fig. 5.3.10.	The same as Fig. 5.1.10 but with Sanba case.	128
--------------	--	-----

---

Fig. 5.3.11.	The same as Fig. 5.1.11 but with Sanba case.	129
--------------	--	-----

---

---

Fig. 5.3.12. The UM parameters obtained from TM and DTM. 131

---

Fig. 5.3.13. The same as Fig. 5.3.8 but in the domain size 64 km × 64 km. 133

---

Fig. 5.3.14. The same as Fig. 5.3.9 but in the domain size 64 km × 64 km. 135

---

Fig. 5.3.15. The same as Fig. 5.3.10 but in the domain size 64 km × 64 km. 137

---

Fig. 5.3.16. The same as Fig. 5.3.11 but in the domain size 64 km × 64 km. 138

---

Fig. 5.3.17. The same as Fig. 5.3.12 but in domain 64 km × 64 km. 140

---

Fig. 5.3.18. The same as Fig. 5.1.18 but with the case of typhoon Sanba. 141

---

---

---

Fig. 5.3.19	The result of spectral analysis by CReSS model dataset in domain 256 km × 256 km.	142
Fig. 5.3.20.	The same as Fig. 5.2.20 but with Sanba case.	143
Fig. 5.3.21.	The same as Fig. 5.2.21 but with Sanba case.	144
Fig. 5.3.22.	The same as Fig. 5.3.19 but in domain 64 km × 64 km.	145
Fig. 5.3.23.	The same as Fig. 5.3.20 but in domain 64 km × 64 km.	146
Fig. 5.3.24.	The same as Fig. 5.3.21 but in domain 64 km × 64 km.	147
Fig. 5.3.25.	The same as Fig. 5.1.24 but with Sanba case.	149

---

---

---

Fig. 5.3.26.

The same as Fig. 5.3.25 but with the domain 64  
km  $\times$  64 km.

150

---

# 1. Introduction

The typhoon has become an essential issue as it brings huge damage and its occurrence frequency has been increased since 2001 in Korea. Many analysis related to typhoon cases has been conducted with many different points of view. Park et al. (2006) found out the change of statistical characteristics of typhoons during 50 years (1954-2003) by analyzing the changes in air temperature and sea surface temperature. Kim et al. (2006) found out the increased heavy rainfall associated with typhoons after 1978. By Park and Lee (2007), synoptic features of typhoon Rusa was investigated by performing the numerical model MM5. Lee and Choi (2010) also used the numerical simulation (WRF) to examine the predictability of the torrential rainfall with the typhoon case of Rusa and its detailed mesoscale precipitation distribution. Kim et al. (2010) used WRF model and dropsonde data assimilation to reduce the typhoon track forecast and determine the sensitivities of storm activities during typhoon Sinlaku and Jangmi in 2008. Park et al. (2011) analyzed the characteristics of typhoon activity from 1977 to 2008 and divided it into two decades and revealed that rainfall increased in the later period due to certain factors led intensification of typhoons, such as warmer sea surface temperature and high humid mid-troposphere and weaker vertical wind shear in the domain. Kim et al. (2011) provided better sensitivity guidance for real-time targeted observation operations when using the MM5 model simulation. Kim et al. (2016) built quantitative statistical datasets from rainfall data during typhoon cases from 1966 to 2009 and analyzed the characteristics of typhoon activity (e.g., TC genesis location, TC path, recurving position, and intensity) and related spatio-temporal changes in rainfall. Kim and Moon (2019) estimated rainfall in typhoons approached Korea during 2001 – 2016 and classified in different types of wind, rain, or wind/rain dominant to guide better prediction with satellite estimated rainfall data.

July, August, and September in 2012, three typhoons (Khanun, Bolaven and Sanba) struck South Korea in each month passing through Jeju Island to the Korean peninsula leading to severe damages. Jeju island is located in the southern part of Korea and is where all of the typhoons made the first landfall. On this island, there are two S-band Doppler radars on the east and west coast operated by Korea Meteorological Administration (KMA) which is useful to obtain the data for radar analysis.

In the past years, many case studies of typhoons were carried out to analyze the phenomenon with the help of two radars on Jeju island. Recently, Yoo and Ku (2017) used radar and rain gauge data to see the orographic effect on the rainfall rate field during typhoon Nakri in 2014. Lee et al. (2018) studied the microphysical process with the orographic effect by analyzing dual Doppler analysis with the radar and numerical model CReSS during typhoon Khanun. Kim et al. (2018) obtained echo motion vectors from the radar to use Variational Echo Tracking (VET) method for nowcasting of precipitation system including six typhoon cases during 2011-2013.

However, there is a lack of studies investigating the linearity of the typhoon especially by using radar data. To see the detailed linearity of the typhoon, the multifractal framework was applied in this study by using the rainfall rate dataset obtained from the radar.

The multifractal framework is known as one of the convenient methods to analyze the variable fields over a wide range of space-time scales in geophysical fields such as rainfall. With the development of multifractals framework, it became possible to define stochastic processes modeling rainfall with the help of the physically meaningful parameters. These parameters characterize how the cascade process concentrates the “activity” of a field (e.g., the precipitation rate above a given threshold) at smaller and smaller scales on smaller and smaller fractions of the space. These sets are some small that their dimension is only fractal, not that of the embedding space, and it is smaller and smaller for higher and higher levels of activity (e.g., Parisi and Frisch (1985), Schertzer and Lovejoy (1987)).

There are various examples of case studies of precipitations such as applying a multifractal approach relating to the shape of the cloud system and rain areas (Lovejoy, 1982) or applying the multifractal framework relating to the shape of a cloud system to rainfall intensity (Schertzer and Lovejoy, 1984). As the multifractals are likely the cascade process output, they have been developed and applied in many analyses and simulations in geophysical fields revealing extreme variabilities over a wide range of scales. (Schertzer and Lovejoy, 1987; Gupta and Waymire, 1993; Harris et al., 1996; Marsan et al., 1996; De Lima and Grasman, 1999; Deidda, 2000; Biaou, 2004; Macor et al., 2007; De Montera et al., 2009; Tchiguirinskaia et al., 2011; Gires et al., 2013; Hoang et al., 2014). Also, the extreme rainfall events were investigated by using multifractal analysis in Hubert et al. (1993), Schertzer et al. (2007), and Schertzer et al. (2010). It also covered explaining the climate by Royer et al. (2008) and Lovejoy and Schertzer (2013). The fractal theory expanded the use

for prediction in Marsan et al. (1996), Schertzer and Lovejoy (2004) and Macor et al. (2007).

Despite the benefits of the multifractal framework, there had not been many studies of typhoons since Chygrynskaia et al. (1995) and Lazarev et al. (1995) on 1D multifractal analysis of the wind field. In Korea, there are only a few studies conducted with the multifractal approach in the meteorological aspect in typhoon cases. Kim et al. (2008) presented a singularity of rainfall to provide evidence of multifractality in four cities in Korea. They found the chaotic property of the moving speed of typhoons is more robust than that of the other three meteorological factors. However, it was not aimed to analyze the precipitation of the typhoon nor did it use the radar data. Also, it was only focused on finding out the multifractal behavior of the chosen factors obtained from the typhoon information provided by KMA.

Therefore, the first motivation of this study is that not enough research was carried out by the approach of explaining the nonlinearity and nonstationary in the multifractal structure by performing the multifractal analysis of typhoons, especially with using the radar data.

Performing the high-resolution numerical experiment for a typhoon is a generally known way to validate the result of observation (Sun and Lee, 2002; Shin and Lee, 2005; Cho and Lee, 2006; Hong and Lee, 2009; Yu and Lee, 2010; Choi et al., 2011). These modeling studies enabled some significant discrepancies between the simulation and observation in both the location and amount of heavy rainfall. In this study, the validation was performed with the numerical model called Cloud Resolving Storm Simulator (CReSS) simulation which provides the high-resolution simulations of high-impact weather systems that are often used for typhoon case studies. Wang et al. (2013) proved that the high-resolution performance of CReSS gave better prediction with the heavy rainfall during the typhoon Morakot. Wang (2015) mentioned that the CReSS model performs the best in the prediction of extreme rainfall events. Also, Chen et al. (2017) used the model to find out the reason of prolonged duration time of the heavy rainfall occurred in Taiwan and Tsujino et al. (2017) revealed that the structure of the outer eyewall plays important roles in the maintenance of long-lived concentric eyewalls by using the CReSS model. The simulation performed for these studies also relatively well capture the location and intensity of the maximum rainfall.

The second motivation of this study is to understand the better dynamics and rainfall by multifractal spatial-temporal analysis with the help of the

measurements of the typhoons by comparing two S-band Doppler radars and the numerical model simulation (CReSS).

The rest of this study is organized as follows. In chapter 2, the explanation of the dataset that was used in this study. Followed up by the chapter 3, the procedure of preparing the dataset of rainfall rate is presented as well as the procedure and the detailed description of the method of the wind field retrieval analysis to find the three-dimensional structure of typhoons (Khanun, Bolaven, and Sanba) during the landfall in Jeju Island. The analysis methodology is described in chapter 4, and the results of the environmental field during each event, wind field analysis and the multifractal analysis by radar data and by the numerical model CReSS are discussed in chapter 5. Finally, some concluding remarks are drawn in chapter 6.

## 2. Data

### 2.1. Typhoon track data

Three typhoons that struck South Korea passed through Jeju Island in 2012. Typhoon Khanun was a typhoon with relatively small among the three

typhoons but bringing 400 mm of rain with the maximum wind speed of  $24.7 \text{ ms}^{-1}$  (55.3 mph), which passed through the southwest side of the Korean peninsula after passing Jeju island. Typhoon Bolaven passed Jeju Island when it was in a phase of weakening stage, but it brought more than 250 mm of the rainfall amount in 2 days with the wind gusts measured up to  $51.8 \text{ ms}^{-1}$  considered as the most powerful storm in nearly a decade. Typhoon Sanba was also a strong typhoon with the minimum center pressure reaching 900 hPa and recorded the maximum wind speed of  $55.9 \text{ ms}^{-1}$  (125 mph) and brought 400 mm of rainfall. After passing Jeju Island, it moved to North Korea, passing through the middle of the Korean peninsula.

The location of the typhoon center (the longitude and latitude) is gathered with the maximum wind speed to demonstrate the intensity of each typhoon. It was given information from the national typhoon center in KMA (Korea Meteorological Administration). The general information of typhoon is updated in real-time containing the location and the minimum pressure of typhoon center, the maximum wind speed, the radius of the typhoon, intensity, size, direction, and speed of the movement of the typhoon.

## 2.2. Automatic weather station (AWS)

An AWS is an automated weather station to measure from remote areas. It will typically contain the data logger and save the data from meteorological sensors. The AWS measures the surface data of the rainfall, temperature, humidity pressure, wind speed, and wind direction. Some stations also have additional instruments, but most of the stations have a thermometer, anemometer, wind vane, hygrometer, and barometer. In Korea, there are 510 sites in total, and the data that were used in this study was obtained from 237 sites, including all the sites (35 sites) in Jeju Island. The locations and the daily accumulated rainfall was obtained to see the accumulated rainfall patterns in each typhoon.

## 2.3. NCEP/NCAR reanalysis data

NCEP/NCAR reanalysis data was provided from Earth system research laboratory and National Oceanic and Atmospheric Administration (NOAA) Office of Oceanic and Atmospheric Research (OAR) laboratories. The NCEP/NCAR reanalysis data has been used to perform data assimilation since 1948. The data contains global grids of spatial coverage and 4-time daily, daily, and monthly temporal coverage with 17 pressure levels and 28 sigma levels (Kalnay et al., 1996). The dataset of wind u, v, air temperature, geopotential height, relative humidity, potential temperature,

and precipitation was used to construct the weather chart for each case.

#### 2.4. Doppler Radar data

The radar dataset was obtained when the typhoon approached Jeju Island on each case. The primarily selected radar site is Gosan (GSN, 33.29°N, 126.16°E, 103 m asl (above sea level)), Seongsanpo (SSP, 33.38°N, 126.88°E, 18.62 m asl) in Jeju Island operated by KMA covering a radius of 360 km and records the sets of volume distribution of reflectivity and Doppler radial velocity every 10 minutes. The obtained radar data was interpolated into a Cartesian coordinate system with horizontal and vertical grid intervals of 1 km and 0.25 km, respectively. A Cressman-type weighting function was used for the interpolation (Cressman, 1959).

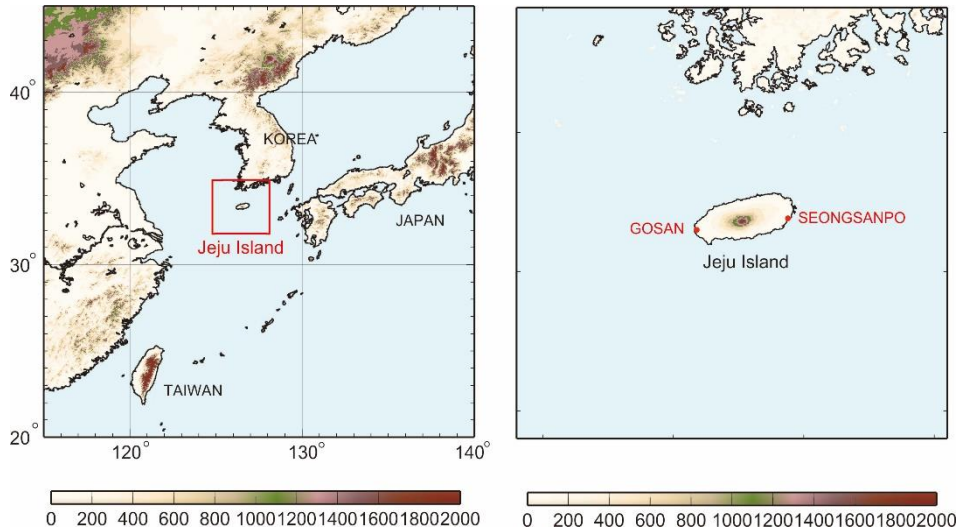


Fig. 2.1. The map of the selected area for this study indicated with the red box and the radar observation sites shown with the red dots (Gosan and Seongsanpo) in Jeju Island, Korea.

#### 2.5. Cloud Resolving Storm Simulator (CReSS)

Cloud Resolving Storm Simulator (CReSS) is a 3-dimensional non-hydrostatic model developed by the Hydrospheric Atmospheric Research Center (HyARC) of Nagoya University, Japan (Tsuboki and Sakakibara, 2002). It is a three-dimensional, regional, compressible non-hydrostatic model, and this numerical model uses a Cartesian horizontal coordinate system follows a terrain-following coordinate and was projected to with a Lambert conical projection. With this coordinate system, the equations for 3-dimensional momentum, pressure, and potential temperature ( $\theta$ ) are generated which is described in detail by Tsuboki and Sakakibara (2002).

The equations used in this model include all types of waves, such as Rossby waves, acoustic waves, and gravity waves.

A severe thunderstorm is composed of intense convective clouds. Since convective clouds are highly complicated systems of the cloud dynamics and microphysics, it is required to formulate detailed cloud physical processes as well as the fluid dynamics. Cloud physical processes in CReSS are formulated by a bulk method of cold rain (e.g., Lin et al., 1983; Cotton et al., 1986; Murakami, 1990; Ikawa and Saito, 1991; and Murakami et al., 1994). The bulk parameterization of cold rain considers water vapor, rain, cloud, ice, snow, and graupel (See, Fig. 2.2.).

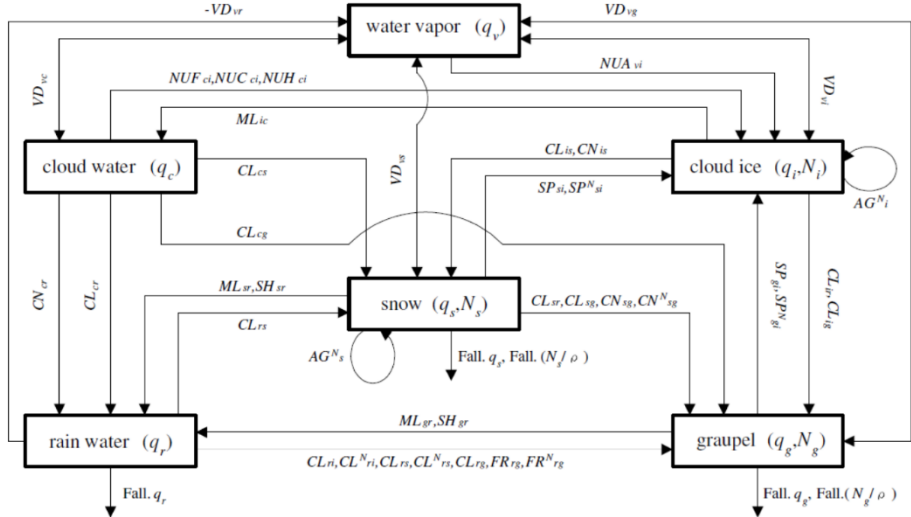


Fig. 2.2. The schematic diagram of microphysical process used in the model calculation.

The initial and lateral boundary conditions were provided by Japan Meteorological Agency Global Spectral model (JMA-GSM) which is a reanalysis data as Grid-Point-Values (GPV) database. It has one of the highest horizontal resolutions of 0.1875 degrees (approximately 20 km) with a time interval of 6 hours. JMA-GSM is more used for deep convection simulation such as typhoon cases since it produces the data up to 10 hPa which contains the information of the lower stratosphere and can detect the effect of significant gravity wave propagation in the upper-level atmosphere. Also, to set the surface fluxes of momentum and energy and surface radiation processes, the sea surface temperature (SST) was used by using one-dimensional, vertical heat diffusion equation (Kondo, 1976; Louis et al., 1981; Segami et al., 1989) are included in the

underground layer for ground temperature prediction. The SST at the initial time is calculated from the dataset of NEAR-GOOS Regional Real-Time Data Base, and it is provided by the Japan Meteorological Agency (JMA). The land use data is used from the dataset of Global Land Cover Characteristics Data Base, which is provided by the U. S. Geological Survey.

The final variables that can be obtained are 3-dimensional wind components ( $u$ ,  $v$ , and  $w$ ), pressure perturbations ( $p'$ ) and potential temperature perturbations ( $\theta'$ ) from the mean state. This is in hydrostatic equilibrium at the starting time of model integration. It can also conduct hydrometeor variables such as mixing ratios of water vapor( $q_v$ ), cloud water( $q_c$ ), rain( $q_r$ ), cloud ice( $q_i$ ), snow( $q_s$ ), and graupel( $q_g$ ), as well as the number densities of cloud ice( $N_i$ ), snow( $N_s$ ), and graupel ( $N_g$ ). Moreover, zonal velocity at an altitude of 10 m ( $us$ ), meridional velocity at an altitude of 10 m ( $vs$ ), pressure at an altitude of 1.5 m ( $ps$ ), potential temperature at an altitude of 1.5 m ( $pts$ ), soil and sea surface temperature ( $qvs$ ), sensible heat over surface ( $tgs$ ), latent heat over surface ( $le$ ), global solar radiation ( $rgd$ ), net downward short wave radiation ( $rsd$ ), downward longwave radiation ( $rld$ ), upward longwave radiation ( $rlu$ ), cloud cover in lower layer ( $cdl$ ), middle layer ( $cdm$ ) and upper layer ( $cdh$ ), averaged cloud cover ( $cda$ ), surface momentum flux for x ( $usflx$ ) and y ( $vsflx$ ) components of velocity, surface heat flux ( $ptsflx$ ), surface moisture flux ( $qvsflx$ ), cloud waterfall fall rate ( $pcr$ ), accumulated cloud waterfall ( $pca$ ), rainfall rate ( $prr$ ), accumulated rainfall ( $pra$ ), cloud ice fall rate ( $pir$ ), accumulated cloud ice fall ( $pia$ ), snowfall rate ( $psr$ ), accumulated snowfall ( $psa$ ), graupel fall rate ( $pgr$ ), accumulated graupel fall ( $pga$ ) can be obtained.

The CReSS model has been used to study many aspects of typhoons (Akter and Tsuboki, 2012; Wang et al., 2012; Tsuboki et al., 2015). In this study, only the rainfall rate ( $prr$ ) was used after all the calculation was conducted.

### 3. Data Processing

#### 3.1. Radar rainfall rate retrieval

The raw data of radar is in Universal Format (UF) which contains the header (mandatory, optional, data, field) and data (DZ, VR, SW, and CZ). The mandatory header includes the information of radar site, the number of sweeps and rays, altitudes angle and azimuth angle. The optional header or local use

header is not commonly used. The data header includes the type of data and the location of where the data is saved. The field header includes the beam width, Nyquist velocity, the number of the bin, and scale factor. The data includes uncorrected reflectivity, radial velocity, spectrum width, and corrected reflectivity.

In this study, corrected reflectivity was used for rainfall rate retrieval. In order to obtain the rainfall rate, the three Cartesian components of reflectivity were calculated. The rainfall rate was computed in separated heights from the reflectivity of Gosan radar, one of the two radars, by using the Z-R relationship ( $Z = aR^b$ , radar reflectivity factor  $Z_{(mm^6m^{-3})}$ , rain rate  $R_{(mm h^{-1})}$ ) with the values of  $a=250$  and  $b=1.2$ , which are the parameters usually used for tropical convective systems.

The retrieved dataset was used for multifractal analysis which was performed on the area of  $256 \text{ km} \times 256 \text{ km}$  at various altitudes, especially where there was the maximum rainfall amount. Further analysis was performed to cover the limitation of missing data due to the lowest elevation scan angles with the smaller domain with the lower altitudes, the size of  $64 \text{ km} \times 64 \text{ km}$ .

### 3.2. Wind field retrieval

Doppler radar is known as a powerful instrument for detecting radial velocity and reflectivity information with high spatial and temporal resolution from the weather system. With the Doppler effect, the Doppler radial wind can be obtained as :

$$f_d = \frac{-2}{\lambda} V_r \quad (3.1)$$

where  $f_d$  is Doppler shift,  $V_r$  is radial wind and wavelength  $\lambda$ . In this case, Positive  $V_r$  means the wind is blowing away from the radar and negative means the wind is blowing toward the radar. To obtain the wind component from a radial velocity at the observation point, a spherical earth coordinate system  $(\gamma, \theta, \varphi)$  is used with x and y.

However, to gain the three-dimensional wind component, the traditional method of dual-Doppler wind retrieval is presented by Armijo (1969). This

study discovered that combining multiple Doppler radars can obtain a three-dimensional wind structure. This technique only needs one interpolation from a regular Cartesian grid to irregular radar observation points due to the Doppler velocity data interpolated into the Cartesian coordinate system by using a Cressman filter (Cressman, 1959).

$$\mathbf{r} \cdot \mathbf{V}_r = ux + vy + (w + V_t)z \quad (3.2)$$

$r$  which is the distance between the grid point,  $u$ ,  $v$ , and  $w$  is the wind component at the specific grid point.  $V_t$  is the terminal velocity of a raindrop which can be estimated from reflectivity.

To calculate  $u$  and  $v$  by using two Doppler radar, it is assumed the  $w=0$ .

$$\text{Radar 1 : } r_1 \cdot V_{r1} = ux_1 + vy_1 + wz_1 \quad (3.3)$$

$$\text{Radar 2 : } r_2 \cdot V_{r2} = ux_2 + vy_2 + wz_2 \quad (3.4)$$

$$u = \frac{r_1 y_2 v_{r1} - r_2 y_1 v_{r2}}{y_2 x_1 - y_1 x_2} \quad (3.5)$$

$$v = \frac{r_2 y_1 v_{r2} - r_1 y_2 v_{r1}}{y_2 x_1 - y_1 x_2} \quad (3.6)$$

By applying  $u$  and  $v$  to vertical integration of the continuity equation,  $w$  can be obtained.

$$\int_{H_1}^{H_2} \frac{\partial w}{\partial z} dz = - \int_{H_1}^{H_2} \left( \frac{\partial u}{\partial x} + \frac{\partial v}{\partial y} \right) dz \quad (3.7)$$

When calculating the vertical integration, it is assumed  $H_1$  is very close to

the ground that we can assume  $w = 0$ . Then vertical integration can be done upward to get  $w$  at any certain height. Or it can be assumed that it is much higher than the echo top and vertical integration can be done downward. Once  $w$  is obtained, it forms an iteration loop to obtain the wind components in the selected domain.

However, this traditional method has limitations that it needs over-lapped data coverage and the wind along the radar baseline between two radars cannot be obtained. Also, the error can be accumulated due to inaccurate top and bottom boundary conditions for  $w$ .

To supplement these limitations, a variational method was developed by Gao et al. (1999, 2004). This method estimates the 3-dimensional wind field by using radial velocity and it prevents the accumulation of errors in the vertical velocity. This method minimizes the sum of squared errors which is indicated a cost function ( $J$ ), due to discrepancies between observations and analyses and additional constraint terms such as the cost functions  $J_O, J_B, J_D$ , and  $J_S$ . The iteration loop of calculation is performed until  $\delta J = 0$ .

$$J = \iiint \sum_{n=1}^m (\text{cost functions})^2 dx dy dz \quad (3.8)$$

Each cost function that was used in this study is defined as follows:

$$J = J_O + J_B + J_D + J_S \quad (3.9)$$

$$J_O = \frac{1}{2} \sum_m \lambda_m (V_r^m - V_{r,ob}^m)^2 \quad (3.10)$$

$$J_B = \frac{1}{2} [\sum_{i,j,k} \lambda_{ub} (u - u_b)^2 + \sum_{i,j,k} \lambda_{vb} (v - v_b)^2 + \sum_{i,j,k} \lambda_{wb} (w - w_b)^2] \quad (3.11)$$

$$J_D = \frac{1}{2} \sum_{i,j,k} \lambda_D D^2 \quad (3.12)$$

$$J_S = \frac{1}{2} [\sum_{i,j,k} \lambda_{us} (\nabla^2 u)^2 + \sum_{i,j,k} \lambda_{vs} (\nabla^2 v)^2 + \sum_{i,j,k} \lambda_{ws} (\nabla^2 w)^2] \quad (3.13)$$

$J_O$  is the difference of radial velocity components derived from  $u$ ,  $v$ , and  $w$  at each grid point in Cartesian coordinates from the analyses ( $V_r^m$ ) and radial velocity components interpolated to each grid point from observations ( $V_{r_{ob}}^m$ ) (Eq. 3.10). The index  $m$  is the number of radars, and  $u$ ,  $v$ , and  $w$  are wind components in Cartesian coordinates ( $x$ ,  $y$ ,  $z$ ) where  $i$ ,  $j$ , and  $k$  indicate a spatial location in the  $x$ ,  $y$ , and  $z$  directions. The cost function is evaluated at each grid point in the Cartesian coordinates, rather than in spherical coordinates.

The second term of the cost function  $J_B$  calculates the differences of variational analysis to the background fields ( $u_b$ ,  $v_b$ ,  $w_b$ ) that can be obtained from sounding or model simulation as examples (Eq. 3.11). However, in this study, the background fields were not used.  $J_D$ , the third term imposes a weak anelastic mass constraint on the analyzed wind field. The last term is a smoothness constraint  $J_S$  that reduces the noise in the analyzed field. Each cost function has a weighting by a factor for its accuracy, and each of them will produce a different result for the best fit solution. Therefore, the derivative of  $J$  must be differentiable.

$$D = \frac{\partial \bar{\rho}u}{\partial x} + \frac{\partial \bar{\rho}v}{\partial y} + \frac{\partial \bar{\rho}w}{\partial z} \quad (3.14)$$

where  $\bar{\rho}$  is the mean air density at the horizontal level.

$$V_r = u \sin \theta \cos \phi + v \cos \theta \cos \phi + (w + w_t) \quad (3.15)$$

$w_t$  is the terminal velocity of precipitation.  $\phi$  and  $\theta$  is the azimuth and elevation angles.

Also, in the cost function, there exist several coefficients such as  $\lambda_{us}$ ,  $\lambda_{vs}$  and  $\lambda_{ws}$  are commonly referred to as penalty constants. These are the scalar coefficients corresponding to matrices used in general data assimilation methods. The parameter settings are identical to those used by Gao et al. (1999) ( $\lambda_m = 1$ ,  $\lambda_d = 1/(0.5 \times 10^5)^2$ ,  $\lambda_{us} = \lambda_{vs} = \lambda_{ws} = 5.0 \times 10^{-3}$ , and  $\lambda_b = 0$ ). The calculation error in the vertical velocity is significant at upper

levels because of signal noise. To account for this uncertainty, airflows are shown only below 8 km above sea level (ASL), and the description of the airflow structure focuses only on the lower and middle levels of the precipitation system.

After, Shimizu and Maesaka (2006) modified the original method of Gao et al. (1999) to apply rigid wall conditions at the top and bottom boundary and evaluated the accuracy of the wind estimated by the method. The components of the gradient of  $J$  can be minimized through several iterations to reduce the cost function to a smaller magnitude. It is as follows:

$$\frac{\partial J}{\partial u} = \lambda_o(-\sin \phi \cos \theta) \times (V_{r,ob}^m - V_r^m) + \lambda_B \times (u - u_b) - \lambda_D \bar{\rho} \frac{-\partial D}{\partial x} - \lambda_{Su} \nabla^2(\nabla^2 u) \quad (3.16)$$

$$\frac{\partial J}{\partial v} = \lambda_o(-\cos \phi \cos \theta) \times (V_{r,ob}^m - V_r^m) + \lambda_B \times (v - v_b) - \lambda_D \bar{\rho} \frac{-\partial D}{\partial y} - \lambda_{Sv} \nabla^2(\nabla^2 v) \quad (3.17)$$

$$\frac{\partial J}{\partial w} = \lambda_o(-\sin \theta) \times (V_{r,ob}^m - V_r^m) + \lambda_B \times (w - w_b) - \lambda_D \bar{\rho} \frac{-\partial D}{\partial z} - \lambda_{Sw} \nabla^2(\nabla^2 w) \quad (3.18)$$

### 3.3. CReSS rainfall rate retrieval

The simulation was done with the horizontal grid resolution was 1 km  $\times$  1 km with a mesh size of 361 km  $\times$  361 km. The vertical grid resolution of 0.5 km contained 40 levels, ranging from near the surface level at 50 m to the top level at 15 km which was set according to the domain size of the radar as well as the duration of each time step (10 minutes). It is selected to include the frozen precipitation in the high altitudes since the scale of the typhoon was very large. Figure 3.1 shows the selected domain for the simulation. The vertical calculation is done with the terrain following coordinate that terrain

effect was also considered during the calculation and the rainfall rate parameter is instantaneous rainfall rate which can be obtained as one of the output parameters. The rainfall rate is calculated with the equation of  $\rho V_t \times \left(\frac{dq_l}{dz}\right)$ , where  $\rho$  is the density,  $V_t$  is terminal velocity of each condensate,  $dz$  is the differential of height in the chosen domain, and  $q_l$  is the mixing ratio for each condensate.

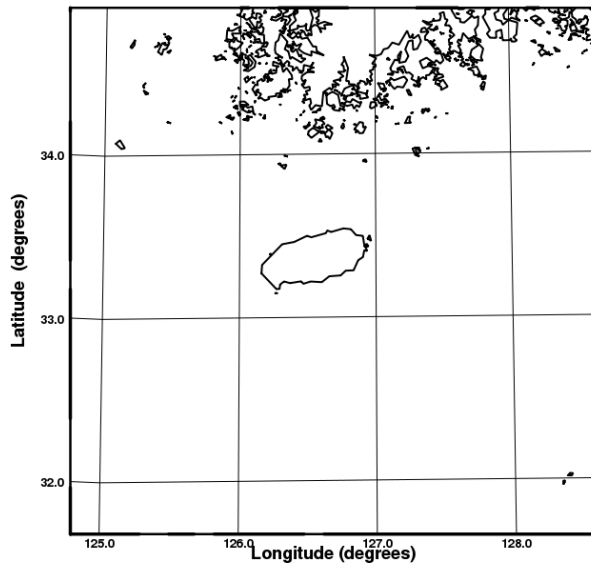


Fig. 3.1. The map of the selected domain when using the numerical model CReSS.

## 4. Multifractal

### 4.1. Fractal dimensions

The fractal structure has a fractal dimension, which is non-integer and quantifies the sparseness of the set. This fractal dimension shows how much the object fills the total space. The conventional technique to estimate a fractal dimension is the box-counting method. In this method, when  $\lambda \rightarrow \infty$ , there is

a power-law relation between the fractal dimension and the number of non-empty pixels of the set  $N_\lambda$  at the scale  $\lambda$ .

$$N_\lambda \approx \lambda^{D_f} \quad (4.1)$$

If we count the numbers of boxes and some of them are empty and some of them are not, the ones that are not empty can be represented as  $N(\ell)$ . Finally, the fractal dimension is given by;

$$N_\lambda(\ell) = \lambda^{D_f} \Rightarrow D_f = \lim_{\lambda \rightarrow \infty} \frac{\ln N}{\ln \lambda^{-1}} = \lim_{\ell \rightarrow 0} \frac{\ln N_\lambda(\ell)}{\ln \ell} \quad (4.2)$$

If  $D_f$  is equal to zero, it means that the area A filled by statistical quantities doesn't exist;  $N_\lambda = 1$  independently of the resolution (it doesn't matter how high the resolution is or how small the pixel is, that there is only one segment of area A so small that it cannot split into more exceptional segments). On the contrary, if  $D_f = D$  ( $= 2$  in this 2D case) it means that the whole area R is covered with the area A, so the probability that pixel will contain information about area A equal to 1.

This consists of plotting on a log-log scale of  $N_\lambda$  by  $\lambda$  and because of the scaling invariance behavior of a fractal set by using Eq. 4.1, the slope of the straight line will be approximately  $D_f$ .

To obtain the fractal dimension from the typhoon case, the rainfall data obtained from the radar reflectivity when the maximum reflectivity showed on the top of the mountain in Jeju Island, the altitude 5 km was selected as 500 hPa is the altitude that the typhoon cases are usually analyzed. Fig. 4.1 shows the schematic graph of the rainfall intensity on the typhoon reflectivity to help the understanding of  $D_f$ . The each grid point shows the rainfall intensity values and depending on the different threshold, the occurrence of the rainfall intensity in the selected domain is different. This leads to obtain the different fractal dimensions can be obtained depending on the different thresholds.

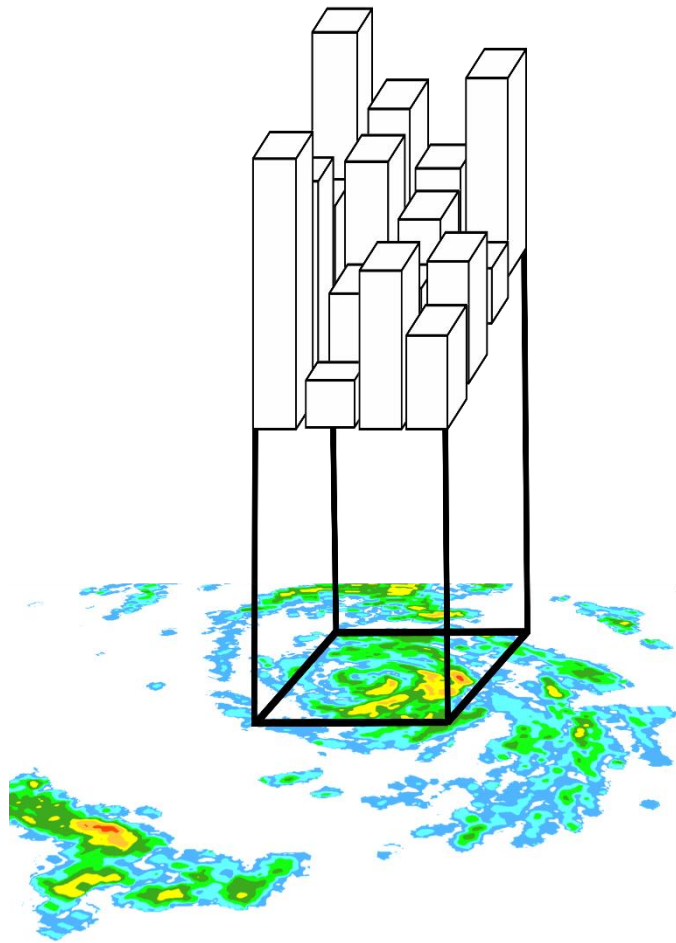


Fig. 4.1. The schematic diagram of the rainfall intensity on the selected domain of typhoon.

The fractal dimension of the three typhoon cases that were analyzed in this study is shown and explained below.

First of all, the fractal dimension was calculated with sizes of the domain at 5 km at 19:40 LST 18 July 2012 (Fig. 4.2). When the maximum reflectivity showed on the top of the mountain in Jeju Island, the altitude 5 km was selected as 500 hPa is the altitude that the typhoon cases are usually analyzed. When choosing the interested area, the maximum rainfall rate existed in both domains (256km × 256 km and 64 km × 64 km).

The threshold, in this case, was set to 1 (mm/hr) and it belongs to the geometrical set by being in a linear line with the slope of 1.618 (Fig. 4.2 (a),

graph line in black). The next threshold was increased to 3 (mm/hr) and the fractal dimension shows the size of geometrical set decreased with the slope of 1.163, but remains in a linear line (Fig. 4.2 (a), graph line in blue) as well as threshold 5 (mm/hr) shown in a graph line in red (Fig. 4.2 (a)). We can quantify how the fractal dimension changes with the threshold, and it means if the field is characterized, it needs to have more than one fractal dimension depending on each threshold. In Fig. 4.2 (c). It is also shown from the graph that the scaling behavior is linear depending on each threshold (1 mm/hr, 3 mm/hr, and 5 mm/hr). As the threshold is becoming larger, the linearity of the fractal dimension becomes smaller due to the existence of the rainfall field in the domain (Fig. 4.2 (b) and (d)).

Second, the fractal dimension was calculated with both sizes of the domain at 5 km at 2330 LST 27 August 2012 (Fig. 4.3). To see the fractal dimension, the thresholds were set to 1 (mm/hr) with the slope of 1.854 (Fig. 4.3 (a), graph line in black), 5 (mm/hr) with the slope of 1.602 (Fig. 4.3 (a), graph line in blue) and 10 (mm/hr) with the slope of 1.393 (Fig. 4.3 (a), graph line in red). The multifractal characteristics of scaling behavior is shown even up to threshold 10 mm/hr. In Fig. 4.3 (c), the scaling behavior is also shown linear depending on each threshold (1 mm/hr, 3 mm/hr, and 5 mm hr). Since the domain is small, the fractal dimension could be obtained up to the rainfall rate of 5 mm/hr. As the threshold is becoming more extensive, the linearity of the fractal dimension becomes smaller due to the existence of the rainfall field in the domain (Fig. 4.3 (b) and (d)).

Lastly, the fractal dimension was calculated with both sizes of the domain at 5 km at 0640 LST 17 September 2012 (Fig. 4.4). Fig. 4.4 (a) and (c) show that the scaling behavior is linear depending on each threshold (1 mm/hr, 3 mm/hr and 5 mm hr). The larger the threshold becomes the smaller the linearity of the fractal dimension becomes smaller due to the existence of the rainfall field in the domain (Fig. 4.4 (b) and (d)).

When the fractal dimension depends on the threshold defining a negligible intensity, the intuitive notion of multifractal fields arises. In all these cases, as the fractal dimension exists along with three different thresholds, it can be considered that the field is fully characterized by the multifractal behavior in both sizes of domains in each case.

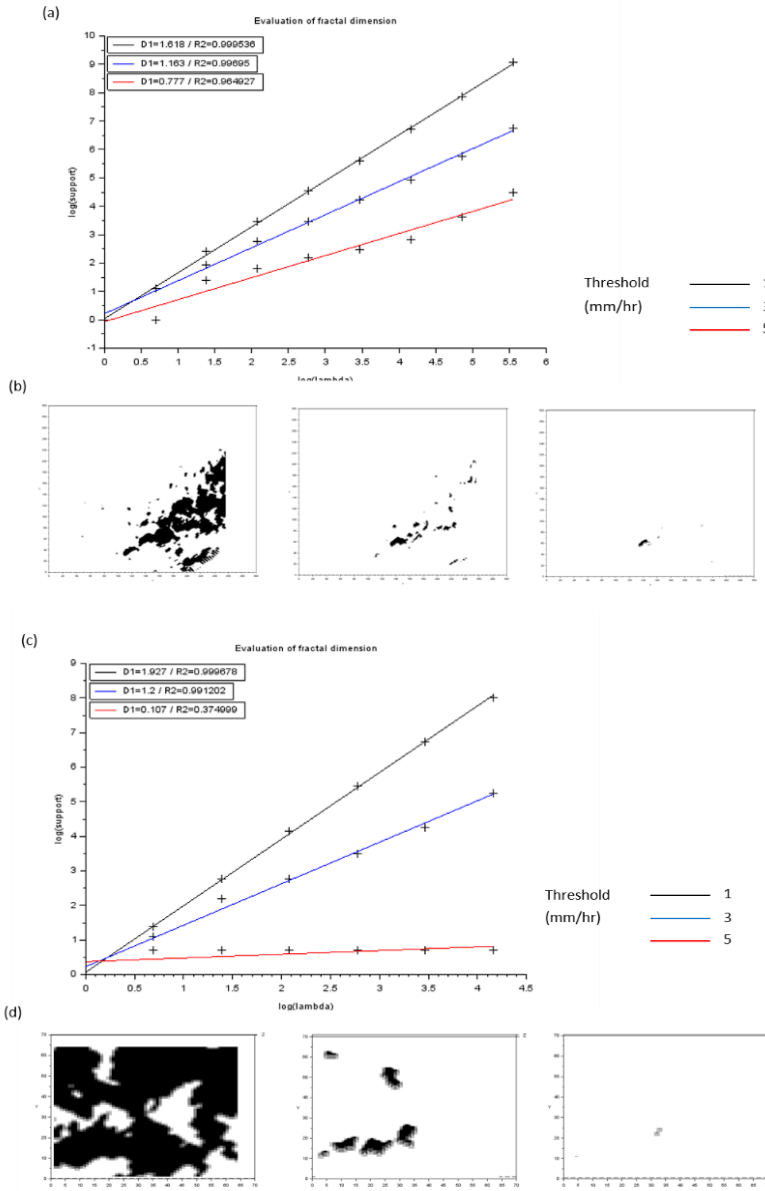


Fig. 4.2. The fractal dimension calculated at 1940 LST 18 July 2012 with (a) radar at 5 km with the domain size  $265 \text{ km} \times 265 \text{ km}$ , (c) in the domain size  $64 \text{ km} \times 64 \text{ km}$  with the threshold 1 mm/hr (black), 3 mm/hr (blue) and 5 mm/hr (red). (b) and (d) indicates the area with the rainfall field with the black shaded area along with the different thresholds.

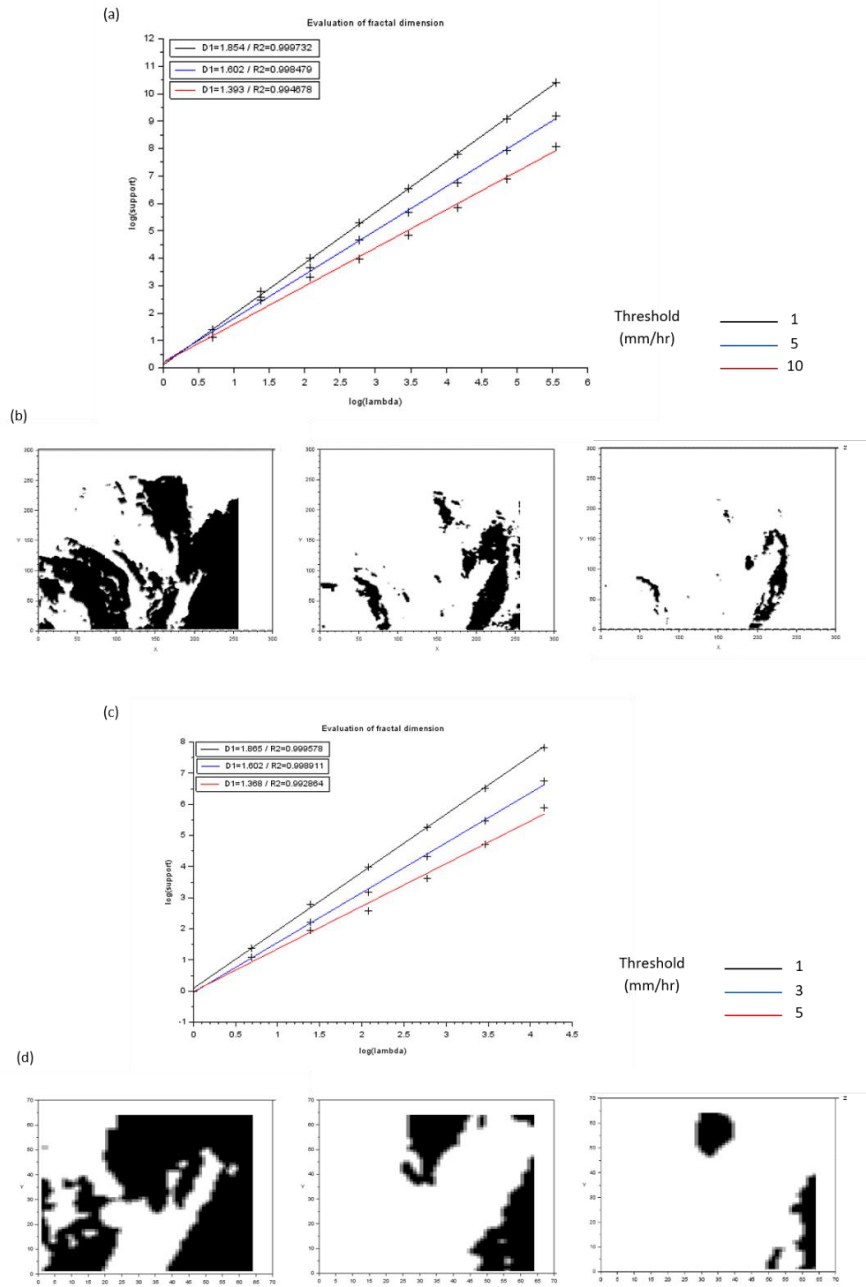


Fig. 4.3. The fractal dimension calculated at 2330 LST 27 August 2012. (a) radar at 5 km with the domain size of  $265 \times 265$  with the threshold 1 mm/hr (black), 5 mm/hr (blue) and 10 mm/hr (red), (c) in the domain size of  $64 \text{ km} \times 64 \text{ km}$  with the threshold 1 mm/hr (black), 3 mm/hr (blue) and 5 mm/hr (red). (b) and (d) indicates the area with the rainfall field with the black shaded area along with the different thresholds.

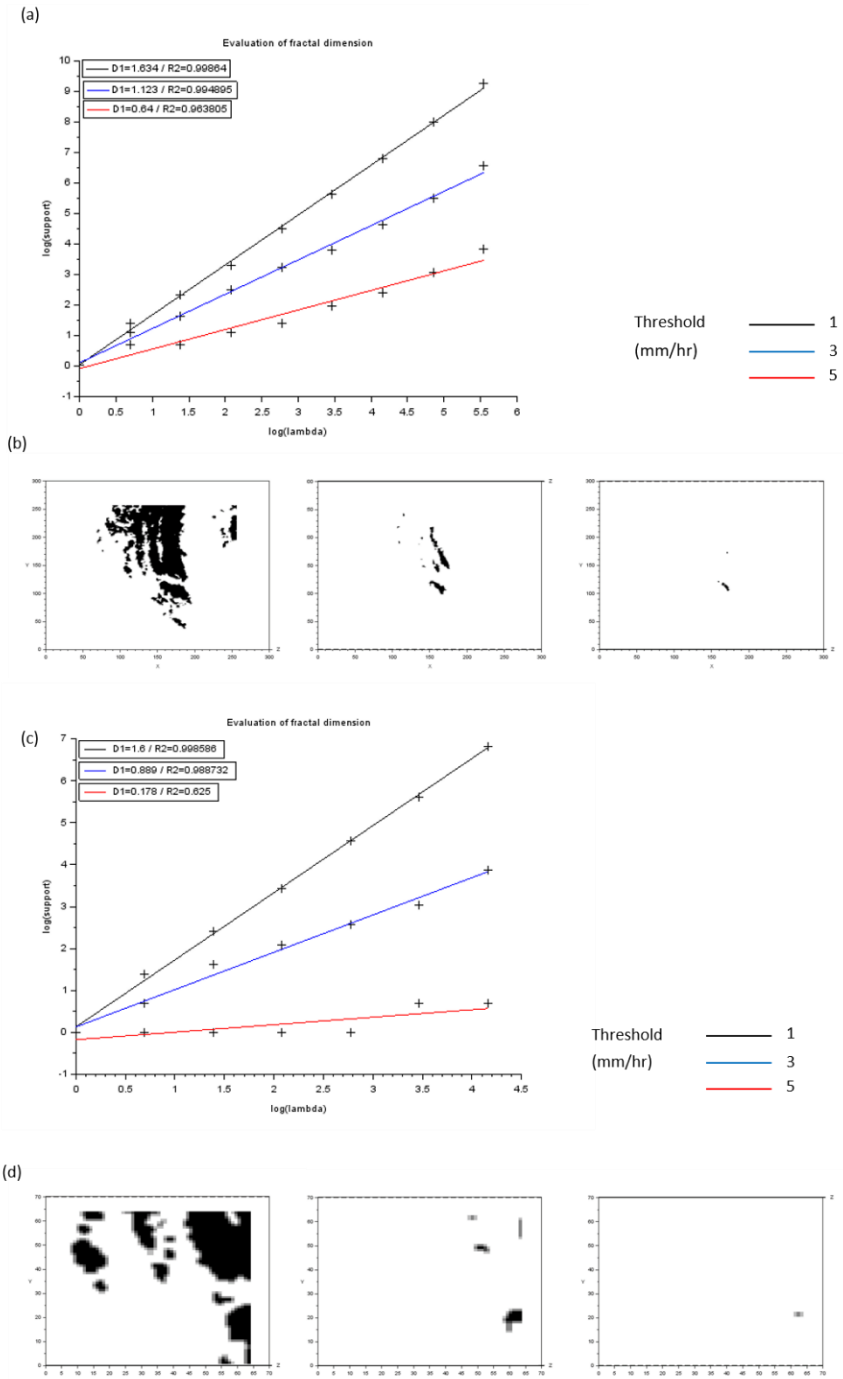


Fig. 4.4. The fractal dimension calculated at 1940 LST 18 July 2012 with (a) radar at 5 km with the domain size 265 km  $\times$  265 km, (c) in the domain size 64 km  $\times$  64 km with the threshold 1 mm/hr (black), 3 mm/hr (blue) and 5 mm/hr (red). (b) and (d) indicates the area with the rainfall field with the black shaded area along with the different thresholds.

## 4.2. The Universal Multifractals (UM)

### 4.2.1. Discrete cascade

The multifractals rely on the assumption of a geophysical field which is generated by a multiplicative cascade process (Schertzer and Lovejoy, 1984b, 1987a, 2011). Cascade phenomenology is based on the idea of the same phenomenon occurring at all scales. This makes the field to become more localized as the scales become small. There are three main properties for cascade phenomenology. First, the scale invariance, which shows the same phenomenon occurs independently of the resolution. Second, the conserved quantity, which means the average value of the observed field at all resolutions has to be the same. Lastly, the localness in Fourier space.

In the case of discrete cascades, estimating how to break structures into substructures should be done. Also the probability distribution of the random increment  $\mu\varepsilon$ . The assumption is that these two mentioned states are the same at all scales which can also be called scale-invariant. There are many models in the literature that are simulating cascade processes ( $\beta$  model,  $\alpha$  model, Universal Multifractals model, etc.).

Fig. 4.5 shows the illustration of the cascade phenomenon. The initial “activity”  $\varepsilon_0$  is uniform over a D-dimensional structure with the length of  $\ell_0 = \ell (\lambda = 1)$ . The each following step consists in breaking each structure into the  $\lambda_1$  smaller structures and multiplying their existing “activities” by the random variables  $\mu\varepsilon$ . After  $n$  steps of the cascade process, the initial activity will be divided into  $(\lambda_1^n)^D$  structures of lengths  $\ell_n = \frac{\ell_0}{\lambda_1^n}$  at the resolution of  $\lambda_1^n = \frac{\ell_0}{\ell_n}$ . The “activity” of each segment can be shown as  $\varepsilon_n = \mu\varepsilon \varepsilon_{n-1}$  (Fig. 4.5).

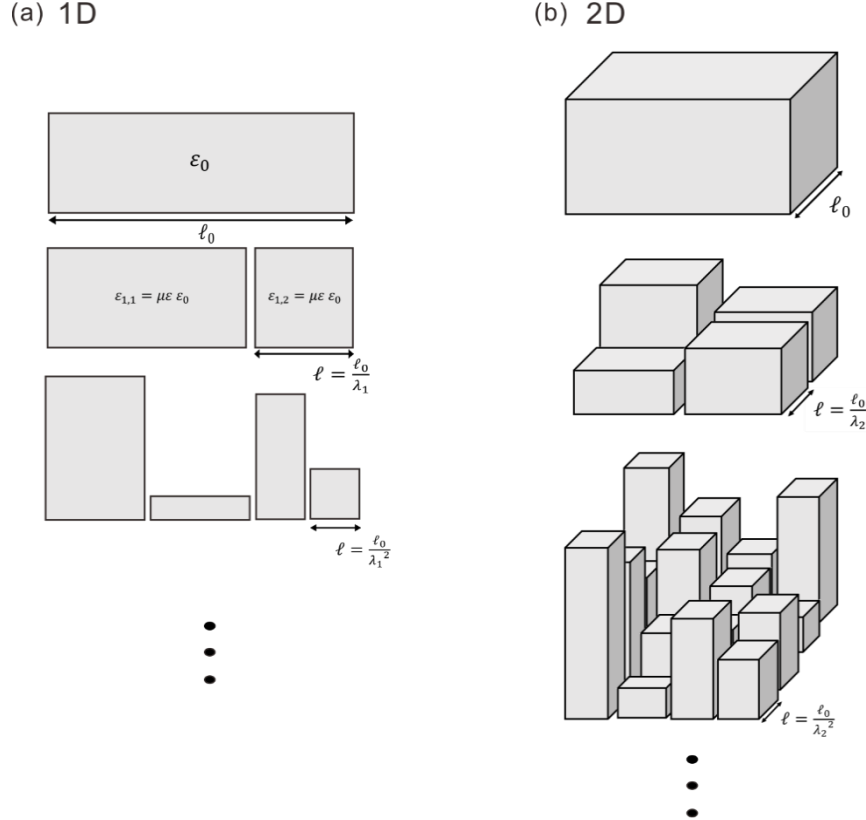


Fig. 4.5. Diagram of cascade phenomenon for (a) 1-dimension and (b) 2-dimension.

#### 4.2.2. Universal Multifractal Framework

Let us consider a specific multifractal field named  $\varepsilon_\lambda$  at a given resolution  $\lambda$ , which is the ratio between the outer scale  $\ell_0$  and the observation scale  $\ell$ . The probability of the scale with the threshold  $\lambda^\gamma$  can be expressed as:

$$P_r (\varepsilon_\lambda > \lambda^\gamma) \approx \lambda^{-c(\gamma)} \quad (4.3)$$

where  $\varepsilon_\lambda$  represents the renormalized intensity of the observed field,  $\gamma$  is the scale-invariant singularity, and  $c(\gamma)$  is the codimension function which describes the probability depending on the singularity  $\gamma$ .

In the fractal theory,  $P_r$  is changing only due to the change of the resolution  $\lambda$ , while in multifractal theory  $P_r$  depends on not only the resolution  $\lambda$  but also on the singularity  $\gamma$ .

Additionally, there is another way of describing the statistical properties of the multifractal field introduced by Schertzer and Lovejoy (1987). They introduced the scaling function  $K(q)$  which is convex and characterizes the multifractal field  $\varepsilon_\lambda$  depending on different variables of statistical moments of order  $q$ . This can be expressed as:

$$\langle \varepsilon_\lambda^q \rangle \approx \lambda^{K(q)} \quad (4.4)$$

where  $\langle \varepsilon_\lambda^q \rangle$  is the average statistical moment of order  $q$  indicates average value). According to Parisi and Frish (1985), by using inverse Legendre transform, the co-dimension function  $c(\gamma)$  and the moment scaling function  $K(q)$  are biunivocally linked with each other. This means that every moment of order  $q$  has the corresponding singularity  $\gamma$  and vice versa. Also, each  $c(\gamma)$  and  $K(q)$  can be presented as:

$$c(\gamma) = \max_q (q\gamma - K(q)) = q_\gamma \gamma - K(q_\gamma) \quad (4.5)$$

$$K(q) = \max_\gamma (q\gamma - c(\gamma)) = q\gamma_q - c(\gamma_q) \quad (4.6)$$

The function  $K(q)$  characterizes the statistical moments that there is a one-to-one correspondence between the moments (or  $q$ ) and probability distribution (or  $\gamma$ ).

The statistical properties of a multifractal field from Universal Multifractals scheme (Schertzer and Lovejoy 1987, Schertzer and Lovejoy 1997), defined by functions  $c(\gamma)$  and  $K(q)$ , can be described with only three universal relevant parameters:  $C_I$  (mean intermittency),  $\alpha$  (multifractality index), and  $H$  (non-conservation parameter).

$$K(q) = qH + \begin{cases} \frac{C_1}{\alpha-1} (q^\alpha - q) & \alpha \neq 1 \\ C_1 q \ln q & \alpha = 1 \end{cases} \quad (4.7)$$

$$c(\gamma + H) = \begin{cases} C_1 \left( \frac{\gamma}{C_1 \alpha'} + \frac{1}{\alpha} \right)^{\alpha'} & \alpha \neq 1 \\ C_1 e^{\left( \frac{\gamma}{C_1} - 1 \right)} & \alpha = 1 \end{cases} \quad (4.8)$$

where  $1 = \frac{1}{\alpha} + \frac{1}{\alpha'}$  for  $\alpha \neq 1$ . As it is explained earlier,  $c(\gamma)$  and  $K(q)$  functions describe the multifractal process with two main equations (Eq. 4.7 and 4.8). Universality is a term related to the processes that should be described with a large number of parameters, but only a small portion of them are relevant.

#### 4.2.3. UM parameters

As it was mentioned, in the framework of Universal Multifractals,  $c(\gamma)$  and  $K(q)$  can be described with three parameters:  $C_1$ ,  $\alpha$ , and  $H$ . The physical meaning of each of these parameters are as following:

- $C_1$  is the codimension of the mean singularity of the field. It measures the mean inhomogeneity in the homogeneous field where  $C_1 = 0$ . The more this parameter increases, the more the singularity of the average field is dispersed.
- $\alpha$  is called Levy's multifractality index. It can measure the degree of multifractality of the process. In other words, it describes how much sparseness varies as it goes away from the mean value of the field. The value of  $\alpha$  is in between 0 and 2. For example, if  $\alpha = 0$ , the field has a monofractal process, and if  $\alpha = 2$ , then the field is at the maximum of multifractality.
- $H$  is Hurst's exponent, which measures the degree of non-conservation of the field. When the value of  $H$  is close to 0, it indicates that the process is almost conservative.

#### 4.2.4. Critical values of moment order ( $q_s$ and $q_D$ )

In order to validate UM, theoretical  $K(q)$  function should be compared with the one obtained from the observation, called empirical  $K(q)$ . However, theoretical  $K(q)$  is able to simulate empirical one only up to the certain critical value of moment order. This critical value is related to what is called multifractal phase transition (Schertzer et al. 1992). It is estimated as  $q_c = \min(q_s, q_D)$ , where  $q_s$  is the maximum-order moment estimated with a finite number of samples and  $q_D$  is the critical moment order of divergence.

The value of  $q_s$  is related with the maximal observable singularity  $\gamma_s$  using Legendre transform and it can be determined using the following equation:

$$q_s = \left( \frac{D+D_s}{C_1} \right)^{1/\alpha} \quad (4.9)$$

For example, in the 1-dimensional field ( $D = 1$ ) with only one data sample is available ( $N_{sample} = 1$ , thus  $D_s = 0$ ), the critical value of moment order is usually  $q_c = q_s$ . This shows a linear behavior of the empirical  $K(q)$  for  $q \geq q_s$ .

Whereas, moment order  $q_D$  represents the critical value of  $q$  for which extreme values of the field is becoming so dominant that the average statistical moment of order  $q \geq q_D$  approaches to infinity:

$$\langle \varepsilon_\lambda^q \rangle = \infty, \quad q \geq q_D \quad (4.10)$$

Moment order  $q_D$  can be determined from the following equation:

$$K(q_D) = (q_D - 1)D \quad (4.11)$$

Determining the value of  $q_D$  can be graphically explained as the

intersection between the theoretical  $K(q)$  function and the linear regression  $K(q) = (q - 1)D$  which corresponds to the theoretical  $K(q)$  with  $C_1 = D$  and  $\alpha = 0$ . Therefore, when  $q_c = q_D$ , the empirical  $K(q)$  function starts approaching infinity for  $q \geq q_D$ .

### 4.3. Universal Multifractal analysis techniques

In order to determine  $C_1$  and  $\alpha$ , different methods can be applied. Probability Distribution Multiple Scaling (PDMS) technique (Schertzer and Lovejoy 1989, LaVallee 1991, etc.) is based on estimating  $c(\gamma)$  relying on the probability Eq. (4.4). On the other hand, trace moment (TM) and double trace moment (DTM) are based on the determination of the UM parameters from  $K(q)$  function properties (Eqs. 4.15 and 4.19). It was proved that PDMS is less reliable than two other techniques, which is a reason why TM and DTM techniques are used in this study (Gires, 2012).

#### 4.3.1 Spectral Analysis

Spectral analysis is used basically for checking the scaling behavior of the field. It shows a power-law relation between the power spectra and the wave number in spatial analysis or a power-law relation between the power spectra and frequency in the temporal analysis. The spectrum shows a power law with a spectral slope  $\beta$ , which can be expressed as follows:

$$E(k) = k^{-\beta} \quad (4.12)$$

The spectral exponent  $\beta$  is linked to the degree of non-conservation  $H$  of the field. When  $H=0$ , it means that the field is conservative.

$$\beta = 1 + 2H - K(2) \quad (4.13)$$

where  $H$  is the Hurst exponent and is 0 for a conservative field,  $K(2)$  is the second-moment scaling function of the conservative part of the field. For a conservative field, the estimate of  $\beta$  is lower than the dimension  $D$  of the embedding space. By Nykanen (2008), if  $\beta > D$ , the field has to be fractionally differentiated before implementing the multifractal analysis.

Once the scaling behavior and the conservativeness of the rainfall field have been done, the multifractal analysis can be performed. Two different methods widely used in geophysics can be used to assess, indirectly and directly, the UM parameters: Trace Moment (TM) (Schertzer and Lovejoy, 1987) and Double Trace Moment (DTM) (Lavallée et al., 1993) methods, respectively.

#### 4.3.2 Trace Moment Method

TM analysis is performed on a broad range of moments  $q$  in order to determine the statistical moment function  $K(q)$ , as presented in the Eq. (4.4). This method is based on the assumption that the field is conservative. The first step is to renormalize the field which can be described as the following:

$$\varepsilon_\lambda = \frac{\varepsilon_\lambda}{\langle \varepsilon_\lambda \rangle} \quad (4.14)$$

The mean value of the renormalized field is  $\langle \varepsilon_\lambda \rangle = 1$ . By averaging  $n$  (most commonly  $n = 2$ ) neighbor values of the field, resolution  $\lambda$  gradually decreases with factor  $n$  up to the uniform field ( $\lambda = 1$ ). At each resolution, the  $\varepsilon_\lambda$  field is raised on the power  $q$  and the average statistical moment of a given order  $q$  is calculated as follows:

$$\langle \varepsilon_\lambda^q \rangle = \frac{\sum_1^\lambda \varepsilon_\lambda^q}{\lambda^D} \quad (4.15)$$

After reaching  $\lambda = 1$ , average statistical moments at each resolution

$\lambda (\langle \varepsilon_\lambda^q \rangle)$  can be plotted versus the corresponding  $\lambda$  for different  $q$  values. If the graph is presented in log-log scale, plotted average moments  $\langle \varepsilon_\lambda^q \rangle$  should follow linear regression for every  $q$  value. It basically consists of taking the  $q^{th}$ -power of a multifractal field  $\varepsilon_\lambda$  at the highest resolution  $\lambda$ , to repeatedly calculate the ensemble average at different scales and to represent the resulting averages  $\langle \varepsilon_\lambda^q \rangle$  in a log-log plot as a function of  $\lambda$ . Once the values of  $K(q)$  are determined for each  $q$ , the UM parameters can be estimated by:

$$C_1 = K'(q) \quad (4.16)$$

$$\alpha = K''(q)/C_1 \quad (4.17)$$

where  $K'(q)$  is the first and  $K''(q)$  the second derivatives of  $K(q)$ , respectively.

#### 4.3.3 Double Trace Moment Method

Double Trace Moment (DTM) technique is also called the direct method (Lavallée et al. 1993, Schmitt et al. 1993) since it enables direct estimation of parameters  $C_1$  and  $\alpha$  after introducing theoretical  $K(q)$  function. DTM, as well as TM, is described on the assumption that the field is conservative.

It is a more reliable way of estimating UM parameters than the trace moment analysis as in the previous method. This technique is based on two steps. The first is to take the  $\eta^{th}$ -power of the conservative field  $\varepsilon_\lambda$ , at the highest resolution  $\lambda$ , and to normalize it:

$$\varepsilon_\lambda^{(\eta)} = \frac{\varepsilon_\lambda^\eta}{\langle \varepsilon_\lambda^\eta \rangle} \quad (4.18)$$

The TM method is applied to the normalized field  $\varepsilon_\lambda^{(\eta)}$ , obtaining the scaling moment function  $K(q, \eta)$  for each  $\eta$  value:

$$\langle \left( \varepsilon_{\lambda}^{(\eta)} \right)^q \rangle \approx \lambda^{K(q,\eta)} \quad (4.19)$$

From Eq. (4.4) and Eq. (4.16),  $K(q, \eta)$  can be presented as follows:

$$K(q, \eta) = \eta^\alpha K(q) = \eta^\alpha \frac{C_1}{\alpha-1} (q^\alpha - q) \quad (4.20)$$

Therefore, for a given  $q$  value,  $K(q, \eta)$  is plotted against  $\eta$  in a log-log plot, and the slope of the curve gives an estimation of  $\alpha$ . Then,  $C_1$  can also be estimated from the interception of the slope and the axis  $\log(\eta) = 0$ .

## 5. Three typhoon cases in 2012

### 5.1. Typhoon Khanun

#### 5.1.1. Environmental description

Typhoon Khanun was a tropical cyclone that made landfall over Korea directly on 12 July 2012. This thunderstorm typed typhoon with cold-core low formed a weak low pressure near northwest of Guam and gradually separated with lower-core and warm-core low which started to form convection. On 14 July, the system was formed as a tropical depression and it became a tropical storm on 16 July. On 17 July, it was developed to a severe tropical storm as the center of Khanun passed over Okinoerabujima Island, Japan. On 18 July, it made landfall over Jeju Island, bringing 400 mm of rain with the maximum wind speed of  $24.7 \text{ ms}^{-1}$  (55.3 mph) and continued to pass through the southwest side of the Korean peninsula. As the typhoon passes through Korea, it was weakened into a tropical depression and dissipated entirely on 22 July.

Fig. 5.1.1 plots the track of the typhoon Khanun with the dots indicating the location of the center of the typhoon that has the lowest pressure. The typhoon passed through the west side of Jeju Island and moved northwardly to the Korean peninsula. By the daily accumulated rainfall amount on 18th July 2012 as shown in Fig. 5.1.2., the maximum accumulated rainfall amount recorded up to 360 mm on the east side of the top of Halla mountain area in Jeju Island. Fig. 5.1.3 shows the values of typhoon center pressure and the maximum wind speed of the typhoon when the typhoon approaches the Korean peninsula.

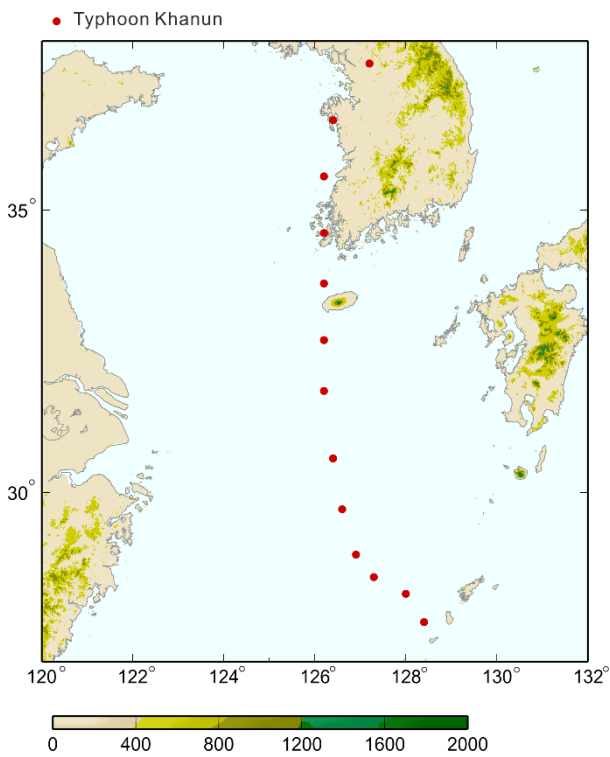


Fig. 5.1.1. The track of typhoon Khanun. The red dots indicate the location of the typhoon center.

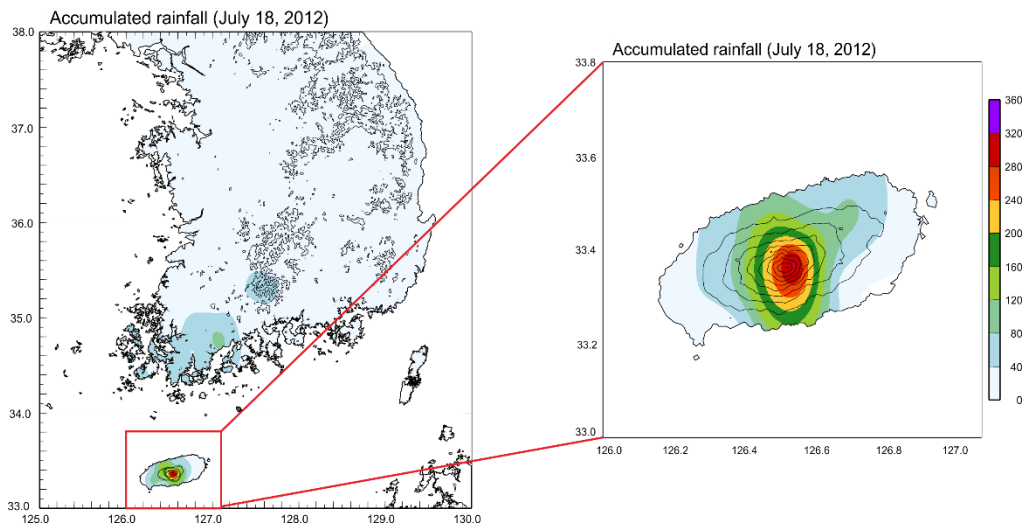


Fig. 5.1.2. The daily accumulated rainfall on 18 July 2012 in Korea.

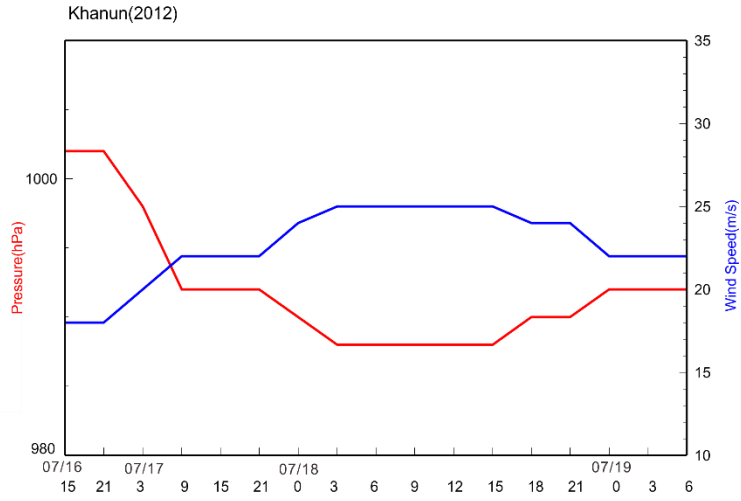


Fig. 5.1.3. The typhoon center pressure (hPa) in red and the maximum wind speed (m/s) in blue.

Fig. 5.1.4 shows the synoptic flow at 1200 UTC on 18 July 2012. The center of typhoon provided from NCEP/NCAR Reanalysis is found near Jeju Island (Fig. 5.1.4 (a)). The convergence areas were formed in the east part of the typhoon due to the southeast monsoon and confluence near the eyewall shows the steady rising motion of the air. The equivalent potential temperature at 850 hPa is much higher in Korea than surrounding areas indicate the instability around the selected area and also appears to supply the warm and humid air from the tropics continuously (Fig. 5.1.4 (b)). At 500 hPa, the contour shows the vorticity with the wind flow. The positive shear vorticity is shown as the wind speed is increasing around the typhoon with the counterclockwise curvature (Fig. 5.1.4 (c)). Lastly, at 300 hPa, an upper-level jet (ULJ) streak of  $\geq 25\text{ms}^{-1}$  is approaching Korea from the west, the sharp ridge exhibits ULJ coupled with the low-level jet (LLJ) of  $\geq 12\text{ms}^{-1}$  resulting the strong instability (Fig. 5.1.4 (d)).

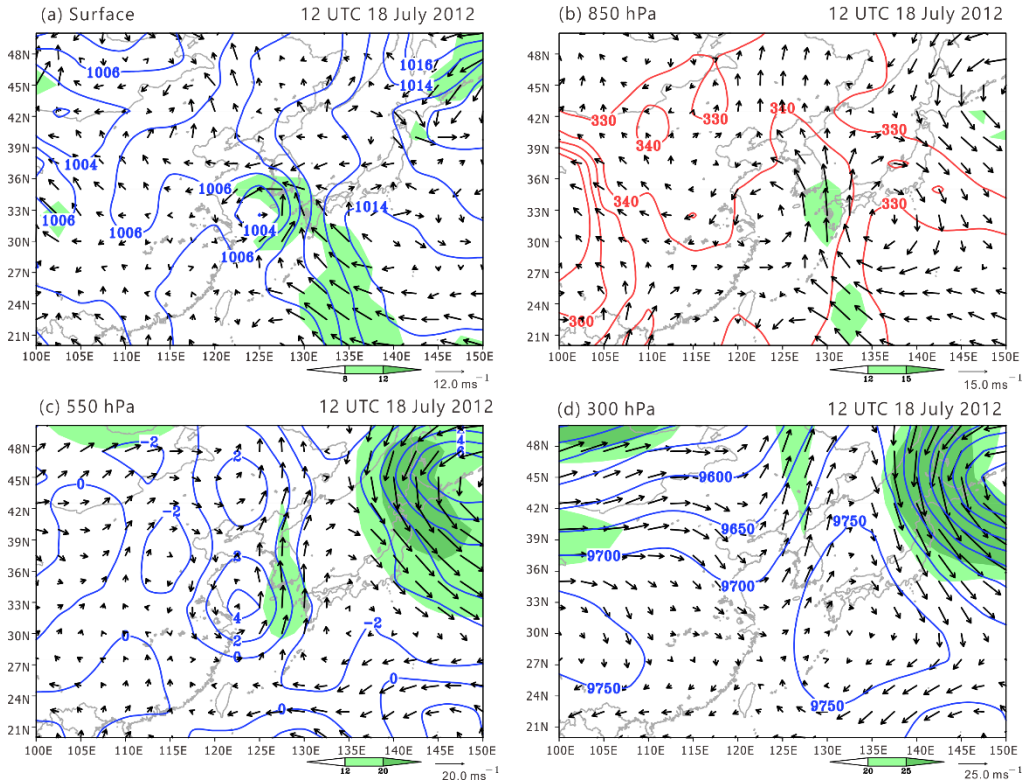


Fig. 5.1.4. The synoptic flow at 1200 UTC on 18 July 2012. (a) at the surface showing the pressure (sea level pressure, hPa), (b) at 850 hPa showing the equivalent potential temperature (K), (c) at 500 hPa showing the relative vorticity ( $10^{-5} \text{ s}^{-1}$ ), and (d) at 300 hPa showing the geopotential height (m) with wind vector.

### 5.1.2. Observation results

The radar data from Gosan and Seongsanpo in Jeju Island, Korea was obtained for the radar analysis. The wind field retrieval method, which was mentioned in chapter 3, is used to show the kinematic structure of the typhoon. Fig. 5.1.5 shows the horizontal wind fields ( $\text{ms}^{-1}$ ) superimposed on the radar reflectivity (dBZ) at each altitude at 1730 LST, 1930 LST, 2030 LST and 2130 LST which is the time when the typhoon is passing through Jeju Island.

The spiral band is entering Jeju Island at 1730 LST with perfectly formed as a typhoon, especially, the full cyclone structure of reflectivity of the typhoon is shown at 4-6 km. The maximum reflectivity of 50 dBZ shows in low altitudes of 1 and 2 km over the top of the mountain in Jeju Island during all four-time steps.

Fig. 5.1.6 shows the vertical cross-section of the wind field with the reflectivity. It shows that the pre-cyclone squall line contains the strong updraft and downdraft to build a convective cell around the cyclone as well as in the spiral band while approaching Jeju Island. Meanwhile, near the eye, the wind is relatively weak as it approaches the island (Fig. 5.1.6 (a)). However, at 1930 LST, it shows dramatic up and down draft wind near the typhoon center with a very high reflectivity measured up to 50 dBZ in low altitudes of 1 and 2 km. This is due to warm frictional inflow near the surface coming from the outer region to cause strong convection (Ishihara et al., 1986). As the typhoon center moves toward the north, the strong convection is formed in the middle altitudes of 4-6 km with strong updraft winds. It shows no more instability of the cyclone, and as expected, the cyclone started to become weakened after one-hour (Fig. 5.1.6 (c) and (d)).

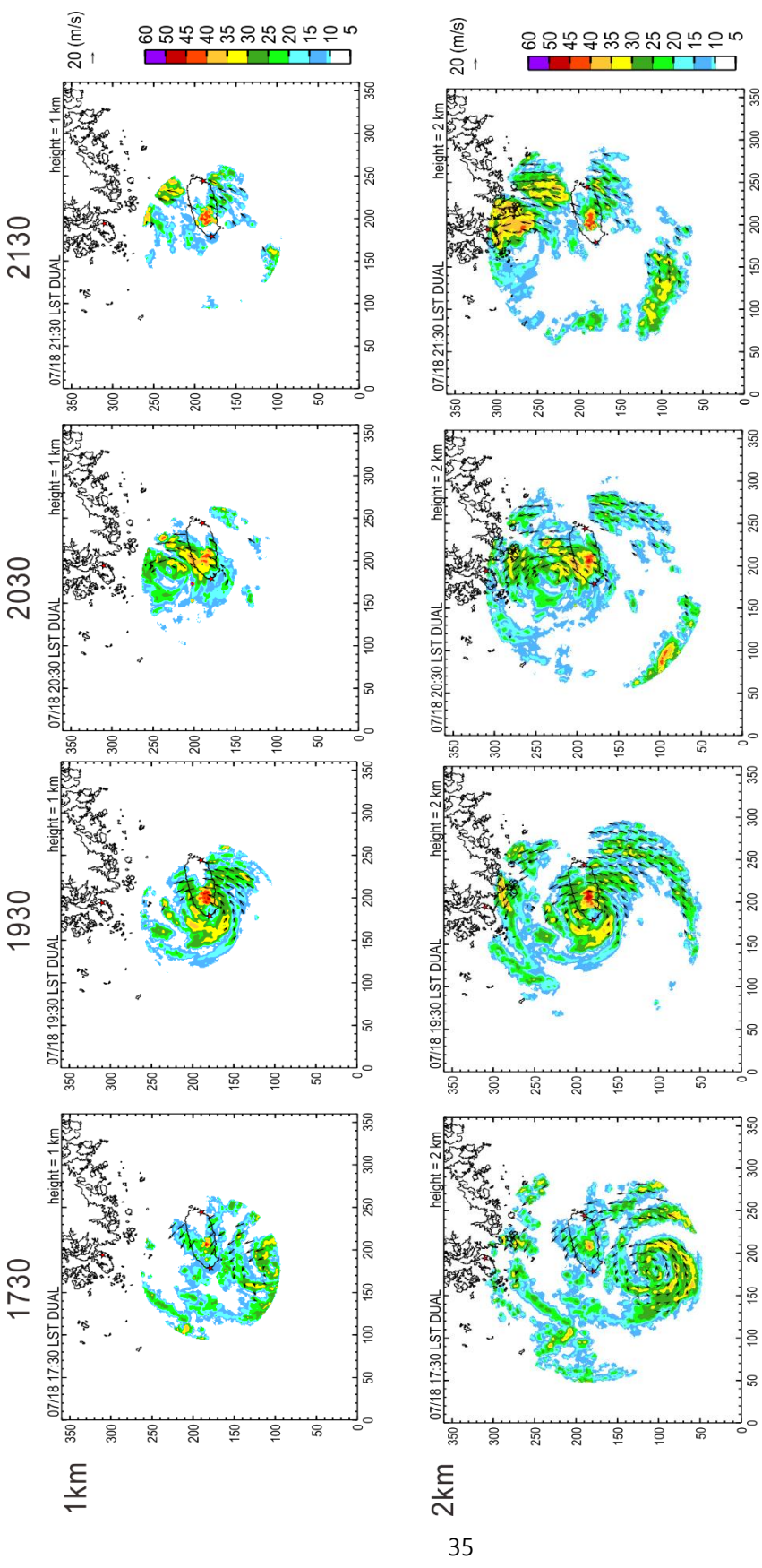


Fig. 5.1.5. The wind field superimposed on the radar reflectivity (dBZ) on each altitude (1, 2, 4, 5, 6, 8 km) at 1730 LST, 1930 LST, 2030 LST and 2130 LST during Typhoon Khanun.

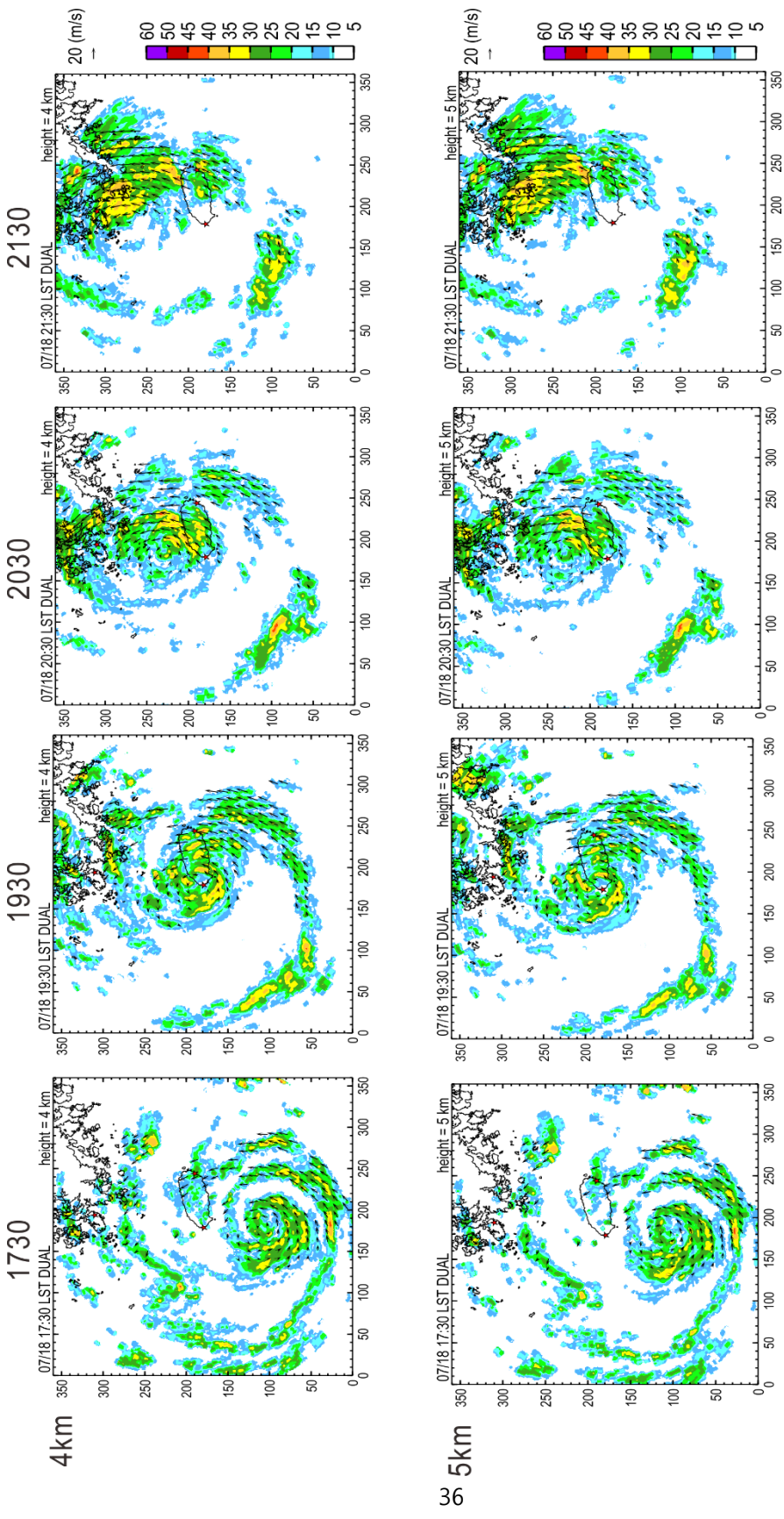


Fig. 5.1.5. Continued

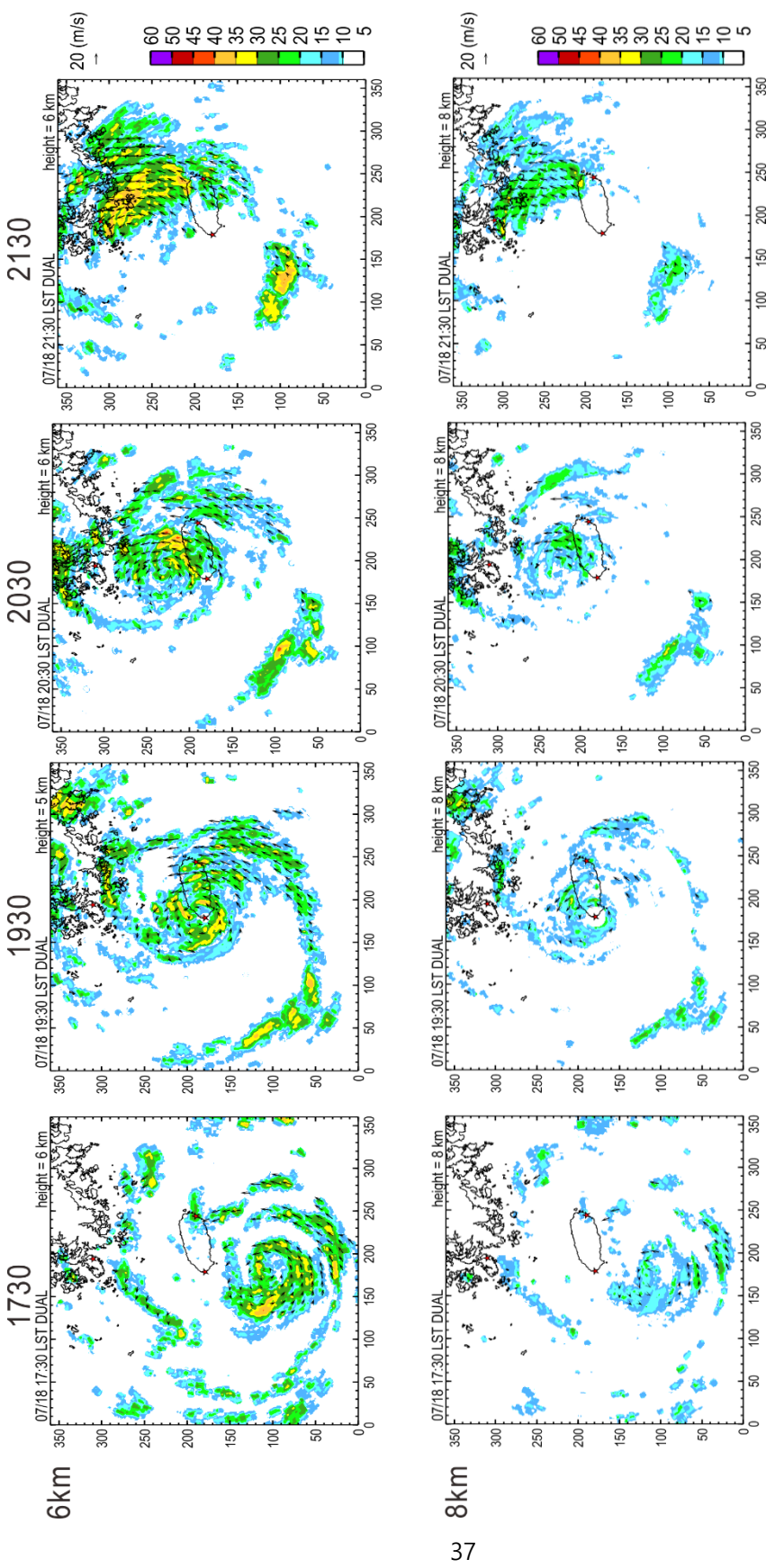


Fig. 5.1.5. Continued

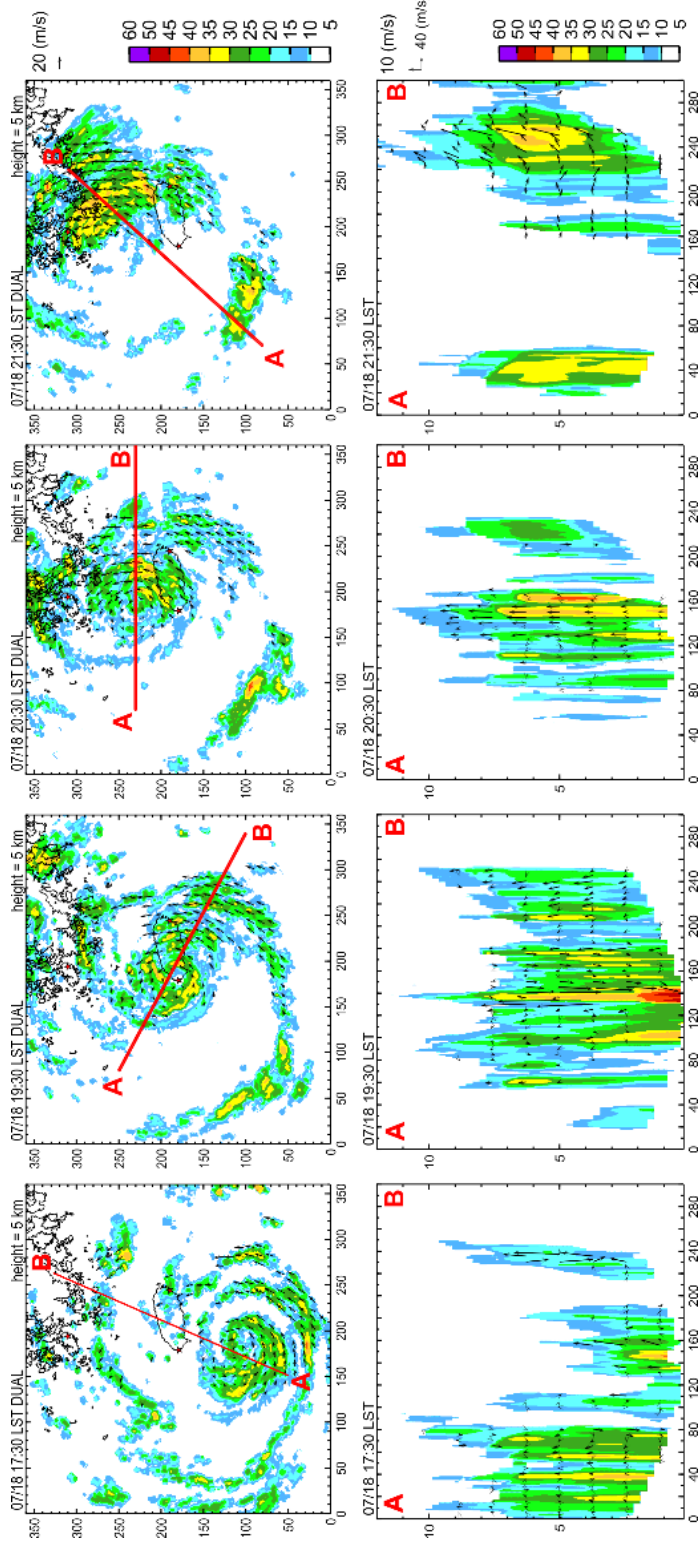


Fig. 5.1.6. The vertical wind field superimposed on the radar reflectivity (dBZ) on each time step. Vertical cross section is indicated with the red line (A-B)

Fig. 5.1.7 shows radar reflectivity with divergence and convergence of horizontal wind at each altitude obtained at 1730 LST, 1930 LST, 2030 LST, and 2130 LST on 18 July 2012. For the reflectivity, constant altitude plan position indicator (CAPPI) data was used and for the horizontal wind divergence and convergence, it was calculated by using horizontal wind distributions retrieved by dual Doppler wind field analysis.

At 1730 LST, as the spiral band makes the landfall on Jeju island, strong convergence is shown over  $-4 \times 10^{-3} S^{-1}$  in the middle of the island at 1 and 2 km altitude with the reflectivity of 40 dBZ. As the typhoon moves to the north, at 1930 LST, the strong convergence continues to be shown over  $-3 \times 10^{-3} S^{-1}$  in 1 km altitude where the reflectivity is over 45 dBZ while the strong divergence is shown over  $3 \times 10^{-3} S^{-1}$  at 4 – 8 km. This behavior continues until 2030 LST, especially on the north side of the island. The convergence and divergence exists on the west and east side with the strength of  $\pm 2 \times 10^{-3} S^{-1}$  at 1 and 2 km while there is only strong divergence at 4 – 8 km in the north of the mountain. After, when the typhoon continues to move to north going through the island, at 2130 LST, strong convergence over  $-3 \times 10^{-3} S^{-1}$  is shown in the middle of the island at 4 – 6 km altitude.

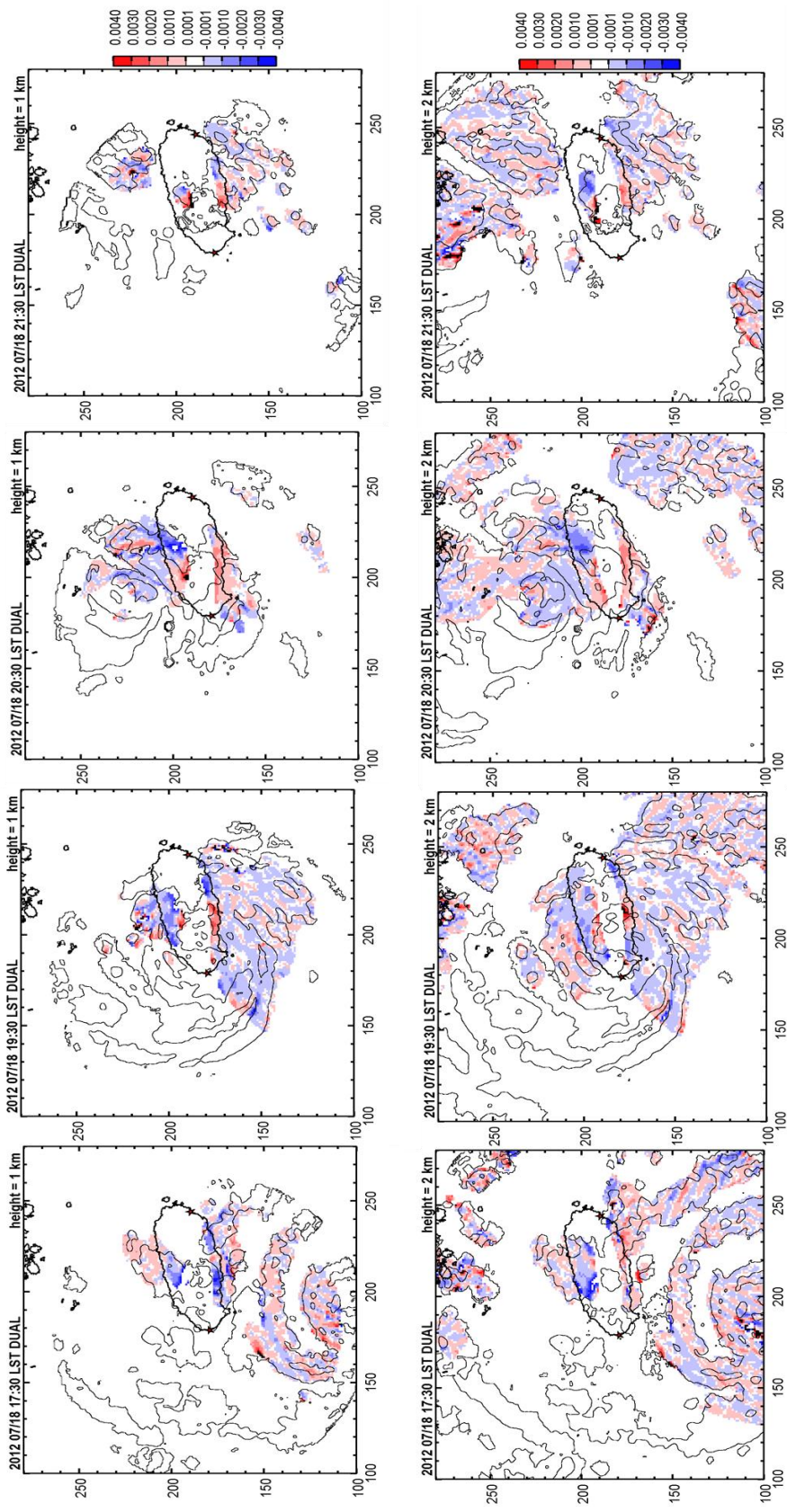


Fig. 5.1.7. The horizontal distribution of wind field of divergence (red) and convergence (blue) with the radar reflectivity (contour).

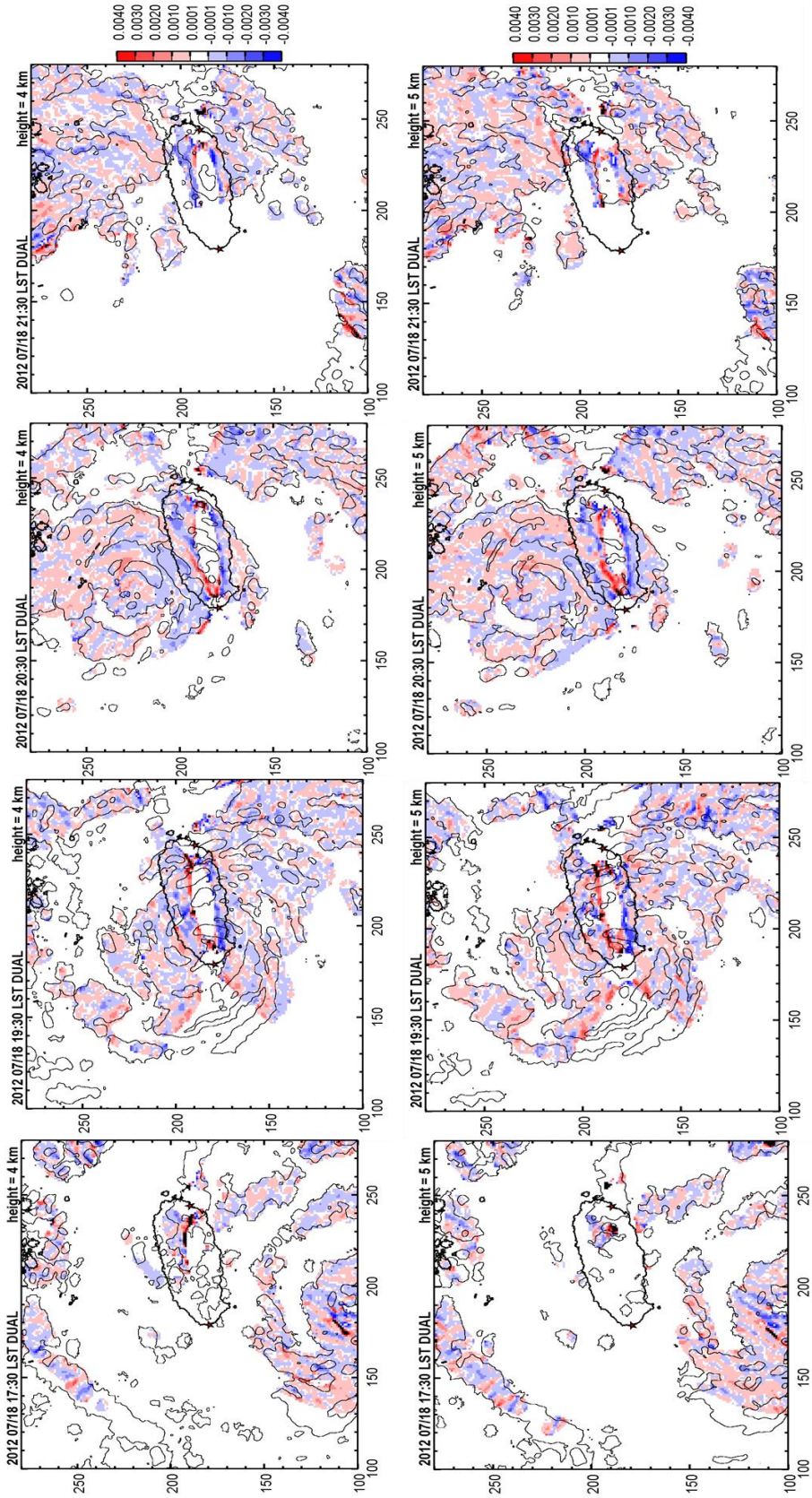


Fig. 5.1.7. Continued

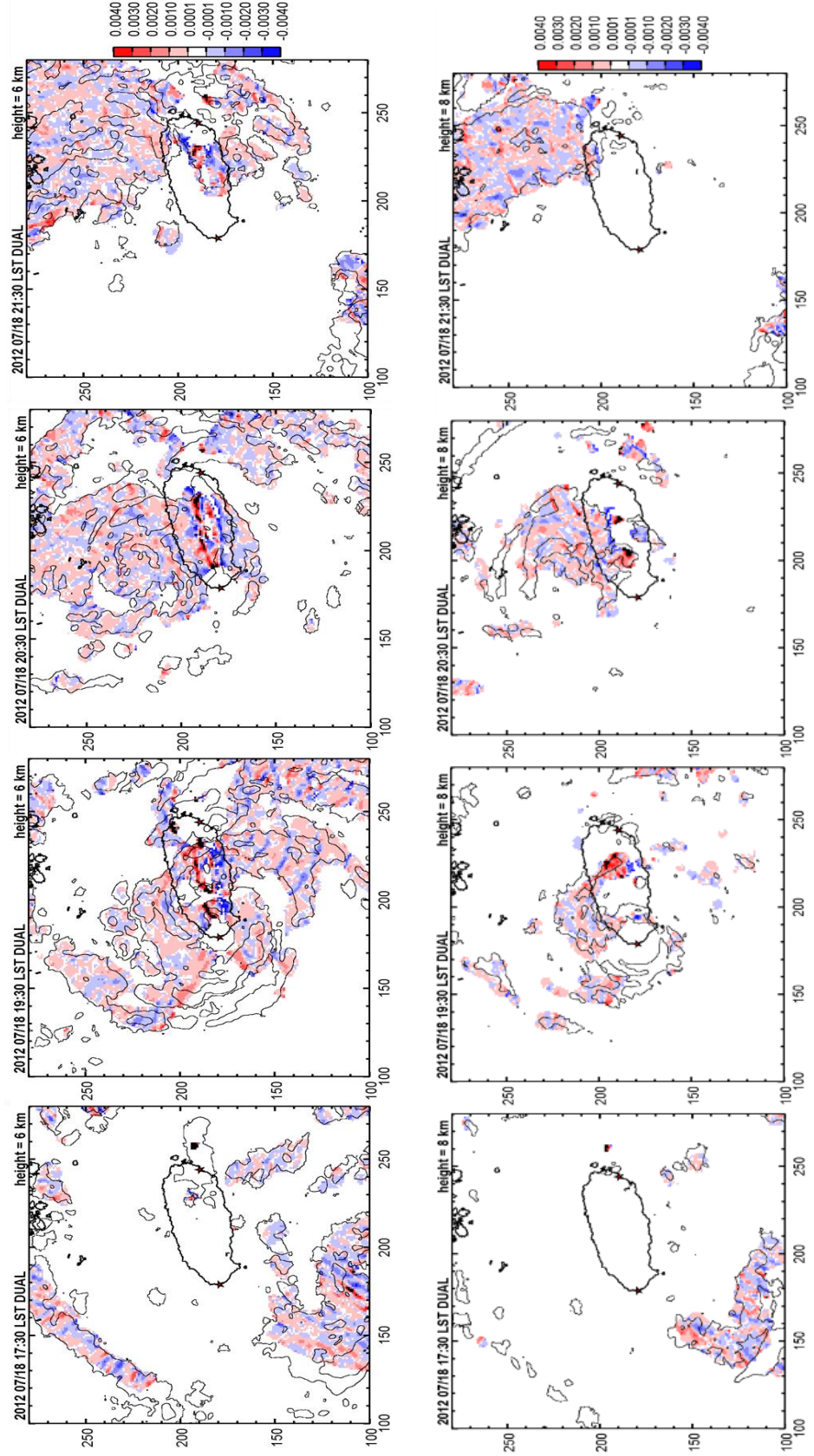


Fig. 5.1.7. Continued

### 5.1.3. Multifractal analysis

The multifractal analysis was performed with the rainfall rate obtained from the radar data in Gosan, Jeju Island, Korea. As the multifractal analysis can be only practiced with the domain size in power of 2, the area of 256 km × 256 km where it covers the most significant rainfall rate is selected. To see in detail without the zero-field which is caused by the observation minimum radar beam elevation angle in the lower altitudes, the domain size of 64 km × 64 km is selected in the middle of the whole observation domain size 360 km × 360 km, where the center is the location of the radar. In this case, the center of the typhoon passes through the radar site that there was not much rain occurred in the center of the domain. There was not enough data for calculating the scaling behavior for the selected domain 64 km×64 km. Instead, the alternative domain was selected in the middle of 256 km × 256 km domain, which excludes the result in the low altitudes (1 km and 2 km).

## 1) Radar

### 1.1) The domain 256 km × 256 km

Before proceeding the multifractal analysis, spectral analysis was performed for all data (different altitudes in both domains). It is to note where it is possible to verify the existence of a scaling break. In Fig. 5.1.8 shows that all dataset were shown the linear scaling behavior up to  $\ln k = 2$  with  $R^2$ (root mean square)  $\geq 0.9$ . The detailed values of  $\beta$  and  $R^2$  is shown in Table 5.1.1. All the cases present good scaling behavior in most of the parts; however, at 2 km, 4 km, 5 km, 8 km presents some instabilities with a strong tail lift. As the TM and DTM techniques for UM analysis are only used in conservative fields, which means  $H=0$ .

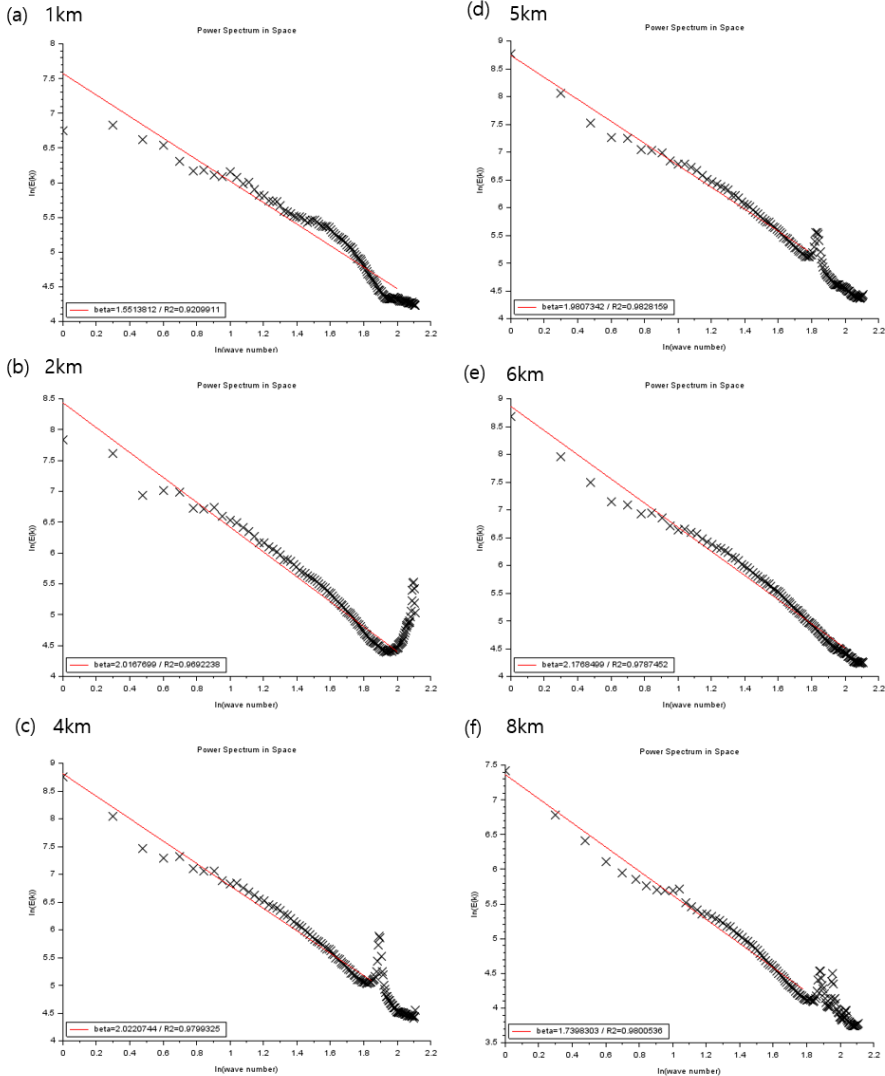


Fig. 5.1.8. The result of spectral analysis,  $\ln E(k)$  as a function of  $\ln k$  with the rainfall rate retrieved from radar data on every height (a) 1 km, (b) 2 km, (c) 4 km, (d) 5 km, (e) 6 km and (f) 8 km in  $256 \text{ km} \times 256 \text{ km}$  size of the domain.

Table 5.1.1. The values of  $\beta$  and  $R^2$  after spectral analysis in the domain size  $256 \text{ km} \times 256 \text{ km}$  with the case of Typhoon Khanun.

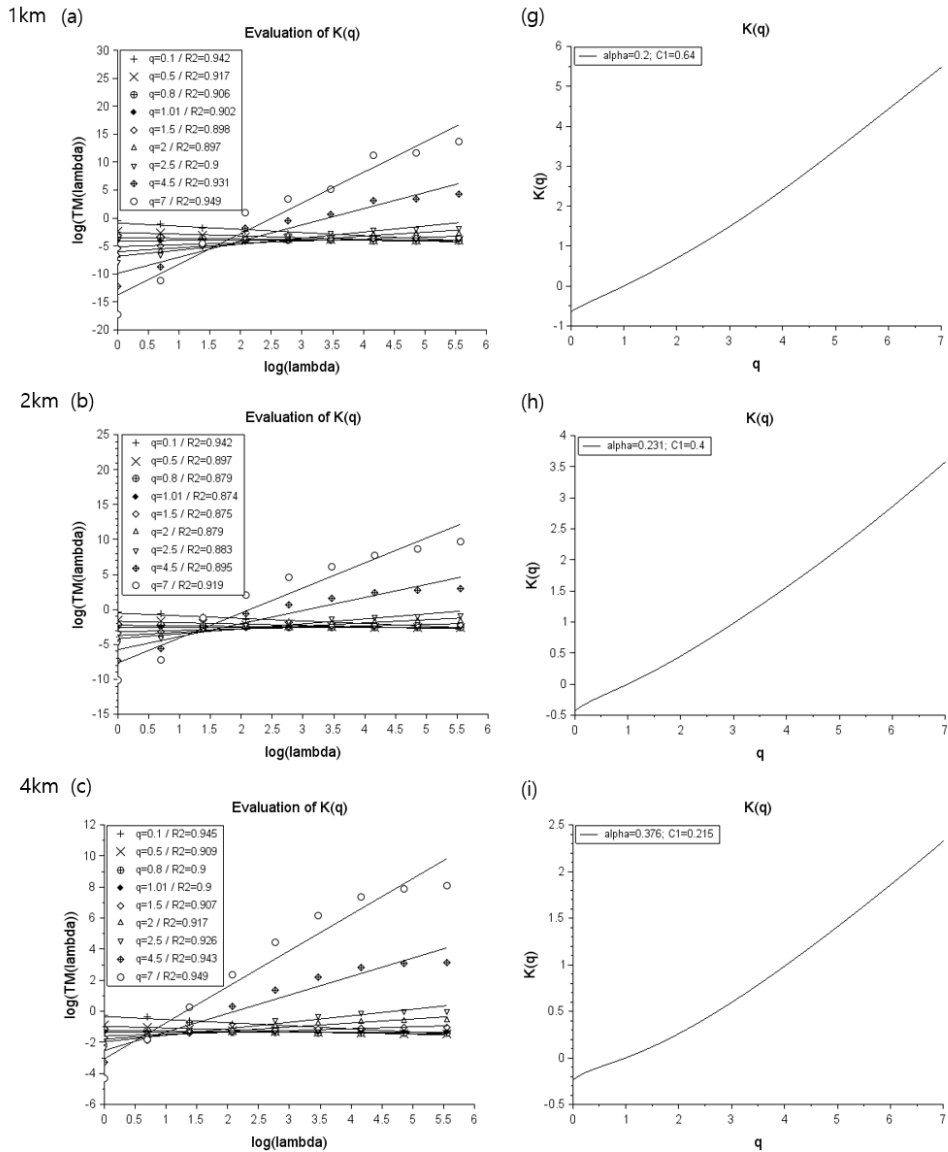
	1 km	2 km	4 km	5 km	6 km	8 km
$\beta$	1.55	2.02	2.02	1.98	2.18	1.74
$R^2$	0.92	0.97	0.98	0.98	0.98	0.98

Following the spectral analysis, the TM and DTM methods were applied to all data. The results of the TM method are presented in Fig. 5.1.9. The graphs on the left (a, b, c, d, e, f) shows the log-log plots of  $\langle \varepsilon_\lambda^q \rangle \approx \lambda^{K(q)}$  with the resolution  $\lambda$  (in this case, it is a set from 1 to 256 km with the rate of increase in power of 2) and the values of  $q$  were freely chosen between 0.1 and 7.0. In most of the cases, the scaling behavior was very good without any scaling break ( $R^2 \geq 0.9$ ) which means that the field is multifractal from  $q = 0.1$  up to  $q = 7$ . The graph of scaling moment function  $K(q)$  is obtained (Fig. 5.1.9 (g, h, i, j, k, l)) and UM parameters are obtained from the slope of  $K(q)$  graphs which shows the moment and singularity behavior.

Fig 5.1.10 shows the estimated (or empirical) scaling moment functions  $K(q)$  (in black) are compared to the semi-theoretical functions that are the curves with the UM parameters  $\alpha$  and  $C_1$  further retrieved from TM (red) and DTM (green) analysis. It shows how the scaling behavior is fitting with each other. In this case, comparing the empirical and DTM semi-theoretical  $K(q)$ , it shows relatively the same scaling behavior until  $q = 7.0$  except at 8 km. The value of  $q$  could be considered as the result of a multifractal phase transition, as predicted by Mandelbrot (1974). This could be caused mainly by two reasons: spatial integration or finite sample size (Schertzer and Lovejoy, 1987).

The results of the DTM method are shown in Fig. 5.1.11. An apparent scaling behavior was retrieved as well as what was noticed with the TM analyses. For each power  $\eta$ , with a fixed value of  $q$  ( $q=1.5$ ), the slope of the linear regression gives an estimate of the scaling moment functions  $K(q, \eta)$ . The S-shape curves (Fig. 5.1.11. (g, h, i, j, k, l)) are conditioned by an appearance of numerical limitations at smaller moments and the critical behavior of extremes at higher statistical moments, both being characterized by the flattening of the double trace moment curves. The slope of the curve gives an estimation of  $\alpha$  and  $C_1$ . The value of  $\alpha$  increases along with the height while the value of  $C_1$  decreases, showing how to concentrate and how quickly the intermittency evolved.

Both  $\alpha$  and  $C_1$ , the UM parameters estimated from TM and DTM are indicated in Table 5.1.2 and shown as a graph in Fig. 5.1.12.



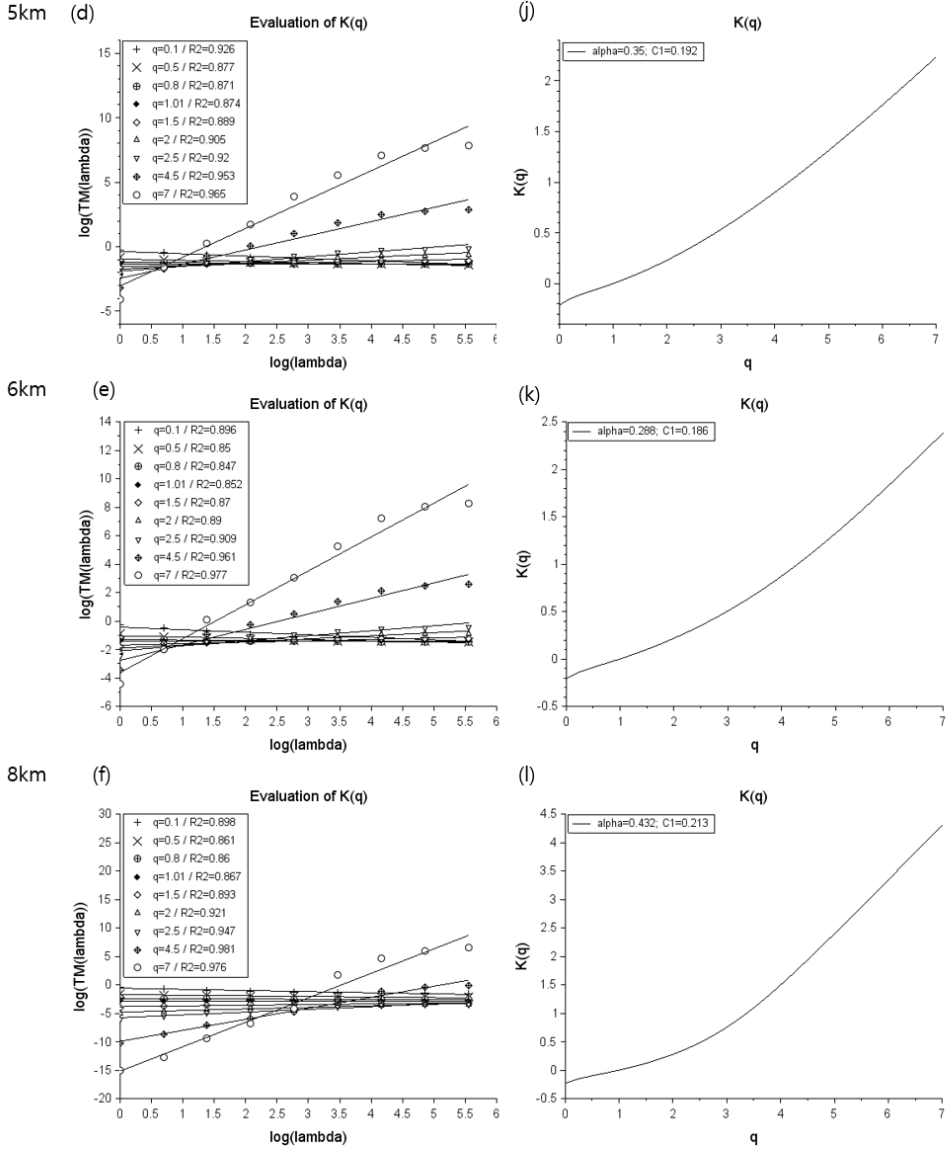


Fig. 5.1.9. The result of TM analysis obtained from the radar dataset in the  $256 \text{ km} \times 256 \text{ km}$  sizes of the domain. The scaling behavior with the value of different  $q$  from 0.1 to 7.0 at 1 km, 2 km, 4 km, 5 km, 6 km and 8 km (a, b, c, d, e, f).  $K(q)$  (black) is obtained in the graph (g, h, i, j, k, l) and the multifractal parameters retrieved from TM analysis are shown on the left top corner.

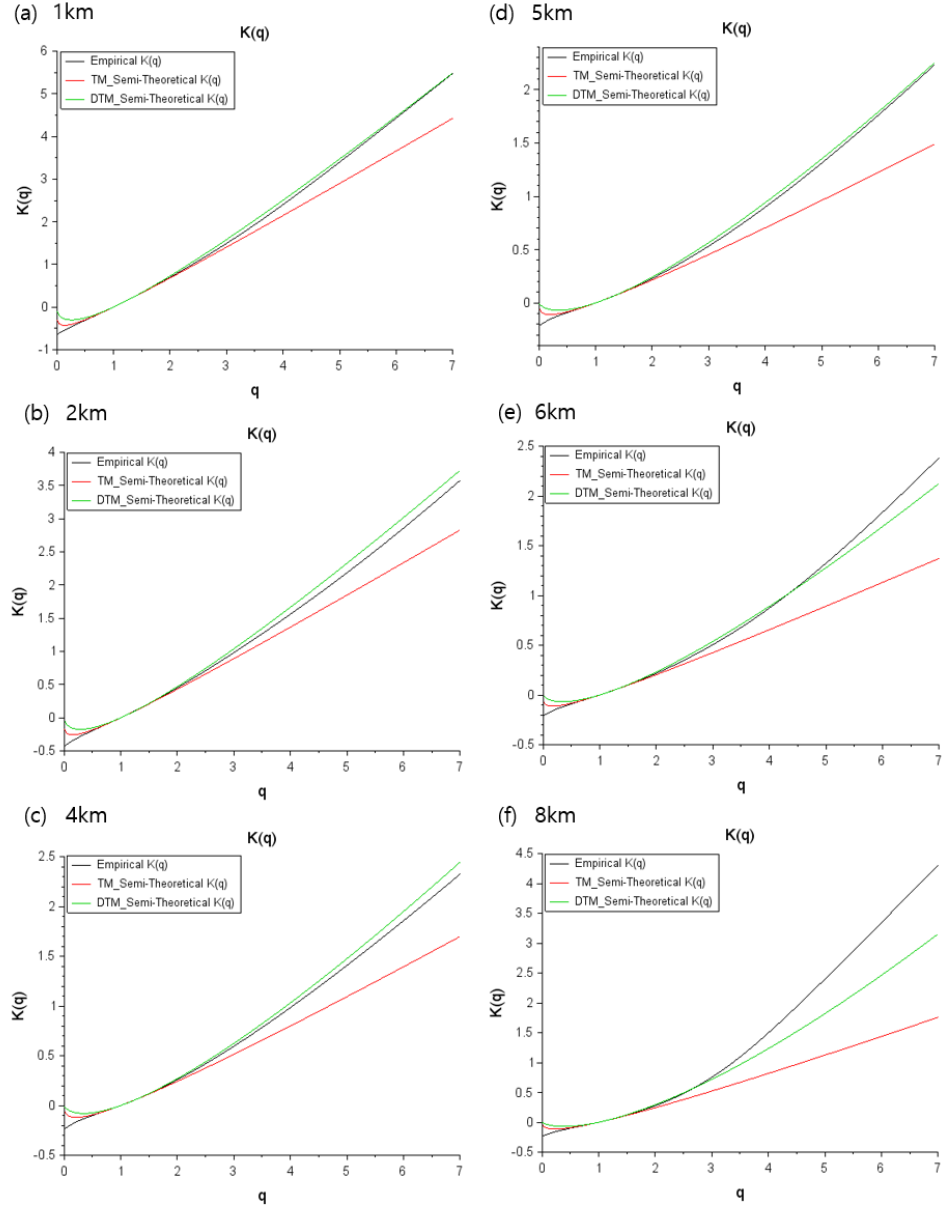
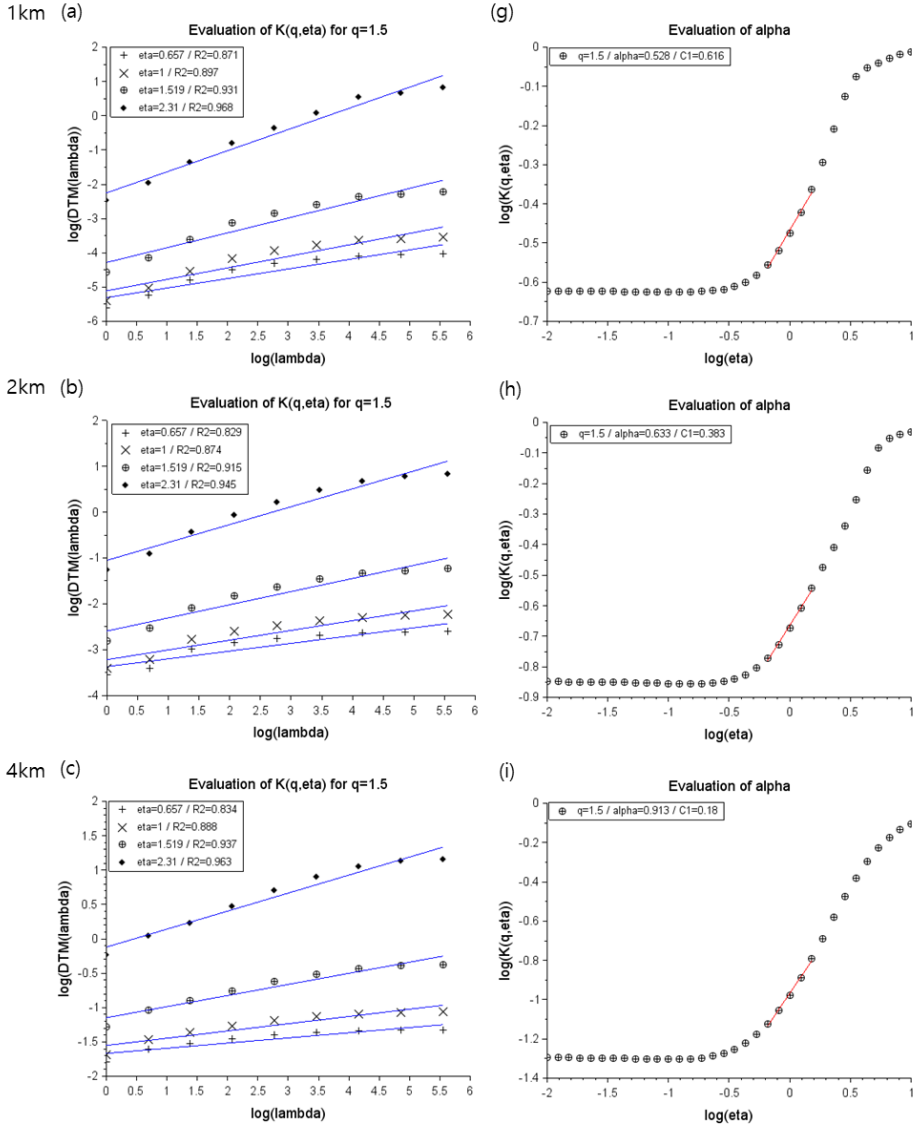


Fig. 5.1.10. The scaling moment function  $K(q)$  obtained from the empirical dataset (black), from using UM parameters obtained from TM (red), from using UM parameters obtained from DTM (green).



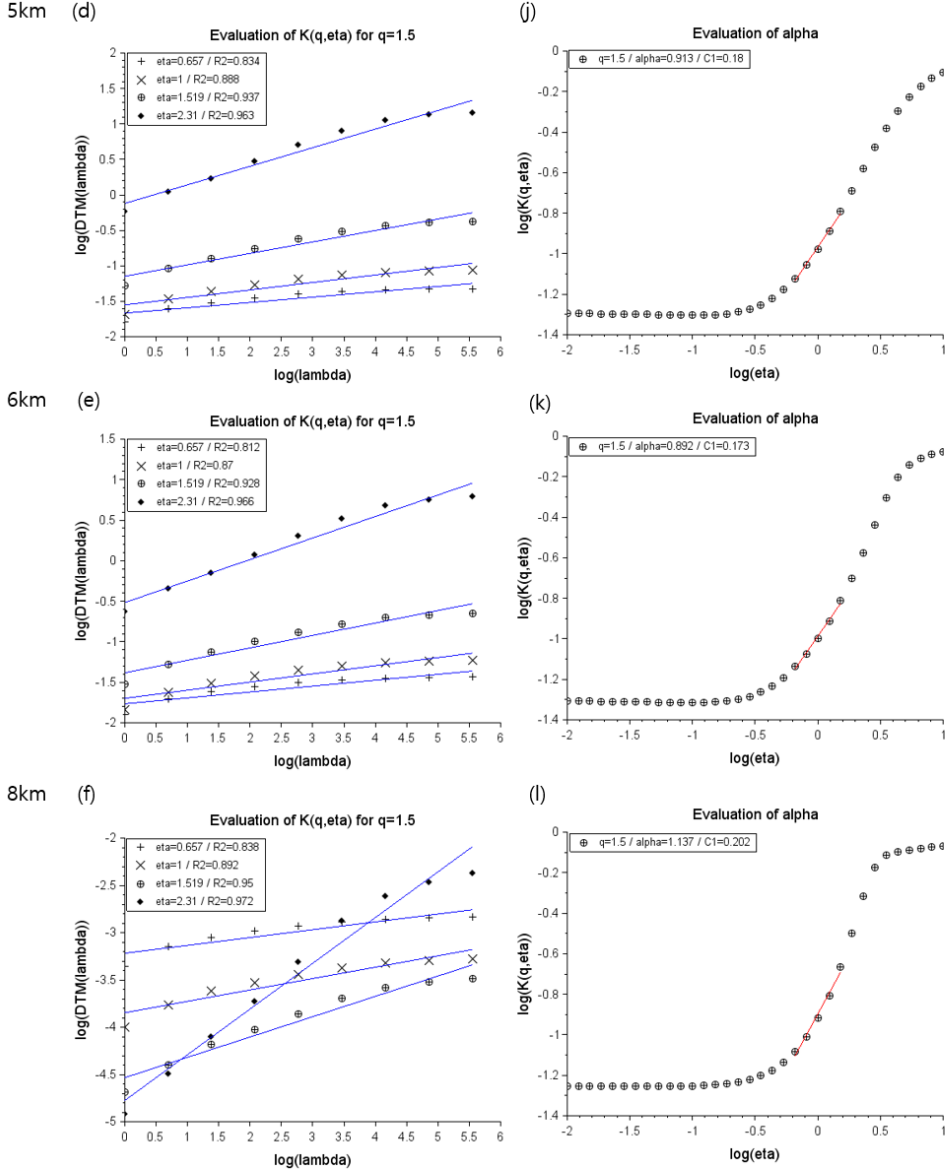


Fig. 5.1.11. The result of DTM analysis obtained from the radar dataset in the  $256 \text{ km} \times 256 \text{ km}$  sizes of the domain. The scaling behavior with the value of different  $\eta$  from 0.1 to 2.5 at 1 km, 2 km, 4 km, 5 km, 6 km and 8 km (a, b, c, d, e, f) at fixed  $q = 1.5$ . DTM curve is shown in (g, h, I, j, k, l).

Table 5.1.2. The estimated UM parameters from TM and DTM in the domain size 256 km × 256 km.

		1 km	2 km	4 km	5 km	6 km	8 km
TM	$\alpha$	0.2	0.231	0.376	0.35	0.288	0.432
	$C_1$	0.64	0.4	0.215	0.192	0.186	0.213
DTM	$\alpha$	0.528	0.633	0.871	0.913	0.892	1.137
	$C_1$	0.616	0.383	0.203	0.18	0.173	0.202

Consequently, the scaling exponent value  $\beta$  for spectral analysis are averagely 1.920 in all heights of the domain sizes 256 km × 256 km with  $R^2 \geq 0.9$  at all altitudes.

The multifractal parameters were obtained from TM and DTM analysis. The value of  $C_1$  is similar between the result of the TM and DTM, but the larger values of  $\alpha$  are obtained from DTM analysis. However, the trend of changing  $\alpha$  is the same.

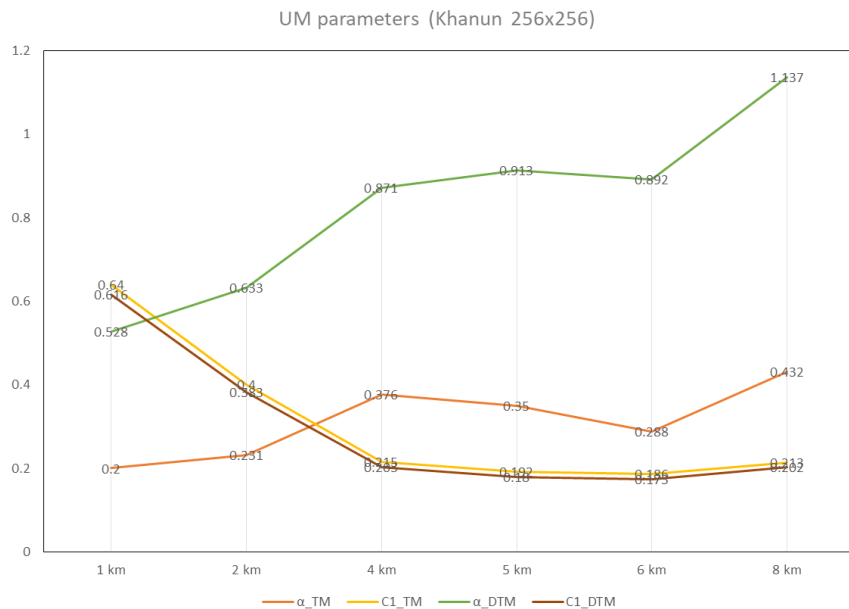


Fig. 5.1.12. The UM parameters obtained from TM and DTM.

## 1.2) The domain $64 \text{ km} \times 64 \text{ km}$

The spectral analysis was performed in the smaller domain size of  $64 \text{ km} \times 64 \text{ km}$ . As it was mentioned before, the main reason for analyzing a smaller domain is due to the zero-field included in 1 km and 2 km in the bigger domain size  $256 \text{ km} \times 256 \text{ km}$ . In this case, since the rainfall did not exist in the center of the observation field, the middle of the maximum rainfall field was selected instead to obtain the fractal dimensions.

From the spectral analysis, it is noted that all dataset were shown the linear scaling behavior up to  $\ln(k) = 1.5$  with  $R^2 \geq 0.9$  (Fig. 5.1.13). The detailed values of  $\beta$  and  $R^2$  is shown in Table 5.1.3. All the cases present good scaling behavior in most of the part, however, at 4 km, and 8 km shows some instabilities with a strong tail lift. As the TM and DTM techniques for UM analysis are only used in conservative fields, the tail lifted part was neglected.

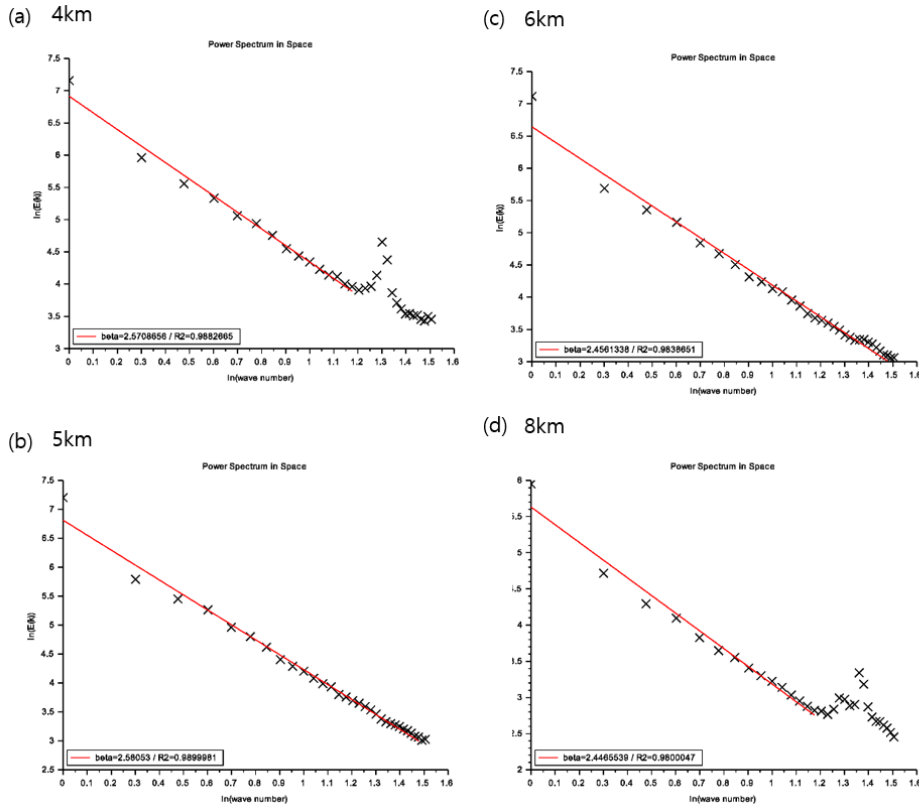


Fig. 5.1.13. The same as Fig. 5.1.8 but in the altitudes of (a) 4 km, (b) 5 km, (c) 6 km, and (d) 8 km in the domain size  $64 \text{ km} \times 64 \text{ km}$ .

Table 5.1.3. The values of  $\beta$  and  $R^2$  after spectral analysis in the domain size 64 km  $\times$  64 km with the case of Typhoon Khanun.

	1 km	2 km	4 km	5 km	6 km	8 km
$\beta$	-	-	2.57	2.58	2.46	2.45
$R^2$	-	-	0.99	0.99	0.98	0.98

The multifractal analysis was done with TM, and DTM techniques applied. As same as the bigger domain,  $q$  was selected freely from 0.1 to 7. The results of the TM method are presented in Fig. 5.1.14. The graphs on the left (a, b, c, d) shows the log-log plots of  $\langle \varepsilon_\lambda^q \rangle \approx \lambda^{K(q)}$  with the resolution  $\lambda$  (in this case, it is a set from 1 to 64 km with the rate of increase in power of 2) and the scaling behavior was very good without any scaling break ( $R^2 \geq 0.9$ ) which means that the field is multifractal from  $q = 0.1$  up to  $q = 7$ . The scaling moment function  $K(q)$  is obtained (Fig. 5.1.14 (e, f, g, h)) and UM parameters are obtained from the slope of  $K(q)$  which shows the moment and singularity behavior.

Fig 5.1.15 shows the estimated (or empirical) scaling moment functions  $K(q)$  (in black) are compared to the semi-theoretical functions that are the curves with the UM parameters  $\alpha$  and  $C_1$  further retrieved from TM (red) and DTM (green) analysis. It shows that the empirical and DTM semi-theoretical  $K(q)$  shows the same scaling behavior until  $q = 7.0$  the most at 5 km.

The results of the DTM method are shown in Fig. 5.1.16. An explicit scaling behavior was retrieved as well as what was noticed with the TM analyses. For each power  $\eta$ , with a fixed value of  $q$  ( $q=1.5$ ), the slope of the linear regression gives an estimate of the scaling moment functions  $K(q, \eta)$ . The slope of S-shape curves (Fig. 5.1.16 (e, f, g, h)) gives an estimation of  $\alpha$  and  $C_1$ . The value of  $\alpha$  shows a peak at 5 km while the value of  $C_1$  relatively decreases, Both  $\alpha$  and  $C_1$ , the UM parameters estimated from TM and DTM are indicated in Table 5.1.4. and shown in Fig. 5.1.17.

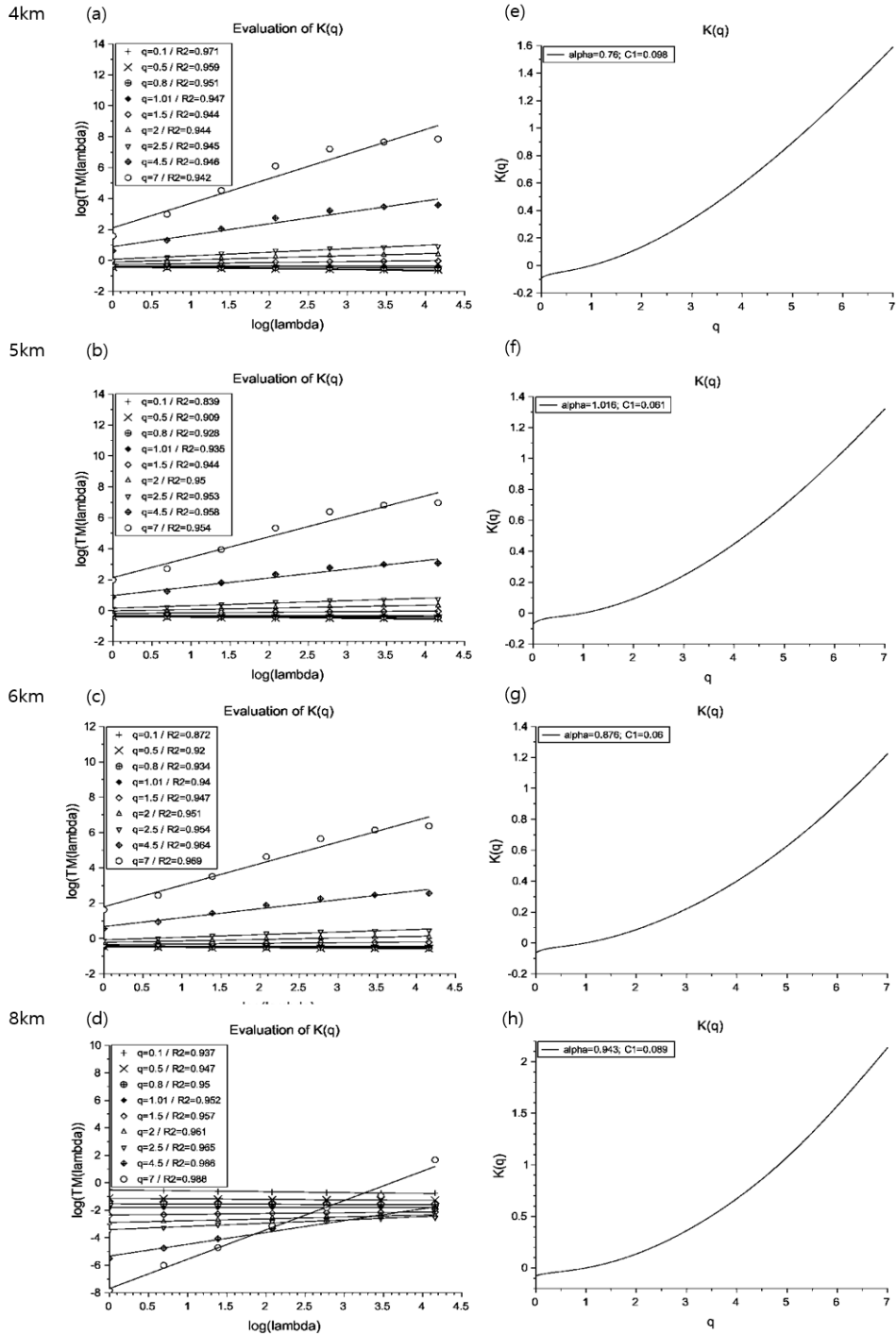


Fig. 5.1.14. The same as Fig. 5.1.9 but in the altitudes of (a,e) 4 km, (b,f) 5 km, (c,g) 6 km, and (d,h) 8 km in the domain size 64 km × 64 km.

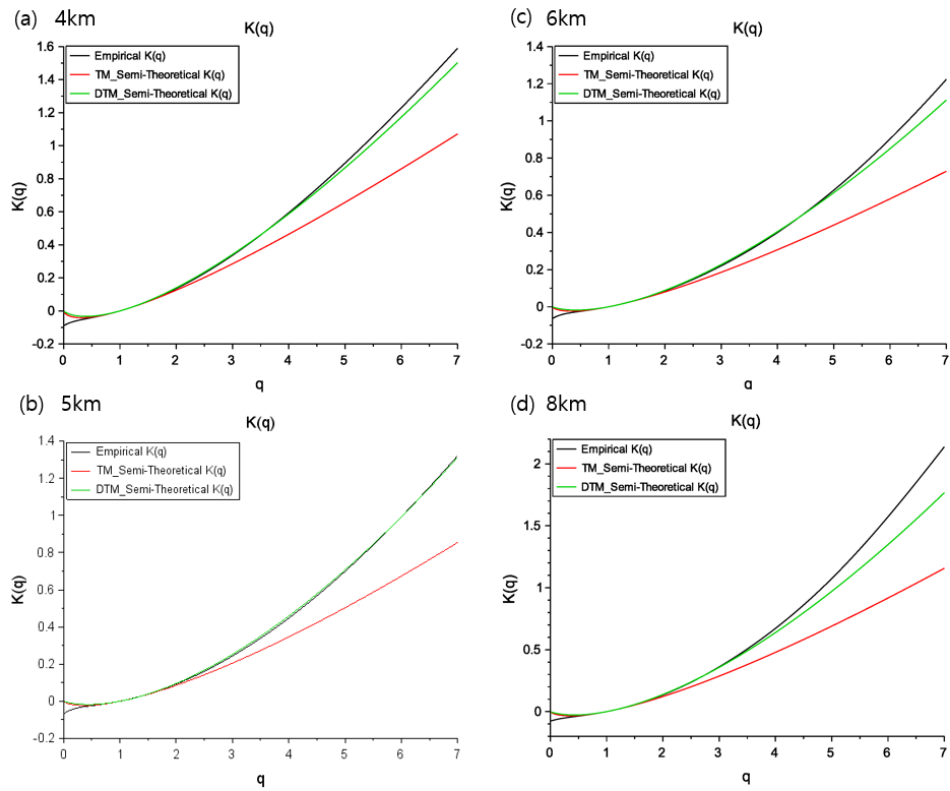


Fig. 5.1.15. The same as Fig. 5.1.10 but in the altitudes of (a) 4 km, (b) 5 km, (c) 6 km, and (d) 8 km in the domain size  $64 \text{ km} \times 64 \text{ km}$ .

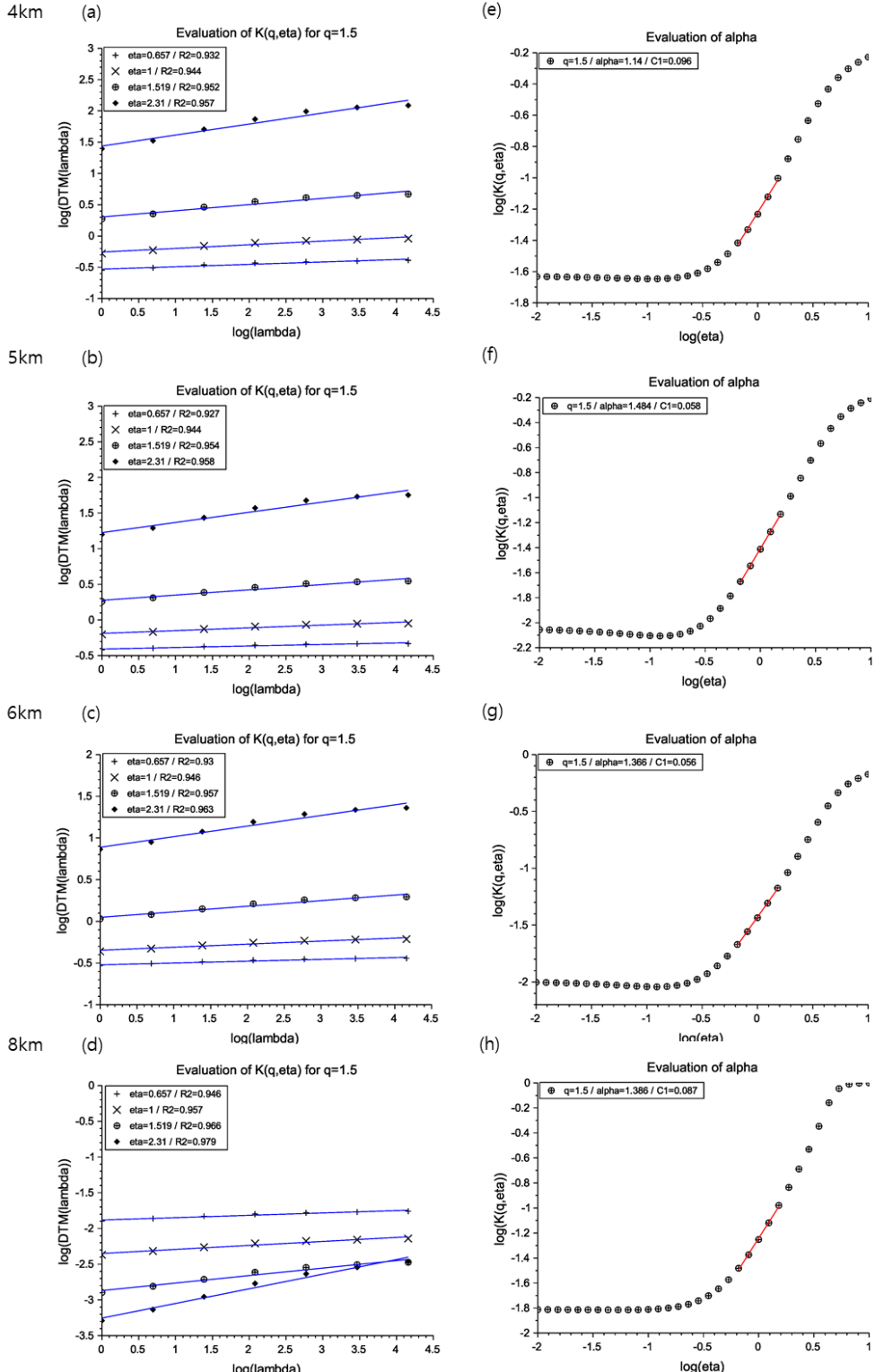


Fig. 5.1.16. The same as Fig. 5.1.11 but in the altitudes of (a,e) 4 km, (b,f) 5 km, (c,g) 6 km, and (d,h) 8 km in the domain size  $64 \text{ km} \times 64 \text{ km}$ .

Table 5.1.4. The estimated UM parameters from TM and DTM in the domain size  $64 \text{ km} \times 64 \text{ km}$ .

	64		1 km	2 km	4 km	5 km	6 km	8 km
TM	$\alpha$	-	-	0.78	1.016	0.876	0.943	
	$C_1$	-	-	0.098	0.061	0.06	0.089	
DTM	$\alpha$	-	-	1.14	1.484	1.366	1.386	
	$C_1$	-	-	0.096	0.058	0.056	0.087	

Consequently, the scaling exponent value  $\beta$  for spectral analysis are averagely 2.515 in  $64 \text{ km} \times 64 \text{ km}$  with  $R^2 \geq 0.9$  in all altitudes in all domains.

The multifractal parameters were obtained from TM and DTM analysis. The value of both  $C_1$  is similar between the result of the TM and DTM but the larger values of  $\alpha$  are obtained from DTM analysis. However, the trend of changes in the values of  $\alpha$  is similar between the result of TM and DTM.

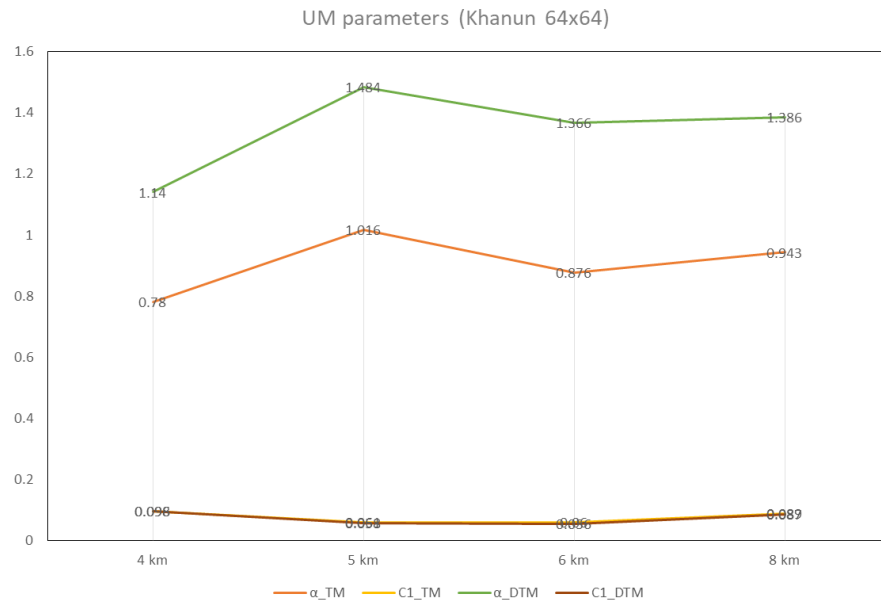


Fig. 5.1.17. The same as Fig. 5.1.12 but in domain  $64 \text{ km} \times 64 \text{ km}$ .

Fig. 5.1.18 shows the deduction of the pattern of the rainfall field in each altitude with the whole domain ( $360 \text{ km} \times 360 \text{ km}$ ) with the typhoon Khanun. It shows the peak of the rainfall field varies from  $0.4 - 0.8 \text{ mm}$ . This shows a dependence of  $\alpha$  along with the altitude. The  $\alpha > 1$ ,  $C_1 = 0.2$  at only  $8 \text{ km}$  altitude in  $256 \text{ km} \times 256 \text{ km}$ , when  $\alpha > 1$ ,  $C_1 < 0.1$  at  $4 - 8 \text{ km}$  in  $64 \text{ km} \times 64 \text{ km}$ . This shows the bigger fluctuation of rainfall field pattern with no limited range of singularities in the smaller domain.

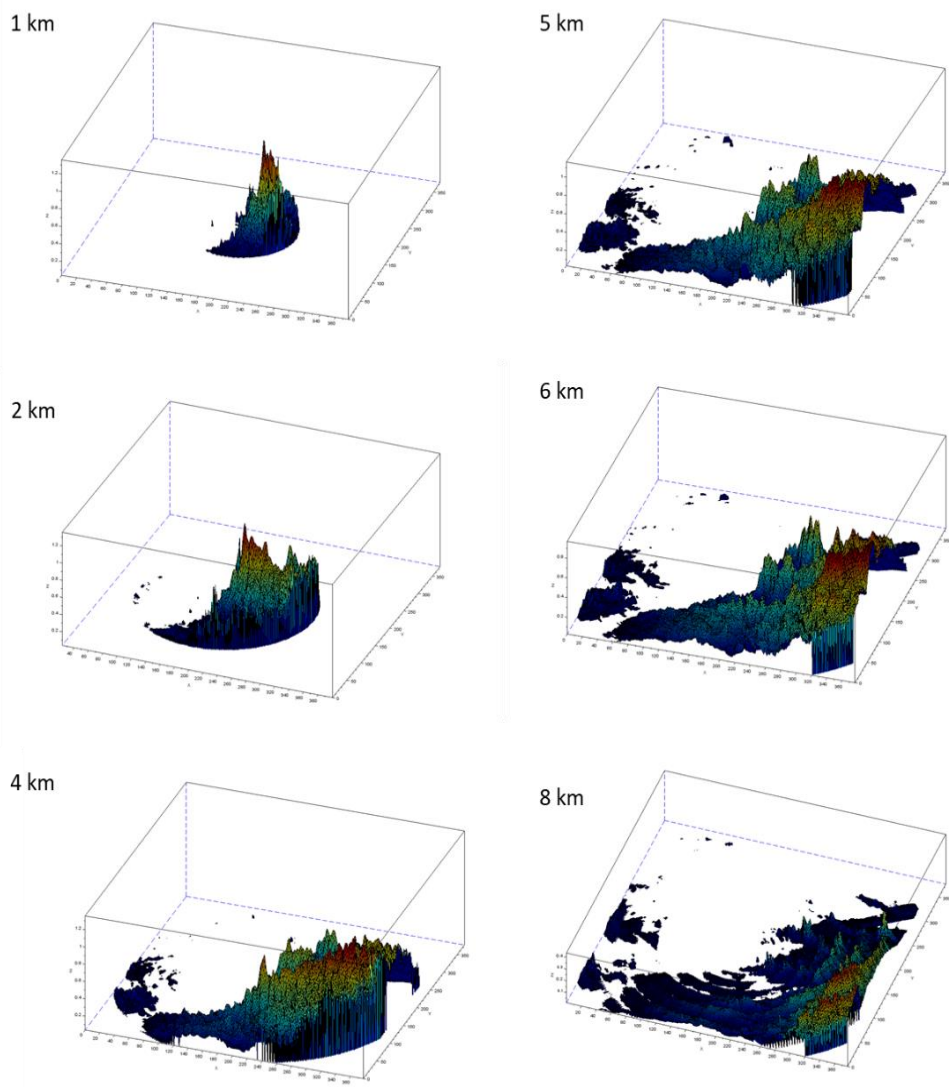


Fig. 5.1.18. The accumulated rainfall field on each altitudes of typhoon Khanun.

## 2) CReSS model

### 2.1) The domain 256 km × 256 km

The multifractal analysis was carried out with CReSS model dataset, which embedded in the microphysics in the vertical calculation. Model provides the rainfall rate field at the surface layer and the settings for model calculation were explained in chapter 3.

Fig. 5.1.19 shows the result of the spectral analysis in domain 256 km × 256 km and it shows the conservative field with  $\beta = 1.5$  and  $R^2 \geq 0.93$ .

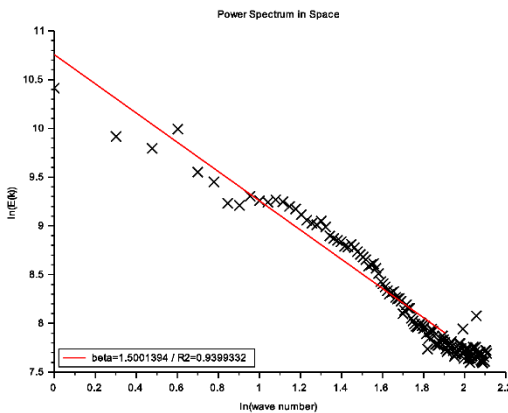


Fig. 5.1.19. The result of spectral analysis from CReSS model dataset.

The result of the TM method is presented in Fig. 5.1.20. The same analysis was performed with the radar dataset to see the scaling behavior with the values of different  $q$  from 0.1 to 7.0 (Fig. 5.1.20 (a)). The scaling behavior from the graph shows almost no scaling break from  $q=0.1$  to  $q=7$  showing  $R^2 \geq 0.9$ . The scaling moment function  $K(q)$  is obtained with the values of multifractal parameters indicated which were obtained from TM analysis (Fig. 5.1.20 (b)). Lastly, in Fig 5.1.20 (c),  $K(q)$  obtained from the empirical dataset in black, from using UM parameters obtained from TM in red, from using UM parameters obtained from DTM in green. It shows how the scaling behavior is fitting with each other. It shows that all the results of scaling behavior are relatively fitting well.

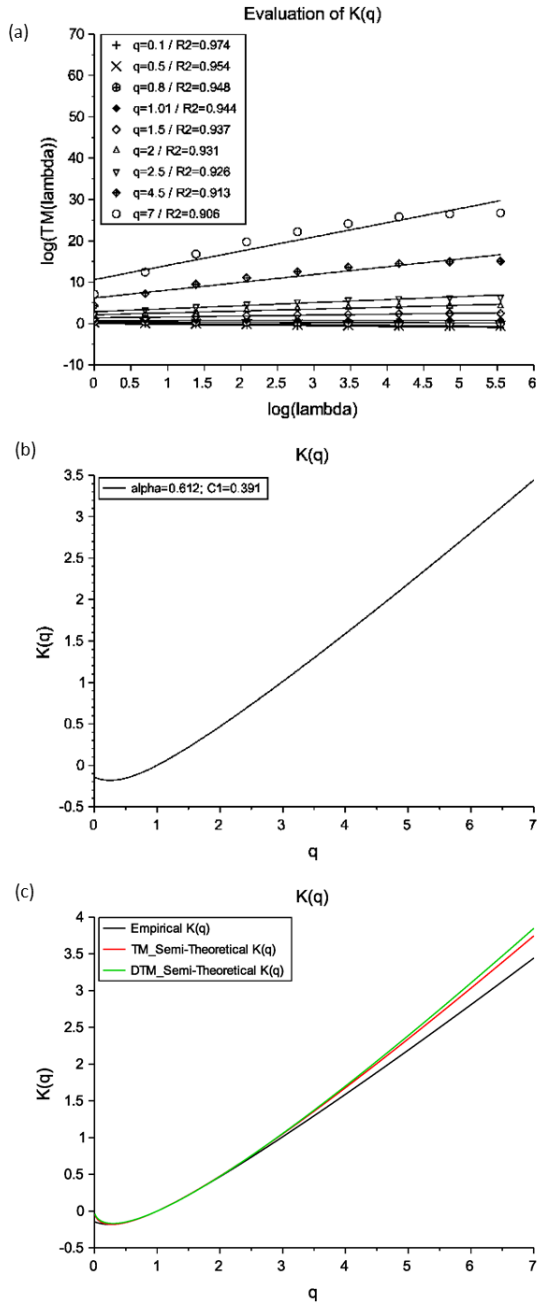


Fig. 5.1.20. The result of TM analysis obtained from CReSS model dataset in domain 256 km  $\times$  256 km. (a) The scaling behavior with the value of different  $q$  from 0.1 to 7.0 and (b) the graph of  $K(q)$  with the values of multifractal parameters indicated which were obtained from TM analysis. (c) The scaling moment function  $K(q)$  obtained from the empirical dataset (black), from using UM parameters obtained from TM (red), from using UM parameters obtained from DTM (green).

The result of the DTM method is shown in Fig. 5.1.21. As it was expected by TM analysis, the DTM result clearly shows a good scaling behavior at  $R^2 \geq 0.94$  with all different  $\eta$ . For each power  $\eta$ , with a fixed value of  $q$  ( $q=1.5$ ), the slope of the linear regression gives an estimate of the scaling moment functions  $K(q, \eta)$ . Fig. 5.1.21 (b) shows the slope of the DTM curve which gives an estimation of  $\alpha$  and  $C_1$ . Detailed values are indicated in Table 5.1.5.

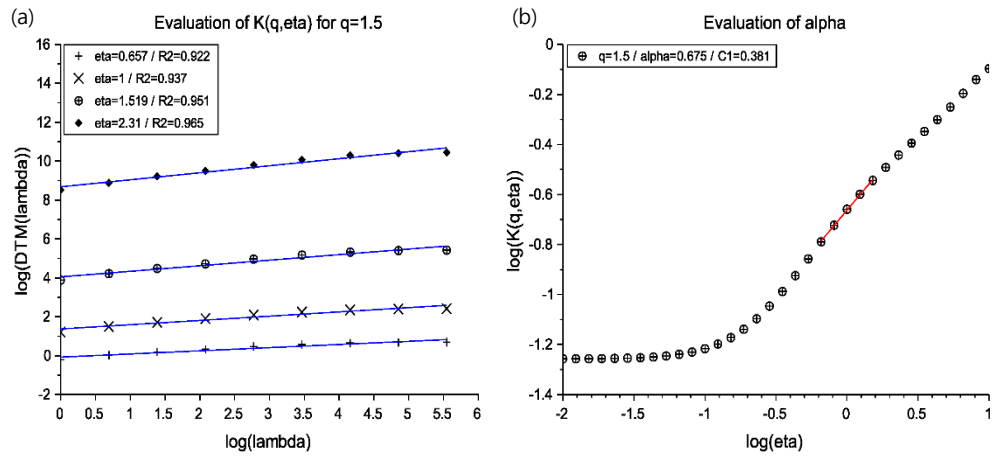


Fig. 5.1.21. The result of DTM analysis with CReSS model dataset in domain 256 km×256 km. (a) The scaling behavior with the value of different  $\eta$  from 0.1 to 2.5 at fixed  $q=1.5$ . (b) DTM curve with multifractal parameters.

## 2.2) The domain 64 km × 64 km

The domain size of 64 km × 64 km was selected from the middle of the whole domain 360 km × 360 km as well as the domain from the radar dataset. In Fig. 5.1.22, the result of spectral analysis in domain 64 km × 64 km is shown. Even though it seems it does not perfectly align in linear line compare to the domain 256 km × 256 km, the scaling behavior highly fits linear with  $\beta = 2.97$  and  $R^2 = 0.94$ .

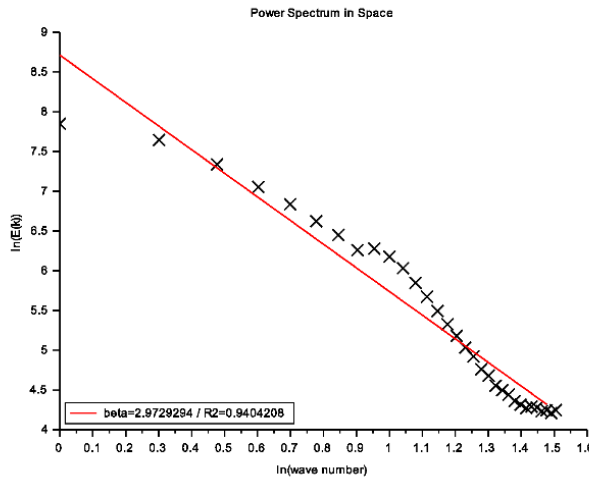


Fig. 5.1.22. The same as Fig. 5.1.19 but in domain 64 km × 64 km.

The TM and DTM result shows that the scaling behavior is very good by showing all  $R^2 \approx 0.9$  (Fig. 5.1.23 (a) and Fig. 5.1.24 (a)). The graph of scaling moment function  $K(q)$  in empirical, TM analysis, and DTM analysis are aligned in best-fitting from  $q = 0$  up to  $q = 7$  (Fig. 5.1.24 (c)). The DTM result shows the linear scaling behavior with the different  $\eta$  at  $q = 1.5$  (Fig. 5.1.24). As the three  $K(q)$  aligned with each other in Fig. 5.1.22 (c), the multifractal parameters obtained from TM and DTM are the same ( $\alpha = 0.35$  and  $C_1 = 0.8$ ).

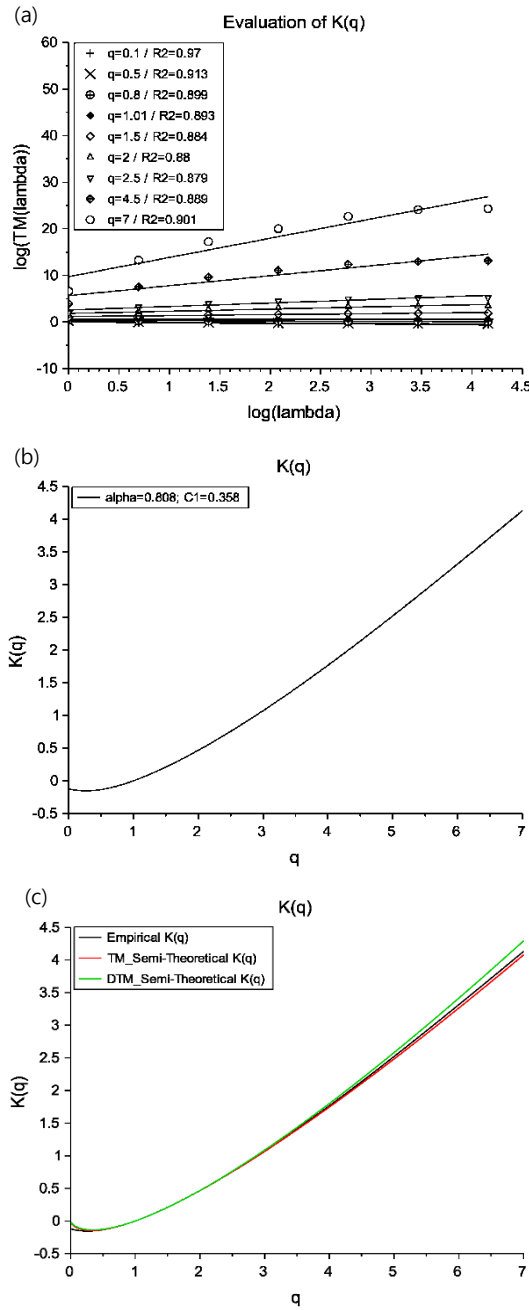


Fig. 5.1.23. The same as Fig. 5.1.20 but in the domain 64 km  $\times$  64 km.

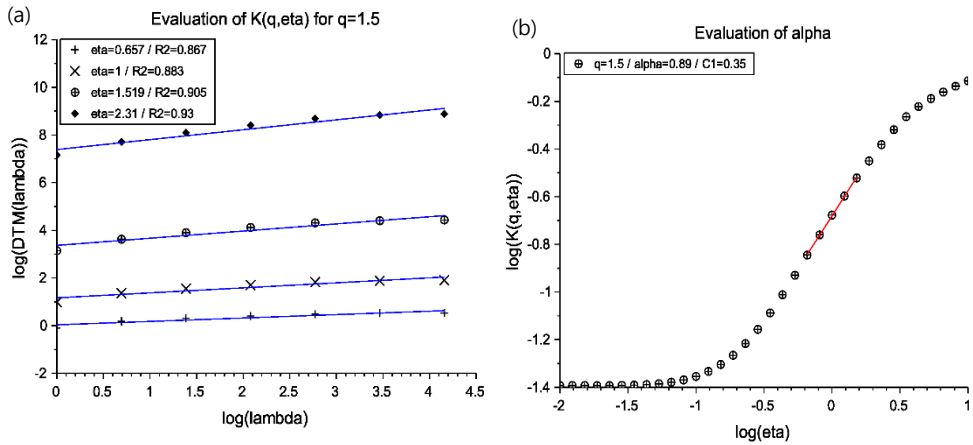


Fig. 5.1.24. The same as Fig. 5.1.21 but in domain 64 km  $\times$  64 km.

Table 5.1.5. The estimated UM parameters from TM and DTM analysis with the dataset of CReSS in the domain 256 km  $\times$  256 km and 64 km  $\times$  64 km.

CReSS		256 $\times$ 256	64 $\times$ 64
TM	$\alpha$	0.612	0.808
	$C_1$	0.391	0.358
DTM	$\alpha$	0.675	0.89
	$C_1$	0.381	0.35

### 3) Comparison of radar and CReSS

In order to obtain a more detailed comparison of linearity between radar data and CReSS data, each of  $K(q)$  of the radar data on each height and  $K(q)$  of the CReSS model data was compared by Fig. 5.1.25 with the domain size of 256 km  $\times$  256 km and Fig. 5.1.26 with 64 km  $\times$  64 km. By comparing  $K(q)$ , if the  $\alpha$  values are considerably similar for two  $K(q)$  functions, these functions would be different from each other only by a ratio of  $C_1$  values.

With the domain size of 256 km  $\times$  256 km, the comparison of  $K(q)$  function shows the consistency between two different datasets the best at 2 km, because of the curvature of blue dots at 2 km aligns the most straight compared to other altitudes, as well as there's no difference of  $C_1$  (departure from the bisectrix), neither with  $\alpha$  (presence of a curvature; departure from the linear regression fit). Meanwhile, the difference of  $\alpha$  is larger when the altitudes are higher when the ratio of  $C_1$  is as follows ;

At 1 km :  $0.381/0.616 = 0.619$ , at 2 km :  $0.381/0.383 = 0.995$ , at 4 km :  $0.381/0.203 = 1.877$ , at 5 km :  $0.381/0.18 = 2.117$ , at 6 km :  $0.381/0.107 = 3.561$ , and at 8 km :  $0.381/0.202 = 1.886$ .

With the domain size 64 km  $\times$  64 km, the limitation of the observation in the low altitudes, the comparison was only done from 4 km and above. As well as the domain 256 km  $\times$  256 km, the difference of  $\alpha$  shows larger in higher altitudes, but the ratio of  $C_1$  shows more than 1 in every altitude.

As it was explained before,  $C_1$  describes the sparseness of the mean value of the field (mean intermittency) and  $\alpha$  describes how much it varies as it goes away from the mean value of the field (variability of intermittency). The set of graphs on both domains demonstrate that the departures from the bisectrix and the linear regression fit are diminishing along the altitudes up to 6 km.

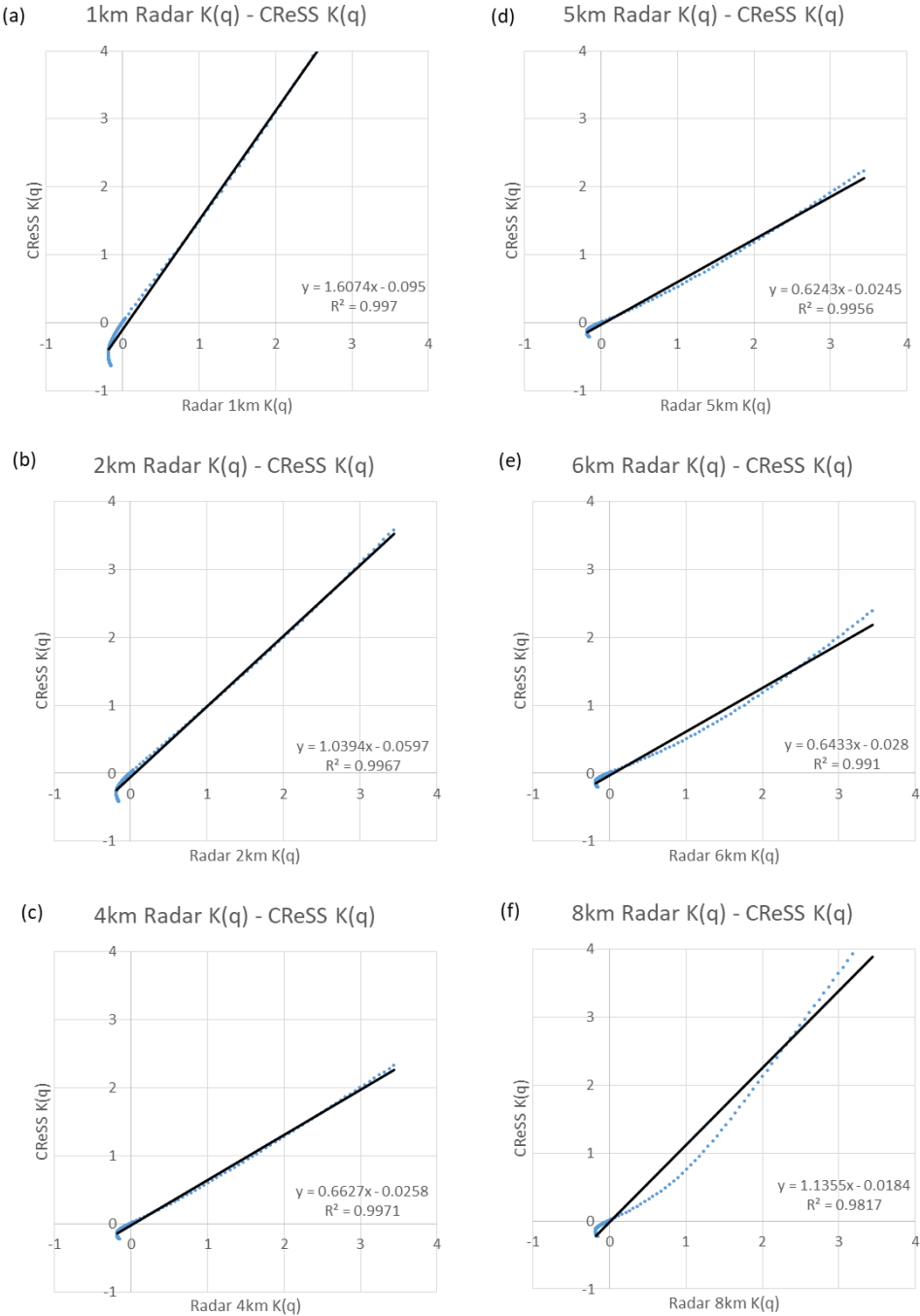


Fig. 5.1.25. Comparison between the empirical  $K(q)$  for each height of the radar data and the CReSS model in the domain size of  $256 \text{ km} \times 256 \text{ km}$  of typhoon Khanun. The blue dots correspond to the  $K(q)$  values for each  $q$  value; the black lines are the linear regression fits.

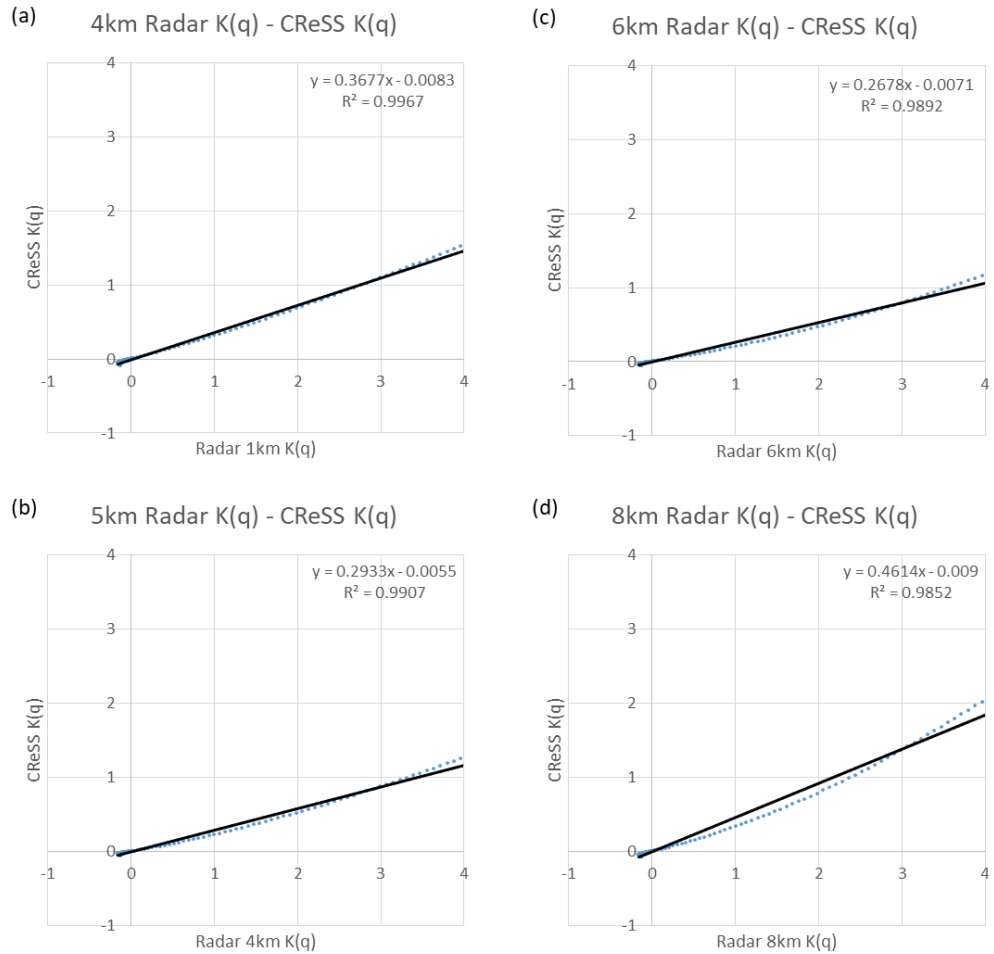


Fig. 5.1.26. The same as Fig. 5.1.24 but with the domain 64 km × 64 km.

## 5.2. Typhoon Bolaven

### 5.2.1. Environmental description

Bolaven was formed as a tropical depression on 19 August 2012 and steadily intensified to a typhoon by 21 August. On 24 August the system attained its peak intensity with the winds of  $51.4 \text{ ms}^{-1}$  (115 mph) and a pressure of 910 hPa. The storm passed and weakened slightly as it moved directly over Okinawa on 26 August as it began accelerating toward the north. The steady weakening continued as Bolaven approached the Korean Peninsula and it eventually made landfall in North Korea late on 28 August before transitioning into an extratropical cyclone. Even though it was at a weakening stage, Bolaven was one of the most massive typhoons which caused a lot of damage with severe rainfall all over Korea including Jeju Island. The rainfall amount was more than 250 mm in 2 days. It was regarded as the most powerful storm to strike the Korean Peninsula in nearly a decade, with wind gusts measured up to  $51.8 \text{ ms}^{-1}$ .

Fig. 5.2.1 shows the track of the typhoon Bolaven with the dots indicating the location of the center of the typhoon where the lowest pressure is. The center of the typhoon passed by the west side of Jeju Island and moved northward along the west side of the Korean peninsula. The surface data, AWS operated by KMA, was additionally collected and obtained the daily accumulated rainfall amount on 27 August 2012, shown in Fig. 5.2.2. Fig. 5.2.2 (b) shows that the maximum accumulated rainfall amount recorded up to 360 mm on the southwest side of the top of Halla mountain area. Fig. 5.2.3 shows the relationship between typhoon center pressure (hPa) in red and the maximum wind speed (m/s) in blue.

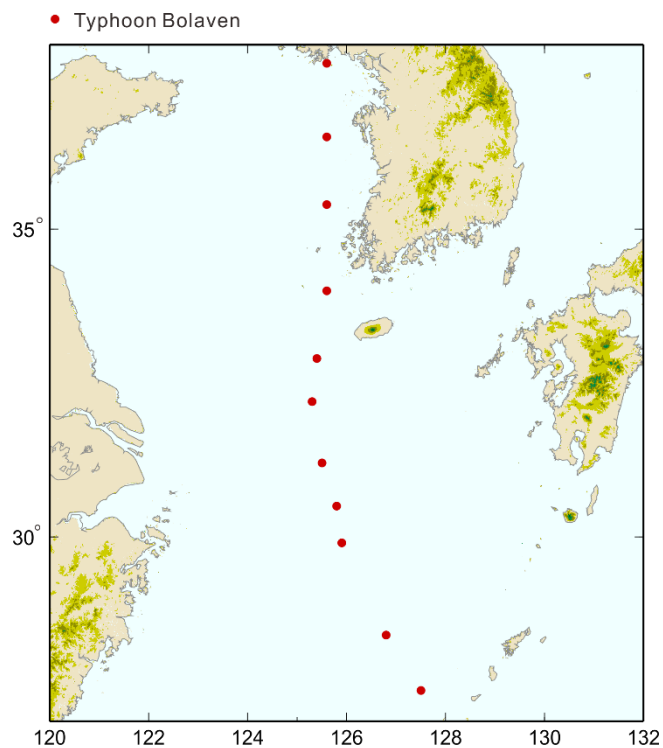


Fig. 5.2.1. The track of Typhoon Bolaven. The red dots indicate the location of the typhoon center.

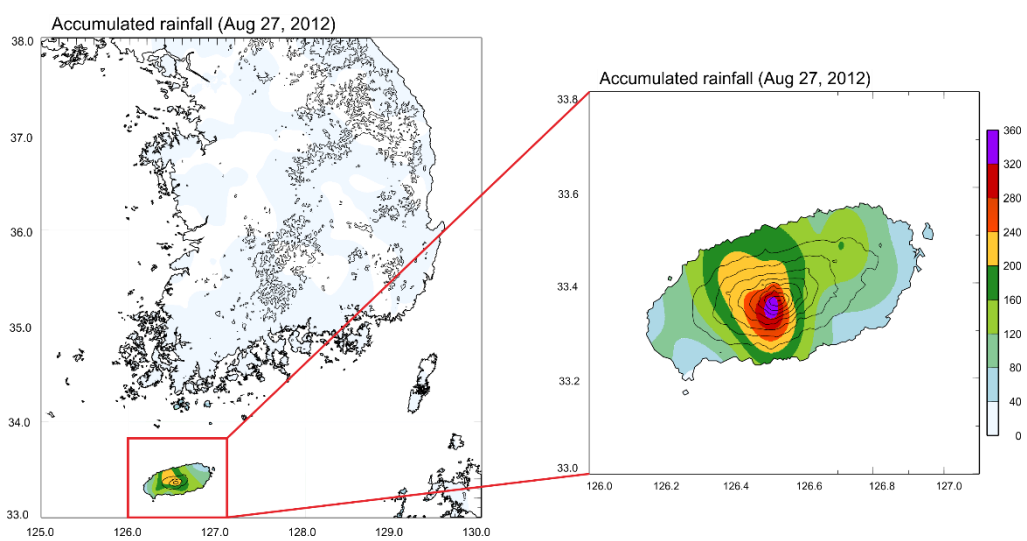


Fig. 5.2.2. The daily accumulated rainfall on 27 August 2012 in Korea.

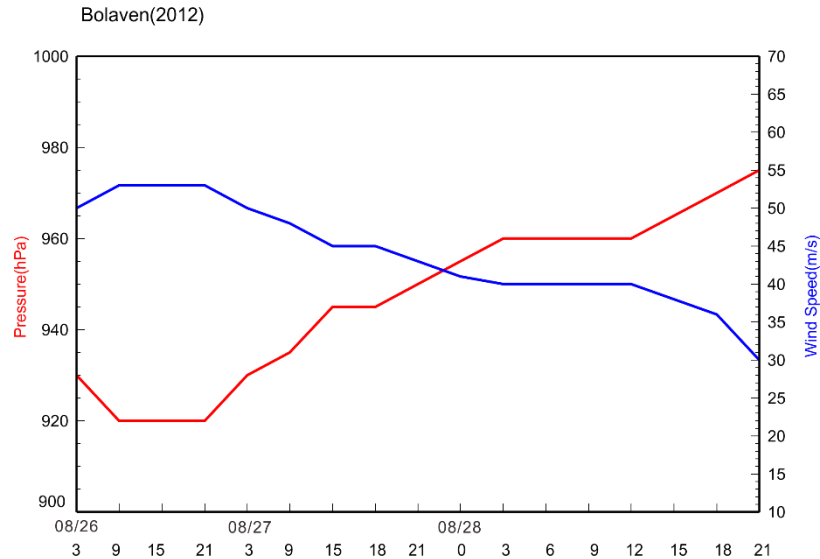


Fig. 5.2.3. The typhoon center pressure (hPa) in red and the maximum wind speed (m/s) in blue.

Fig. 5.2.4 shows the synoptic flow at 1200 UTC on 27 August 2012. The description in detail is provided from NCEP/NCAR Reanalysis. The center of typhoon is found in the southwest of Jeju Island (Fig. 5.2.4 (a)). The convergence areas were formed in the northeast part of the typhoon right on Jeju Island, and the active confluence area shows the development of the eyewall due to the sharp rising motion of the air. Also, the equivalent potential temperature at 850 hPa is much higher around the typhoon than surrounding areas that it indicates how unstable it is around the selected area and also appears to supply the warm and humid air from the tropics continuously (Fig. 5.2.4 (b)). At 500 hPa, the contour shows the vorticity with the wind flow. The strong positive shear vorticity is shown as the wind speed is increasing around the typhoon, especially on the right side of the center of the typhoon (Fig. 5.2.4 (c)). Lastly, at 300 hPa, an upper-level jet (ULJ) streak of  $\geq 25 \text{ ms}^{-1}$  is shown in the north of the Korean peninsula from the west and the upper-level divergence is shown which enhances rising air as warm air advection is occurring in the lower levels (Fig. 5.2.4 (d)).

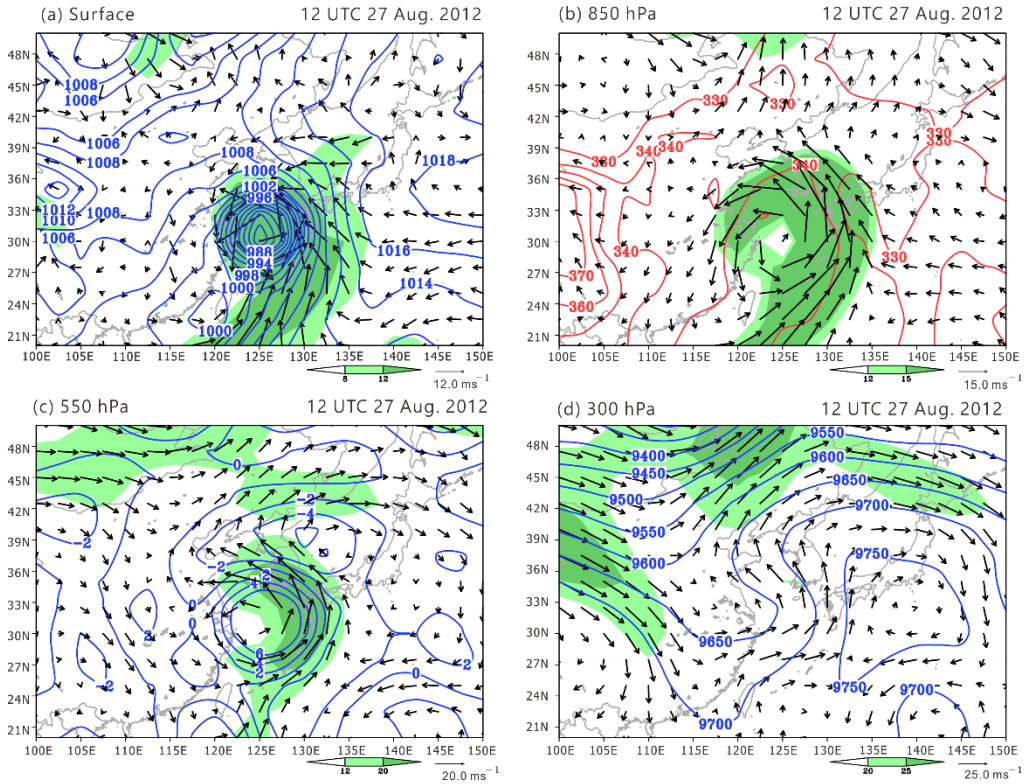


Fig. 5.2.4. The synoptic flow at 1200 UTC on 27 August 2012. (a) at the surface showing the pressure (sea level pressure, hPa), (b) at 850 hPa showing the equivalent potential temperature (K), (c) at 500 hPa showing the relative vorticity ( $10^{-5} s^{-1}$ ), and (d) at 300 hPa showing the geopotential height (m) with wind vector.

### 5.2.2. Observation results

Fig 5.2.5 displays the horizontal wind field with the reflectivity during the typhoon Bolaven approaches Jeju Island. As the typhoon was relatively much bigger than the previous case of typhoon Khanun, the 4-time steps are

selected (1730 LST, 1930 LST, 2130 LST, and 2330LST) on 27 August which was the day when the maximum accumulated rainfall was recorded in Jeju Island. The spiral band in with the reflectivity of 50 dBZ appears in every height until 6 km (mostly up to 4 km). As the spiral band makes landfall on the island, the strong convection appeared near the top of the Halla mountain area. The typhoon is moving to the northward with the weakened intensity near the typhoon center.

Fig. 5.2.6 shows the vertical cross-section of the wind field. On the first time step (1730 LST), the strong downdraft is shown in the pre-squall line while the an squall line is slowly evolving with the strong reflectivity up to 7 km altitudes. It is due to the downdraft in low altitude below 5 km while above 5 km, there is strong updraft wind that it stretches the cyclone vertically spreading the convection vertically. As the vertical wind in pre-squall line changes to the updraft, the convection activity developed. Meanwhile, the spiral band started to build stronger downdrafts, and the convections are more horizontally distributed but less vertically stretched. As the spiral band moves north passing through the island, the convection is more spattered. Also, the center of typhoon approaches the island with a strong downdraft.

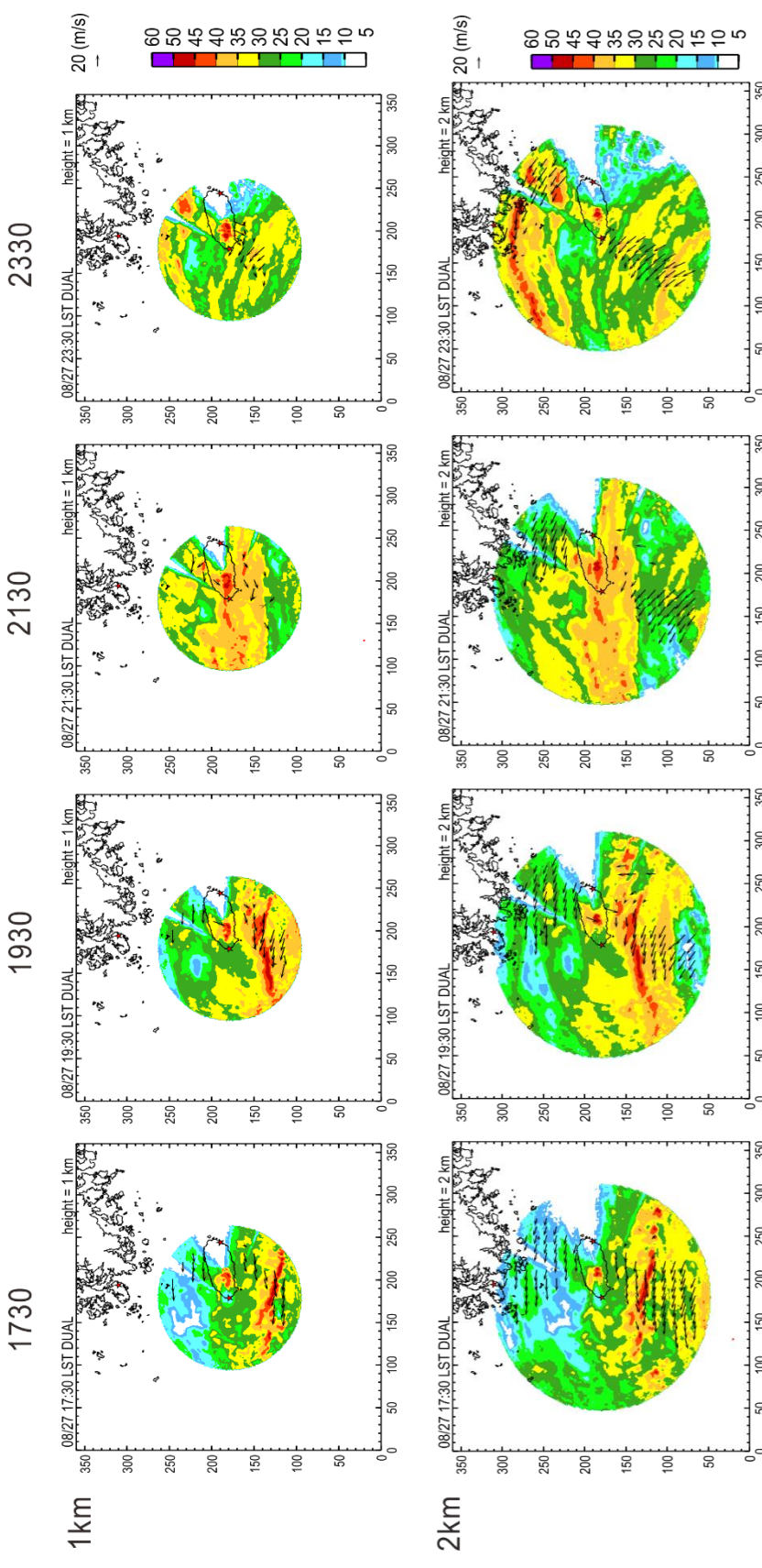


Fig. 5.2.5. The same as Fig. 5.1.5 but with Bolaven case.

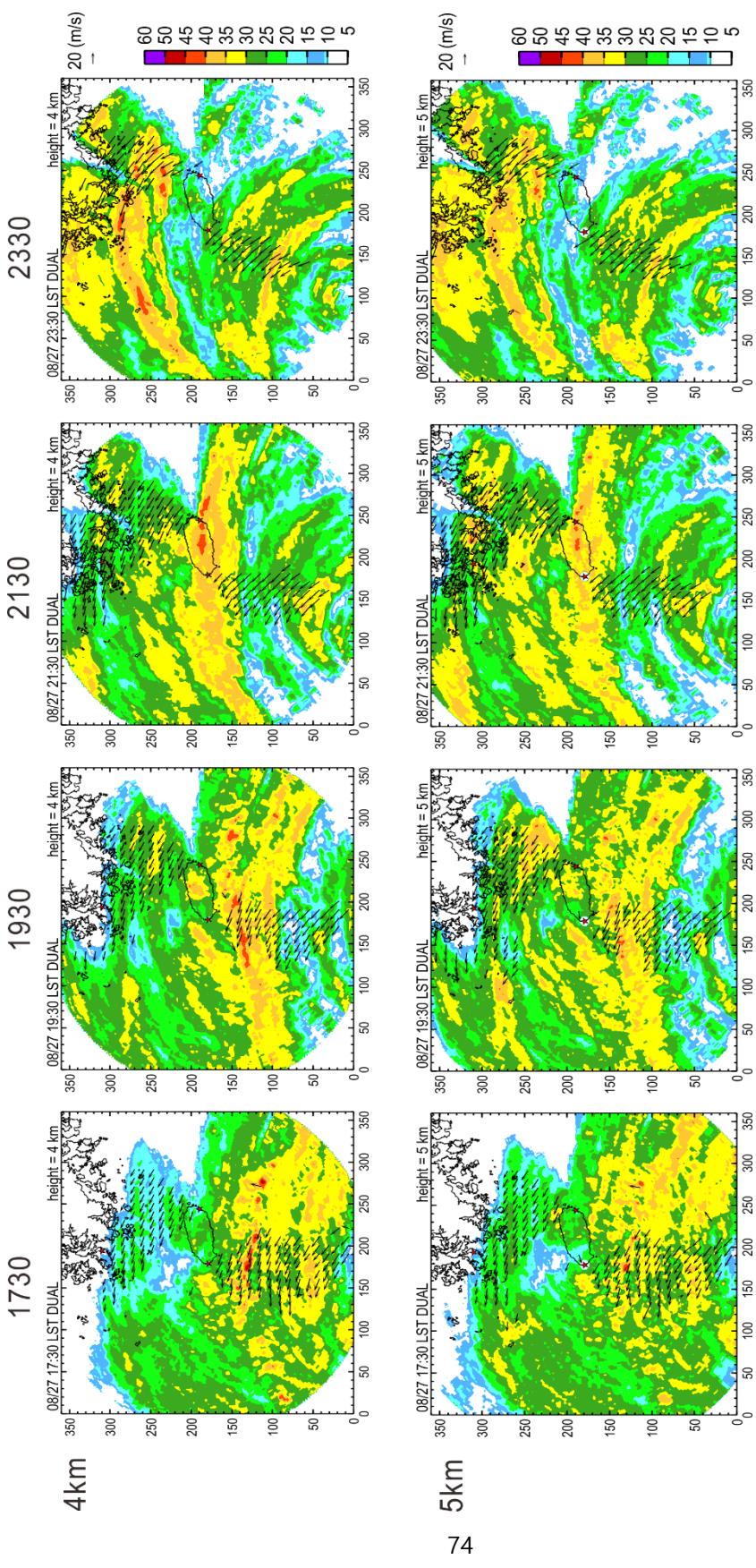


Fig. 5.2.5. Continued

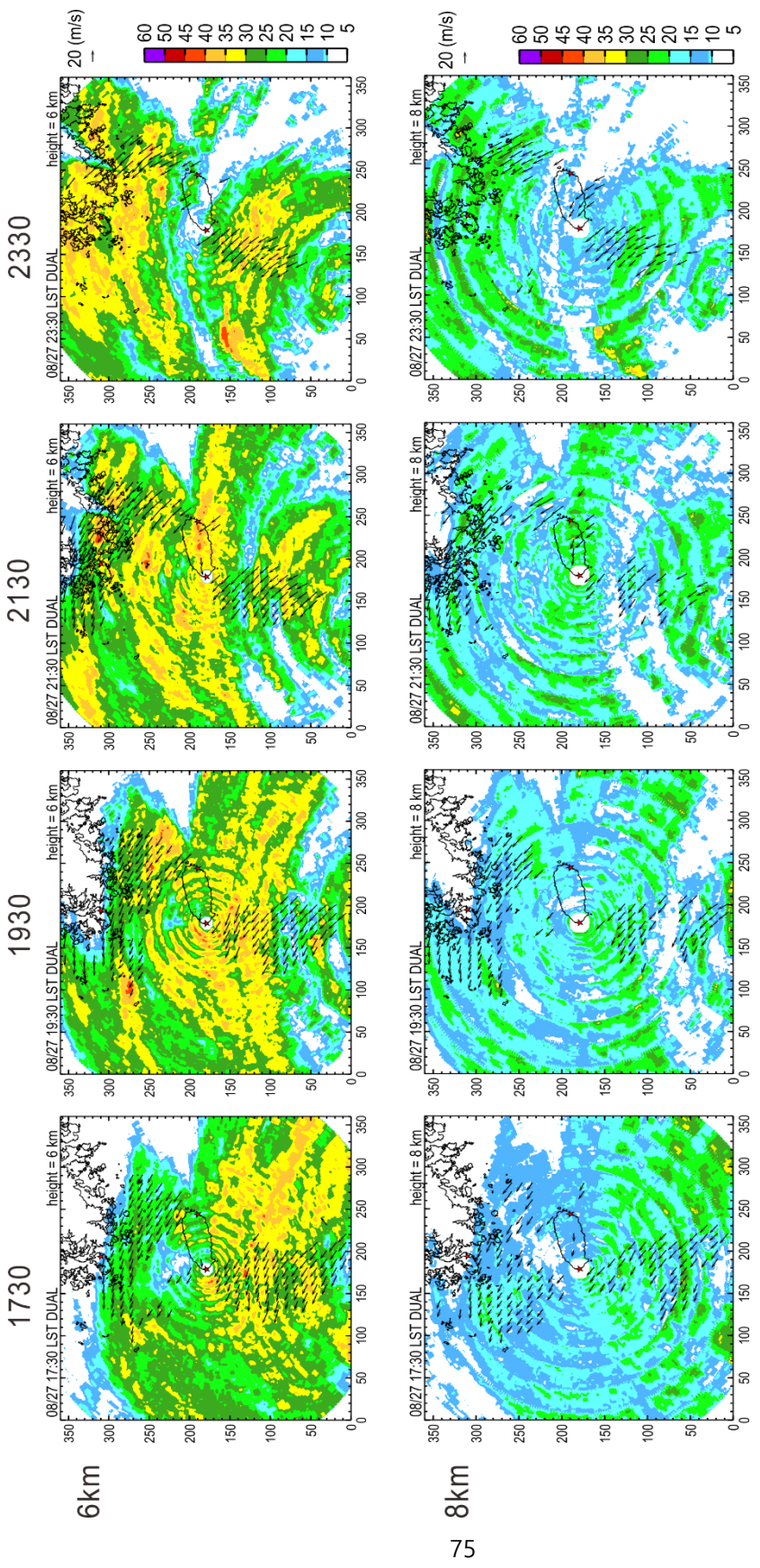


Fig. 5.2.5. Continued

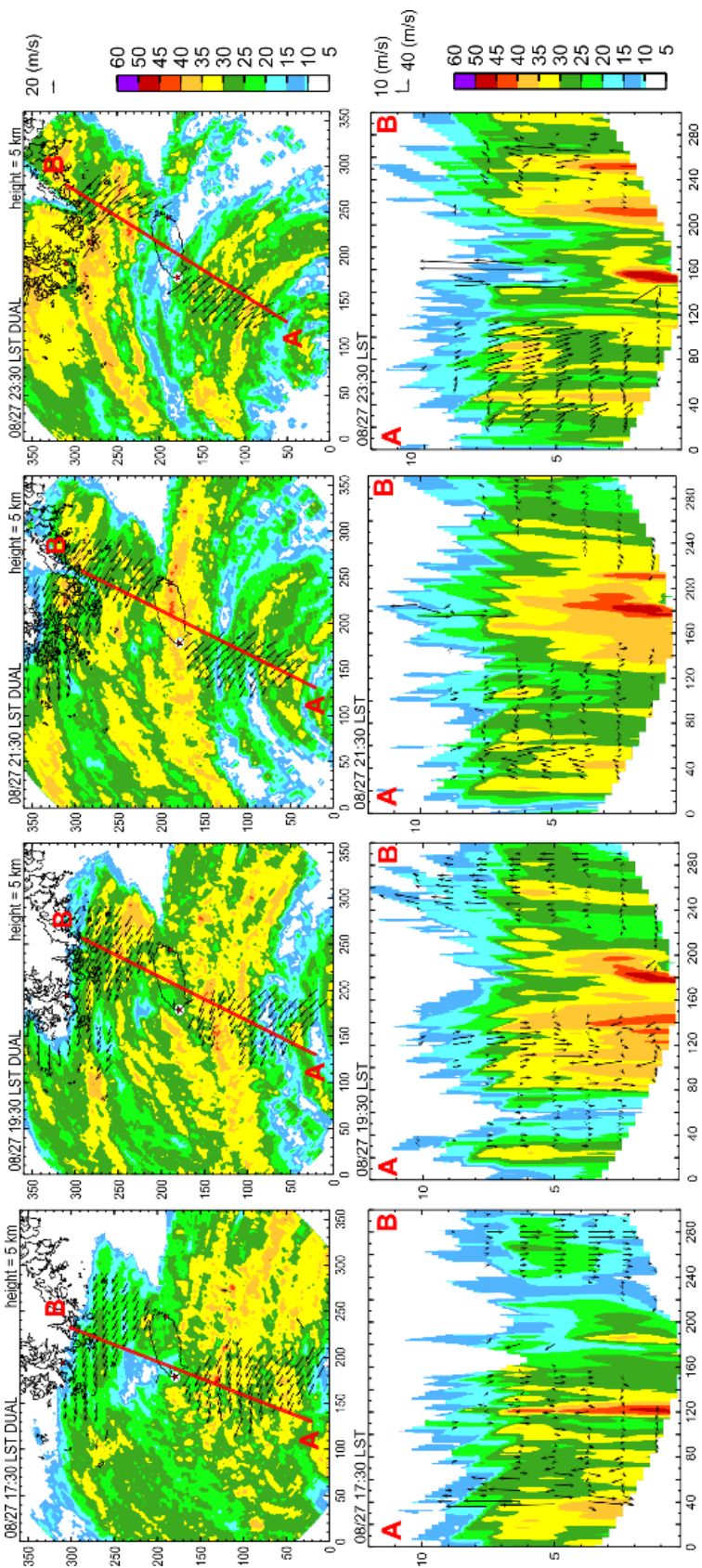


Fig. 5.2.6. The same as Fig. 5.1.6 but with the Bolaven case.

Fig. 5.2.7 shows radar reflectivity (contour) with divergence (red shading) and convergence (blue shading) of horizontal wind at each altitude obtained at 1730 LST, 1930 LST, 2130 LST, and 2330 LST on 27 August 2012.

At 1730 LST, the outer band of the typhoon starts to make landfall on Jeju Island. The strong convergence is shown over  $-4 \times 10^{-3} S^{-1}$  in 1 and 2 km altitude where the reflectivity is over 45 dBZ when the substantial divergence is shown over  $4 \times 10^{-3} S^{-1}$  at 5 – 6 km and the strong divergence is shown at 8 km altitude. Both of the convergence and divergence weakens to over  $-3 \times 10^{-3} S^{-1}$  at every altitude as the time passes to 2130 LST. However, at 2330 LST, the intense convergence shows near the island in low altitudes of 1 – 2 km and the substantial divergence shows in the middle of the island at 6 and 8 km.

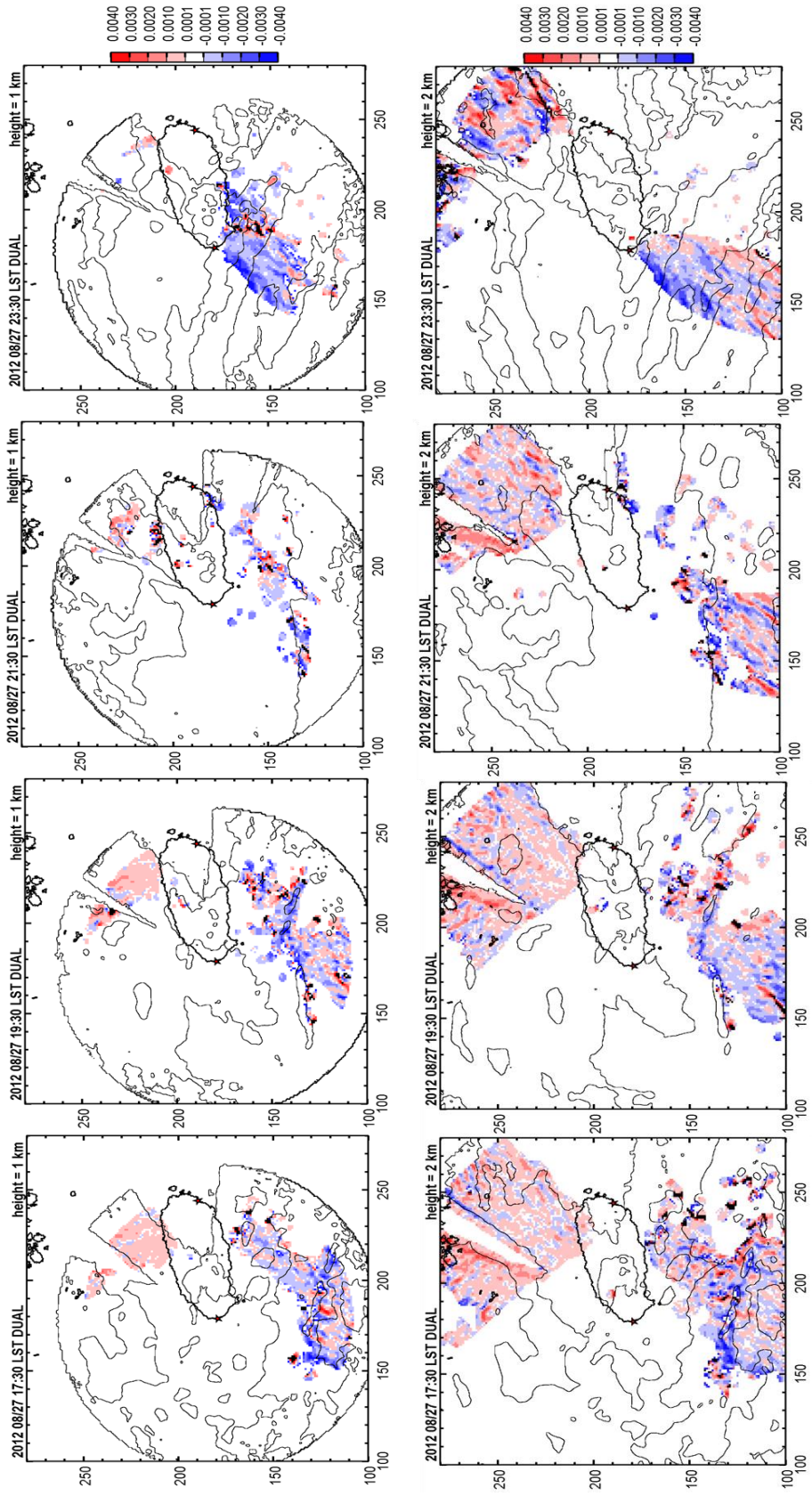


Fig. 5.2.7. The same as Fig. 5.1.7 but with the case of typhoon Bolaven.

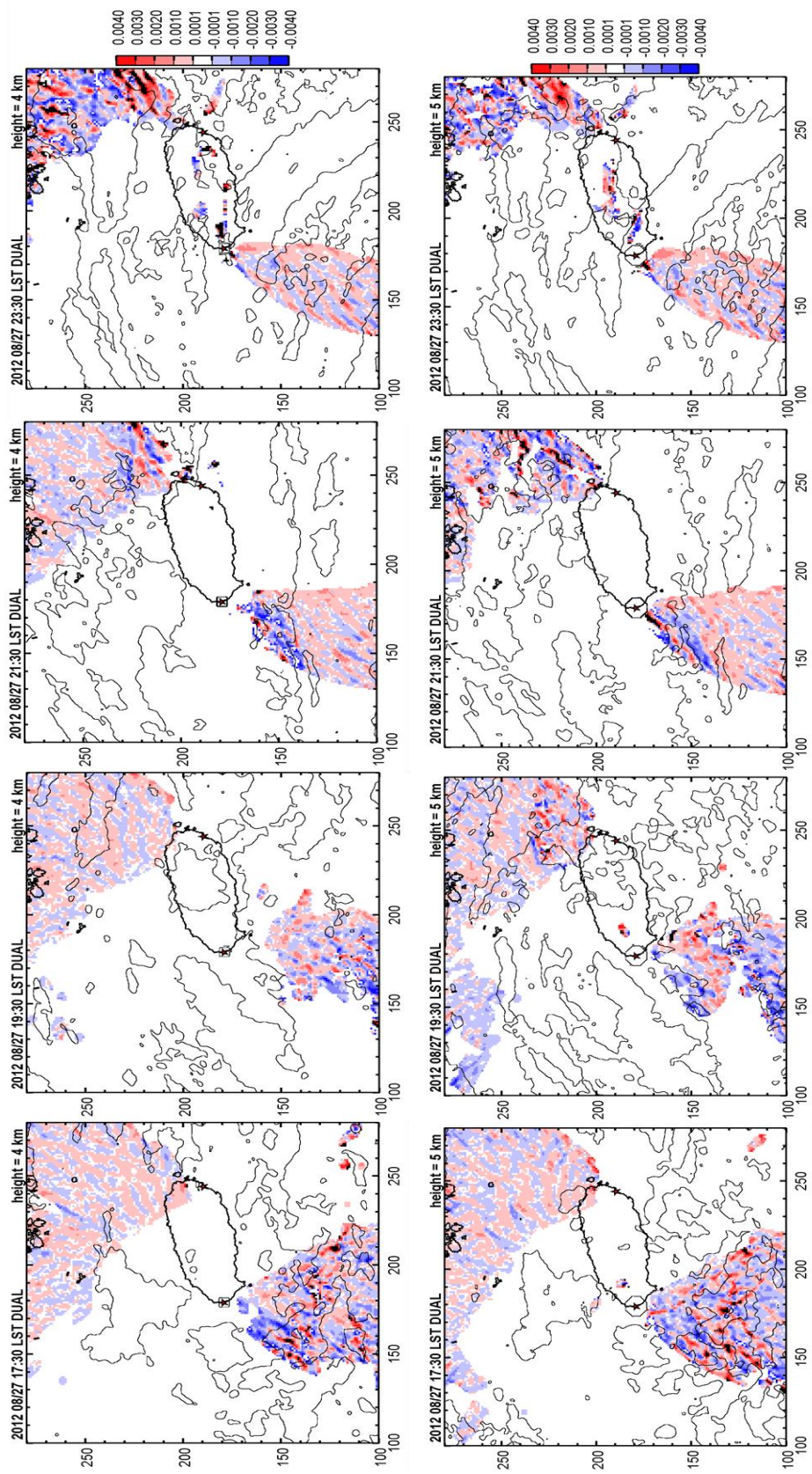


Fig. 5.2.7. Continued.

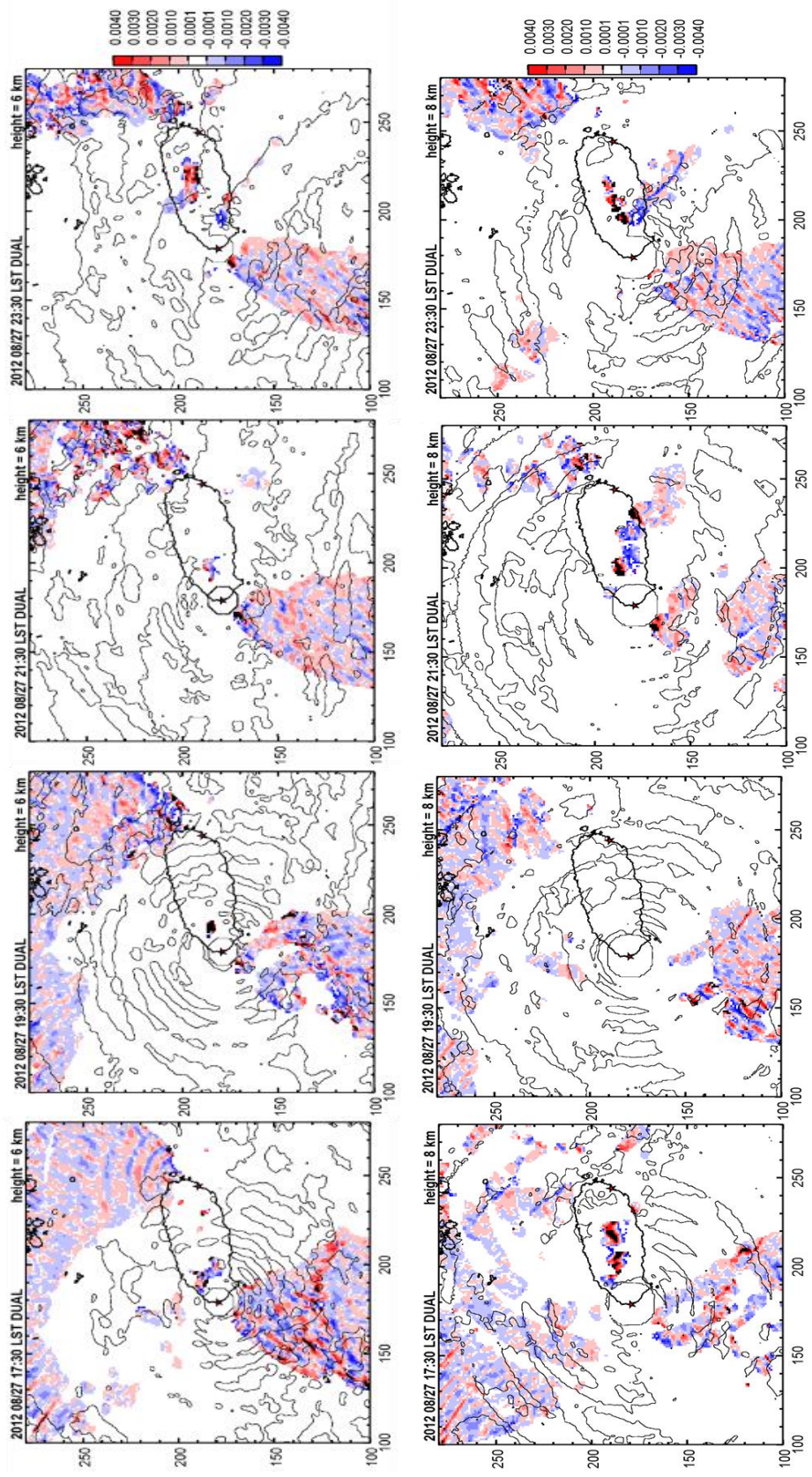


Fig. 5.2.7. Continued

### 5.2.3. Multifractal analysis

The multifractal analysis was performed with the rainfall rate obtained from the radar reflectivity data from Gosan, Jeju Island, Korea. As the multifractal analysis can be only done with the domain size in power of 2, the domain size of  $256 \text{ km} \times 256 \text{ km}$  is selected with the area covering the most massive rainfall rate is occurred. To see in detail without the zero-field which is caused by the observation minimum radar beam elevation angle in the lower altitudes, the size of  $64 \text{ km} \times 64 \text{ km}$  is selected in the middle of the whole domain ( $360 \text{ km} \times 360 \text{ km}$ ) where the center is the location of the radar.

## 1) Radar

### 1.1) The domain $256 \text{ km} \times 256 \text{ km}$

The spectral analysis was performed for all data to see the conservativeness of the field (different altitudes in both domains). Fig. 5.2.8 shows that there was no extreme scaling break in any altitudes. Also, all dataset were showing the linear scaling behavior up to  $\ln(k) = 2$  with  $R^2 \geq 0.9$ . All the cases present good scaling behavior in most of the parts except at 2 km, where it shows some instabilities with a strong tail lift. The detailed values of  $\beta$  and  $R^2$  is shown in Table 5.2.1.

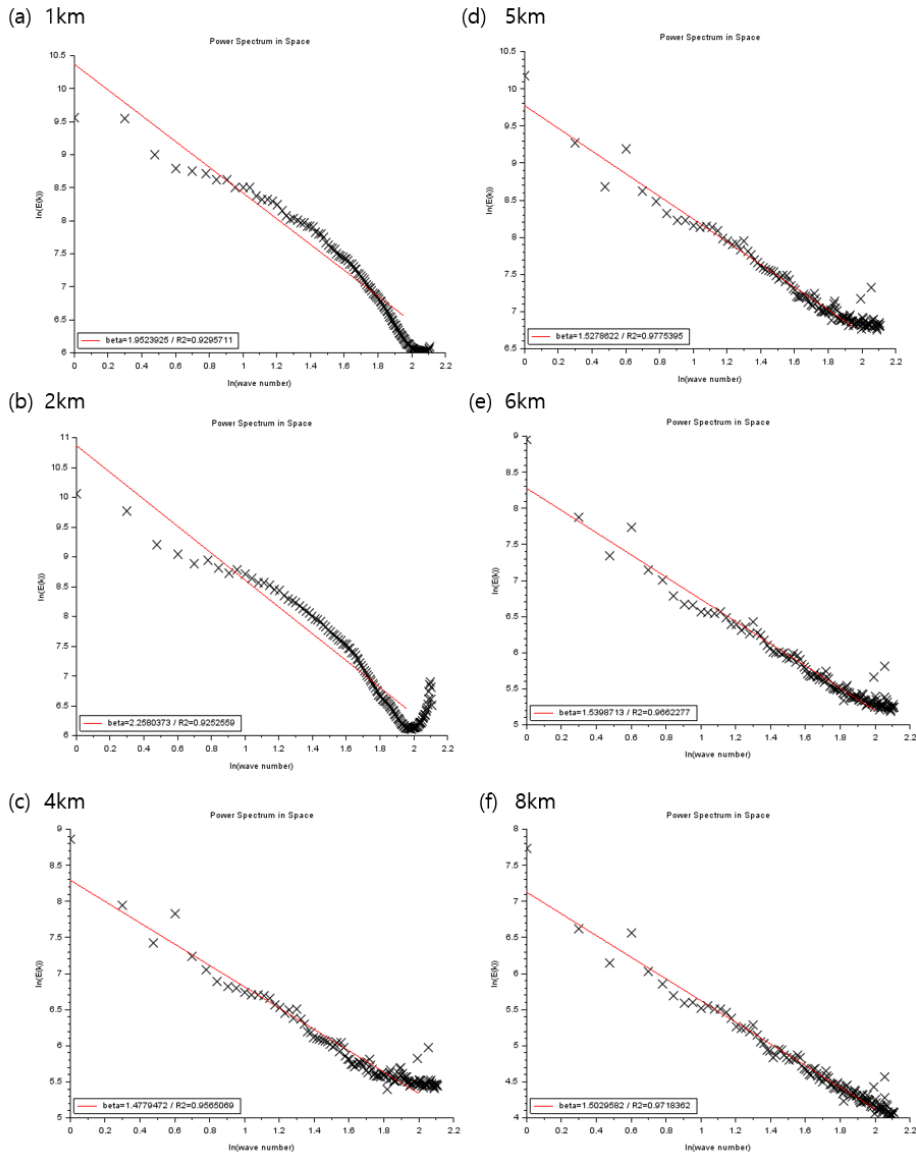


Fig. 5.2.8. The same as Fig. 5.1.8 but with the Bolaven case.

Table 5.2.1. The same as Table 5.1.1 but with Typhoon Bolaven.

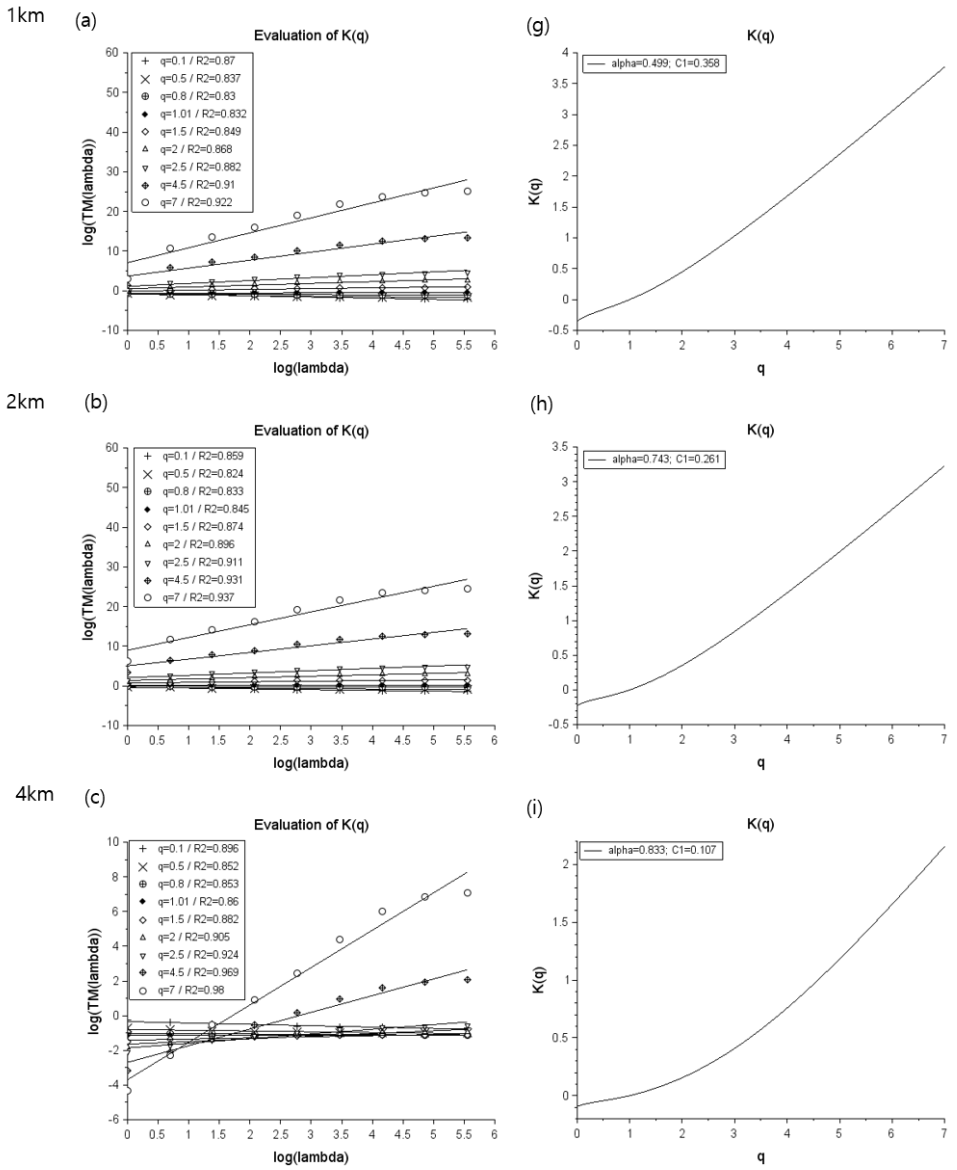
	1 km	2 km	4 km	5 km	6 km	8 km
$\beta$	1.95	2.26	1.48	1.53	1.54	1.50
$R^2$	0.93	0.93	0.96	0.98	0.97	0.97

TM and DTM analysis were done with all data. The results of the TM method are presented in Fig. 5.2.9. The graphs on the left (a, b, c, d, e, f) shows the log-log plots of  $\langle \varepsilon_\lambda^q \rangle \approx \lambda^{K(q)}$  with the resolution  $\lambda$  (in this case, it is a set from 1 to 256 km with the rate of increase in power of 2) and the values of  $q$  were freely chosen between 0.1 and 7.0. In most cases, the scaling behavior was very good without any scaling break ( $R^2 \geq 0.9$ ) which means that the field is multifractal from  $q = 0.1$  up to  $q = 7$ . The scaling moment function  $K(q)$  is obtained (Fig. 5.2.9 (g, h, i, j, k, l)) and UM parameters are obtained from the slope of  $K(q)$  graphs which shows the moment and singularity behavior.

Fig 5.2.10 shows the estimated (or empirical) scaling moment functions  $K(q)$  (in black) are compared to the semi-theoretical functions that are the curves with the UM parameters  $\alpha$  and  $C_1$  further retrieved from TM (red) and DTM (green) analysis. It shows how the scaling behavior is fitting with each other. By comparing the empirical and DTM semi-theoretical  $K(q)$ , all the  $K(q)$  shows the same scaling behavior until  $q = 3.0$ . At 1 km and 2 km, the slope of  $K(q)$  calculated from DTM shows the behavior of UM parameter  $C_1$  is more extreme than in other altitudes due to a multifractal phase transition.

The results of the DTM method are shown in Fig. 5.2.11. A clear scaling behavior was retrieved as well as the TM analysis. For each power  $\eta$ , with a fixed value of  $q$  ( $q=1.5$ ), the slope of the linear regression gives an estimate of the scaling moment functions  $K(q, \eta)$ . The S-shape curves (Fig. 5.2.11 (g, h, i, j, k, l)) are conditioned by an appearance of numerical limitations at smaller moments and the critical behavior of extremes at higher statistical moments, both being characterized by the flattening of the double trace moment curves. The slope of the curve gives an estimation of  $\alpha$  and  $C_1$ . The value of  $\alpha$  increases along with the height while the value of  $C_1$  decreases, showing how to concentrate and how quickly the intermittency evolved.

Both  $\alpha$  and  $C_1$ , the UM parameters estimated from TM and DTM are indicated in Table 5.2.2. and shown in Fig. 5.2.12.



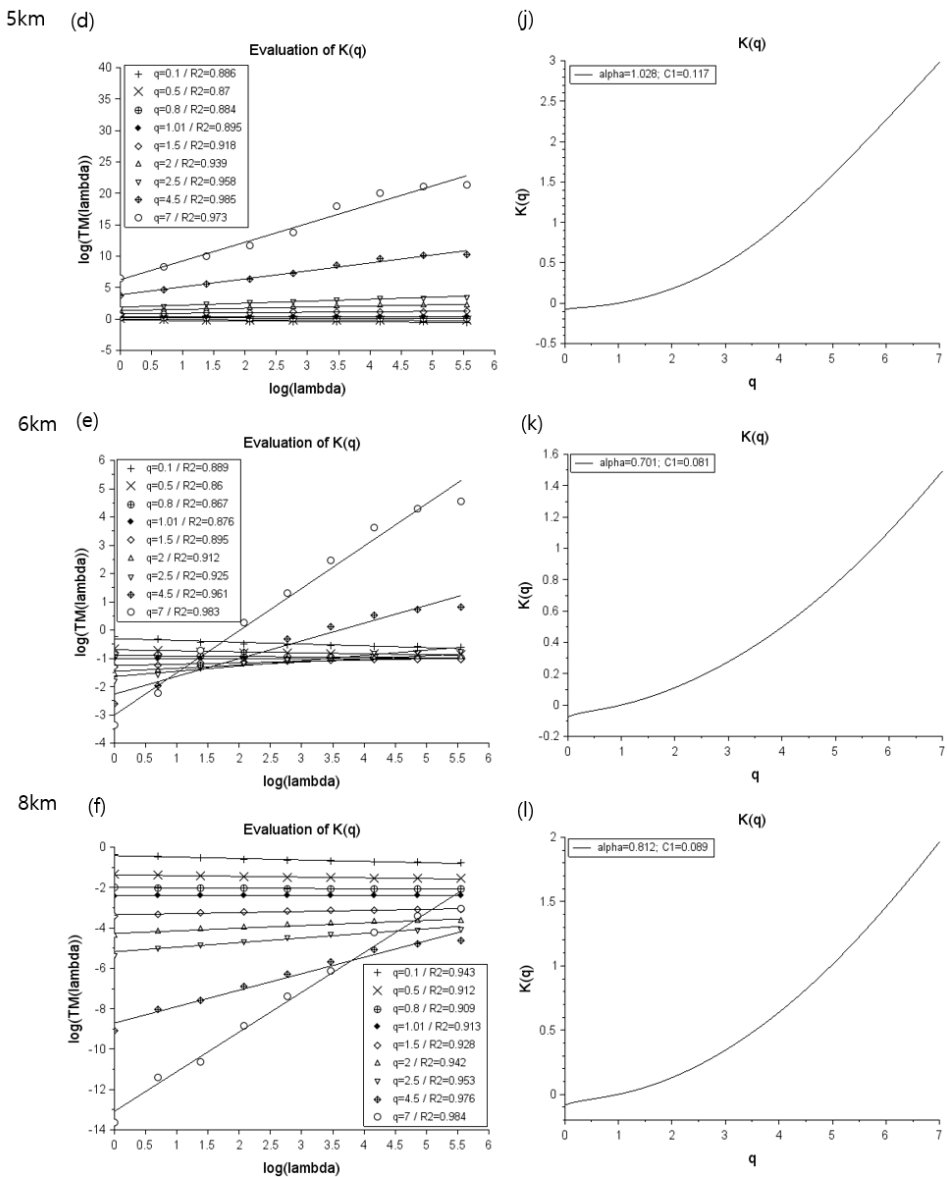


Fig. 5.2.9. The same as Fig. 5.1.9 but with the Bolaven case.

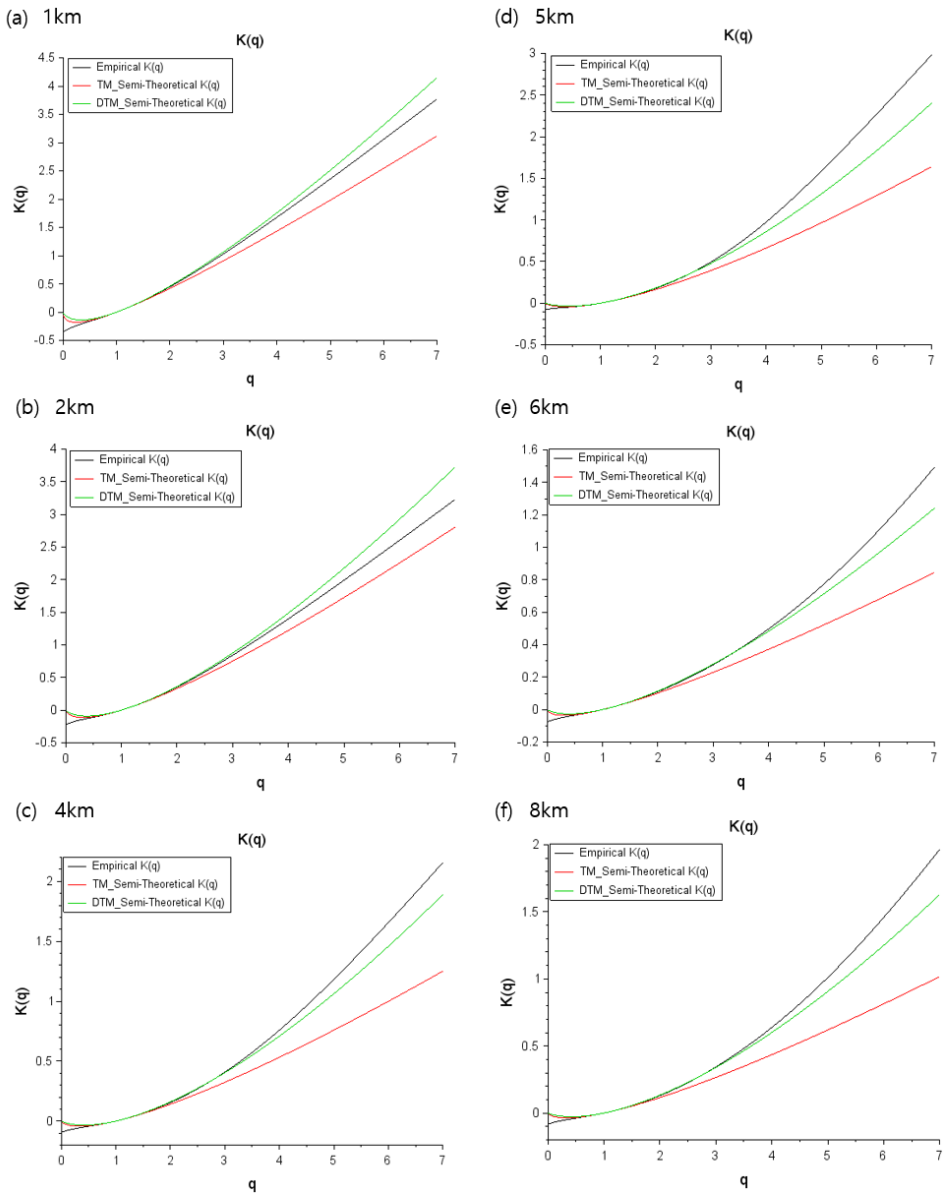
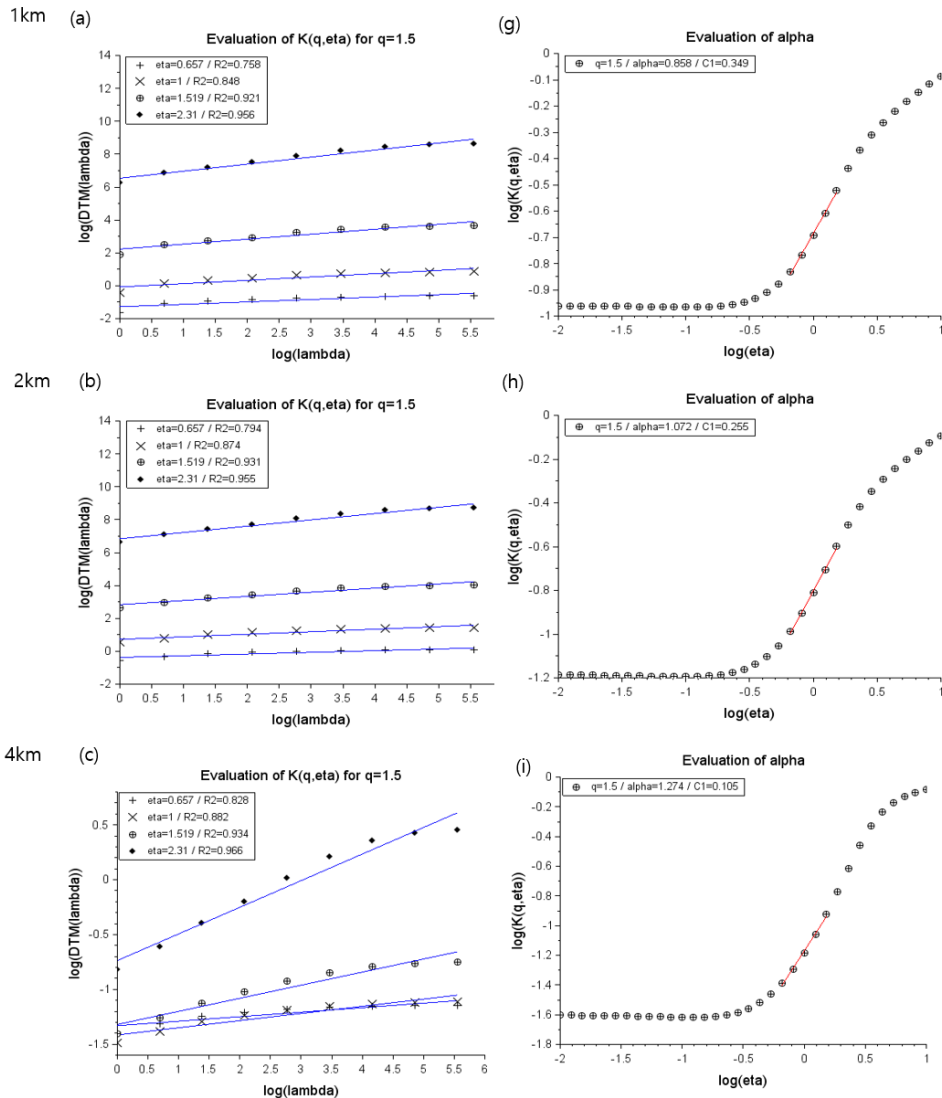
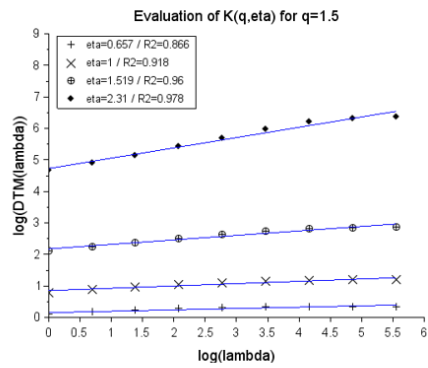


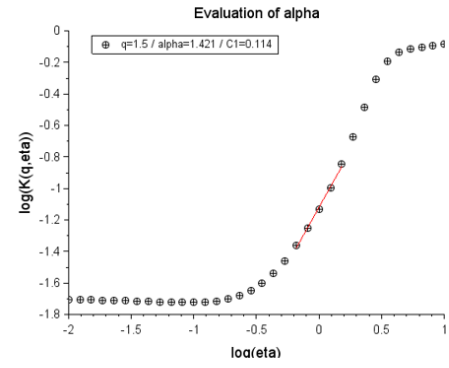
Fig. 5.2.10. The same as Fig. 5.1.10 but with the Bolaven case.



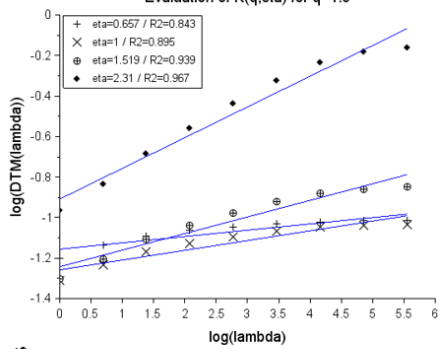
5km (d)



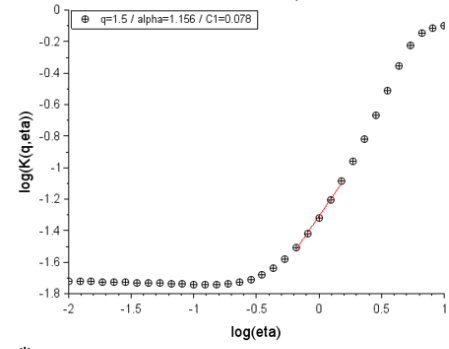
(j)



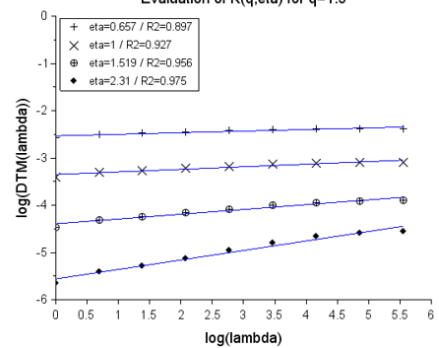
6km (e)



(k)



8km (f)



(l)

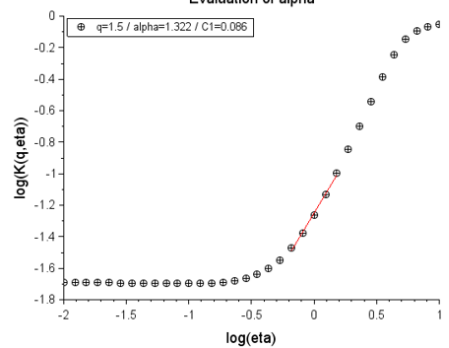


Fig. 5.2.11. The same as Fig. 5.1.11 but with the Bolaven case.

Table 5.2.2. The same as Table 5.1.2 but with Typhoon Bolaven.

		1 km	2 km	4 km	5 km	6 km	8 km
TM	$\alpha$	0.499	0.743	0.833	1.028	0.701	0.812
	$C_1$	0.358	0.261	0.107	0.117	0.081	0.089
DTM	$\alpha$	0.858	1.072	1.274	1.421	1.156	1.322
	$C_1$	0.349	0.255	0.105	0.114	0.078	0.086

Hence, the scaling exponent value  $\beta$  for spectral analysis are averagely 1.710 in all heights of the domain sizes 256 km  $\times$  256 km with  $R^2 \geq 0.9$  at all altitudes.

The multifractal parameters were obtained from TM and DTM analysis. The value of  $C_1$  is almost the same between the result of the TM and DTM but the larger values of  $\alpha$  are obtained from DTM analysis. However, the pattern of the changes in the values is the same.

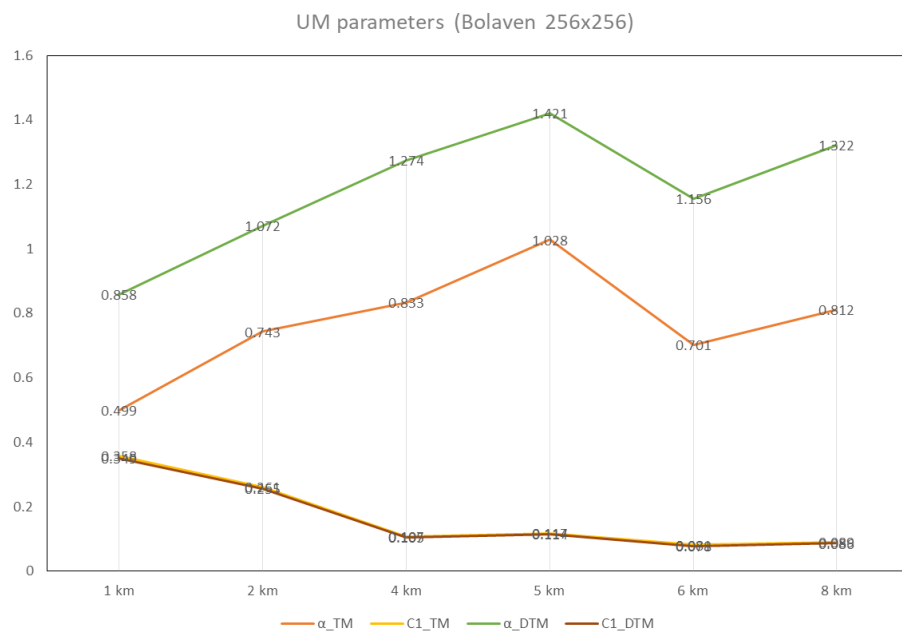


Fig. 5.2.12. The UM parameters obtained from TM and DTM.

## 1.2) The domain $64 \text{ km} \times 64 \text{ km}$

The spectral analysis was performed in the smaller domain size of  $64 \text{ km} \times 64 \text{ km}$ . As well as the previous case of Khanun, the analysis was done in a smaller domain is due to the zero-field included in 1 km and 2 km in the bigger domain size  $256 \text{ km} \times 256 \text{ km}$ . However, in this case, the domain was selected in the middle of the whole observation field.

From the spectral analysis, it is noted that all dataset were showing the linear scaling behavior up to  $\ln(k) = 1.5$  with  $R^2 \geq 0.9$ . All the cases present good scaling behavior in most of the parts, especially at 4 km, and 5 km presents the best and at 8 km presents the worst scaling behavior (Fig. 5.2.13). The detailed values of  $\beta$  and  $R^2$  is summarized in Table 5.2.3.

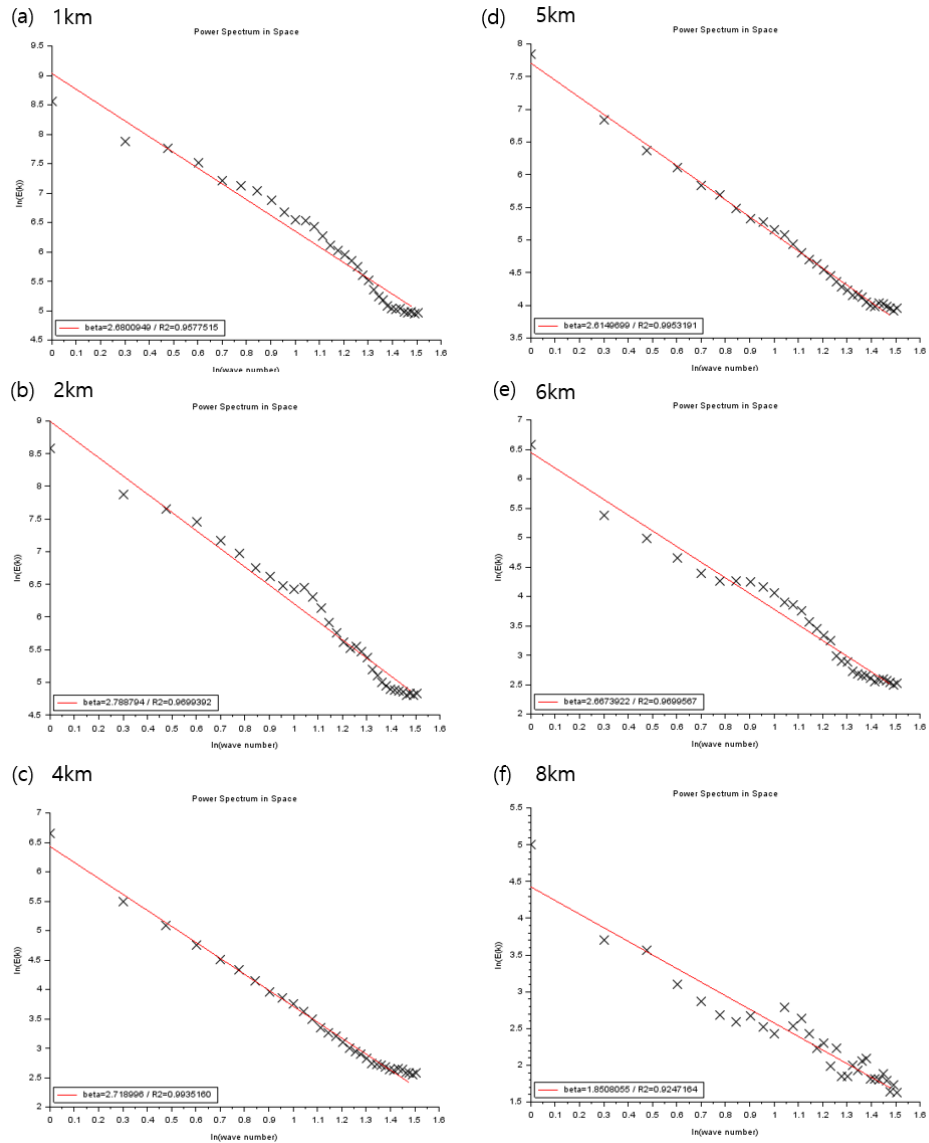


Fig. 5.2.13. The same as Fig. 5.2.8 but in the domain size  $64 \text{ km} \times 64 \text{ km}$ .

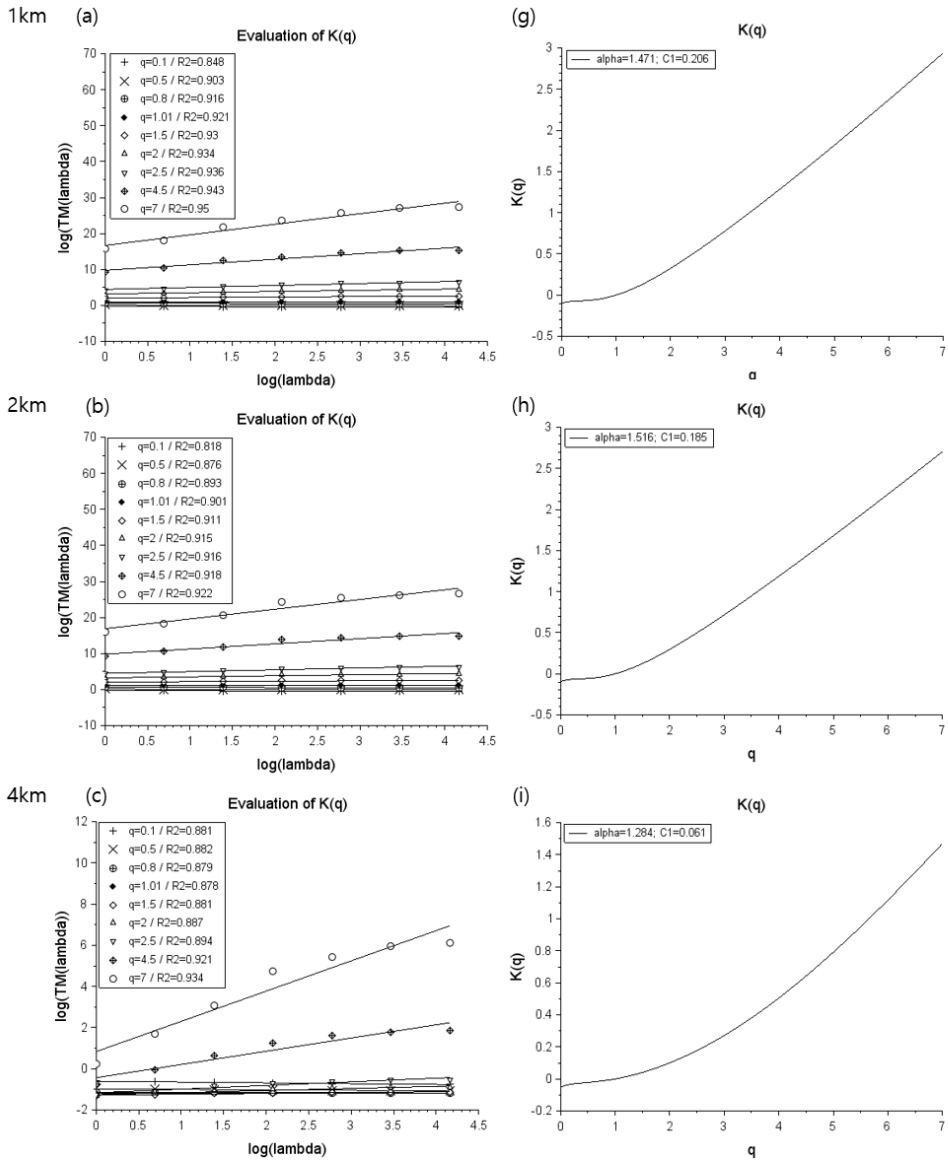
Table 5.2.3. The same as Table 5.1.3 but with Typhoon Bolaven.

	1 km	2 km	4 km	5 km	6 km	8 km
$\beta$	2.68	2.79	2.72	2.61	2.67	1.85
$R^2$	0.96	0.97	0.99	0.99	0.97	0.92

The multifractal analysis was done with TM, and DTM techniques applied. As same as the bigger domain,  $q$  was selected freely from 0.1 to 7. The results of the TM method are presented in Fig. 5.2.14. The graphs on the left (a, b, c, d, e, f) shows the log-log plots of  $\langle \varepsilon_\lambda^q \rangle \approx \lambda^{K(q)}$  with the resolution  $\lambda$  (in this case, it is a set from 1 to 64 km with the rate of increase in power of 2) and the good scaling behavior was shown without any scaling break ( $R^2 \geq 0.9$ ) which means that the field is multifractal from  $q = 0.1$  up to  $q = 7$ . The graph of scaling moment function  $K(q)$  is obtained (Fig. 5.2.14 (g, h, i, j, k, l)) and UM parameters are obtained from the slope of  $K(q)$  graphs which shows the moment and singularity behavior.

Fig. 5.2.15 shows the estimated (or empirical) scaling moment functions  $K(q)$  (in black) are compared to the semi-theoretical functions that are the curves with the UM parameters  $\alpha$  and  $C_1$  further retrieved from TM (red) and DTM (green) analysis. It shows the semi-theoretical TM and DTM fit well with each other in 1km and 2km when the empirical graph shows the smaller  $q_D$  which means the smaller  $C_1$ . At 8 km, the moment behavior shows the opposite of low altitudes. The empirical graph shows larger  $C_1$  than semi-theoretical TM or DTM.

The results of the DTM method are shown in Fig. 5.2.16. An explicit scaling behavior was retrieved as shown in the TM analysis. For each power  $\eta$ , with a fixed value of  $q$  ( $q=1.5$ ), the slope of the linear regression gives an estimate of the scaling moment functions  $K(q, \eta)$ . The slope of S-shape curves (Fig. 5.2.16 (g, h, i, j, k, l)) gives an estimation of  $\alpha$  and  $C_1$ . The value of  $\alpha$  decreases while the value of  $C_1$  is relatively remaining the same. The UM parameters estimated from TM and DTM are indicated in Table 5.2.4 and shown in Fig. 5.2.17.



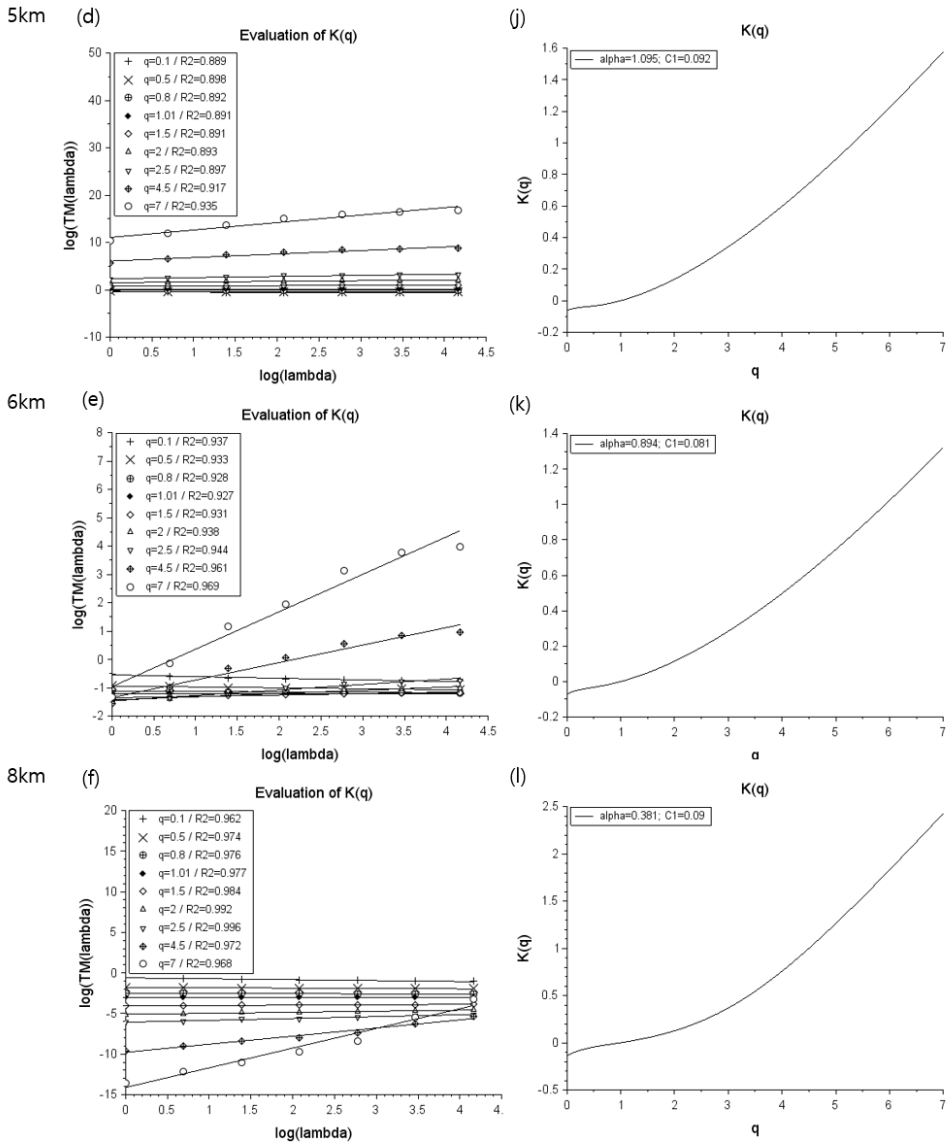


Fig. 5.2.14. The same as Fig. 5.2.9 but in the domain size  $64 \text{ km} \times 64 \text{ km}$ .

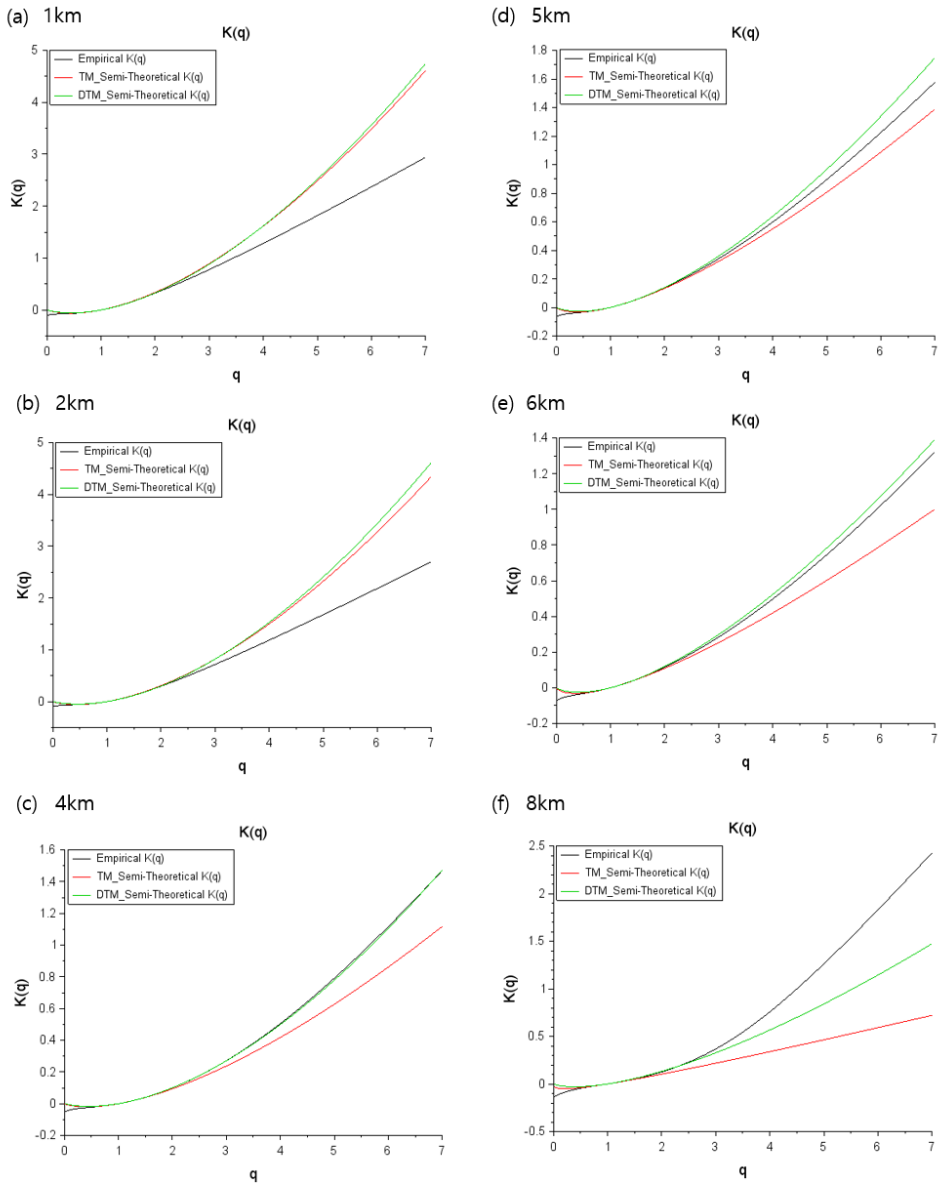
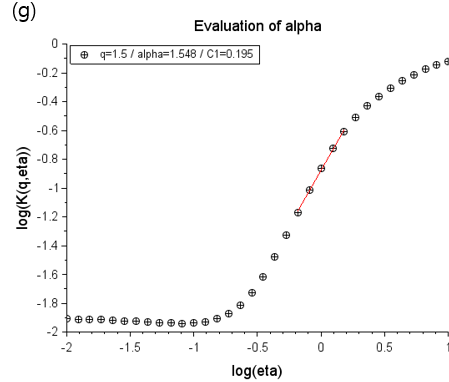
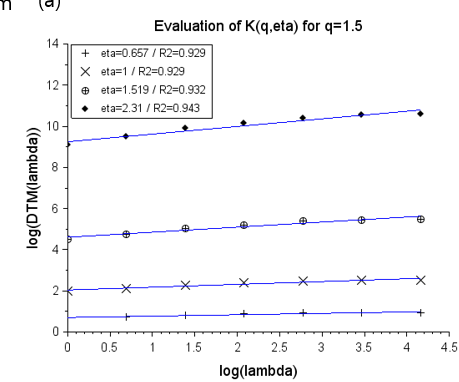
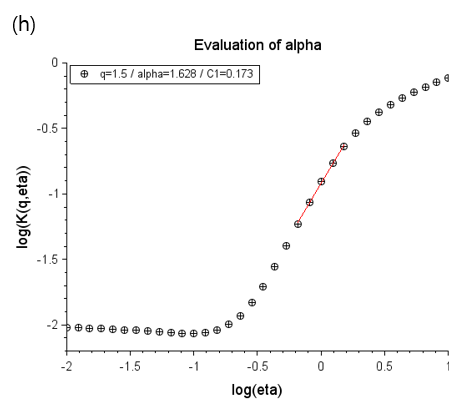
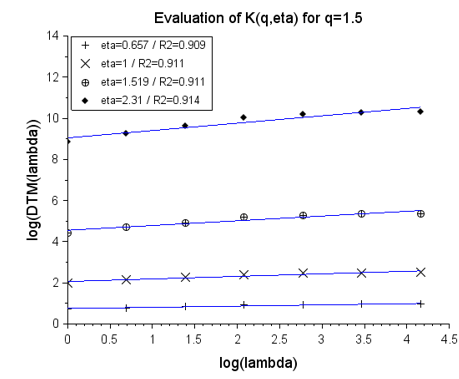


Fig. 5.2.15. The same as Fig. 5.2.10 but in the domain size  $64 \text{ km} \times 64 \text{ km}$ .

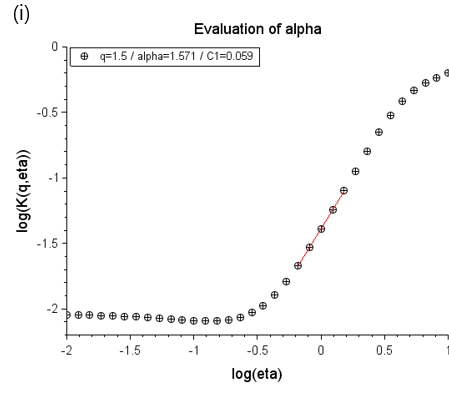
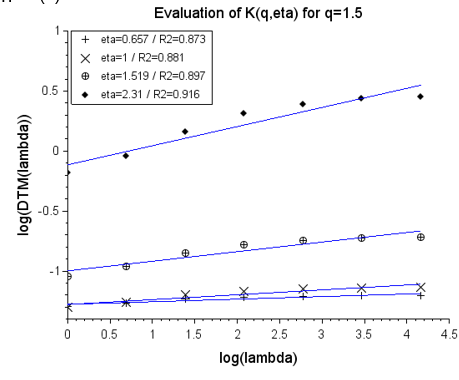
1km



2km



4km



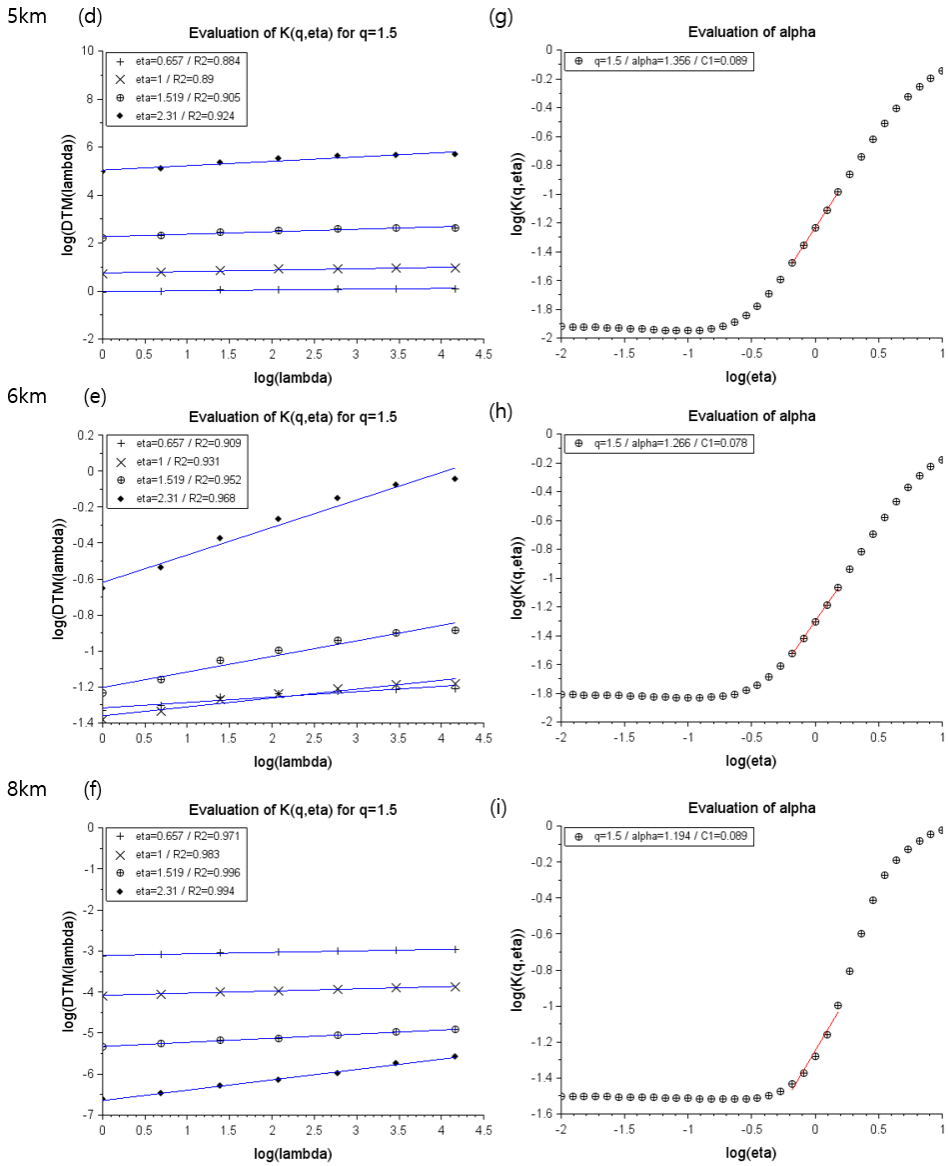


Fig. 5.2.16. The same as Fig. 5.2.11 but in the domain size  $64 \text{ km} \times 64 \text{ km}$ .

Table 5.2.4. The same as Table 5.1.4 but with Typhoon Bolaven.

		1 km	2 km	4 km	5 km	6 km	8 km
TM	$\alpha$	1.471	1.516	1.284	1.095	0.894	0.381
	$C_1$	0.206	0.185	0.061	0.092	0.081	0.09
DTM	$\alpha$	1.548	1.628	1.571	1.356	1.266	1.194
	$C_1$	0.195	0.173	0.059	0.089	0.078	0.089

Lastly, the scaling exponent value  $\beta$  for spectral analysis are averagely 2.553 in all heights of the domain sizes  $64 \text{ km} \times 64 \text{ km}$  with  $R^2 \geq 0.9$  at all altitudes.

The multifractal parameters were obtained from TM and DTM analysis. The value of  $C_1$  is almost the same between the result of the TM and DTM but the larger values of  $\alpha$  are obtained from DTM analysis. However, the pattern of the changes in the values is the same except at 8 km. As it was shown in Fig. 5.2.5, the reflectivity showed the poor quality of the data in high altitudes that different values of  $\alpha$  can be explained from this.

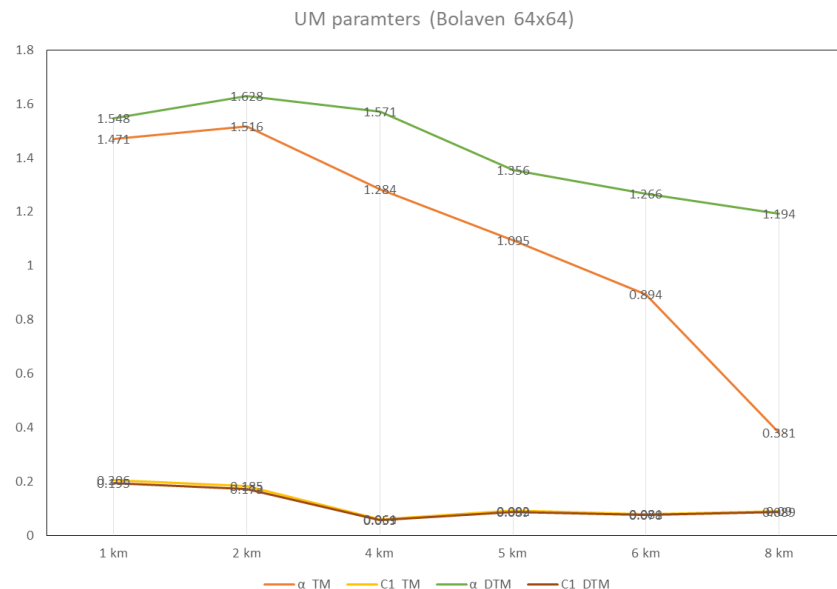


Fig. 5.2.17. The same as Fig. 5.2.12 but in domain  $64 \text{ km} \times 64 \text{ km}$ .

Fig. 5.2.18 also shows the pattern of the rainfall field of accumulated rainfall from typhoon Bolaven in each altitude. It shows the fluctuation of the whole observation domain  $360 \text{ km} \times 360 \text{ km}$ . It shows the high peak of the rainfall up to 40mm at 1, 2 km altitude and this is relative with the UM parameters indicating  $\alpha=0.89, 1.07$  in  $256 \text{ km} \times 256 \text{ km}$ ,  $\alpha=1.5, 1.6$  in  $64 \text{ km} \times 64 \text{ km}$ . To compare the UM parameters from the both domains,  $\alpha$  decreases along the altitudes in  $64 \text{ km} \times 64 \text{ km}$  when  $\alpha$  increases up to 5 km in  $256 \text{ km} \times 256 \text{ km}$  even though almost all the values of  $\alpha > 1$  in both domains. However,  $C_1$  from  $256 \text{ km} \times 256 \text{ km}$  is almost twice larger than the ones from the small domain at 1 – 4 km showing the higher homogeneity in smaller domain.

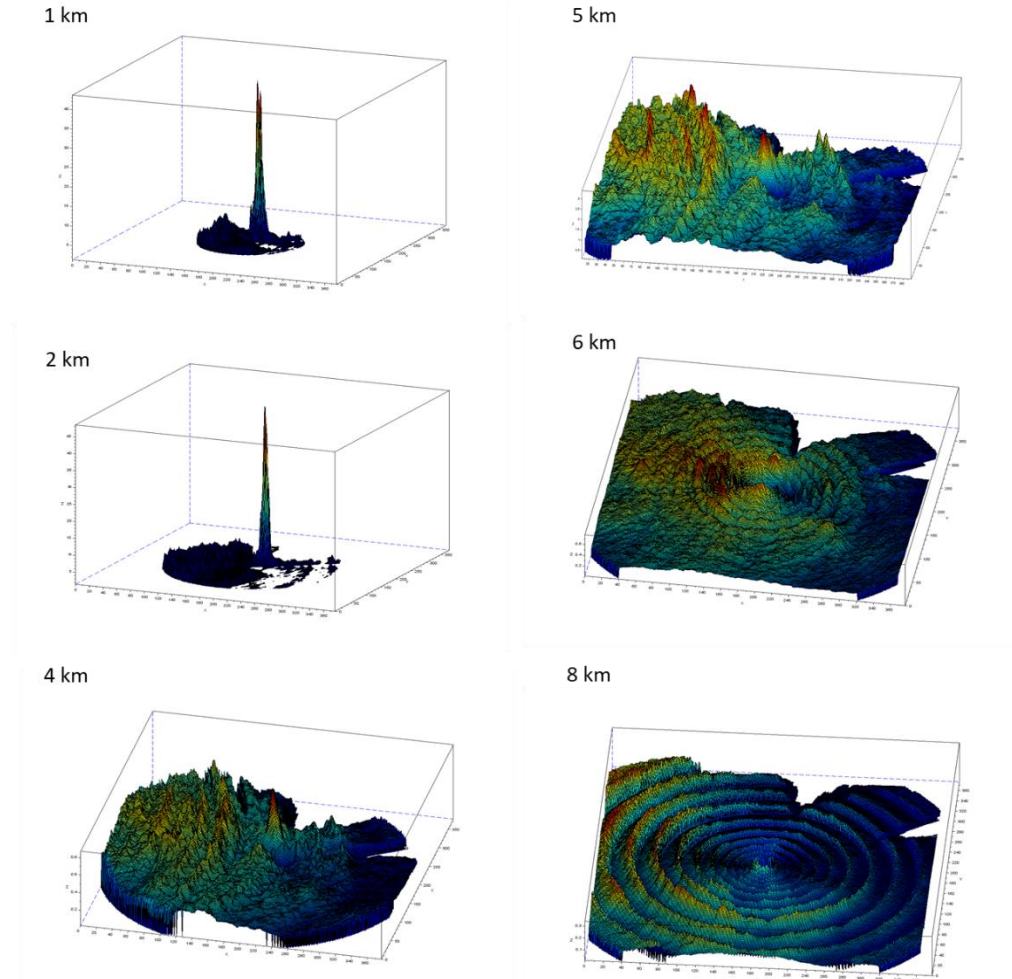


Fig. 5.2.18. The same as Fig. 5.1.18 but with the case of typhoon Bolaven.

## 2) CReSS model

### 2.1) The domain 256 km × 256 km

The multifractal analysis was practiced with CReSS model dataset as well as with the radar dataset. Firstly, the domain 256 km × 256 km was selected, like the preceding analysis with the radar dataset.

Fig. 5.2.19 presents the result of the spectral analysis in domain 256 km × 256 km and it shows the conservative field with  $\beta = 1.6$  and  $R^2 \geq 0.94$ . The scaling break is slightly apparent compared to the result of radar dataset but as  $R^2 \geq 0.94$ , the field can still be considered as a conservative field to proceed with the multifractal analysis with the whole field.

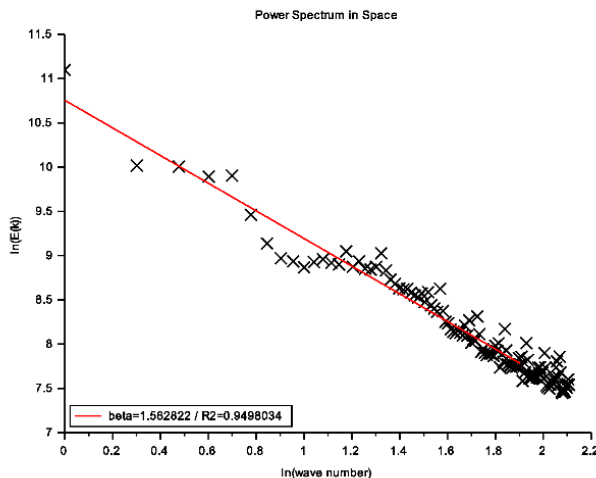


Fig. 5.2.19. The result of spectral analysis from CReSS model dataset with domain 256 km × 256 km.

Then TM and DTM analysis were practiced. The result of the TM method is presented in Fig. 5.2.20. The scaling behavior with the value of different  $q$  from 0.1 to 7.0 is shown in Fig. 5.2.20 (a). The scaling behavior from the graph shows there is no apparent scaling break from  $q = 0.1$  to  $q = 7$ . Although all of the graphs show  $R^2 \geq 0.8$ , as the value of  $q$  is larger than 1.5, the  $R^2$  becomes larger than 0.9. Then, the scaling moment function  $K(q)$  is obtained (Fig. 5.2.20 (b)). Lastly, in Fig 5.2.20 (c),  $K(q)$  obtained from the empirical dataset in black, from using UM parameters obtained from TM in red, from using UM parameters obtained from DTM in green. It shows how the scaling behavior is fitting with each other. It shows that all the results of DTM and empirical relatively fit well.

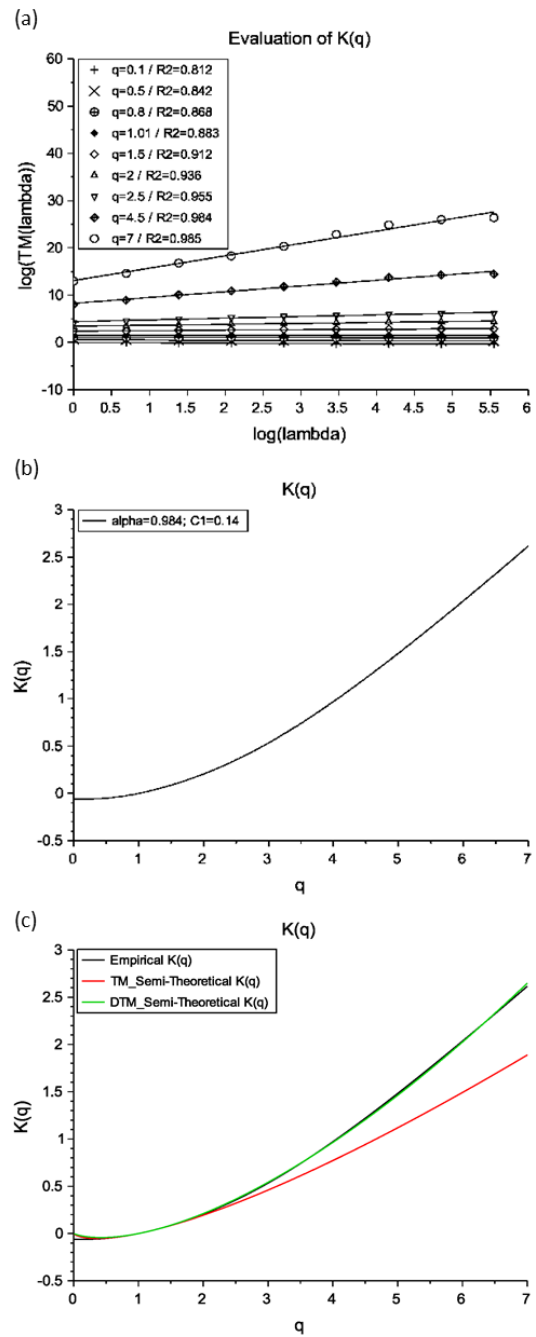


Fig. 5.2.20. The same as Fig. 5.1.20 but with Bolaven case.

The result of the DTM method is shown in Fig. 5.2.21. The result clearly shows a good scaling behavior with  $R^2 \geq 0.94$  with all different  $\eta$ . For each power  $\eta$ , with a fixed value of  $q$  ( $q=1.5$ ), the slope of the linear regression gives an estimate of the scaling moment functions  $K(q, \eta)$ . Fig. 5.2.21 (b) shows the slope of the DTM curve which gives an estimation of  $\alpha$  and  $C_1$ . The UM parameters are noted in table 5.2.5.

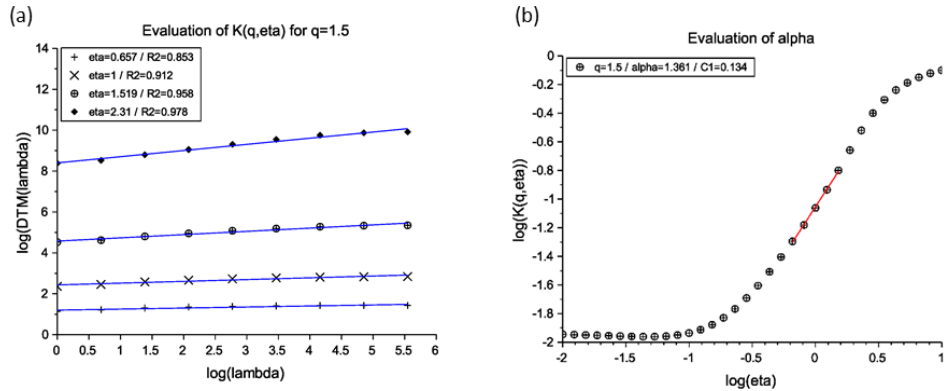


Fig. 5.2.21. The same as Fig. 5.1.21 but with Bolaven case.

## 2.2) The domain 64 km × 64 km

The domain size of 64 km × 64 km was selected in the middle of the whole domain size 360 km × 360 km, the same area as the 64 km × 64 km domain from the radar dataset. Fig. 5.2.22 shows the curve follows a similar shape as 256 km × 256 km. Even though it is less fitted with the red linear line, the scaling behavior highly fits linear with  $\beta = 3.1$  and  $R^2 = 0.95$ .

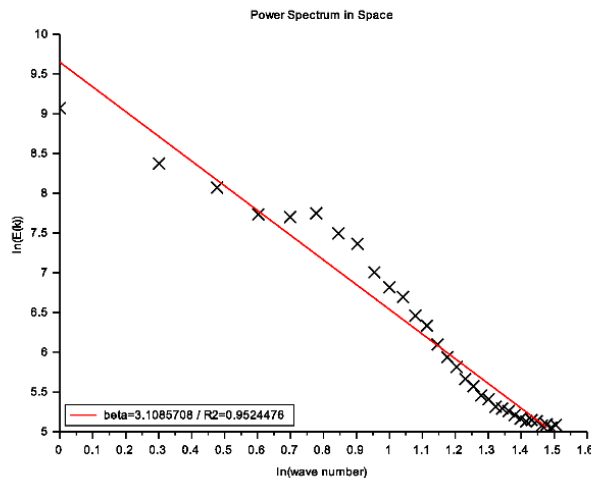


Fig. 5.2.22. The result of spectral analysis by CReSS model dataset in domain 64 km × 64 km.

The TM and DTM method was applied, and the result shows that the scaling behavior is outstanding by showing  $R^2 \approx 0.9$  except when  $q = 0.1$ . (Fig. 5.2.23 (a) and Fig. 5.2.24 (a)). Also, the graph of scaling moment function  $K(q)$  in empirical, TM, and DTM analysis are aligned only up to  $q = 2.5$  while TM and DTM graphs aligned to each other (Fig. 5.2.23 (c)). As the TM graphs, the DTM result also shows good scaling behavior along with different  $\eta$  at fixed  $q = 1.5$ . All the values of UM parameters are shown in table 5.2.5.

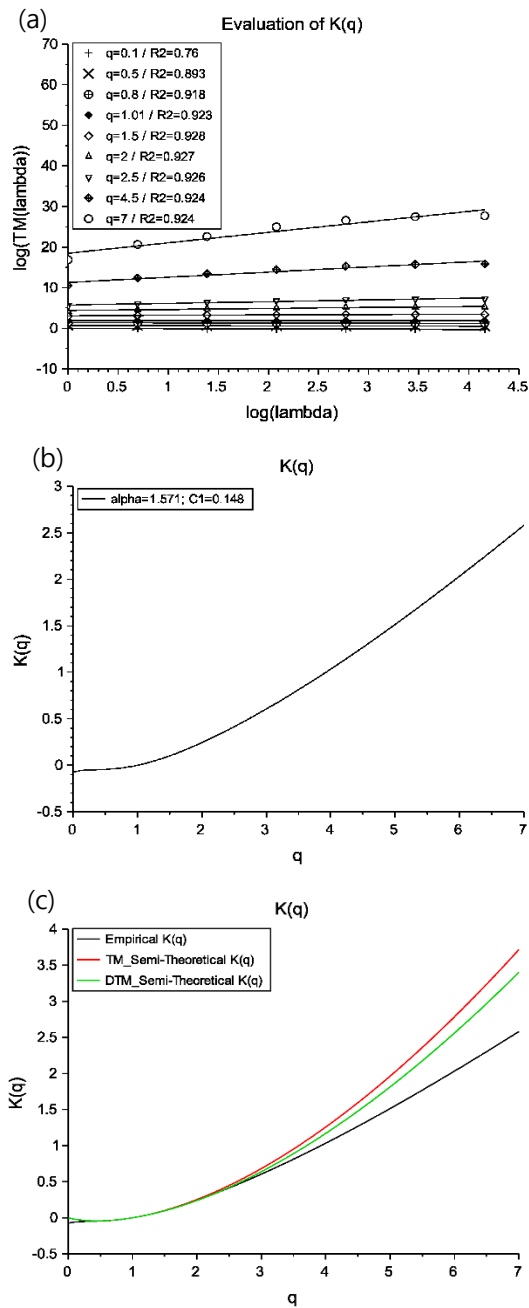


Fig. 5.2.23. The same as Fig. 5.2.20 but in domain 64 km  $\times$  64 km.

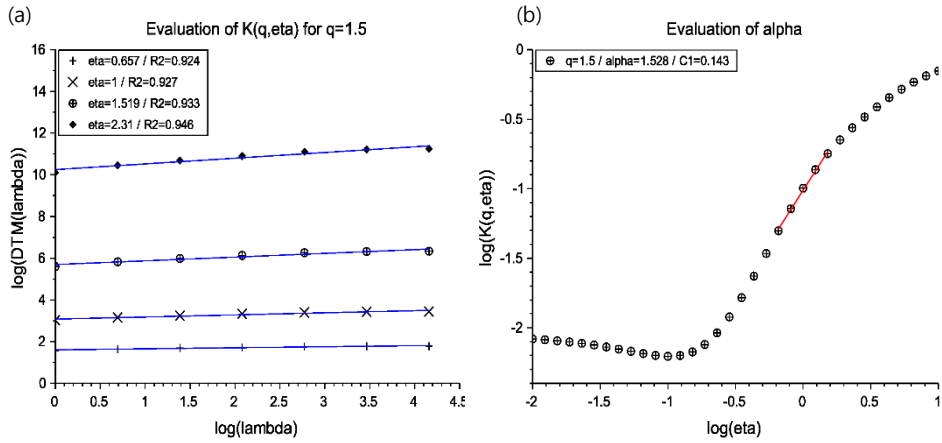


Fig. 5.2.24. The same as Fig. 5.2.21 but in domain 64 km  $\times$  64 km.

Table 5.2.5. The same as Table 5.1.5 but with Typhoon Bolaven.

CReSS		256 $\times$ 256	64 $\times$ 64
TM	$\alpha$	0.984	1.571
	$C_1$	0.14	0.148
DTM	$\alpha$	1.381	1.528
	$C_1$	0.134	0.143

### 3) Comparison of radar and CReSS

Fig. 5.2.25 with the domain size of 256 km × 256 km and Fig. 5.2.26 with 64 km × 64 km shows the comparison of  $K(q) - K(q)$  plot of the radar data and the CReSS model data on each height.

With the domain 256 km × 256 km, the comparison of  $K(q)$  function shows the consistency between two different datasets the best at 5 km, even though the curvature of blue dots at 4 – 6 km aligns straight, the bisectrix fits the best at 5 km which means there's less difference of  $C_1$  and  $\alpha$  between radar and CReSS. Meanwhile, the difference in  $\alpha$  is larger in the low altitudes of 1 and 2 km. The ratio of  $C_1$  is as follows ;

At 1 km :  $0.134/0.349 = 0.384$ , at 2 km :  $0.134/0.255 = 0.525$ , at 4 km :  $0.134/0.105 = 1.277$ , at 5 km :  $0.134/0.114 = 1.175$ , at 6 km :  $0.134/0.078 = 1.718$ , and at 8 km :  $0.134/0.086 = 1.558$ .

With the domain size 64 km × 64 km, the difference of  $\alpha$  shows larger in higher altitudes as the domain 256 km × 256 km with the ratio of  $C_1$  shows as follows ;

At 1 km :  $0.143/0.195 = 0.733$ , at 2 km :  $0.143/0.173 = 0.827$ , at 4 km :  $0.143/0.059 = 2.424$ , at 5 km :  $0.143/0.089 = 1.607$ , at 6 km :  $0.143/0.078 = 1.833$ , and at 8 km :  $0.143/0.089 = 1.607$ .

The set of graphs on the domain 256 km × 256 km shows the most bisectrix at 4 -5 km altitudes while the domain 64 km × 64 km shows at 1-2- km. The linear regression fit is diminishing at low altitudes in both domains.

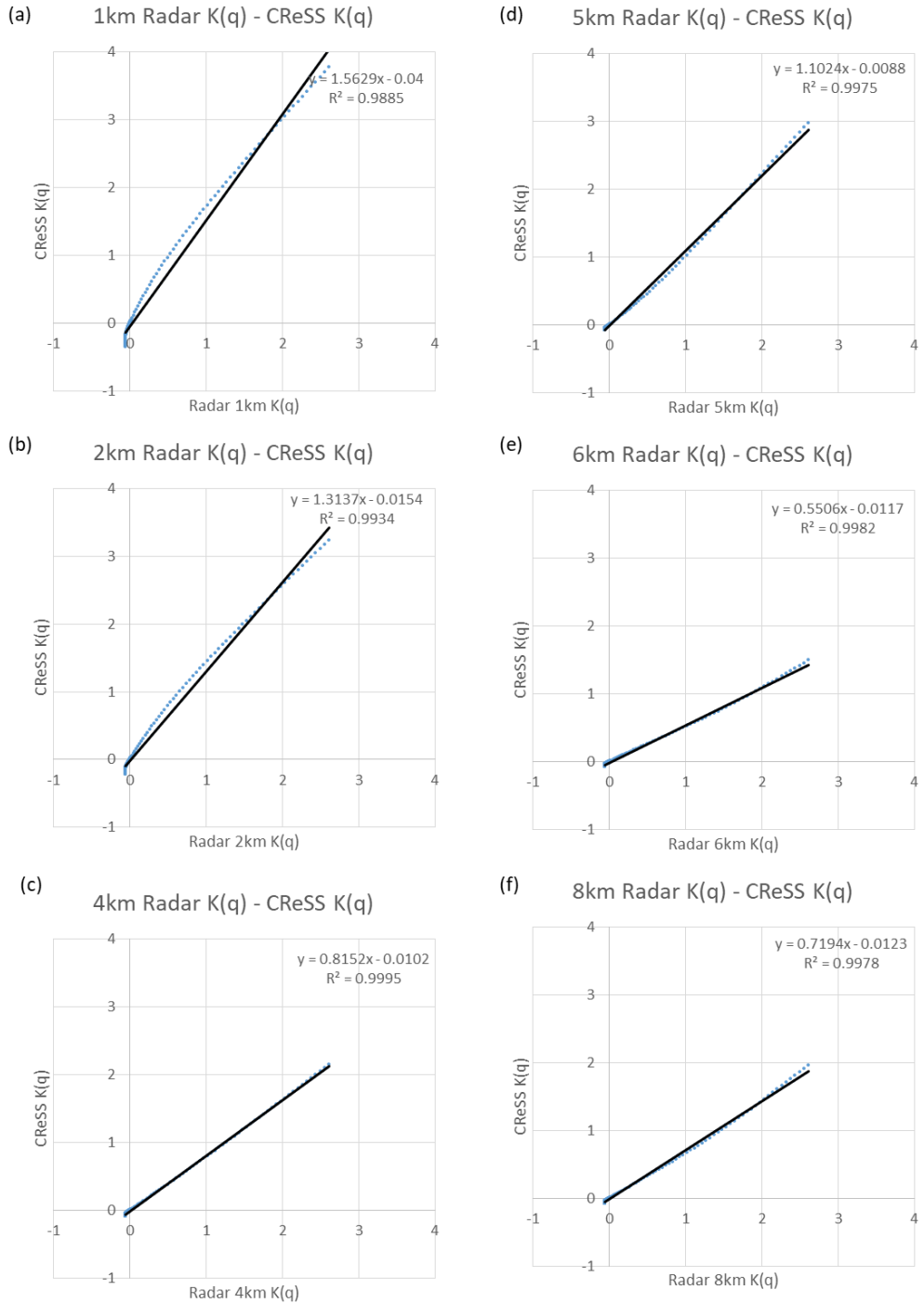


Fig. 5.2.25. The same as Fig. 5.1.24 but with the case of Typhoon Bolaven.

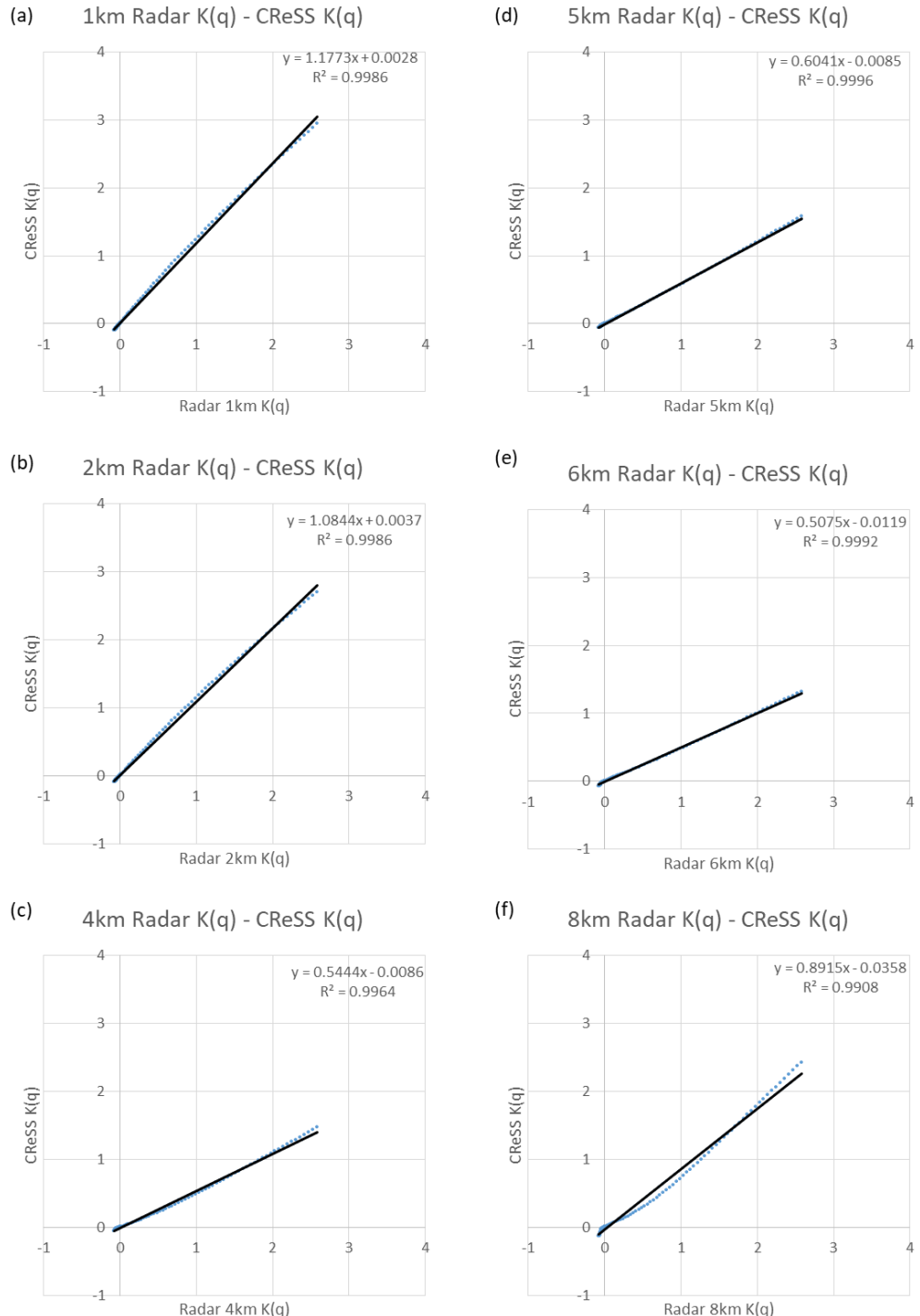


Fig. 5.2.26. The same as Fig. 5.2.24 but in the domain size of  $64 \text{ km} \times 64 \text{ km}$ .

### 5.3. Typhoon Sanba

#### 5.3.1. Environmental description

Typhoon Sanba was one of the most active tropical cyclones worldwide in 2012. It was formed as a tropical depression in the east of the Philippines on 10 September. The storm intensified steadily as it moved northward and became to a tropical storm, then to a typhoon on 12 September entering a phase of explosive intensity strengthening the characteristics. The next day, the typhoon entered a phase of intensification and reached the peak intensity. The peak of intensity was on 13 September with maximum sustained winds of  $55.9 \text{ ms}^{-1}$  (125 mph) and a minimum pressure of 900 hPa. It made landfall on Jeju Island on 17 September before transitioning into an extratropical cyclone and tracked into eastern Russia dissipating on 19 September.

Fig. 5.3.1 shows the track of the typhoon Sanba with the dots indicating the location of the center of the typhoon where the lowest pressure is. The center of the typhoon passed by the west side of Jeju Island and moved northward and passed through the middle of the Korean peninsula. The surface data of AWS operated by KMA was additionally collected and obtained the daily accumulated rainfall amount on 17 September 2012, showing in Fig. 5.3.2. Fig. 5.3.2 (b) shows that the maximum accumulated rainfall amount recorded more than 360 mm all around the top of the mountainous area. Fig. 5.3.3 shows the graph of typhoon center pressure and the maximum wind speed.

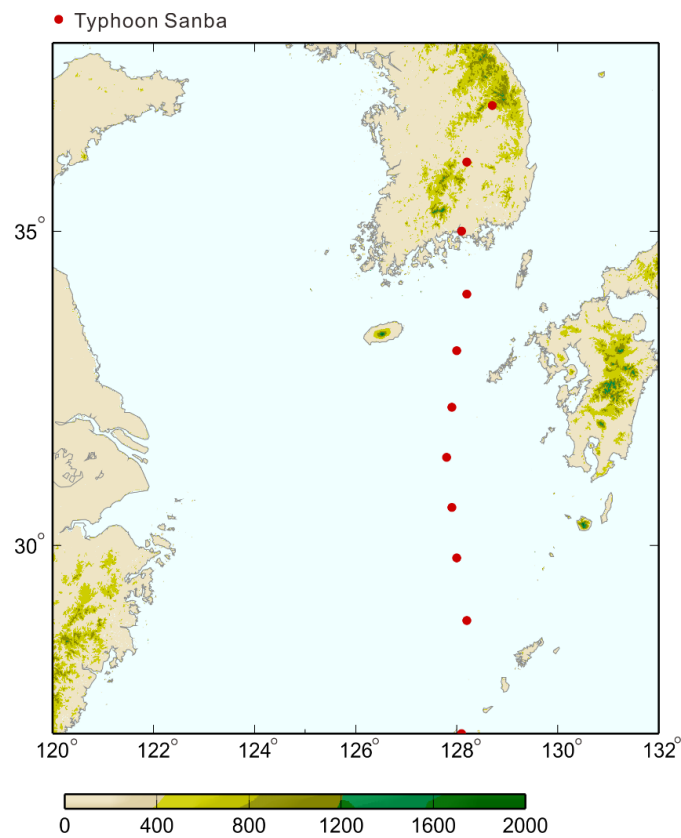


Fig. 5.3.1. The track of Typhoon Sanba. The red dots indicate the location of the typhoon center.

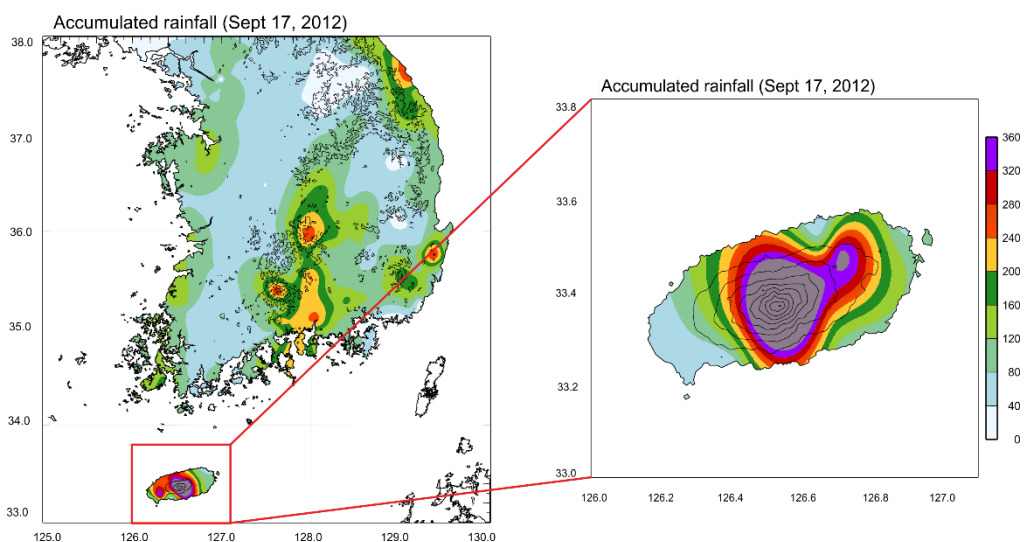


Fig. 5.3.2. The daily accumulated rainfall on 17 September 2012 in Korea.

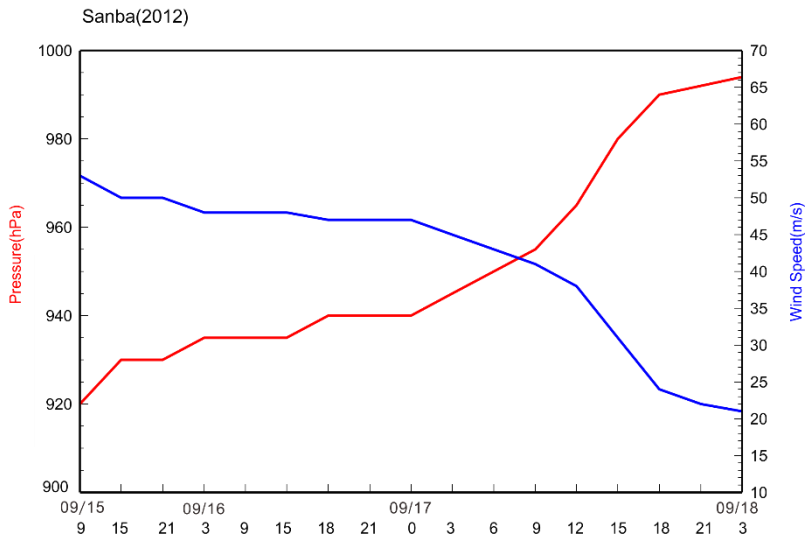


Fig. 5.3.3. The graph of typhoon center pressure (hPa) in red and the maximum wind speed (m/s) in blue.

Fig. 5.3.4 shows the synoptic flow at 1800 UTC on 16 September 2012. The description in detail is provided from NCEP/NCAR Reanalysis. The center of typhoon is found in the south of Jeju Island (Fig. 5.3.4 (a)). The convergence areas were formed from the southeast of the typhoon near Japan with extremely strong wind, and the strong confluence area shows the development of the eyewall due to the strong rising motion of the air. Also, the equivalent potential temperature at 850 hPa is much higher around the typhoon than surrounding areas that it indicates how unstable it is around the selected area and also appears to supply the warm and humid air from the southeast side of tropics continuously (Fig. 5.3.4 (b)). At 500 hPa, the contour shows the vorticity with the wind flow. The strong positive shear vorticity is shown as the wind speed is increasing around the typhoon, especially on the right side of the center of the typhoon (Fig. 5.3.4 (c)). Lastly, at 300 hPa, an upper-level jet (ULJ) streak of  $\geq 25 \text{ ms}^{-1}$  is passing above the Korean peninsula. The jet stream approaches to Korea from the west and as it gets close to the Korean peninsula, the deep ridge has occurred with upper-level divergence as negative vorticity, and warm air advection causes the upper-level forcing. (Fig. 5.3.4 (d)).

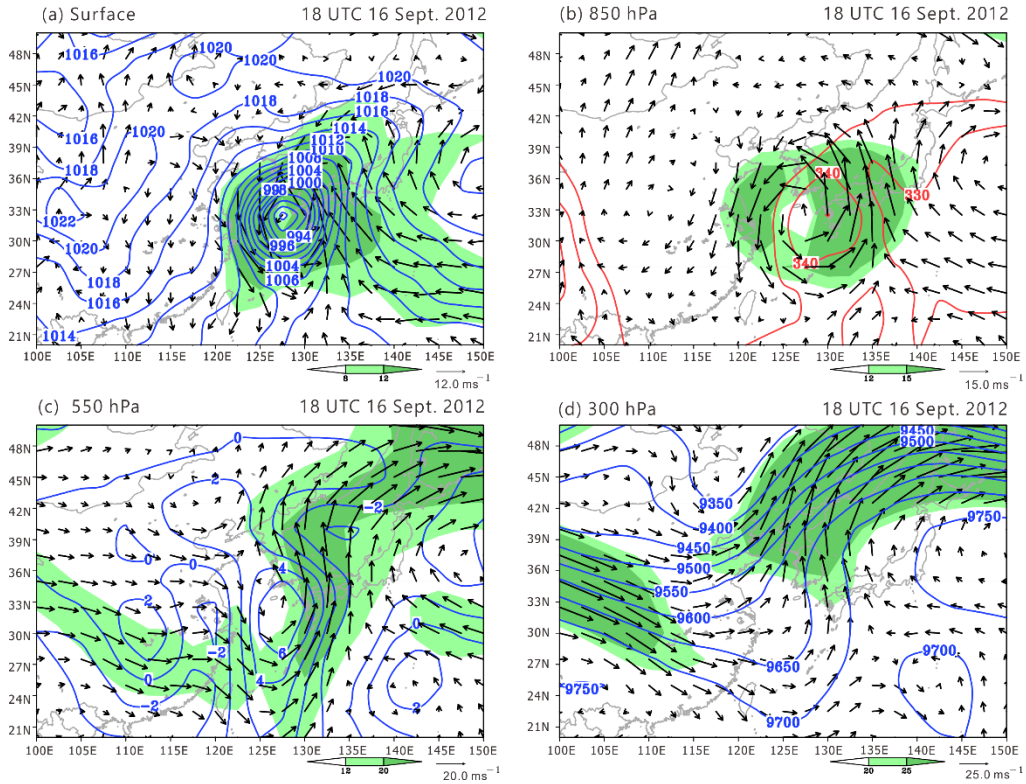


Fig. 5.3.4. The synoptic flow at 1800 UTC on 16 September 2012. (a) at the surface showing the pressure (sea level pressure, hPa) and wind vector, (b) at 850 hPa showing the equivalent potential temperature (K) and wind vector, (c) at 500 hPa showing the relative vorticity ( $10^{-5} \text{ s}^{-1}$ ) and wind vector, and (d) at 300 hPa showing the geopotential height (m) and wind vector.

### 5.3.2. Observation results

During the typhoon Sanba, even three days before the typhoon

approaches, the convective activities occurred. However, 4-time steps (0030 LST, 0300 LST, 0630 LST, and 0930 LST) were selected when the spiral band approaches Jeju Island. The wind field is shown in Fig. 5.3.5 in each altitude. As the typhoon is passing from the east side of the island, the mainstream of wind direction is different from the previous two cases. The high reflectivity is not only showing in low altitudes (1, 2 km) but also in high altitudes (5, 6 km). Instead of accumulating the rainfall amount on the top of the mountain as previous cases, at 0330 LST in low altitudes, the rainfall converged on the windward side and leeward side of the mountain due to the orographic effect.

To see the detailed structure of the typhoon, Fig 5.3.6 shows the vertical cross-section of the wind field and reflectivity in each time step. The strong convergence at 0030 LST in 5 km develops the strong convections at 5 km on the next time step (0330 LST). As the typhoon passing the island, the convections merged with strong downdraft and updraft near the center of the typhoon which shows the eyewall bringing the most intense rainfall in the typhoon cyclone over Jeju Island. At 0930 LST, the typhoon moved northward and the streamers are shown, which is the near ends of the spiral band with one straight convective line at the end of the cyclone.

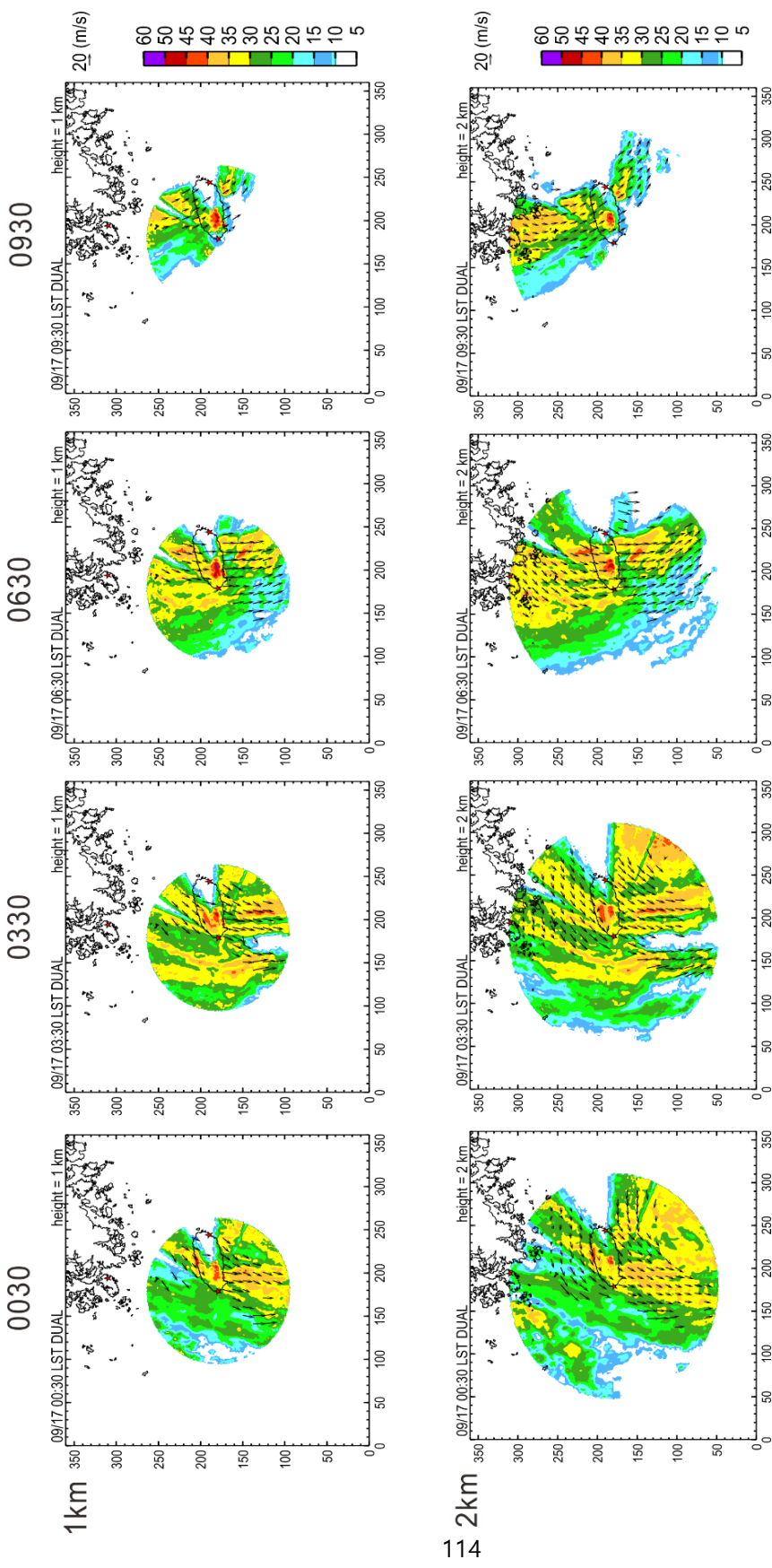


Fig. 5.3.5. The same as Fig. 5.1.5 but with Typhoon Sanba case.

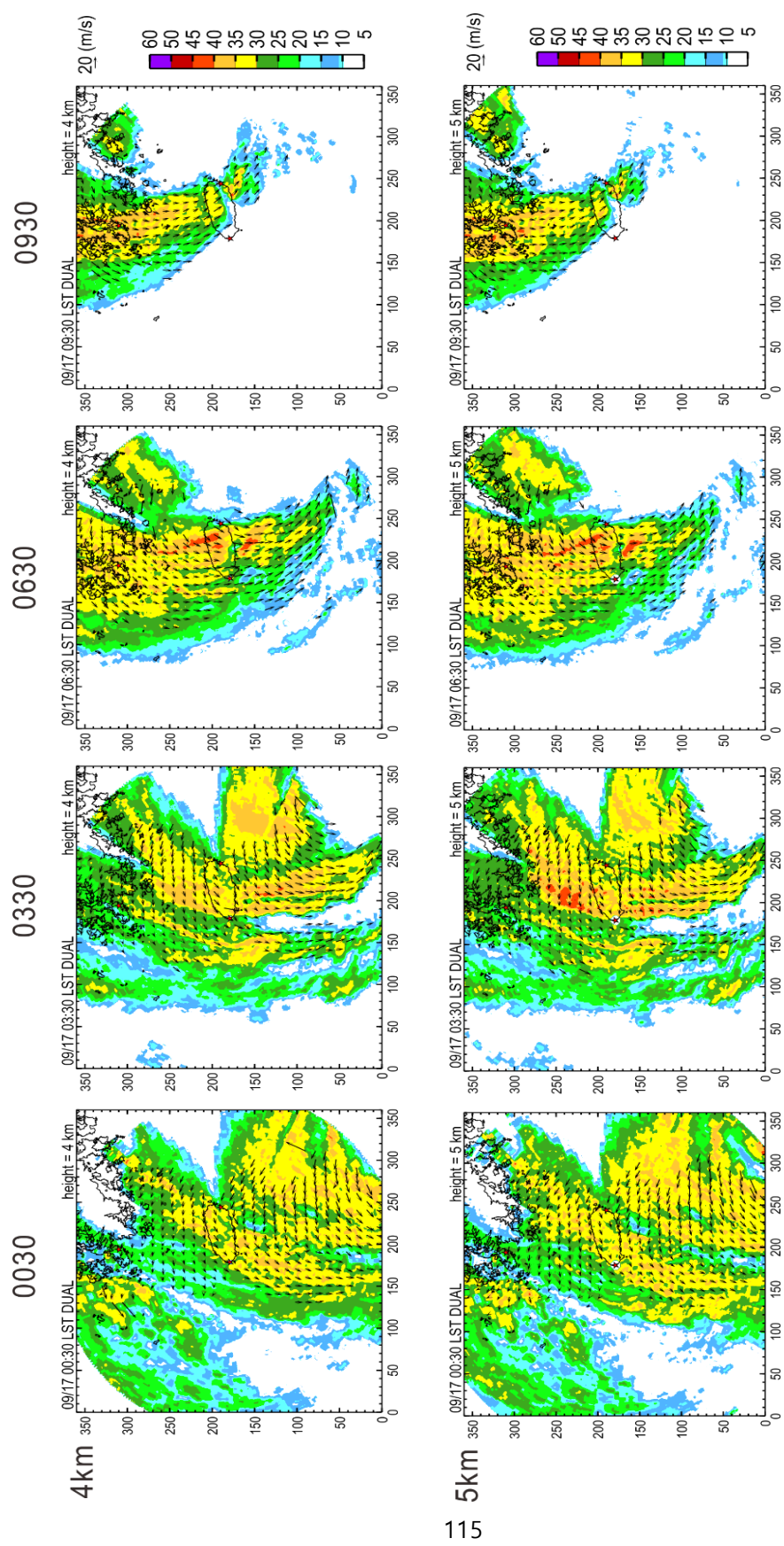


Fig. 5.3.5. Continued.

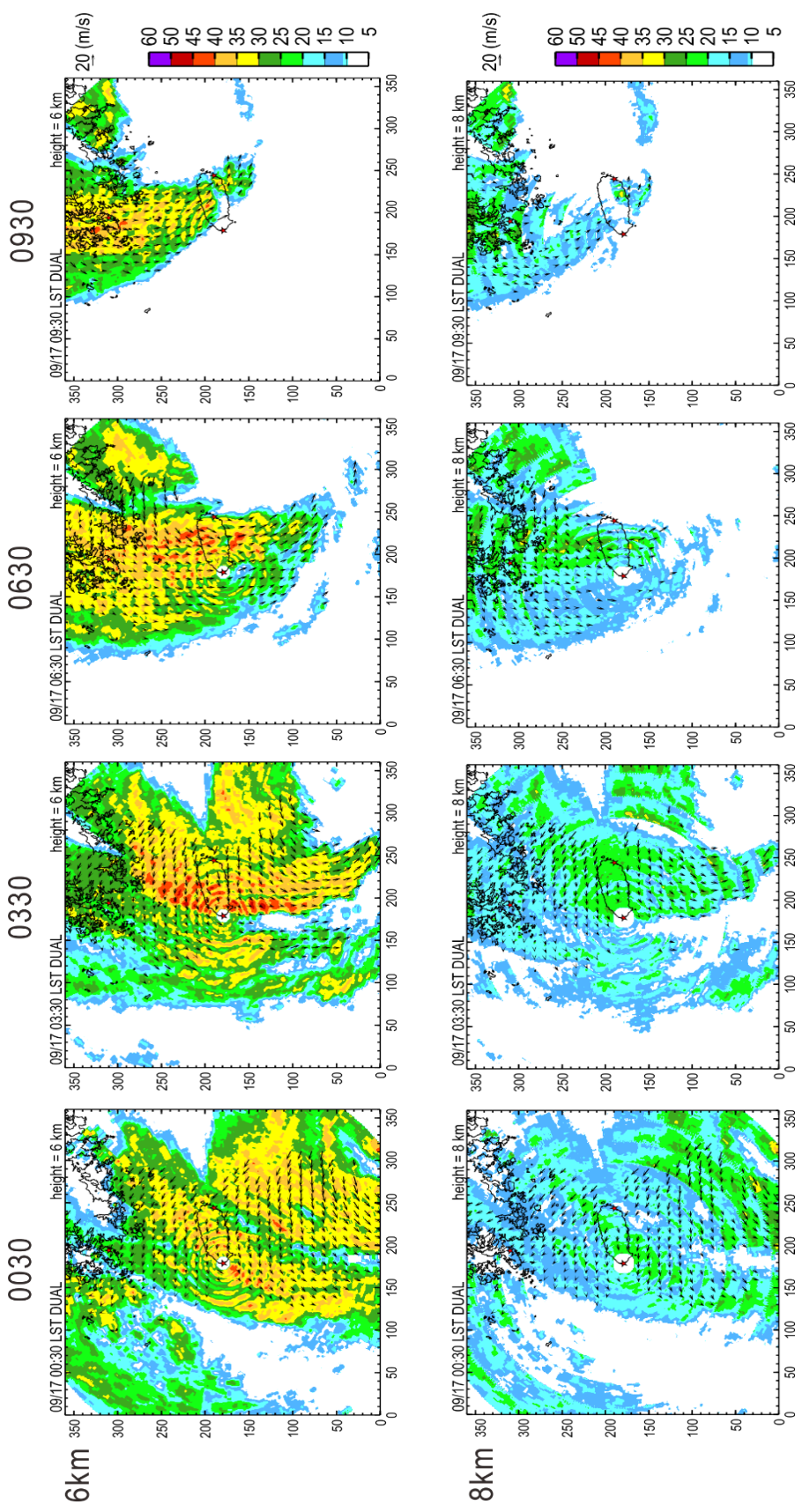


Fig. 5.3.5. Continued.

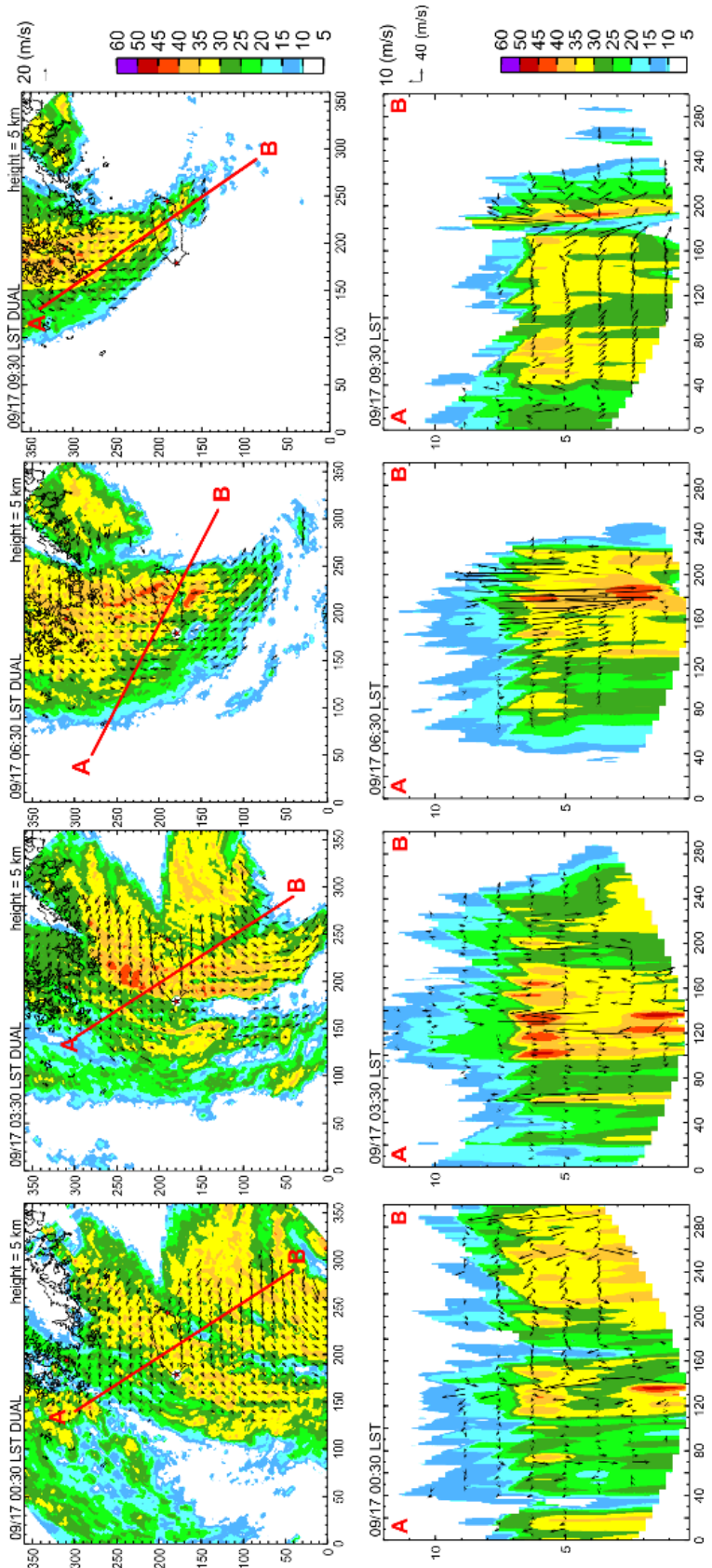


Fig. 5.3.7 shows radar reflectivity (contour) with divergence (red) and convergence (blue) of horizontal wind at each altitude obtained at 0030 LST, 0330 LST, 0630 LST, and 0930 LST on 17 September 2012.

At 0030 LST, the significantly strong convergence line over  $3 \times 10^{-3} S^{-1}$  is shown in the southwest of the island. Next to it, the strong divergence of over  $4 \times 10^{-3} S^{-1}$  on the southeast side of the island is shown at 1 km altitude. It is where the reflectivity shows around 40 dBZ. At the rest of the altitudes, the convergence and divergence become more fluctuated. At 0330 LST, the left side of spiral band passes through the island which brings the strong convergence over  $4 \times 10^{-3} S^{-1}$ . It is where the strong updraft and downdraft meets at 1 and 2 km altitudes. As the typhoon moves to the north, the edge of the spiral band brings the strong convergence line where the reflectivity is over 45 dBZ at 4 – 6 km altitudes at 0630 LST. Lastly, the typhoon moves through the island and the divergence over  $2 \times 10^{-3} S^{-1}$  is shown over the island at all altitudes.

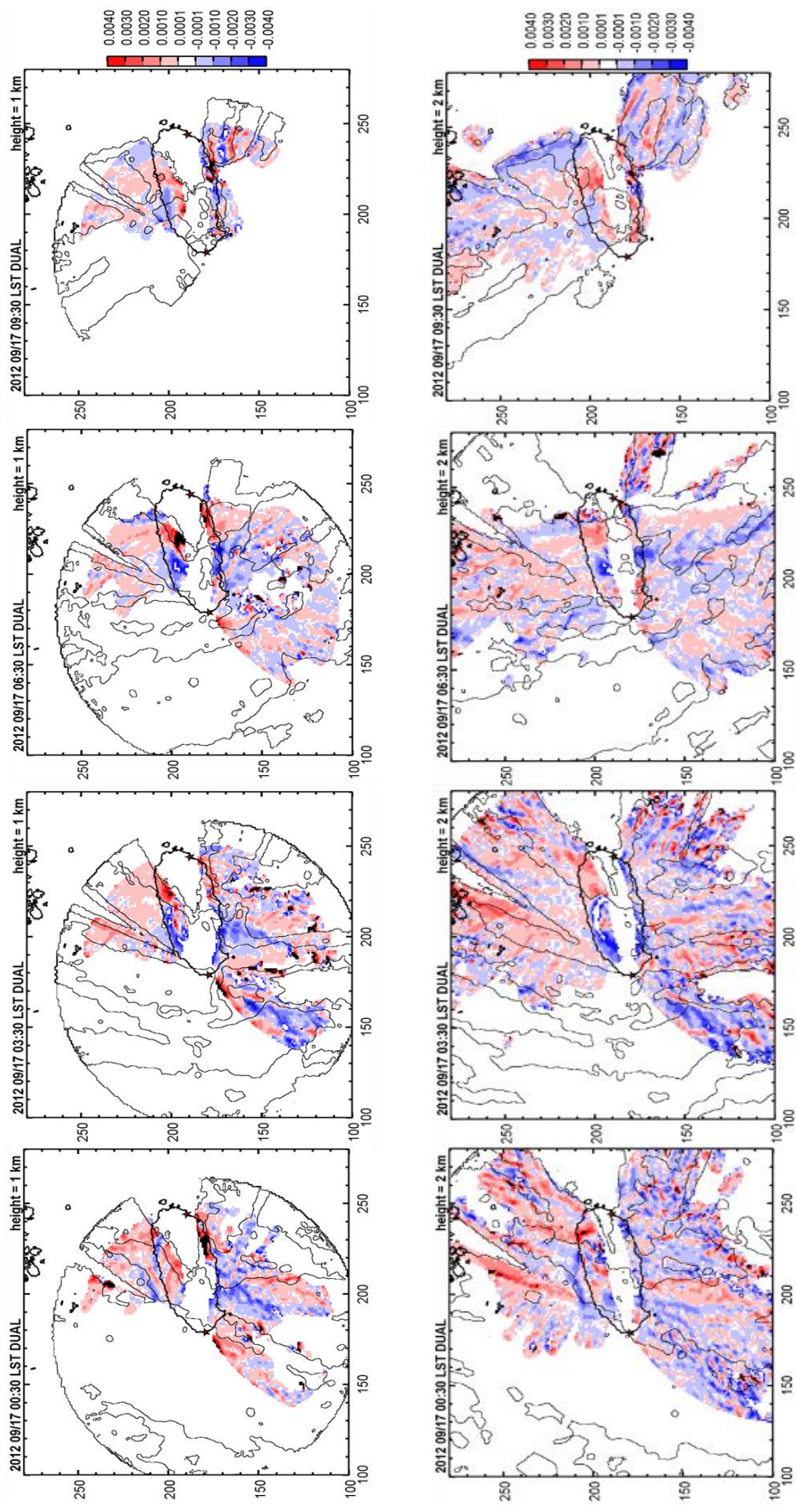


Fig. 5.3.7. The same as Fig. 5.1.7 but with typhoon Sanba.

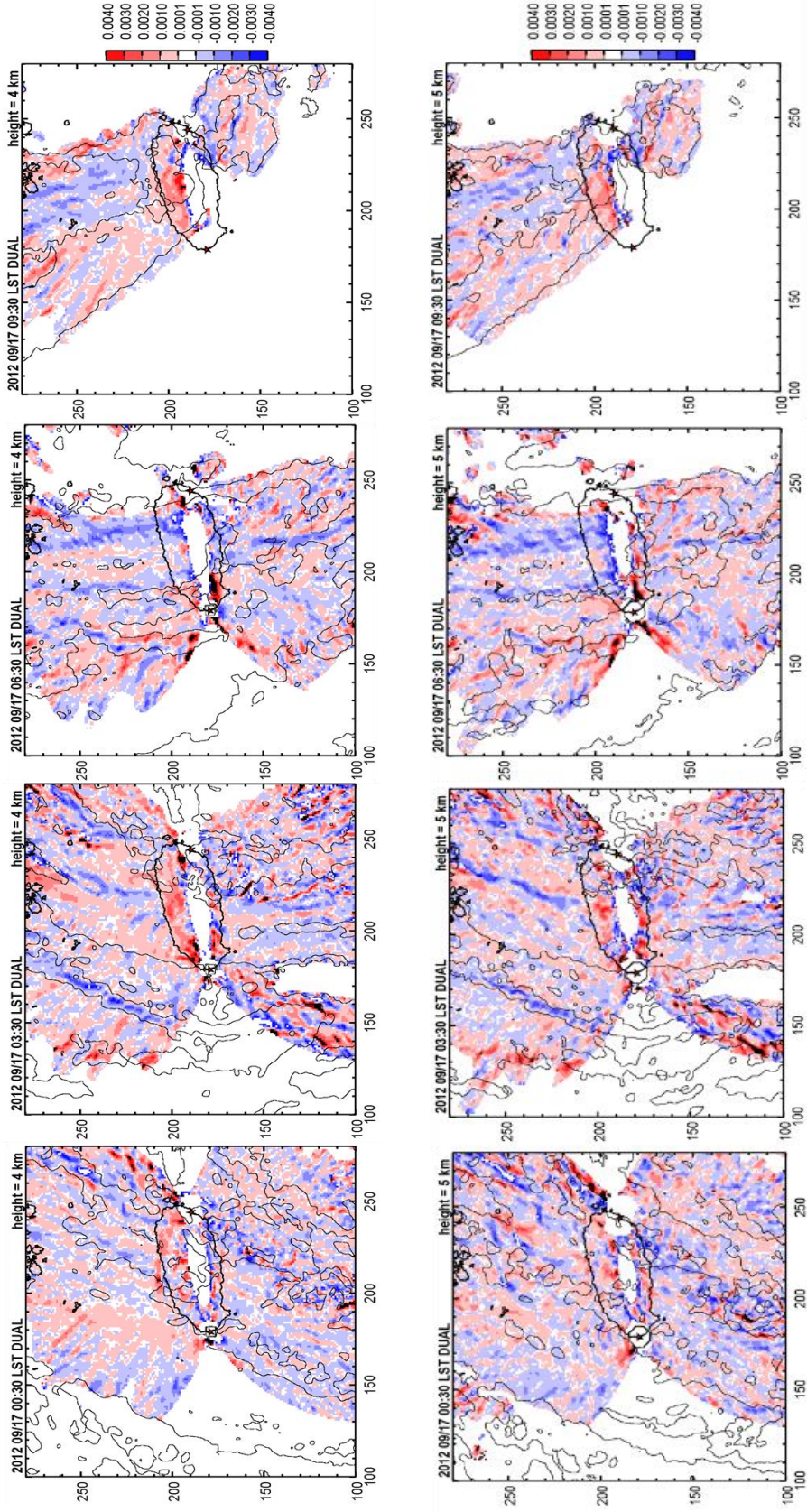


Fig. 5.3.7. continued.

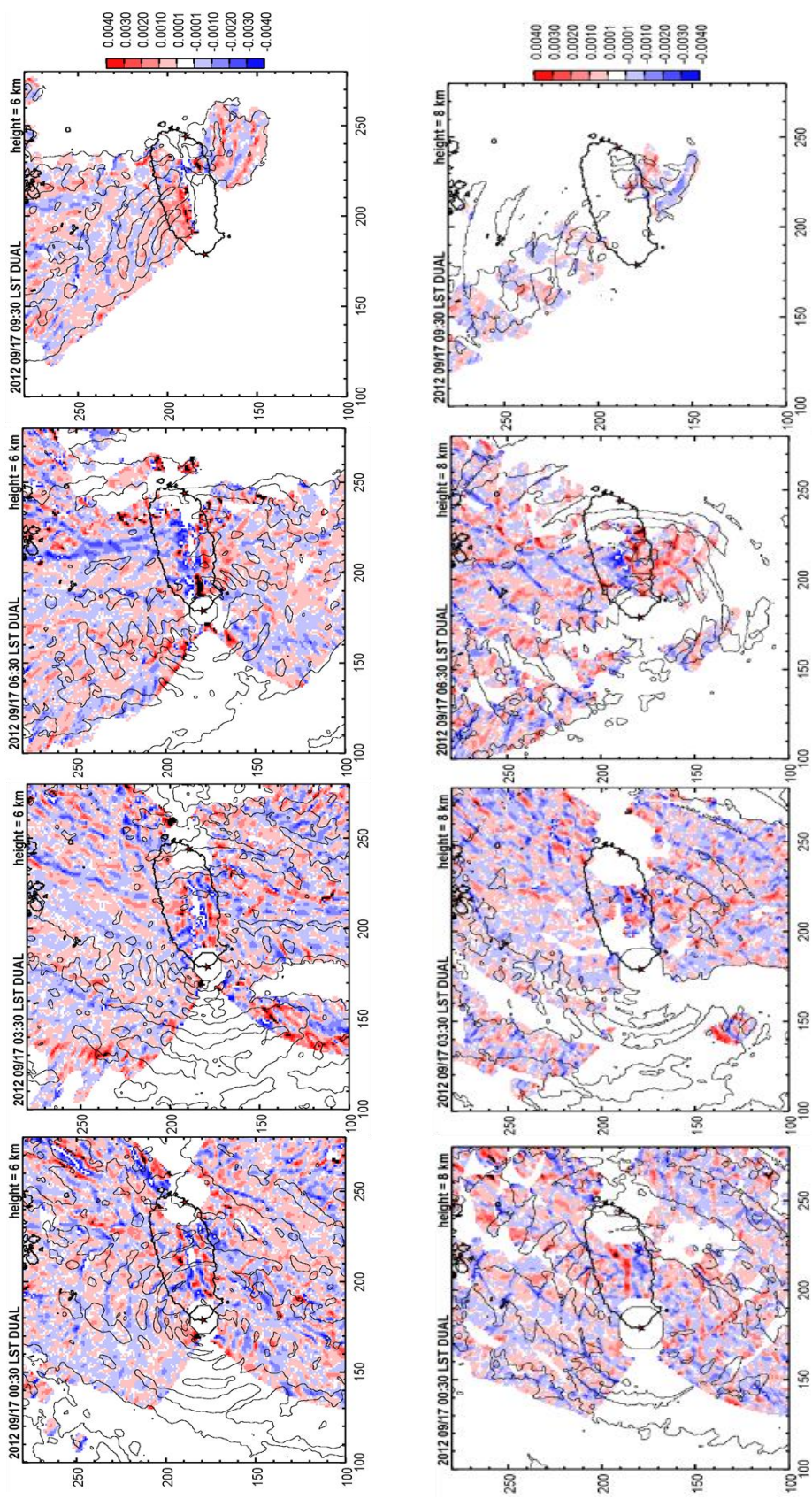


Fig. 5.3.7. continued.

### 5.3.3. Multifractal analysis

The multifractal analysis was done with the rainfall rate obtained from the radar data in Gosan, Jeju Island, Korea. As the previous cases, the domain  $256 \text{ km} \times 256 \text{ km}$  is selected with the area where the most significant rainfall rate was observed. Additionally, the domain  $64 \text{ km} \times 64 \text{ km}$  is selected without the zero-field in the lower altitudes. The small domain is selected in the middle of the whole domain size  $360 \text{ km} \times 360 \text{ km}$  where the center is the location of the radar.

#### 1) Radar

##### 1.1) The domain $256 \text{ km} \times 256 \text{ km}$

The spectral analysis was conducted at different altitudes from 1 km to 8 km to see the conservativeness of the field in Fig. 5.3.8. It shows that there was no extreme scaling break in any altitudes as all dataset were shown the linear scaling behavior up to  $\ln(k) = 2$  with  $R^2 \geq 0.9$ . All the cases present good scaling behavior in most of the part except at 2 km, where it shows some instabilities with a strong tail lift (Fig. 5.3.8). The detailed values of  $\beta$  and  $R^2$  are shown in Table 5.3.1.

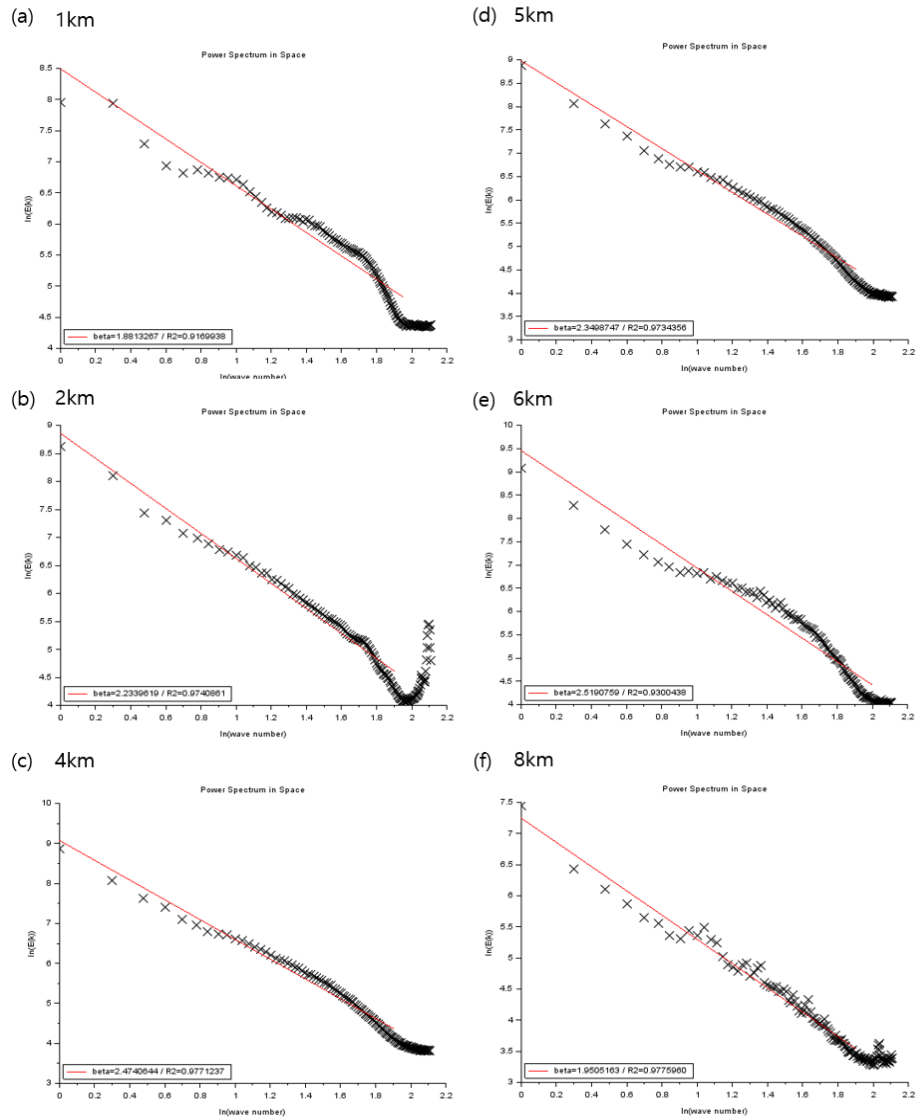


Fig. 5.3.8. The same as Fig. 5.1.8 but with Sanba case.

Table 5.3.1. The same as Table 5.1.1 but with Typhoon Sanba.

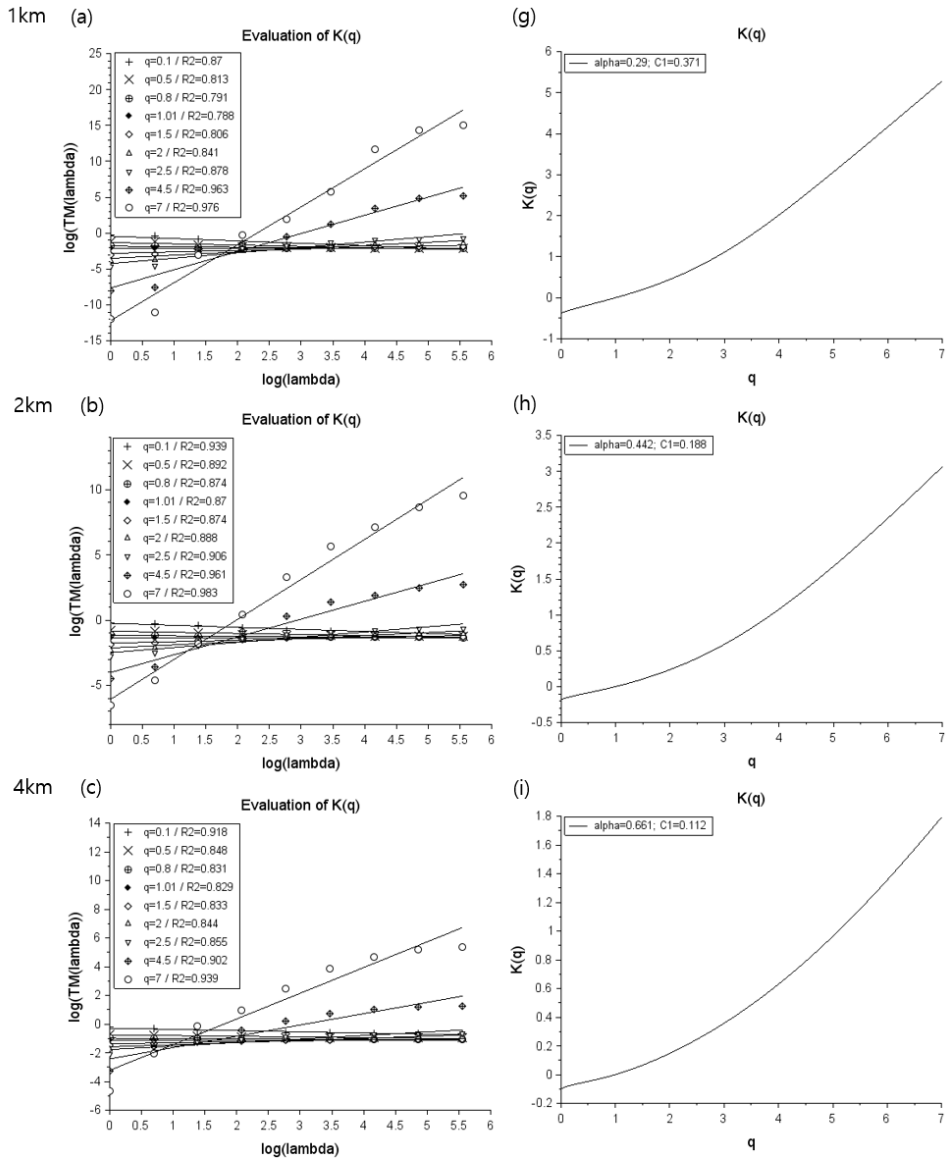
	1 km	2 km	4 km	5 km	6 km	8 km
$\beta$	1.88	2.23	2.47	2.35	2.52	1.95
$R^2$	0.92	0.97	0.98	0.97	0.93	0.98

As the field can be considered conservative, TM and DTM method was applied on all data. The results of the TM method are presented in Fig. 5.3.9. Fig. 5.3.9 (a, b, c, d, e, f) shows the log-log plots of  $\langle \varepsilon_\lambda^q \rangle$  with  $q$  between 0.1 and 7.0. In most cases, the scaling behavior was excellent without any scaling break ( $R^2 \geq 0.9$ ) which means that the field is multifractal from  $q = 0.1$  up to  $q = 7$ . Fig. 5.3.9 (g, h, i, j, k, l) shows the scaling moment function  $K(q)$  and UM parameters are obtained.

Fig 5.3.10 shows the estimated (or empirical) scaling moment functions  $K(q)$  are compared to the semi-theoretical functions that are the curves with the UM parameters  $\alpha$  and  $C_1$  further retrieved from TM and DTM analysis. It enables to compare the scaling behaviors obtained and see if the graph is fitting with each other. By comparing the empirical and DTM semi-theoretical  $K(q)$ , all the  $K(q)$  shows the same scaling behavior until  $q = 3.0$  at 1 km and 2 km, until  $q = 4.0$  at the rest of the altitudes. The slope of  $K(q)$  calculated from empirical data shows the behavior of UM parameter  $C_1$  is more extreme than in other  $K(q)$  at all altitudes.

The results of the DTM method are shown in Fig. 5.3.11. An apparent scaling behavior was shown with the result of TM analysis. For each power  $\eta$ , with a fixed value of  $q$  ( $q=1.5$ ), the slope of the linear regression gives an estimate of the scaling moment functions  $K(q, \eta)$ . The S-shape curves (Fig. 5.3.11. (g, h, i, j, k, l)) are conditioned by an appearance of numerical limitations at smaller moments and the critical behavior of extremes at higher statistical moments, both being characterized by the flattening of the double trace moment curves. The slope of the curve gives an estimation of  $\alpha$  and  $C_1$ . The value of  $\alpha$  increases along with the height while the value of  $C_1$  decreases, showing how to concentrate and how quickly the intermittency evolved.

For  $\alpha$  and  $C_1$ , the UM parameters estimated from TM and DTM are summarized in Table 5.3.2 and shown in Fig. 5.3.12.



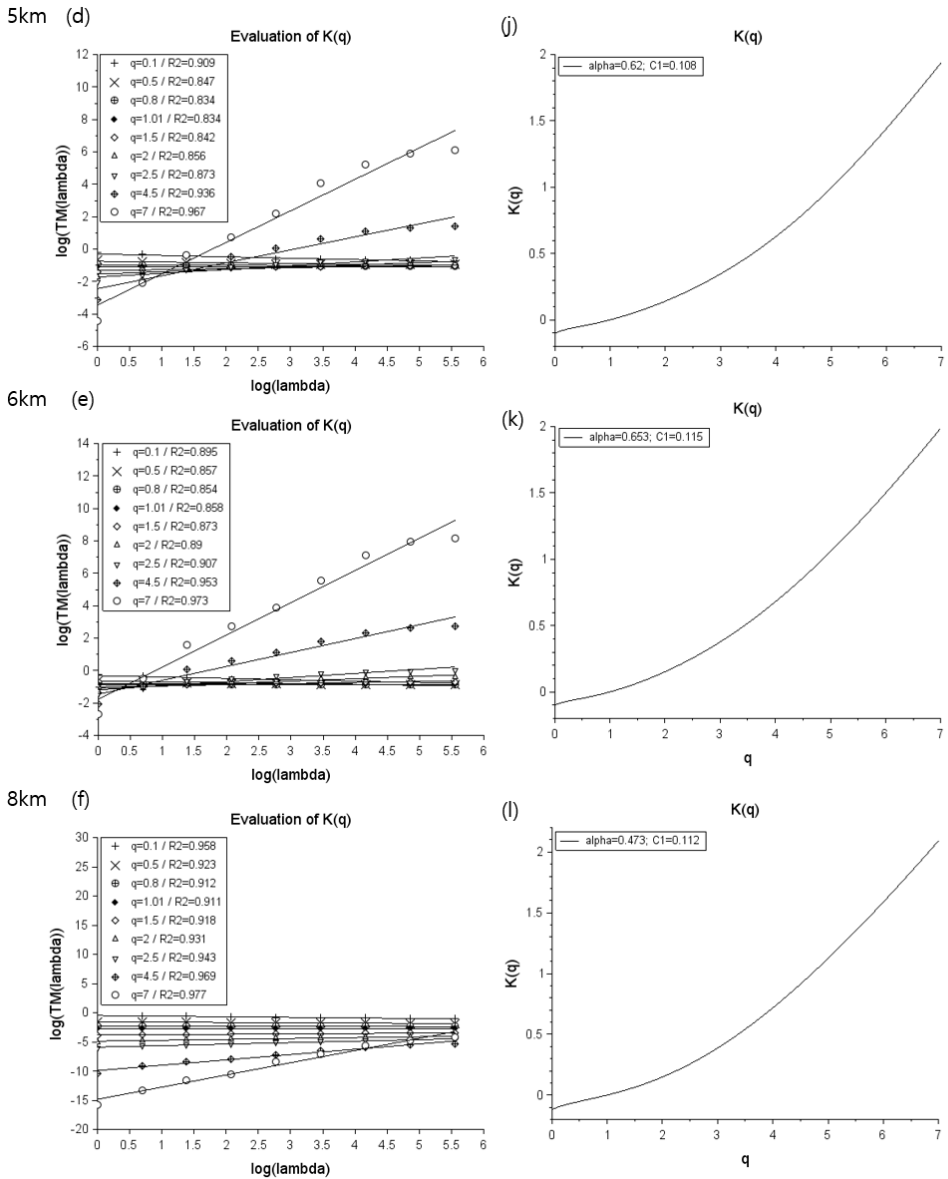


Fig. 5.3.9. The same as Fig. 5.1.9 but with Sanba case.

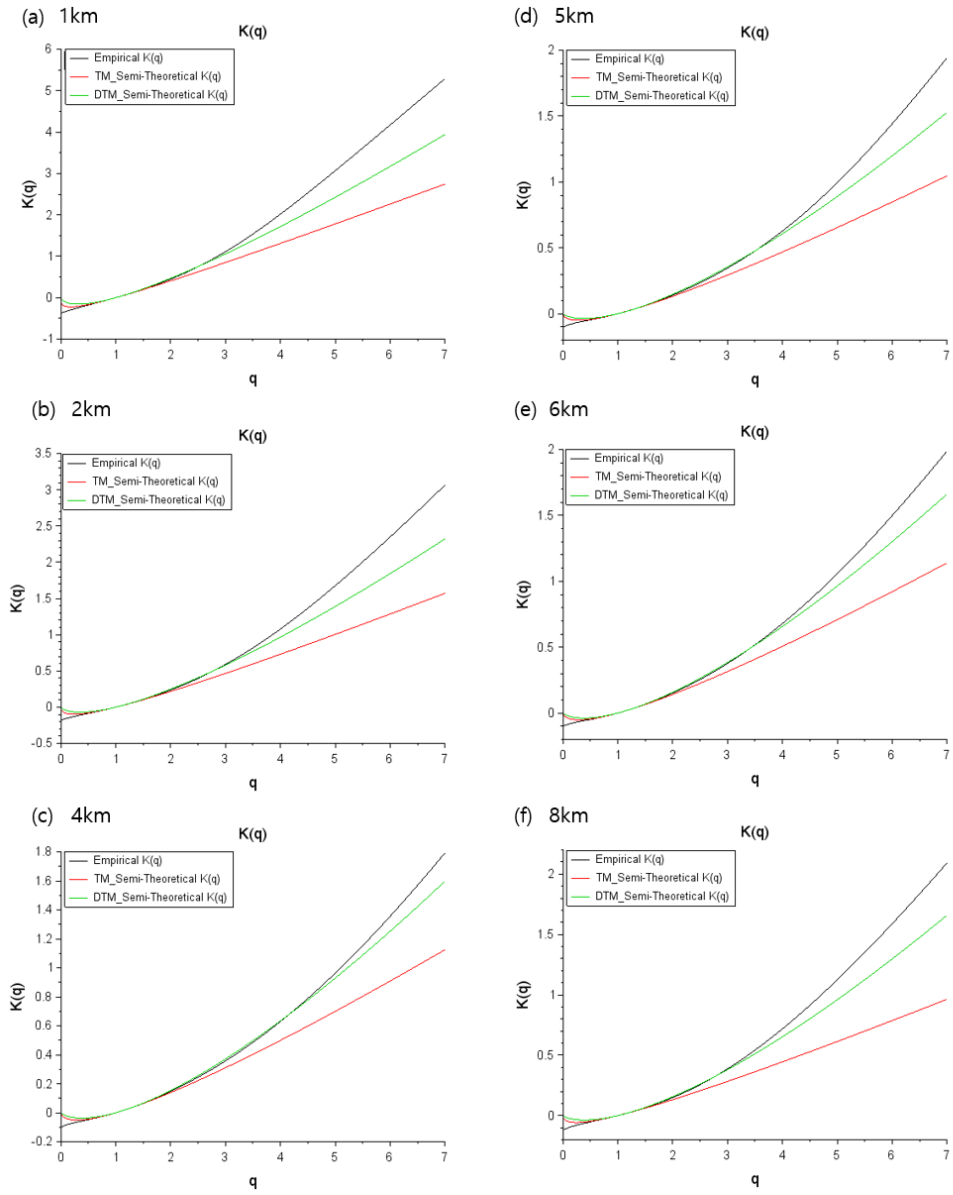
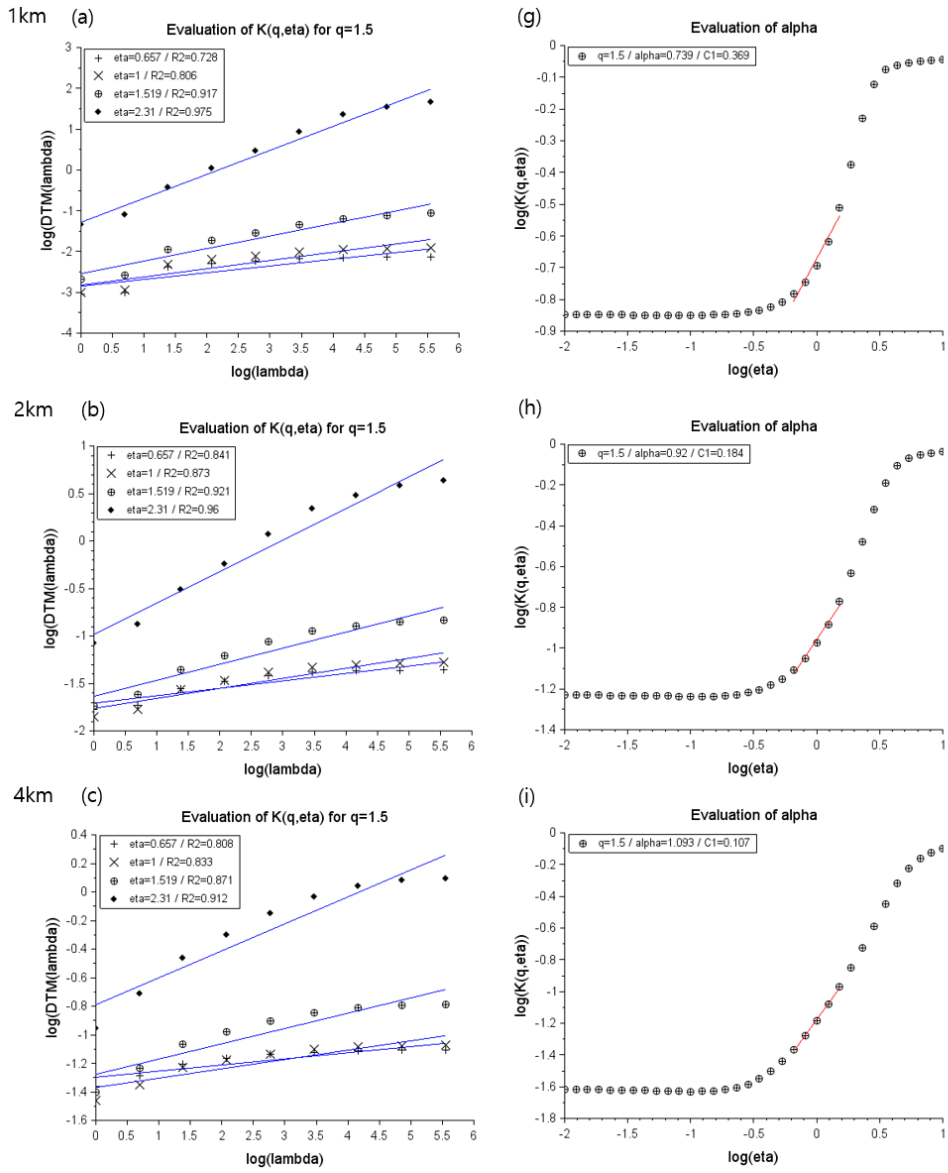


Fig. 5.3.10. The same as Fig. 5.1.10 but with Sanba case.



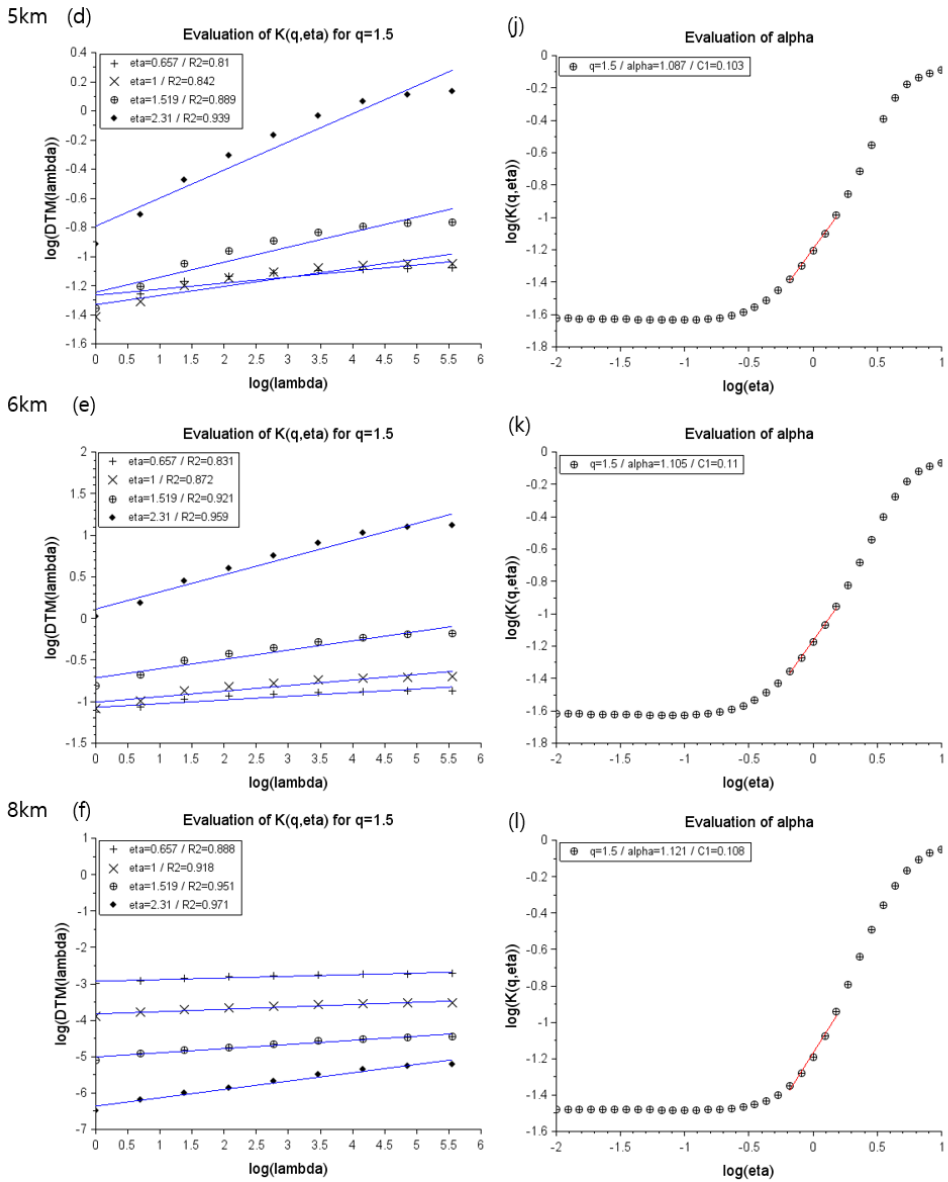


Fig. 5.3.11. The same as Fig. 5.1.11 but with Sanba case.

Table 5.3.2. The same as Table 5.1.2 but with Typhoon Sanba.

		1 km	2 km	4 km	5 km	6 km	8 km
TM	$\alpha$	0.29	0.442	0.661	0.62	0.653	0.473
	$C_1$	0.371	0.188	0.112	0.108	0.115	0.112
DTM	$\alpha$	0.739	0.92	1.093	1.087	1.105	1.121
	$C_1$	0.369	0.184	0.107	0.103	0.11	0.108

Lastly, the scaling exponent value  $\beta$  for spectral analysis are averagely 2.233 in all heights of the domain sizes  $256 \text{ km} \times 256 \text{ km}$  with  $R^2 \geq 0.9$  at all altitudes.

The multifractal parameters were obtained from TM and DTM analysis. The value of  $C_1$  is almost the same between the result of the TM and DTM but the larger values of  $\alpha$  are obtained from DTM analysis. However, the pattern of the changes in the values is the same, except at 4 and 8 km.

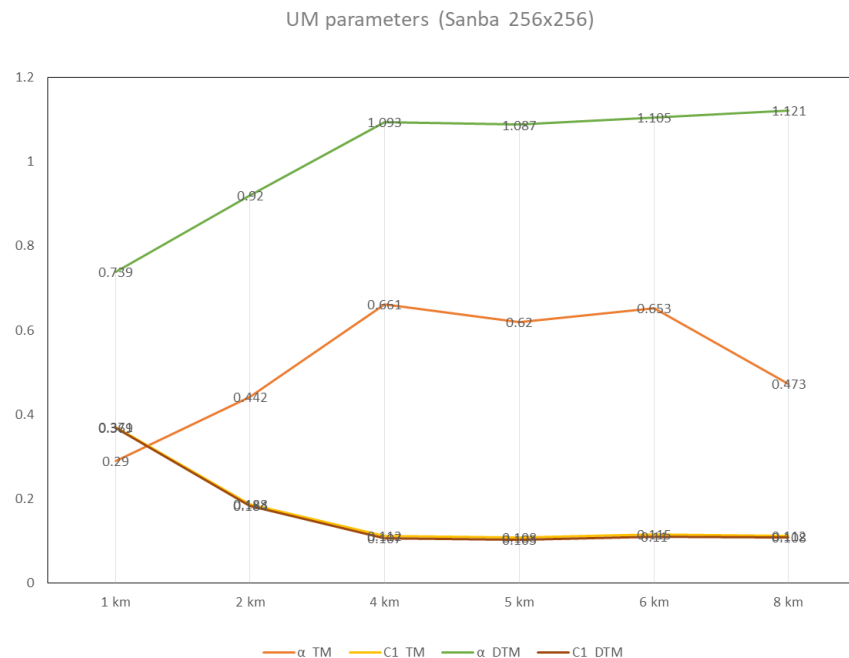


Fig. 5.3.12. The UM parameters obtained from TM and DTM.

## 1.2) The domain $64 \text{ km} \times 64 \text{ km}$

The spectral analysis was performed in the smaller domain size of  $64 \text{ km} \times 64 \text{ km}$  in Fig. 5.3.13. Like the previous cases, the analysis was done in a smaller domain is due to the zero-field included in 1 km and 2 km in the bigger domain size  $256 \text{ km} \times 256 \text{ km}$ . From the spectral analysis, it is noted that all the dataset were showing the linear scaling behavior up to  $\ln(k) = 1.5$  with  $R^2 \geq 0.9$ . However, 4 km and 5 km presents the best scaling behavior (Fig. 5.3.13). The detailed values of  $\beta$  and  $R^2$  is summarized in Table 5.3.3.

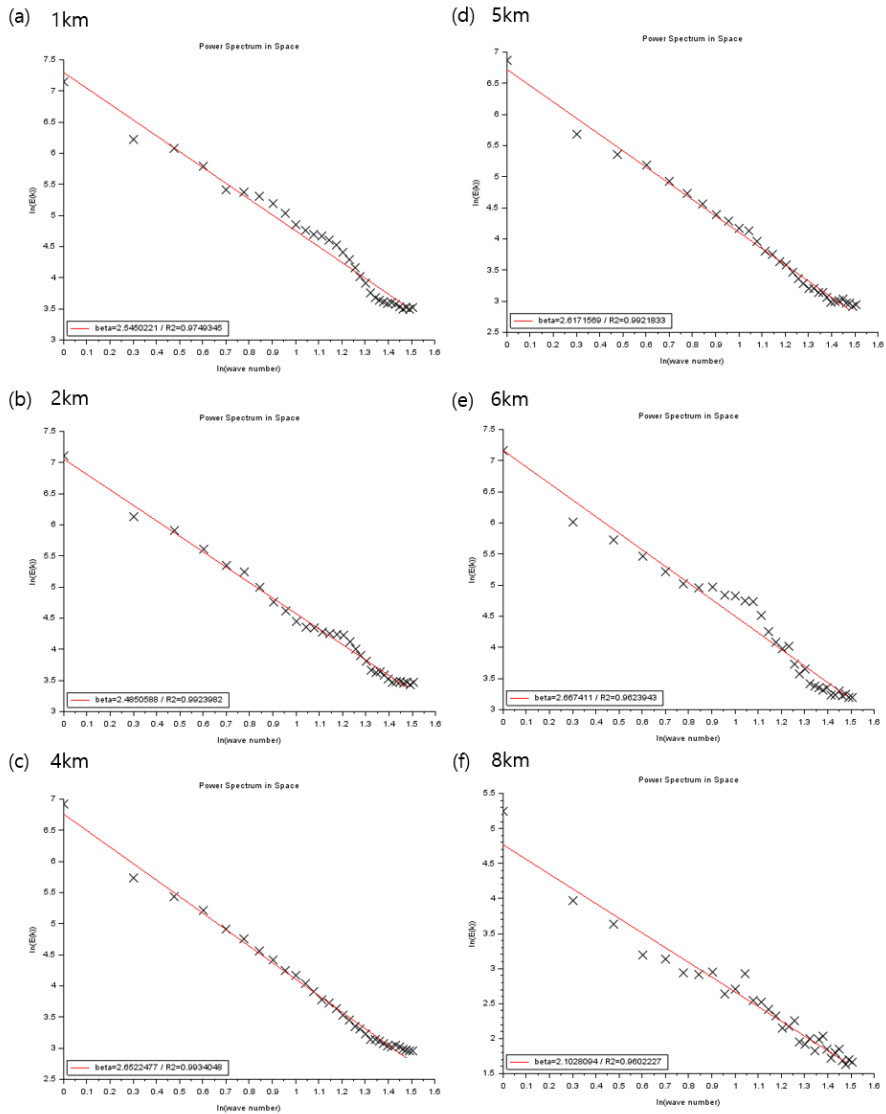


Fig. 5.3.13. The same as Fig. 5.3.8 but in the domain size  $64 \text{ km} \times 64 \text{ km}$ .

Table 5.3.3. The same as Table 5.1.3 but with Typhoon Sanba.

	1 km	2 km	4 km	5 km	6 km	8 km
$\beta$	2.55	2.49	2.65	2.62	2.67	2.10
$R^2$	0.97	0.99	0.99	0.99	0.96	0.97

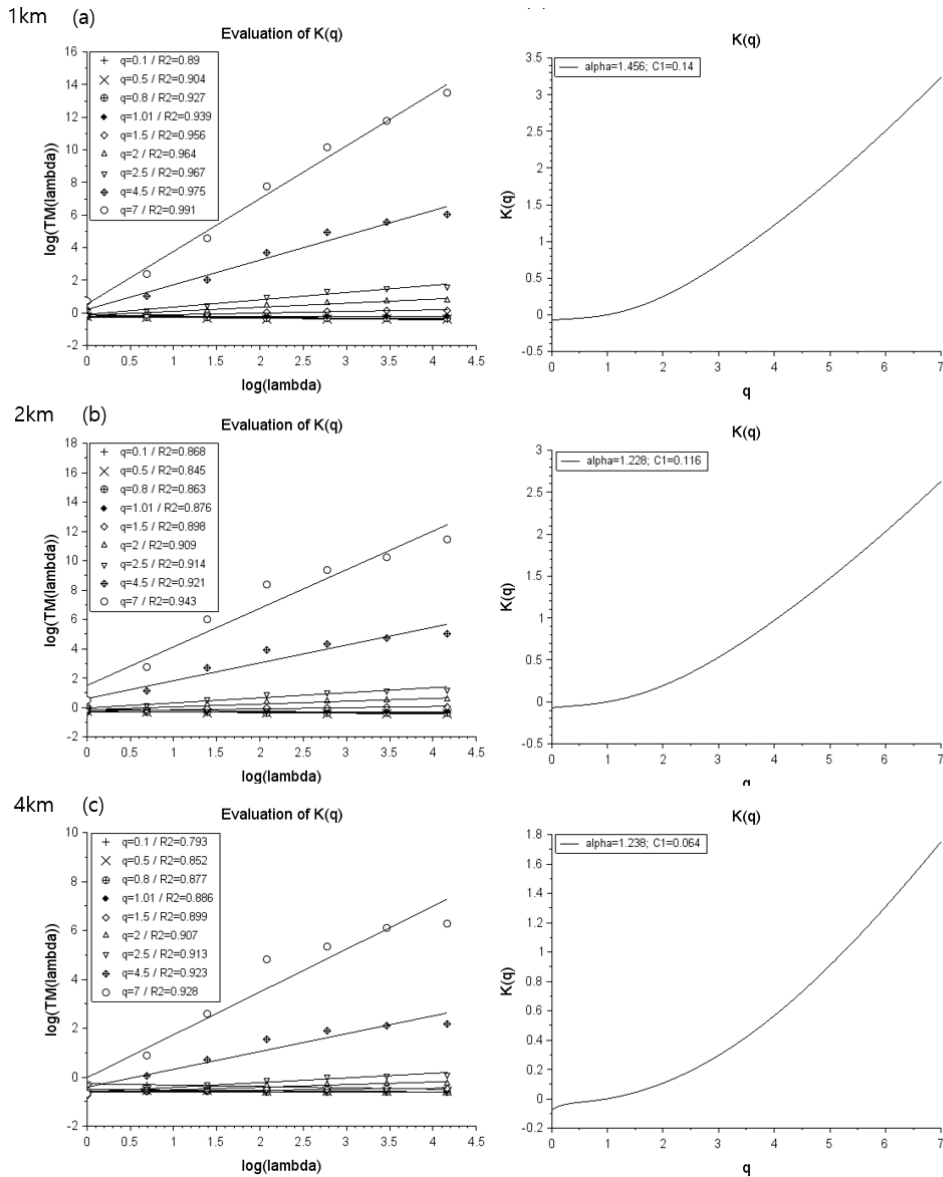
The multifractal analysis was done with TM, and DTM techniques applied. The same as the bigger domain,  $q$  was selected from 0.1 to 7. The results of the TM method are presented in Fig. 5.3.14. The graphs on the left, Fig. 5.3.14 (a, b, c, d, e, f), shows the log-log plots of  $\langle \varepsilon_\lambda^q \rangle \approx \lambda^{K(q)}$  with the resolution  $\lambda$  and the scaling behavior was very good without any scaling break ( $R^2 \geq 0.9$ ) which means that the field is multifractal at all moment order. The graph of scaling moment function  $K(q)$  is obtained (Fig. 5.3.14 (g, h, i, j, k, l)) and UM parameters are obtained from the slope of  $K(q)$  graphs which shows the moment and singularity behavior.

Fig 5.3.15 shows the empirical scaling moment functions  $K(q)$  are compared to the semi-theoretical functions applying UM parameters  $\alpha$  and  $C_1$  retrieved from TM and DTM analysis. In low level (1 km and 2 km), semi-theoretical DTM graph shows the smallest  $q_D$ , when the empirical graph and semi-theoretical DTM are fitting well with each other from 4 km to 6km. However, at 8 km height, the empirical graph shows the smaller  $q_D$ .

The results of the DTM method are shown in Fig. 5.3.16. The result of DTM analysis shows good scaling behavior as well as the result of TM analysis. For each power  $\eta$ , the slope of the linear regression gives an estimate of the scaling moment functions  $K(q, \eta)$  with a fixed value of  $q$  ( $q=1.5$ ). The slope of S-shape curves (Fig. 5.3.16. (g, h, i, j, k, l)) gives an estimation of  $\alpha$  and  $C_1$ . The value of  $\alpha$  decreases while the value of  $C_1$  relatively remains the same.

The detailed UM parameters estimated from TM and DTM are indicated in Table 5.3.4 and shown in Fig. 5.3.17.

1km



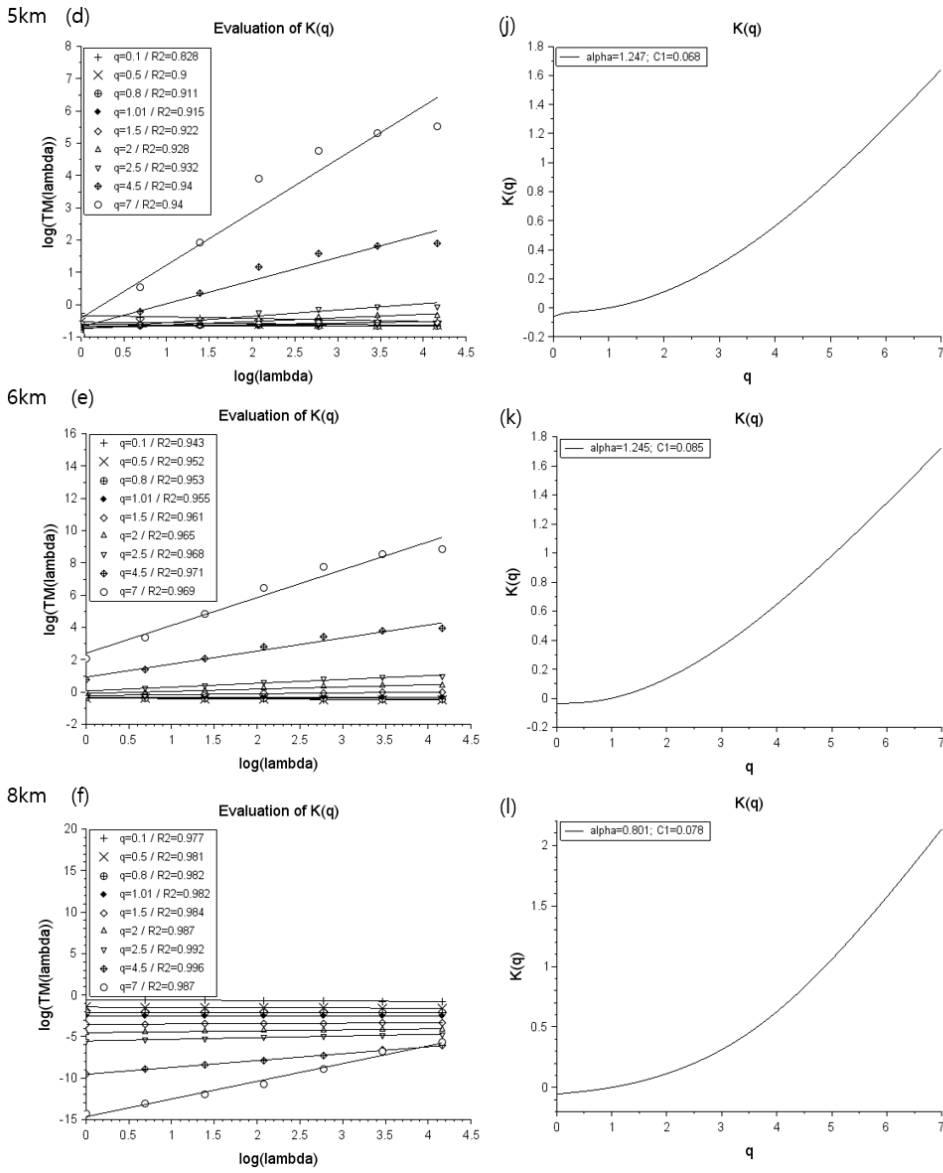


Fig. 5.3.14. The same as Fig. 5.3.9 but in the domain size  $64 \text{ km} \times 64 \text{ km}$ .

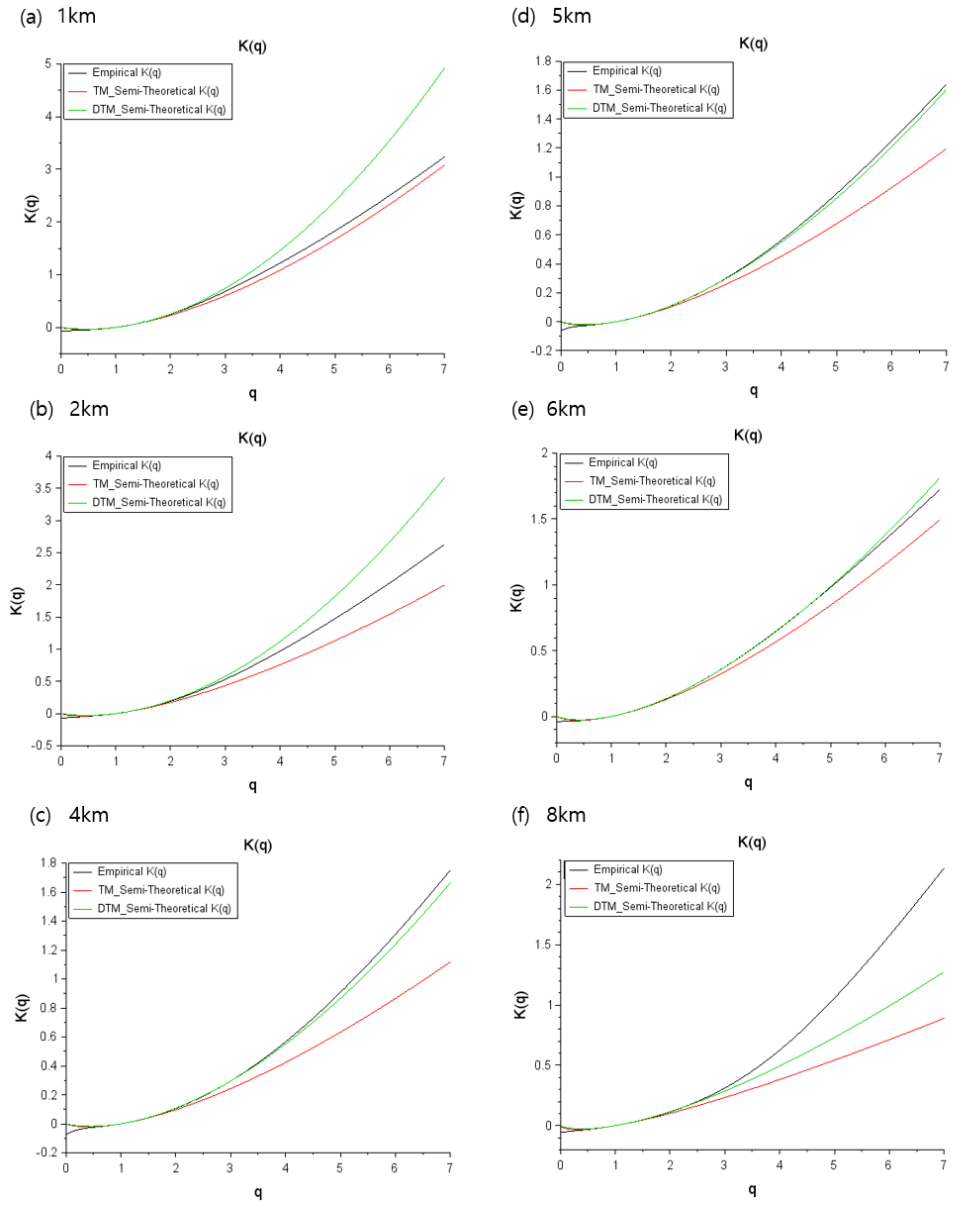
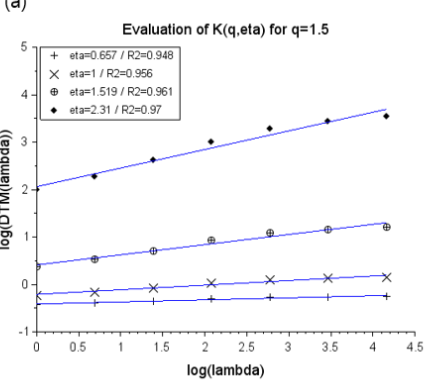
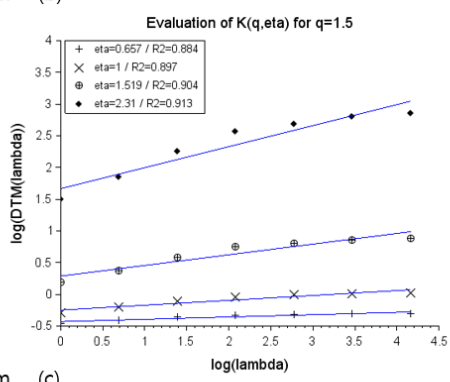


Fig. 5.3.15. The same as Fig. 5.3.10 but in the domain size  $64 \text{ km} \times 64 \text{ km}$ .

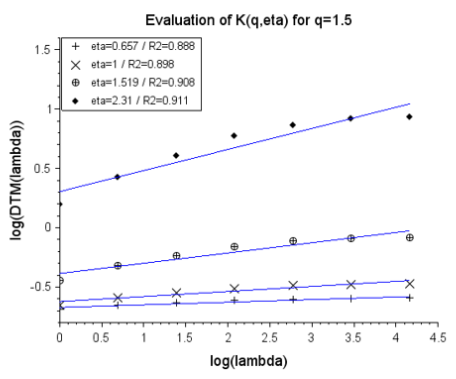
1km



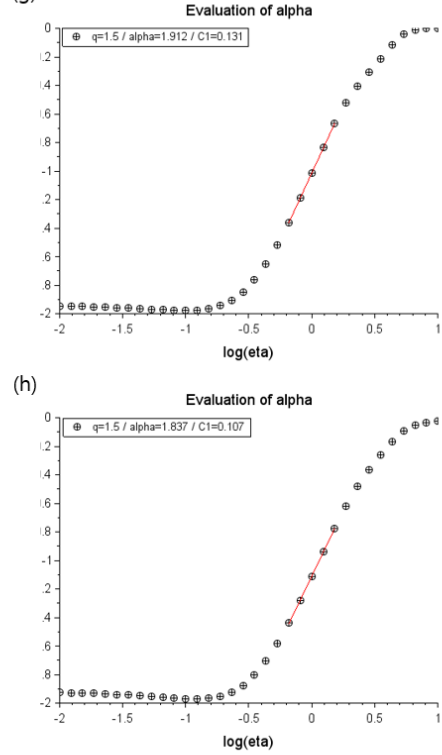
2km



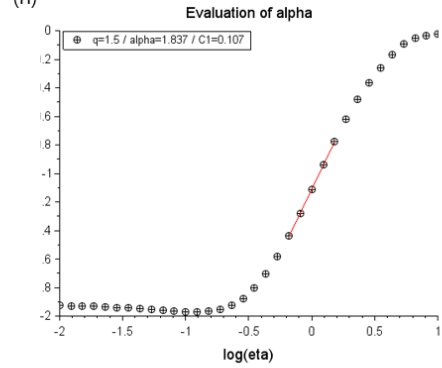
4km



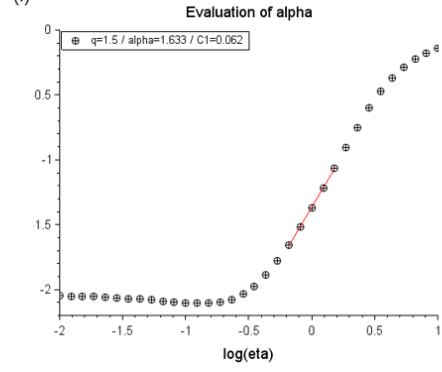
(g)



(h)



(i)



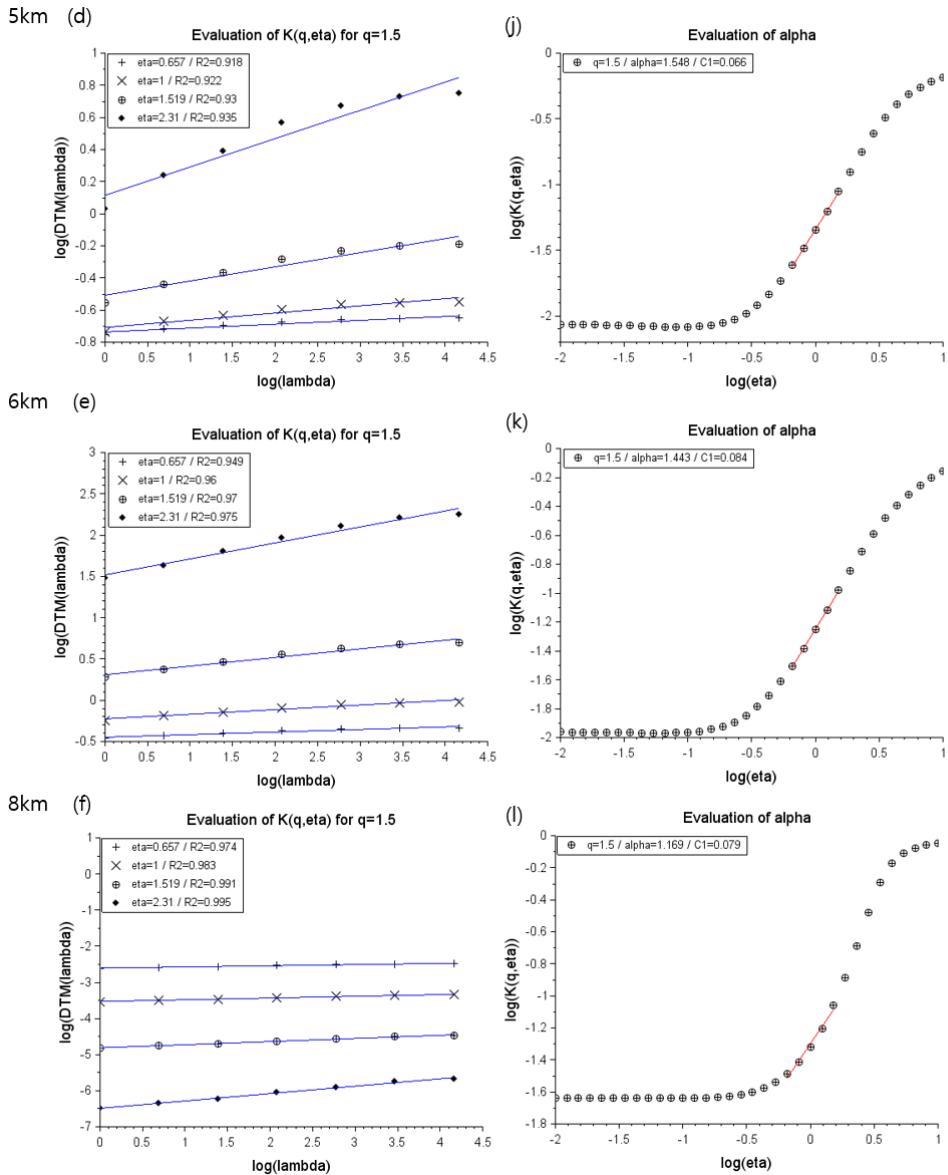


Fig. 5.3.16. The same as Fig. 5.3.11 but in the domain size  $64 \text{ km} \times 64 \text{ km}$ .

Table 5.3.4. The same as Table 5.1.4 but with Typhoon Sanba.

		1 km	2 km	4 km	5 km	6 km	8 km
TM	$\alpha$	1.456	1.228	1.238	1.247	1.245	0.801
	$C_1$	0.14	0.116	0.064	0.068	0.085	0.078
DTM	$\alpha$	1.912	1.837	1.633	1.548	1.443	1.169
	$C_1$	0.131	0.107	0.062	0.066	0.084	0.079

Lastly, the scaling exponent value  $\beta$  for spectral analysis are averagely 2.513 in all heights of the domain sizes  $64 \text{ km} \times 64 \text{ km}$  with  $R^2 \geq 0.9$  in all altitudes.

The multifractal parameters were obtained from TM and DTM analysis. The value of  $C_1$  is almost the same between the result of the TM and DTM but the larger values of  $\alpha$  are obtained from DTM analysis. The behavior of values of  $\alpha$  obtained from TM between 2 km and 6 km increases while the one from DTM decreases.

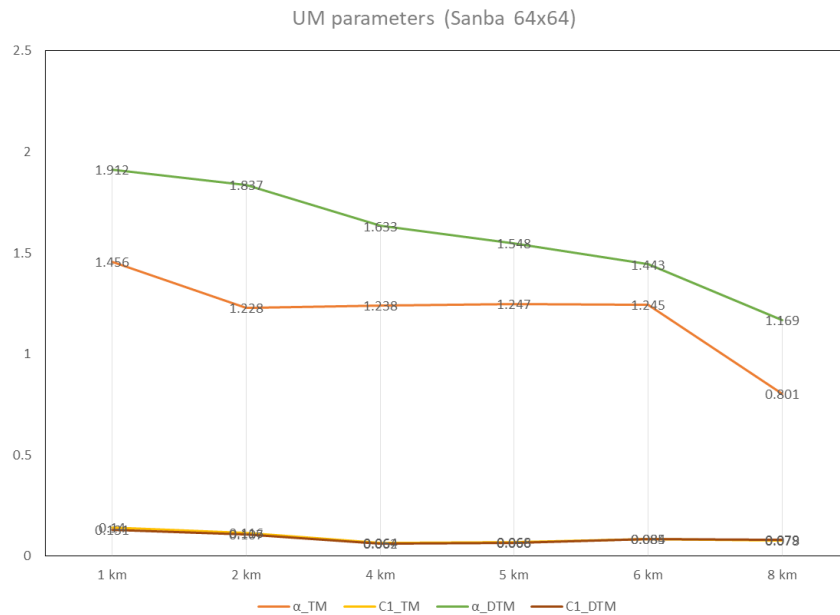


Fig. 5.3.17. The same as Fig. 5.3.12 but in domain  $64 \text{ km} \times 64 \text{ km}$ .

Fig. 5.3.18 shows the accumulated rainfall field from the radar observation ( $360 \text{ km} \times 360 \text{ km}$ ) in each altitude with typhoon Sanba. The peak of the rainfall field reaches up to 10 mm at lower altitudes while it reaches less than 1.5 mm at other altitudes. It shows the dependence of  $\alpha$  especially with the UM parameters obtained from DTM.  $\alpha > 1.8$ ,  $C_1 \approx 0.2$  in  $64 \text{ km} \times 64 \text{ km}$  at low altitudes when  $\alpha < 1$ ,  $C_1 \approx 0.1$  in  $256 \text{ km} \times 256 \text{ km}$ . This shows the intensive development of the rainfall field in low altitudes.

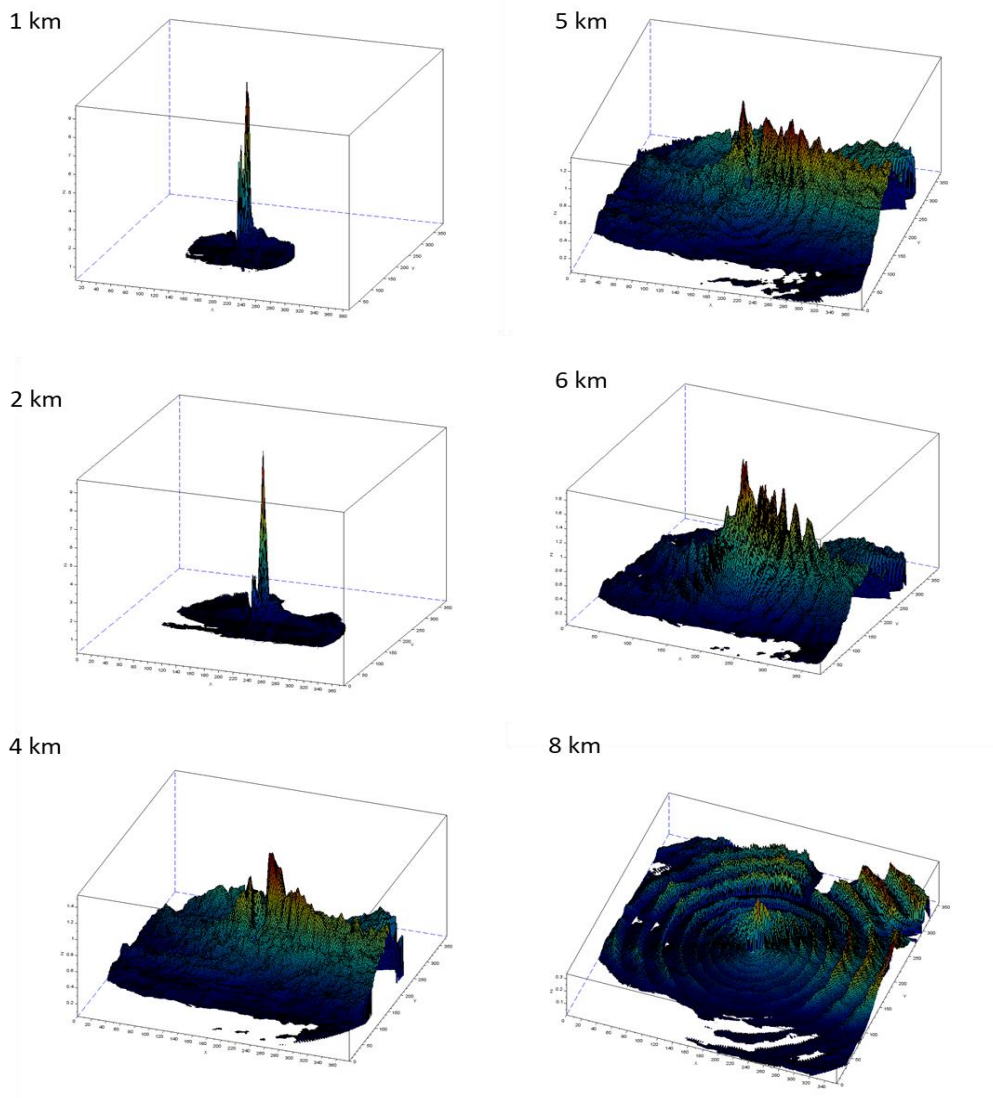


Fig. 5.3.18. The same as Fig. 5.1.18 but with the case of typhoon Sanba.

## 2) CReSS model

### 2.1) The domain 256 km × 256 km

The spectral analysis was performed with the rainfall rate field obtained from the numerical model CReSS with the case of typhoon Sanba. Fig. 5.3.19 shows the result of spectral analysis in a domain size of 256 km × 256 km.  $\beta = 1.46$  with  $R^2 = 0.92$  was obtained showing no apparent scaling break in the field.

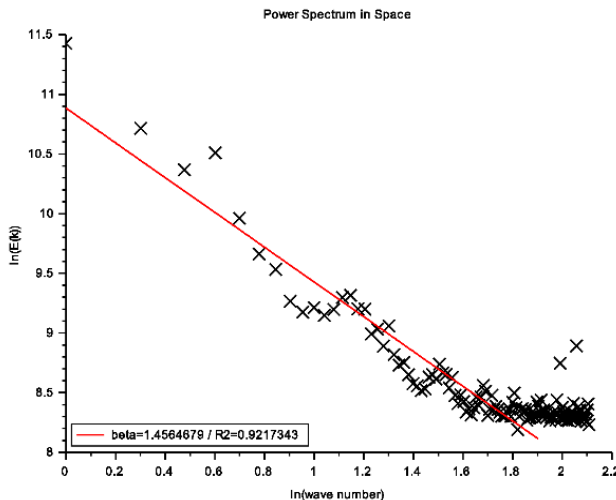


Fig. 5.3.19. The result of spectral analysis by CReSS model dataset in domain 256 km × 256 km.

Then TM and DTM analysis were practiced. The result of the TM method is presented in Fig. 5.3.20 and DTM method in Fig. 5.3.21. As the same as the analysis done with the radar dataset, The scaling behavior with the value of different  $q$  from 0.1 to 7.0 (Fig. 5.3.20 (a)). The scaling behavior on each graph shows from  $q=0.1$  to  $q=7$  with  $R^2 \geq 0.7$  which is relatively lower than the first 2 cases. However, the graph does not show extreme scaling break as it is aligned in a straight line. Then, the scaling moment function  $K(q)$  is obtained with the values of multifractal parameters indicated which were obtained from TM analysis (Fig. 5.3.20 (b)). Lastly, in Fig. 5.3.20 (c), empirical  $K(q)$ ,  $K(q)$  obtained from using UM parameters obtained from TM, and  $K(q)$  obtained using UM parameters are compared. It shows that all the results are relatively fitting well but especially with empirical  $K(q)$  and the one obtained from TM analysis.

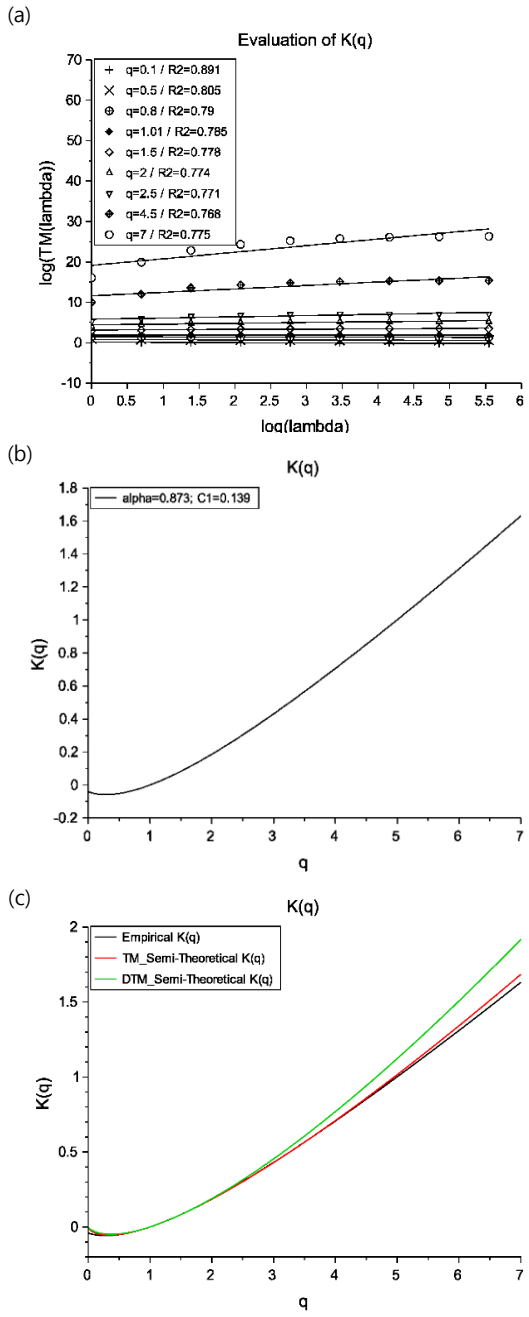


Fig. 5.3.20. The same as Fig. 5.2.20 but with Sanba case.

The result of the DTM method is shown in Fig. 5.3.21. For each power  $\eta$ , with a fixed value of  $q$  ( $q=1.5$ ), the slope of the linear regression gives an estimate of the scaling moment functions  $K(q, \eta)$  with showing the good scaling behavior as well as the result of TM analysis. Fig. 5.2.21 (b) shows the slope of the DTM curve which gives an estimation of  $\alpha$  and  $C_1$ . The UM parameters are summarized in table 5.3.5.

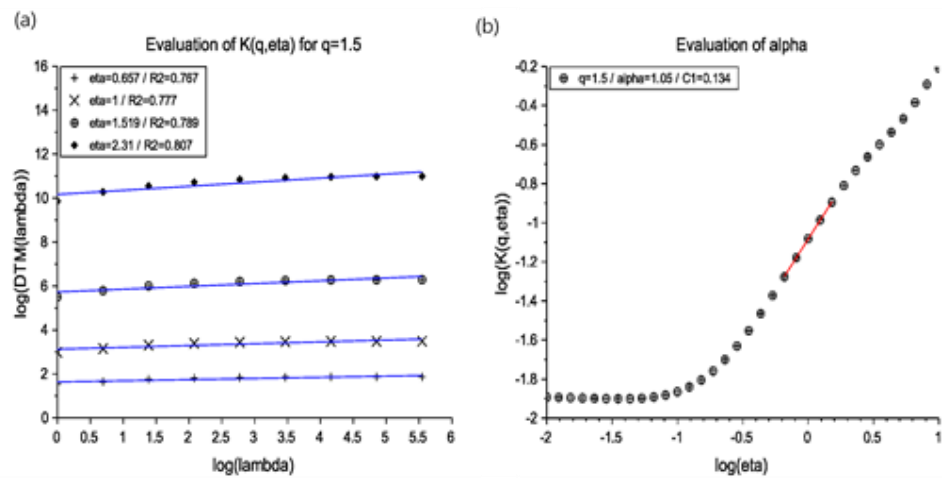


Fig. 5.3.21. The same as Fig. 5.2.21 but with Sanba case.

## 2.2) The domain 64 km × 64 km

The spectral analysis was performed with the domain size of 64 km × 64 km which was selected from the middle of the whole domain 360 km × 360 km. Fig. 5.3.22 shows the result of a linear scaling behavior with  $\beta = 2.97$  and  $R^2 = 0.94$ .

The results of TM and DTM analysis show that the scaling behavior is good by showing  $R^2 \approx 0.9$  in all ranges (Fig. 5.1.23 (a) and Fig. 5.1.24 (a)). The graph of scaling moment function  $K(q)$  obtained from empirical, TM analysis, and DTM analysis are aligned in best-fitting from  $q = 0$  up to  $q = 2.5$  (Fig. 5.1.22 (c)).

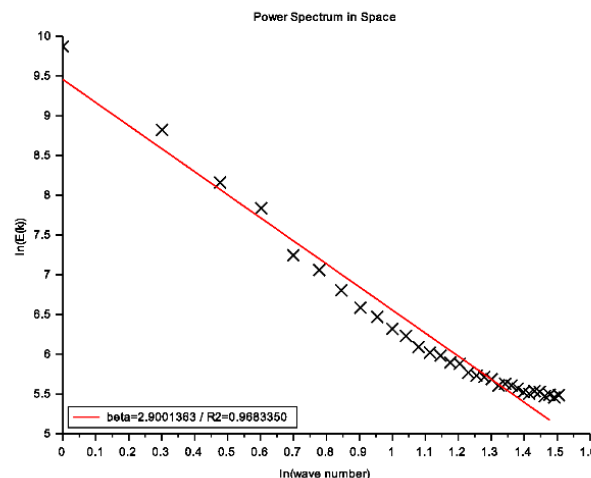


Fig. 5.3.22. The same as Fig. 5.3.19 but in domain 64 km × 64 km.

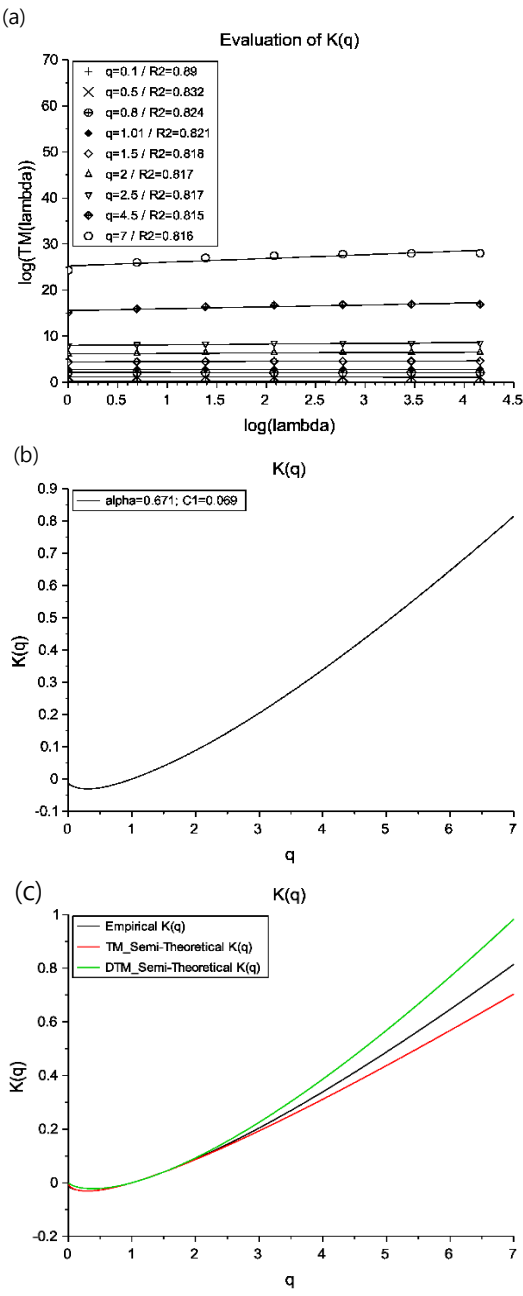


Fig. 5.3.23. The same as Fig. 5.3.20 but in domain 64 km  $\times$  64 km.

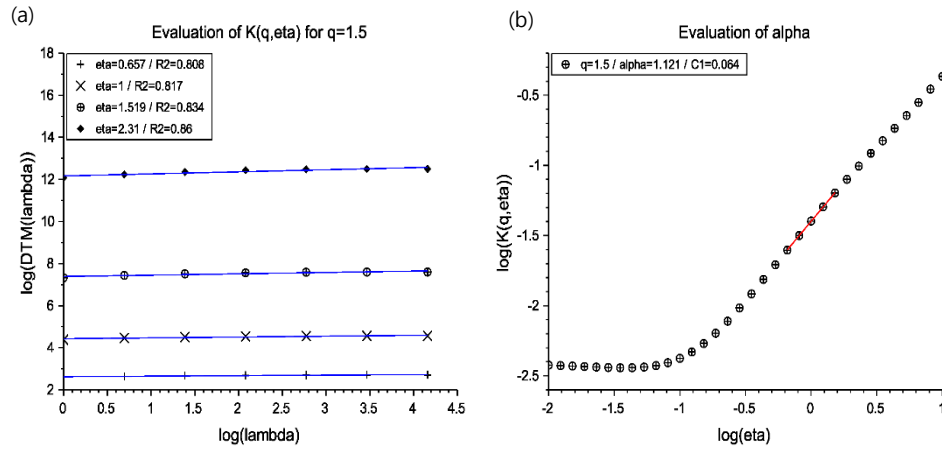


Fig. 5.3.24. The same as Fig. 5.3.21 but in domain 64 km  $\times$  64 km.

Table 5.3.5. The same as Table 5.1.5 but with Typhoon Sanba.

CReSS		256 $\times$ 256	64 $\times$ 64
TM	$\alpha$	0.873	0.671
	$C_1$	0.139	0.069
DTM	$\alpha$	1.05	1.121
	$C_1$	0.134	0.064

### 3) Comparison of radar CReSS

As the previous case studies, Fig. 5.3.25 with the domain size of 256 km  $\times$  256 km and Fig. 5.3.26 with 64 km  $\times$  64 km shows  $K(q)$  -  $K(q)$  plots in order to see the comparison of linearity between radar data and CReSS data.

Fig. 5.3.25 shows the comparison of  $K(q)$  in the domain size of 256 km  $\times$  256 km. The best consistency between two different datasets is at 4 km even the blue dots aligns with the black line the most at 1 km, the slope close to 1 shows at 4 km. The ratio of  $C_1$  is as follows ;

At 1 km :  $0.134/0.369 = 0.363$ , at 2 km :  $0.134/0.184 = 0.728$ , at 4 km :  $0.134/0.107 = 1.252$ , at 5 km :  $0.134/0.103 = 1.301$ , at 6 km :  $0.134/0.11 = 1.218$ , and at 8 km :  $0.134/0.108 = 1.241$ .

Fig. 5.3.26 shows the comparison of  $K(q)$  with the domain size 64 km  $\times$  64 km. The difference of  $\alpha$  becomes larger at 8 km than other altitudes but the ratio of  $C_1$  shows less than 1 in every altitude. The ratio of  $C_1$  is as follows ;

At 1 km :  $0.064/0.131 = 0.489$ , at 2 km :  $0.064/0.107 = 0.598$ , at 3 km :  $0.064/0.062 = 1.032$ , at 5 km :  $0.064/0.066 = 0.97$ , at 6 km :  $0.064/0.084 = 0.762$ , and at 8 km :  $0.064/0.079 = 0.81$ .

This bias yields a complex evolution of the extremes concerning the altitude and especially a sharp contrast in this case at a low level of 1 and 2 km.

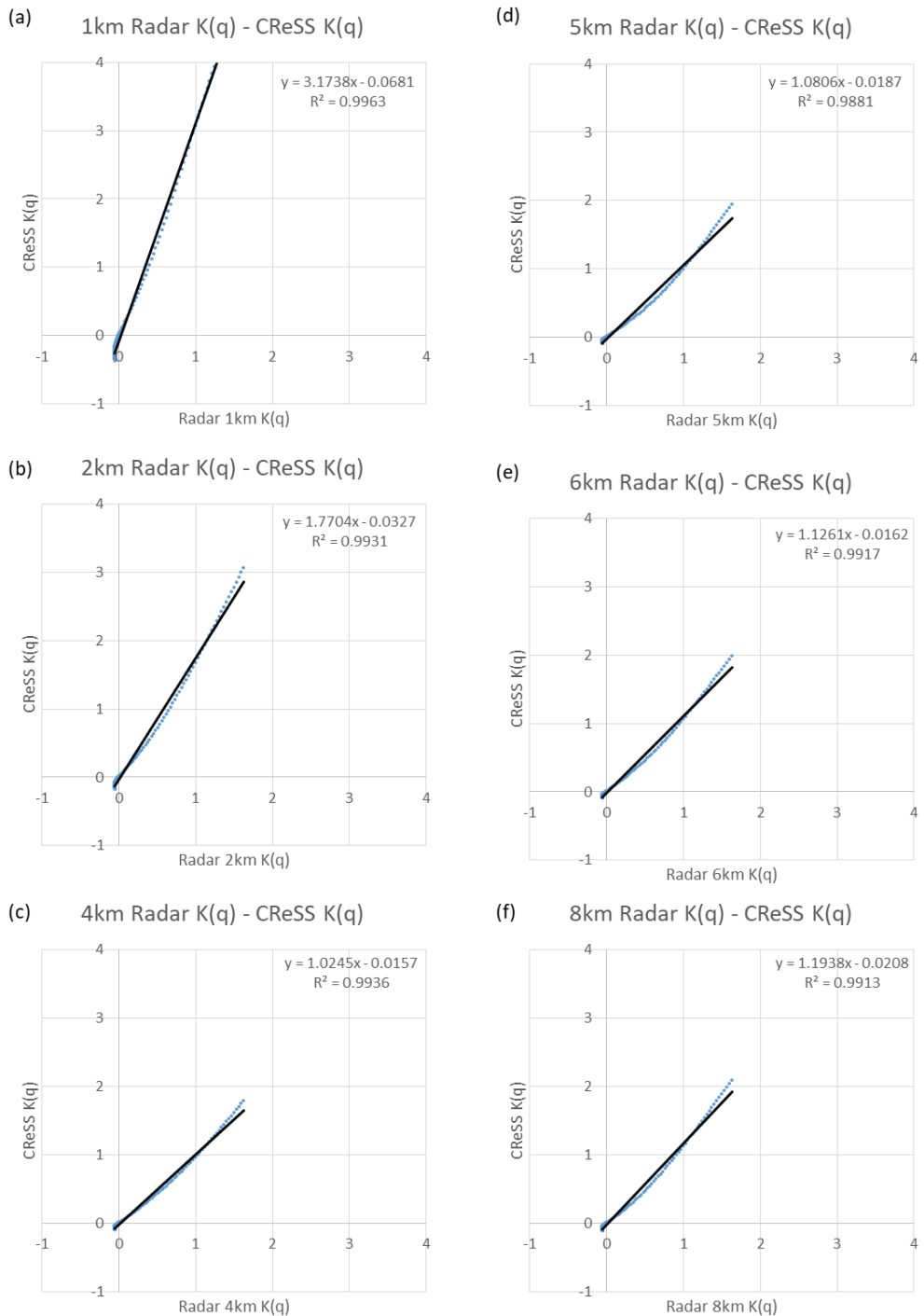


Fig. 5.3.25. The same as Fig. 5.1.25 but with Sanba case

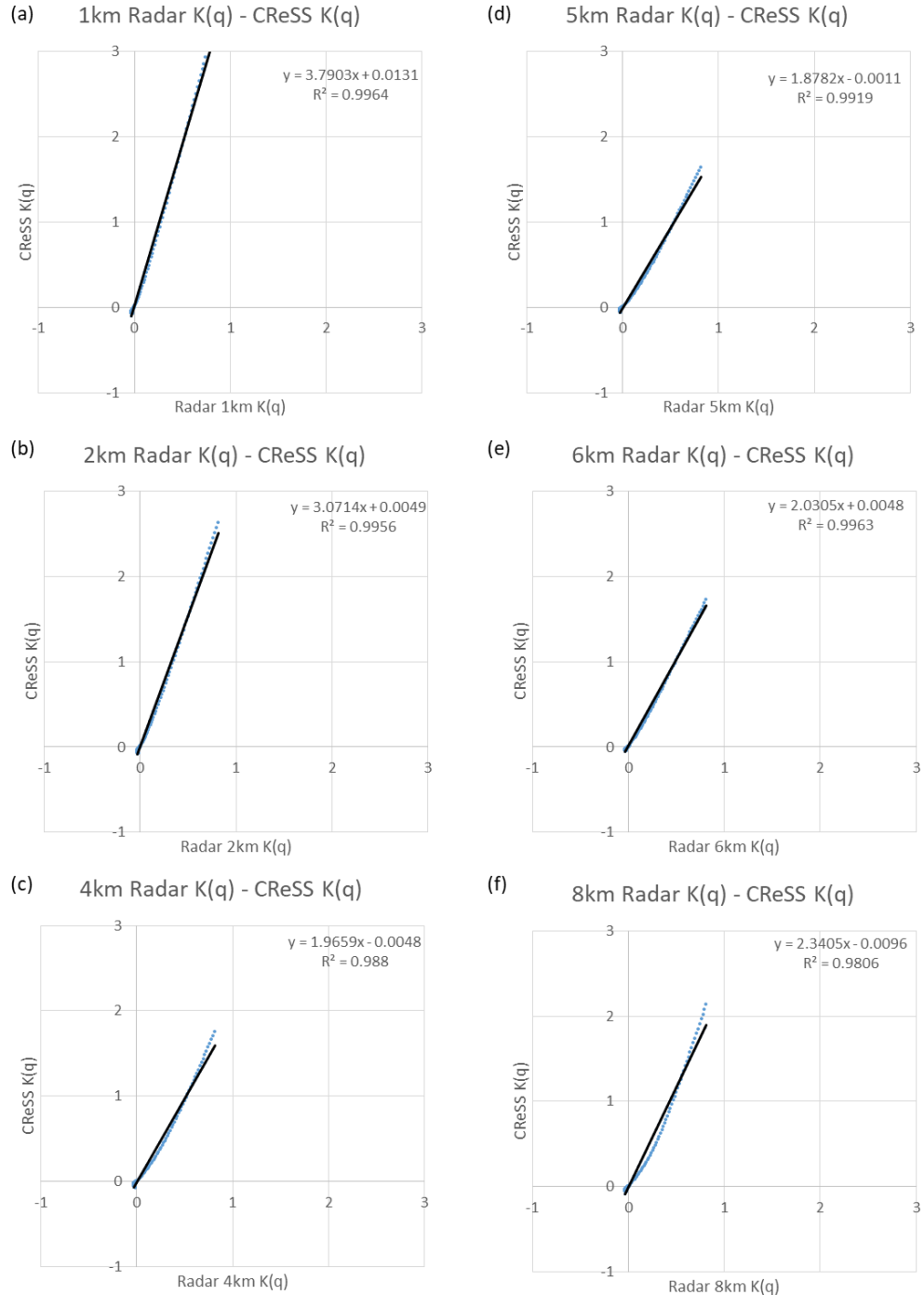


Fig. 5.3.26. The same as Fig. 5.3.25 but with the domain 64 km × 64 km.

## 6. Summary and Conclusion

This study was conceived to discuss the strong intermittency of extreme rainfall events such as typhoons with the multifractals. The multifractal framework was applied to the three typhoon cases (Khanun, Bolaven, Sanba), which struck South Korea passing through Jeju Island in 2012. All cases were in the decaying stage when they passed the interested domain.

To get the general information of the typhoon and its environmental field, the NCEP/NCAR reanalysis data were used to see the synoptic flow. Also, the S-band Doppler radar data was obtained to demonstrate the structure of the typhoon with reflectivity, and the horizontal and vertical wind field. With the radar dataset, the rainfall rate was extracted by using the Z-R relationship in each altitude (1, 2, 4, 5, 6, and 8 km) after obtaining Constant Altitude Plan Position Indicator (CAPPI). With the rainfall rate data in each altitude, spectral analysis was done to check the conservativeness of the field and proceeded with the multifractal analysis by using the Trace Moment (TM) and the Double Trace Moment (DTM) method.

First of all, to see the structure of the typhoon, the reflectivity with the wind field was analyzed. The result of typhoon Khanun showed the highly distributed rainfall field with a constant intensity of the rainfall covering most parts of the domain in 4-6 km as it is shown with the reflectivity. Secondly, the result of typhoon Bolaven showed the high intensity of rainfall along with the spiral band that the rainfall field was very inconstant as well as the typhoon Sanba.

From the multifractal analysis, the scaling moment functions  $K(q)$  from TM and  $K(q,\eta)$  from DTM showed the good scaling behavior of the typhoons at different altitudes. All the UM parameters were obtained from TM and DTM. In all three typhoon cases, the rainfall field ( $C_1$ ) is becoming more homogeneous along with altitudes. However, the extreme appearance ( $\alpha$ ) varied in three cases. Typhoon Khanun case presented the large mean intermittency ( $C_1$ ) in low altitudes (1, 2 km) with the smallest  $\alpha$  which is Levy's multifractality index. It

means that in low altitudes, the rainfall field is steady, yet in 8 km, the field has more fluctuation. In the typhoon Bolaven, even the value of  $C_1$  is smaller and  $\alpha$  is larger than the ones of typhoon Khanun case, it still shows that low altitudes (1, 2 km) in a typhoon is more steady than the higher altitudes, especially at 5 and 8 km. Also, the typhoon Sanba showed a relatively large number of  $C_1$  with the low value of  $\alpha$  at low altitudes (1, 2 km).

The smaller domain was chosen to analyze with  $64 \text{ km} \times 64 \text{ km}$ , due to the limitation of the observation in low altitudes in 1 and 2 km (but as it was mentioned earlier, the result of typhoon Khanun in low altitudes were not possible to be obtained). Since the domain size is smaller, it is more focused on the intensive rainfall field and the value of  $\alpha$  is significant in all the cases even when  $C_1$  is small. It seems that by analyzing smaller domain size, Universal Multifractal (UM) parameters can show the definite trend of the development of the rainfall fields, especially in low altitudes.

Comparing  $\alpha$  from the two domains, the value of  $\alpha$  is less than 1 in the domain  $256 \text{ km} \times 256 \text{ km}$  at low altitude (1, 2 km) despite the possibility to know the real values of typhoon Khanun in the low altitudes. However, the domain  $64 \text{ km} \times 64 \text{ km}$  shows  $\alpha > 1$  with all cases (all altitudes with Bolaven and Sanba, but only above 4 km for Khanun). When  $\alpha$  is less than 1, it means the limited range of singularities, while  $\alpha$  larger than 1 means there is no limit.

To compare the result of the radar observation, the rainfall rate obtained by CReSS model simulation was also used. As a result of the UM parameters of all cases from CReSS model, only with the Khanun case,  $\alpha$  is less than 1 in both domains which means it showed the sparseness of rainfall field is large, the variability is low in both domains. On the other hand,  $\alpha$  is larger than 1 with Bolaven and Sanba in both domains which showed the sparseness of rainfall field is small, the variability is high in both domains. as it does not provide rainfall rate on each altitude. Unfortunately, the limitation of the CReSS simulation is that it does not allow the rainfall rate parameter which is an instantaneous rainfall rate on the surface. To get the detailed difference,  $K(q)$  of

radar and CReSS was compared. Variability is similar at all altitudes in both domains in three cases but in three cases, CReSS over-estimates the sparseness of rainfall field. This shows that in CReSS simulation, only variability can be estimated. Also, there is a dependence of  $\alpha$  along with the altitude which shows the deduction of the pattern of the rainfall field in each altitude with the UM parameters. This enables to see the development of the rainfall field.

To understand the exact reasons for the difference, we need much more research work of data qualification since it is the remained limitations of handling artificial zeros caused by the scanning angle of the radar observation in the low altitudes, especially when comparing  $\alpha$  with the respect of critical value 1 when looking at a big domain. Also, the study about thermodynamics and microphysics of rainfall in the typhoon structure are needed to understand the different process of development of the rainfall in each altitude.

In this study, the multifractal approach was applied to analyze the typhoon cases with strong intermittency which is a new technique to analyze the extreme variability using the radar data and CReSS model data. By this study, two interpretation was obtained. (1) Even though there was a limitation of observation causing artificial zero fields in low altitude, it was possible to select the smaller domain size and detect the dependence of  $\alpha$  on the focused area on the island. (2) It was possible to compare the result from the observation and model simulation which showed consistency despite the CReSS model producing only rainfall rate output data from the surface. These results show that the multifractal framework is a way of using the assimilated big data to widely extend in various heights and domains and provides considerable improvement in the representation of domain characteristics. The multifractals have been used in analyzing many different rainfall events (local heavy rains, floods, etc.), but this study was the first case used in disasters such as typhoons with large vortex with the radar and model simulation CReSS that shows the multifractals can be used for defining the characteristics and similarities to the development mechanism and the structure of the typhoon. Furthermore, this can

be applicable to categorize the typhoon types by different rainfall characteristics defined by the UM parameters. With the help of Multifractal analysis, the sparseness of rainfall field and its variability along with altitudes can be estimated by using the radar data. However, only variability can be estimated by numerical model.

## References

- Akter, N. and Tsuboki, K., 2012: Numerical Simulation of Cyclone Sidr Using Cloud Resolving Model: Characteristics and Formation Process of an Outer Rainband. *Monthly Weather Review*. **140**, 789-810.
- Barndorff-Nielsen, O. E. and Prause, K., 2001: Apparent scaling. *Finance and Stochastics*, **5**, 103 – 113.
- Biaou, A., 2004: De la méso-échelle à la micro-échelle: Désagrégationspatio-temporellemultifractale des précipitations. PhD thesis, Paris, ENMP.
- Calvet L. and Fisher, A., 2001: Forecasting multifractal volatility. *Journal of Econometrics*, **105**, 27 – 58.
- Cawley, R. and Mauldin, R.D., 1992: Multifractal decompositions of Moran fractals. *Advances in Mathematics*. **92**, 196-236.
- Chai, X. and Wang, L., 2019: A Multiscale Energetic Diagnosis of the Response of Mokpo Sea to Typhoon Bolaven. *Journal of Geoscience and Environment Protection*. **07**, 251-267.
- Chen, Y. H., Kuo, H. C., Wang, C. C., and Yang, Y. T., 2017: Influence of southwest monsoon flow and typhoon track on Taiwan rainfall during the exit phase: modelling study of typhoon Morakot (2009). *Quarterly Journal of the Royal Meteorological Society*, **143**, 3014-3024.

Cho, N.S. and Lee, T.Y., 2006: A numerical study of multiple convection bands over the Korean peninsula. *J. Korean Meteorol. Soc.*, **42**, 87-105.

Choi, H.Y., Ha, J.H., Lee, D.K., Kuo, Y.H., 2011: Analysis and simulation of mesoscale convective system accompanying heavy rainfall: the Goyang case. *Asia Pac. J. Atmos. Sci.*, **47**, 265-279.

Choi, K.S. and Kim, T.R., 2010 b: Change of TC activity around Korea by Arctic Oscillation phase, *Atmosphere*, **20**, 387-398.

Choi, K.S., and Kim, B.J., 2007: Climatological characteristics of tropical cyclones making landfall over the Korean peninsula, *J. Korean Meteorol. Soc.*, **434**, 97– 109.

Chou, Y. J., 2003: Short-term rainfall prediction using a multifractal model. PhD thesis, Massachusetts Institute of Technology, USA.

Cotton, W.R., Tripoli, G.J., Rauber, R.M. and Mulvihill, E.A., 1986: Numerical Simulation of the Effects of Varying Ice Crystal Nucleation Rates and Aggregation Processes on Orographic Snowfall. *J. Climate Appl. Meteor.*, **25**, 1658–1680.

Cressman, G., 1959: An operational objective analysis system. *Mon. Wea. Rev.*, **87**, 367–374.

De Lima, M. I. P and Grasman, J., 1999: Multifractal analysis of 15-min and daily rainfall from a semi-arid region in Portugal. *J. Hydrol.*, **220**, 1-11.

De Montera, L., Barth`es, L., Mallet, C. and Gol'e, P., 2009: The effect of rain–no rain intermittency on the estimation of the universal multifractals model parameters. *J. Hydrometeor.*, **10(2)**, 493–506.

Deidda, R., 2000: Rainfall downscaling in a space-time multifractal framework. *Water Resources Research*, **36**, 1779–1794.

Gao, J. and Droege, K. K., 2004: A three-dimensional variational data assimilation method with recursive filter for single-Doppler radar. *J. Atmos. Oceanic Technol.*, **21**, 457–469.

Gao, J., Xue, M., Shapiro, A., and Droege, K. K., 1999: A variational method for the analysis of three-dimensional wind fields from two Doppler radars. *Mon. Wea. Rev.*, **127**, 2128–2142.

Gires, A., Tchiguiringskaia, I., Schertzer, D. and Lovejoy, S., 2013: Development and analysis of a simple model to represent the zero rainfall in a universal multifractal framework. *Nonlinear Processes in Geophysics*, **20**, 343–356.

Gupta, V. K., and Waymire, E. C., 1993: A statistical analysis of mesoscale rainfall as a random cascade. *J. Appl. Meteor.*, **32**(2), 251–267.

Hahm, J. H., Jeong, H. Y., and Kwak, K. H., 2019: Estimation of Strong Wind Distribution on the Korean Peninsula for Various Recurrence Periods: Significance of Nontyphoon Conditions. *Advances in Meteorology*, **2019**, 1-10.

Halsey, T. C., Jensen, M. H., Kadano, L. P., Procaccia, I. and Shraiman, B., 1986: Fractal measures and their singularities: the characterization of strange sets. *Physical Review A*, **33**, 1141–1151.

Han, L., Wang, H. and Lin, Y., 2008: Application of optical flow method to nowcasting convective weather. *Beijing Daxue Xuebao Ziran Kexue Ban/Acta Scientiarum Naturalium Universitatis Pekinensis*, **44**(5), 751-755.

Harris, D., Menabde, M., Seed, A. and Austin G., 1996: Multifractal characterization of rain fields with a strong orographic influence. *Journal of Geophysical Research: Atmospheres*, **101(D21)**, 26405–26414.

Hoang, C. T., Tchiguirinskaia, I., Schertzer D., and Lovejoy, S., 2014: Caractéristiques multifractales et extrêmes de la précipitation à haute résolution, application à la détection du changement climatique. *Revue des sciences de l'eau/Journal of Water Science*, **27(3)**, 205–216.

Hong, S.Y. and Lee, J.W., 2009: Assessment of the WRF model in reproducing a flash-flood heavy rainfall event over Korea. *Atmos. Res.*, **93**, 818-831.

Hubert, P. and Carbonnel, J., 1989: Dimensions fractales de l'occurrence de pluie en climat soudano-sahélien. *Hydrologie continentale*, **4(1)**, 3-10.

Hubert, P., Tessier, Y., Lovejoy, S., Schertzer, D., Schmitt, F., Ladoy, P., J.P. Carbonnel, J. P., Violette, S., Desurosne, I., 1993: Multifractals and extreme rainfall events. *Geophys. Res. Lett.*, **20**, 931-934.

Ikawa, M. and Saito, K., 1991: Description of a Non-hydrostatic Model Developed at the Forecast Research Department of the MRI. *Technical Reports of the Meteorological Research Institute*. **28**. 238.

Im, E.S., In, S.R. and Han, S.O., 2017: Numerical simulation of the heavy rainfall caused by a convection band over Korea: a case study on the comparison of WRF and CReSS. *Natural Hazards*, **69**, no.3, 1681-1695.

Kalnay, E., Kanamitsu, M., Kistler, R., Collins, W., Deaven, D., Gandin, L., Iredell, M., Saha, S., White, G., Woolen, J., Zhu, Y., Leetmaa, A., Reynolds, R., Chellian, M., Ebisuzaki, W., Higgins, W., Janowiak, J., Mo, K. C., Ropelewski, C., Wang, J., Jenne, R., and Joseph, D., 1996: The NCEP/NCAR 40-year reanalysis project, *Bull. Amer. Meteor. Soc.*, **77**, 437-470.

Kim, D. K., Kim, Y. H., and Chung, K. Y., 2013: Vertical structure and microphysical characteristics of Typhoon Kompasu (2010) at landfall. *Asia-Pacific Journal of Atmospheric Sciences*, **49**, 161–169.

Kim, H. J. and Moon I. J., 2019: Determination of Rain-/Wind-Dominant Type for Typhoons Approaching South Korea Based on Satellite-Estimated Rainfall and Best-Track Data, *Journal of Coastal Research*, **90**, 340-345.

Kim, H. M., Kim, S. M., and Jung, B. J., 2011: Real-Time Adaptive Observation Guidance Using Singular Vectors for Typhoon Jangmi (200815) in T-PARC 2008. *Weather and Forecasting*, **26**, 634-649.

Kim, J. H., Ho, C. H., Lee, M. H., Jeong, J. H., and Chen, D., 2006: Large increase in heavy rainfall associated with tropical cyclone landfalls in Korea after the late 1970s. *Geophysical Research letters*, **33**, L18706.

Kim, J. S., and Jain, S., 2011: Precipitation trends over the Korean peninsula: Typhoon-induced changes and a typology for characterizing climate-related risk. *Environ. Res. Lett.*, **6(3)**, 034033.

Kim, J. S., Kang, H. W., Son, C. Y., and Moon, Y. I., 2016: Spatial variations in typhoon activities and precipitation trends over the Korean Peninsula. *Journal of Hydro-environment Research*, **13**, 144-151.

Kim, K. I., Lee, H. W., Jung, S., H., Lyu, G., and Lee, G. W., 2018: Characteristics of Summer Season Precipitation Motion over Jeju Island Region Using Variational Echo Tracking. *Korean Meteorological Society*, **28**, 443-455.

Kim, K. S. and Seo, S. K., 2014: Dynamical behavior of multifractals in typhoons. EGU General Assembly 2014, held 27 April - 2 May, 2014 in Vienna, Austria, id.1586.

Kim, Y. H., Jeon, E. H., Chang, D. E., Lee, C. H. and Park, J. I., 2010: The impact of T-PARC 2008 dropsonde observations on typhoon track forecasting. *Asia-Pacific J Atmos Sci*, **46**, 287–303.

Kondo, J. and Akashi, S., 1976: Numerical Studies of the Two-Dimensional Flow in Horizontally Homogeneous Canopy Layers. *Boundary-Layer Meteorol.*, **10**, 255–272.

Ku, J. M. and Yoo, C. S., 2017: Calibrating Radar Data in an Orographic Setting: A Case Study for the Typhoon Nakri in the Hallasan Mountain, Korea. *Atmosphere 2017*, **8**, 250.

Kwon, I. H., Cheong, H. B., Kang, H. G., Han, H. J., and Park, J. R., 2010: Structure change of Typhoon Nari (2007) in the weakening stage. *Asia-Pacific Journal of Atmospheric Sciences*, **46**, 327–340.

Lavallée, D & Lovejoy, Shaun & Schertzer, Daniel & Schmitt, François. (1992). On the Determination of Universal Multifractal Parameters in Turbulence. *Topological Aspects of the Dynamics of Fluids and Plasmas*. 463-478.

Lavallée, D., 1991: Multifractal techniques: analysis and simulation of turbulent fields. Ph.D. Thesis, McGill University, Canada.

Lavallée, D., Lovejoy, S., Schertzer, D. and Ladoy, P., 1993: Nonlinear variability and landscape topography: analysis and simulation. *Fractals in Geography*, edited by: De Cola, L., and Lam, N., Prentice-Hall, 171-205.

Lee, D. K. and Choi, S. J., 2010 : Observation and numerical prediction of torrential rainfall over Korea caused by Typhoon Rusa (2002). *Journal of geophysical research*, **115**, D12105.

Lee, J. T., Ko, K. Y., Lee, D. I., You, C. H., and Liou, Y. C., 2018: Enhancement of orographic precipitation in Jeju Island during the passage of Typhoon Khanun (2012). *Atmospheric Research*, **201**, 58-71.

Lee, K.O., Shimizu, S., Maki, M., You, C.H., Uyeda, H., Lee, D.I., 2010: Enhancement mechanism of the 30 June 2006 precipitation system observed over the north-western slope of Mt Halla, Jeju Island, Korea. *Atmos. Res.*, **97**, 348-358.

Lilley, M., Lovejoy, S., Desaulnier-Soucy, N., and Schertzer, D. 2006: Multifractal large number of drops limit in rain. *J. Hydrology*, **328**, 20–37.

Lin, Y. L., Farley, R. D. and Orville H. D., 1983: Bulk parameterization of the snow field in a cloud model. *J. Climate Appl. Meteor.*, **22**, 1065–1092.

Liu, K. S. and Chan, J. C. L., 2018: Inter-decadal variability of the location of maximum intensity of category 4–5 typhoons and its implication on landfall intensity in East Asia. *International Journal of Climatology*, **39**, 1839-1852.

Louis, J.F., Tiedtke, M. and Geleyn, J.F., 1981: A short history of the operational PBL-parameterization at ECMWF, *Workshop on Planetary Boundary Layer Parameterization*, 25-27 Nov. 1981, 59-79.

Lovejoy, S. and Schertzer, D., 1990: Multifractals, universality classes and satellite and radar measurements of cloud and rain fields. *J. Geophys. Res.*, **95(D3)**, 2021–2034.

Lovejoy, S. and Schertzer, D., 1992: Multifractals and Rain. In *New Uncertainty Concepts in Hydrology and Water Resources*, Z. W. Kundzewicz, ed., 62–103, Cambridge UK. Cambridge University Press.

Lovejoy, S., 1982: Area-Perimeter relation for rain and cloud areas. *Science*, **216**, 185–187.

Lovejoy, S., Duncan, M. and Schertzer, D., 1996: Scalar multifractal radar observer's problem. *J. Geophys. Res.*, **101(D21)**, 26479–26492.

Macor, J., Schertzer, D. and Lovejoy S., 2007: Multifractal methods applied to rain forecast using radar data. *La Houille Blanche-Revue internationale de l'eau*, **4**, 92–98.

Mandelbrot, B. B., 1974: Intermittent turbulence in self-similar cascades: divergence of high moments and dimension of the carrier. *Journal of Fluid Mechanics*, **62(2)**, 331–358.

Marsan, D., Schertzer, D. and Lovejoy, S., 1996: Causal space-time multifractal processes: Predictability and forecasting of rainfields. *J. Geophys. Res.*, **101**, 26333-26346.

Meneveau, C. and Sreenivasan, K.R., 1991: The multifractal nature of turbulent energy dissipation. *J. Fluid Mech.* **224**, 429–84.

Moon, I. J. and Choi, E. S., 2011: A Definition and Criterion on Typhoons Approaching to the Korean Peninsula for the Objective Statistical Analysis. *Atmosphere. Korean Meteorological Society*, **21**, 45–55.

Murakami, M., 1990: Numerical Modeling of Dynamical and Microphysical Evolution of an Isolated Convective Cloud, *Journal of the Meteorological Society of Japan*. **68**, 107-128.

Murakami, R., Shigenaga, A., Kawano, E., Matsumoto, A., Yamaoka, I.,

Tanimura, T., 1994: Novel tissue units of regional differentiation in the gut epithelium of *Drosophila*, as revealed by P-element-mediated detection of enhancer. *Roux's Arch. Dev. Biol.* **203(5)**, 243-249.

Muzy J. F., Delour, J. and Baryc, E., 2000: Modelling fluctuations of financial time series: from cascade process to stochastic volatility model *Eur. Phys. J. B.*, **17**, 537-548.

Nogueira, M., Barros, A. P., 2015: Transient stochastic downscaling of quantitative precipitation estimates for hydrological applications. *J. Hydrol.*, **529 (3)**, 1407-1421.

Nykanen, D. K., 2008: Linkages between orographic forcing and the scaling properties of convective rainfall in mountainous regions. *J. Hydrometeorol.*, **9**, 327-347.

Paladin, G. and Vulpiani, A., 1987: Anomalous scaling laws in multifractal objects. *Phys. Rep.*, **156**, 147-225.

Parisi, G. and Frish, U., 1985: A multifractal model of intermittency. *Turbulence and predictability in geophysical fluid dynamics*, edited by: Ghill, M., Benzi, R., and Parisi, G., Elsevier North Holland, 84-88.

Park, D. S. R., Ho, C. H., Kim, J. H., and Kim, H. S., 2011: Strong landfall typhoons in Korea and Japan in a recent decade. *Journal of Geophysical research*, **116**, D07105.

Park, D.S., Ho, C.H., Kim, J.H. and Kim, H.S., 2011: Strong landfall typhoons in Korea and Japan in a recent decade. *Journal of Geophysical Research*, **116(D07)**, 105.

Park, J. K., Kim, B. S., Jung, W. S., Kim, E. B., and Lee, D. G., 2006: Change in Statistical Characteristics of Typhoon Affecting the Korean Peninsula. *Korean Meteorological Society*, **16**, 1-17.

Park, K. and Willinger, W., 2000: Self-similar network traffic and performance evaluation (1<sup>st</sup> ed.).

Park, S. K. and Lee, E. H., 2007: Synoptic features of orographically enhanced heavy rainfall on the east coast of Korea associated with Typhoon Rusa (2002). *Geophysical Research letters*, **34**, L02803.

Pecknold, S., Lovejoy, S. and Schertzer, D., 1996: The morphology and texture of anisotropic multifractals using generalized scale invariance. In *Stochastic Models in Geosystems*, W. A. Woyczyński and S. S. Molchanov, eds., 269–311, New-York. Springer-Verlag.

Pflug, K., Lovejoy, S. and Schertzer, D., 1992. Generalized Scale Invariance and differentially rotating cloud rariances. *Physica A*, **185**(1-4), 121–128.

Schertzer, D. and Lovejoy S., 1984b: On the dimension of atmospheric motions. *Turbulence and Chaotic phenomena in Fluids*, 505-512.

Schertzer, D. and Lovejoy, S., 1984a: Elliptical turbulence in the atmosphere. In *Symposium on Turbulent Shear Flows*, 4th, Karlsruhe, West Germany, P. 11.

Schertzer, D. and Lovejoy, S., 1987: Physical modeling and analysis of rain and clouds by anisotropic scaling and multiplicative processes. *J. Geophys. Res.*, **92**, 9693-9714.

Schertzer, D. and Lovejoy, S., 1989: Generalised scale invariance and multiplicative processes in the atmosphere. *Pure and applied Geophysics*. **130**,

57-81.

Schertzer, D. and Lovejoy, S., 1992: Hard and Soft Multifractal processes. *Physica A*, **185(1-4)**, 187–194.

Schertzer, D. and Lovejoy, S., 1997: Universal multifractals do exist!: Comments on “a statistical analysis of mesoscale rainfall as a random cascade”. *J. Appl. Meteorol.*, **36(9)**, 1296–1303.

Schertzer, D. and Lovejoy, S., 2004: Space-time Complexity and Multifractal Predictability. *Physica A*, **338(1-2)**, 173–186.

Schertzer, D. and Lovejoy, S., 2011: Multifractals, generalized scale invariance and complexity in geophysics. *International Journal of Bifurcation and Chaos*, **21(12)**, 3417–3456.

Schertzer, D. and Tchiguirinskaia, I., 2015: Multifractal vector fields and stochastic clifford algebra. *Chaos*, **25**, 123–127.

Schertzer, D., Bernardara, P., Biaou, A., Tchiguirinskaia, I., Lang, M., Sauquet, E., Bendjoudi, H., Hubert, P., Lovejoy, S., and Veysseire, J. M., 2007: Extremes and multifractals in hydrology : results, validation and prospects. *Houille Blanche*, **5**, 112–119.

Schertzer, D., Lovejoy, S. and Hubert, P., 2002a: An Introduction to Stochastic Multifractal Fields. In *ISFMA Symposium on Environmental Science and Engineering with related Mathematical Problems*, A. Ern and W. Liu, eds., **4**, 106–179, Beijing. High Education Press.

Schertzer, D., Tchiguirinskaia, I., Lovejoy, S. and Hubert, P., 2010: No monsters, no miracles: in nonlinear sciences hydrology is not an outlier!. *Hydrological Sciences Journal*, **55(6)**, 965–979.

Schertzer, D., Tchiguirinskaia, I., Lovejoy, S., Hubert, P. and Bendjoudi, H., 2002b: Which chaos in the rain-runoff process?. *J. Hydrological Sciences*, **47**(1), 139– 148.

Segami, A., Kurihara, K., Nakamura, H., Ueno M. and Takano, I., 1989: Description of Japan Spectral Model, *JMA/NPD Technical Reports*, №.25, Japan Meteor. Agency.

Seo, S. K., Kim, K. S., Chang, K. H., Lee, J. H., Kim, B. J., and Park, J. K., 2014: Multifractal intensity in dynamical behaviors of multifractals. *Journal of the Korean Physical Society*, **65**, 125–129.

Shimizu, S. and Maesaka, T., 2006: Multiple Doppler radar analysis using variational technique to retrieve three-dimensional wind field. *Technical Report* **70**, 1-8, National Research Institute for Earth Science and Disaster Prevention, Japan.

Shin, C.S. and Lee, T.Y., 2005: Development mechanisms for the heavy rainfalls of 6-7 August 2002 over the middle of the Korean Peninsula. *J. Meteorol. Soc. Jpn.*, **83**, 683-709.

Sun, J. and Lee, T.Y., 2002: A numerical study of an intense quasi-stationary convection band over the Korean peninsula. *J. Meteorol. Soc. Jpn.*, **80**, 1221-1245.

Tchiguirinskaia, I., Schertzer, D. and Lovjeoy S., 2014: Multifractals and Physically Based Estimates of Extreme Floods. *CEATI International Inc.*

Tchiguirinskaia, I., Schertzer, D. Hoang, C. T. and Lovejoy S., 2011: Multifractal study of three storms with different dynamics over the Paris region. In Weather Radar and Hydrology Symposium. Exeter, UK: IAHS Red book.

Tessier, Y., Lovejoy, S. and Schertzer, D., 1993: Universal Multifractals: theory and observations for rain and clouds. *J. Applied Meteorology*, **23**, 223-250.

Tsuboki, K. and Sakakibara, A., 2002: Large-scale parallel computing of Cloud Resolving Storm Simulator. High Performance Computing: Proceedings of the Fourth International Symposium on High Performance Computing, H. P. Zima et al., Eds., *Springer*, 243–259.

Tsuboki, K., 2004: High resolution modeling of multi-scale cloud and precipitation systems using a cloud resolving model. *Annual report of the Earth Simulator Center*, April 2003–March 2004, 21–26.

Tsuboki, K., Yoshioka, M. K., Shinoda, T., Kato, M., Kanada, S. and Kitoh, A., 2015: Future increase of supertyphoon intensity associated with climate change. *Geophys. Res. Lett.*, **42**, 646–652.

Tsujino, S., Tsuboki, K., and Kuo, H. C., 2017: Structure and Maintenance Mechanism of Long-Lived Concentric Eyewalls Associated with Simulated Typhoon Bolaven (2012), *Journal of the Atmospheric Sciences*, **74**, 3609-3634.

Tsujino, S., Tsuboki, K., and Kuo, H., 2017: Structure and Maintenance Mechanism of Long-lived Concentric Eyewalls Associated with Simulated Typhoon Bolaven (2012). *J. Atmos. Sci.*, **74**, 3609-3634.

Wang, C. C., 2015: The More Rain, the Better the Model Performs—The Dependency of Quantitative Precipitation Forecast Skill on Rainfall Amount for Typhoons in Taiwan. *Monthly Weather Review*, **143**, 1723-1748.

Wang, C. C., Kuo, H. C., Yeh, T.C., Chung, C. H., Chen, Y. H., Huang, S. Y., Wang, Y. W., and Liu, C. H., 2013: High-resolution quantitative precipitation forecasts and simulations by the Cloud-Resolving Storm Simulator (CReSS) for

Typhoon Morakot (2009). *Journal of Hydrology*, **506**, 26-41.

Wang, C., Huang, S., Chen, S., Chang, C. and Tsuboki, K., 2016: Cloud-Resolving Typhoon Rainfall Ensemble Forecasts for Taiwan with Large Domain and Extended Range through Time-Lagged Approach. *Wea. Forecasting*, **31**, 151–172.

Wolfensberger, D., Gires, A., Tchiguirinskaia, I., Schertzer, D., and Berne, A., 2017: Multifractal evaluation of simulated precipitation intensities from the COSMO NWP model, *Atmos. Chem. Phys.*, **17**, 14253-14273

Yoo, C. S. and Ku, J. M., 2017: Vertical Variation of Z-R Relationship at Hallasan Mountain during Typhoon Nakri in 2014. *Advances in Meteorology*, **2017**, 1927012.

Yu, X. and Lee, T.Y., 2010: Role of convective parameterization in simulations of a convection band at grey-zone resolutions. *Tellus*, **62A**, 617-632.

Yuk, J. H and Joh, M. S., 2019: Prediction of Typhoon-induced Storm Surge, Waves and Coastal Inundation in the Suyeong River Area, South Korea: A Case Study during Typhoon Chaba. *Journal of Coastal Research*, **91**, 156-160.

## Appendix A

### The Comparison between radar and model dataset for the case of Bolaven.

The paper “Multifractal Analysis of rainfall rate datasets obtained by radar and numerical model: the case study of Typhoon Bolaven (2012)” is in the press of publishing in Journal of applied meteorology and climatology (American Meteorological Society).

#### **Multifractal Analysis of rainfall rate datasets obtained by radar and numerical model: the case study of Typhoon Bolaven (2012)**

J. Lee<sup>\*1,2</sup>, I. Paz<sup>1,3</sup>, D. Schertzer<sup>1</sup>, D.I. Lee<sup>2</sup> and I. Tchiguirinskaia<sup>1</sup>

<sup>1</sup>HM&Co, Ecole Nationale des Ponts et Chaussées, 6-8, avenue Blaise Pascal, Cité Descartes, 77455 MARNE-LA-VALLEE Cedex, France

<sup>2</sup>Department of Environmental Atmospheric Sciences, Pukyong National University, 45, Yongso-ro, Nam-gu, Busan, Republic of Korea

<sup>3</sup>Instituto Militar de Engenharia, Praça General Tibúrcio, 80, Praia Vermelha, Urca, Rio de Janeiro, RJ, 22290-270, Brazil

*Correspondence to:* Dong In Lee (leedi@pknu.ac.kr)

**Abstract.** Typhoon Bolaven caused significant damage with severe rainfall all over Korea, including Jeju island which received more than 250 mm in 2 days in August 2012. It was regarded as the most powerful storm to strike the Korean Peninsula in nearly a decade. The rainfall rate datasets were obtained from S-band radar operated by KMA (Korea Meteorological Administration) to be analyzed and compared with the mesoscale Cloud Resolving Storm Simulator (CReSS) model simulation. The multifractal analysis was conducted to understand the structure of the rainfall rate with height in the typhoon system. The Radar rainfall data presented with strong intermittency across scales at lower altitudes (1 km and 2 km) and a more homogeneous rainfall field at high altitude (5 km) with two parameters (fractal codimension and multifractality index). The statistical scaling moment function and maximal singularities show clear significant differences between radar and CReSS model.

## 1 Introduction

Multifractals represent a framework for the analysis and simulation of geophysical fields, such as rainfall, over the wide range of spatio-temporal scales. It was found and introduced in the eighties following discussions on the scale invariance properties of the geophysical field (Schertzer and Lovejoy, 2011). Multifractals are based on the assumption of the rainfall generated by a multiplicative cascade process, and it distributes the intensity structures from large to small scales. For many years, multifractal tools have been commonly used for studying rainfall fields as well as geophysical fields over a wide range of scales (Schertzer and Lovejoy, 1987; Gupta and Waymire, 1993; Harris et al., 1996; Marsan et al., 1996; De Lima and Grasman, 1999; Deidda, 2000; Biaou, 2004; Macor et al., 2007; De Montera et al., 2009; Tchiguirinskaia et al., 2011; Gires et al., 2013; Hoang et al., 2014; and etc.). The concept of multifractal analysis is scale-invariant. It uses the way of dividing structures and the random multiplicative increments in probability distribution are the same at each step of the cascade process which is more fitted to rainfall fields than an ad hoc statistical tool since it is physically based on the agreement of the scale invariance properties of the Navier-Stokes equation. It can govern the atmospheric behavior and is assumed to be transmitted to the unknown equations for rainfall processes. By Ordanovich and Chigirinskaya, (1993), it was pointed out that inhomogeneity plays a significant role by increasing the stability of the structures such as typhoons. Also, Chigirinskaya et al., (1994) indicated that the most straightforward framework for considering the extreme nonlinear variability over a wide range of scales is multifractals, and it is a result of an elementary scale-invariant process when the generator of the field reproduces itself from scale to scale.

Furthermore, multifractals are understood as the tool which provides the natural framework for scale-invariant nonlinear dynamics (Tessier et al., 1993) and has become somewhat a standard tool to analyze and simulate meteorological and hydrological data, especially radar data that have the rare advantage of providing space-time (3D+1) fields. A unified multifractal model of atmospheric dynamics was developed by Schertzer and Lovejoy (1983, 1985) and Lovejoy et al. (1993).

Despite the capacity of dealing with extreme multiscale phenomena with the high-quality data, there have been few multifractal studies of typhoons since Chygrynskaia et al. (1994) and Lazarev et al. (1994). These studies relied on time series data obtained from 1D aircraft or balloon trajectories without any radar data. Therefore, to see the detailed structure of rainfall rate with height in the typhoon, the multifractal framework was applied in this study by using radar.

Additionally, with the selected case typhoon Bolaven, most of the studies were focused on the Fujiwhara effect between Bolaven and Tembin. Although, the typhoon itself caused much damage and the scale was large, very few case studies were conducted with different observation equipment such as rain gauges, satellite, radar, etc. Also, the different model simulations were performed to investigate the structure and the characteristics of the typhoon, but the studies were focused on the prediction of the track of the typhoon directions or the intensities. Figure 1 shows the track of the typhoon and the accumulated rainfall amount.

Looking at previous studies about Typhoon Bolaven, Origuchi et al. (2013) explained that updrafts of middle eyewall were stronger than those of other eyewalls, and the middle eyewall had abundant water substances below 6 km AGL (above ground level) in cloud-resolving

ensemble model experiments. The regions of the strong tangential velocity existed at the outer edges of the eyewalls. Though the outer eyewall was not compared with the central eyewall, it had a similar structure. Downdrafts existed between the eyewalls. Although the updrafts and the liquid water substances in the lower layer appeared at the radius 10km, the formation of the most inner eyewall was insufficient by the simulation of JMA (Japan Meteorological Agency) non-hydrostatic model (JMANHM). Ryu and Lee (2012) showed the reliability of the radar rainfall rate dataset obtained by the Korea Meteorological Administration (KMA) during this event by comparing with the satellite Chullian dataset. Also, Liu et al. (2015) presented a framework of Fujiwhara effect between Typhoon Bolaven and Tembin by using remote sensing imagery and image processing techniques which explains how Bolaven was intensified and changed its direction by the impact of combined interactions. Sun et al. (2015) mentioned the torrential rain during the Bolaven was caused by increased cyclonic vorticity. The warm-moist air mass from the southeast of the rainfall area caused the strong ascending motion upward while the conditional symmetric instability was the important instability mechanism for the torrential rain enhancement.

There are several references describing the development mechanisms and the structure of the convection bands causing the heavy rainfall over Korea based on case studies and numerical modelling (Sun and Lee, 2002; Shin and Lee, 2005; Cho and Lee, 2006; Hong and Lee, 2009; Yu and Lee, 2010; Choi et al., 2011). By performing the high-resolution numerical experiment for typhoon Bolaven, the maintenance mechanism of long-lived concentric eyewall is explained by the lack of dissipation of the inner eyewall and the constancy of the large radius of the outer eyewall (Tsujino et al., 2017). Generally, these modeling studies demonstrated some significant discrepancies between the simulation and observation in both the location and amount of heavy rainfall. However, the Cloud Resolving Storm Simulator (CReSS) relatively well captures the location and intensity of the maximum rainfall. Lee et al. (2010) have applied CReSS in experiments of multi-scale cloud and precipitation systems to simulate topographically induced localized intense rainfall over Jeju Island, Korea. Therefore, the CReSS model was chosen for our selected case study of Typhoon Bolaven rainfall on Jeju Island.

This study was motivated by the fact that not only there are not enough studies focused on Bolaven alone, but also no research was carried out with the approach of explaining the nonlinearity of the scaling exponents of the rainfall structure by performing a multifractal analysis of the typhoon Bolaven. To jointly understand the dynamics and rainfall by multifractal space-time analysis, the Doppler S-band radars and mesoscale simulation CReSS model are compared during the typhoon Bolaven. In the following sections, a detailed description of the three-dimensional structure of Bolaven during the landfall in Jeju Island measured by different observation instruments and the procedure of preparing the dataset of rainfall rate is presented. We introduce the data in section 2, and the analysis methodology is described in section 3. The results of the multifractal analysis performed on radar data and CReSS model simulation are discussed in section 4 including a comparison between the radar data and the model simulation. Lastly, the summary and conclusion of the results are in section 5.

## 2 Data

Typhoon Bolaven was formed as a tropical depression on 19 August 2012 and steadily intensified to a typhoon by 21 August. On 24 August, the system attained its peak intensity with a wind speed of  $51.4 \text{ ms}^{-1}$  (115 mph) and a barometric pressure of 910 hPa. The storm passed over Okinawa on 26 August and it began accelerating toward the north phasing into the weakening stage. As Typhoon Bolaven approached the Korean Peninsula, it continued to

weaken and eventually made landfall in North Korea late on 28 August before transitioning into an extratropical cyclone. Even though Typhoon Bolaven was in its weakening stage, it was an extremely powerful typhoon that caused a lot of damage with severe rainfall all over Korea including Jeju Island. The rainfall amount was more than 250 mm in two days. It was regarded as the most powerful storm to strike the Korean Peninsula in nearly a decade.

Information on the typhoon location and its lowest pressure was recorded by the National Typhoon Center in Jeju Island. Fig. 1(a) shows the track of the typhoon and its center is indicated by red dots. Also, surface station data were collected by 22 sites in Jeju Island. Fig. 1(b) shows the daily accumulated rainfall on 27 August. This data was collected by an automatic weather system (AWS) operated by the KMA. The maximum accumulated rainfall amount was detected in the middle of Jeju Island where the mountain Halla (1,950 m above sea level) is located.

The radar dataset was obtained from 06:00–23:50 LST on 27 August 2012 when the typhoon approached Jeju Island. The selected radar site was Gosan in Jeju Island operated by the KMA and covering a radius of 360 km. It recorded volume scans of reflectivity and Doppler velocity every 10 min. The data were interpolated in a Cartesian coordinate system with 1-km-horizontal and 0.25-km-vertical grid intervals (CAPPI), and the three Cartesian components of reflectivity were calculated. Fig. 2 shows the wind field superimposed on the radar reflectivity (dBZ) at an altitude of 5 km on the left of the figure. The location of the Gosan radar is shown as the red star with a white circle in the middle of the figure. The vertical cross-section of the red line on the left of the figure is shown on the right of the figure. Updrafts and downdrafts are clearly shown in the vertical cross-section. However, there were missing radar data that were obtained as zero values at the lowest altitudes due to the minimum radar beam elevation angle of 0.5 degrees. The multifractal analysis was performed on the same area of 256 km × 256 km at various altitudes. Further analysis was performed to cover the limitations of the missing data with a smaller domain that was 64 km × 64 km. Then, the rainfall rate was computed at separate altitudes using the reflectivity of the Gosan radar, which is one of the three radars, by using the Z-R relationship ( $Z = aR^b$ , radar reflectivity factor  $Z_{(mm^6 m^{-3})}$ , rain rate  $R_{(mm h^{-1})}$ ) with the values of  $a = 250$  and  $b = 1.2$ , which are the parameters usually used for tropical convective systems.

The numerical simulation model CReSS is a three-dimensional non-hydrostatic model developed by the Hydropheric Atmospheric Research Center (HyARC) of Nagoya University, Japan (Tsuboki and Sakakibara, 2002). The initial and lateral boundary conditions were provided by the Japan Meteorological Agency Global Spectral model (JMA-GSM), which is a Grid-Point-Values (GPV) database reanalysis data. It has one of the highest horizontal resolutions of 0.1875 degrees (approximately 20 km) with a time interval of six hours. The JMA-GSM is often used for deep convection simulations, such as typhoon cases, since it produces data up to 10 hPa, which contains information on the lower stratosphere and can detect the effect of significant gravity wave propagation in the upper-levels of the atmosphere.

Also, to set the surface fluxes of momentum and energy and surface radiation processes, the sea surface temperature (SST) was calculated by using a one-dimensional, vertical heat diffusion equation (Kondo, 1976; Louis et al., 1981; Segami et al., 1989) that included an underground layer for ground temperature prediction. The SST at the initial time was calculated from the dataset of the NEAR-GOOS Regional Real-Time Data Base, which was provided by the JMA. The land-use data was obtained from the dataset of the Global Land Cover Characteristics Data Base, which was provided by the U.S. Geological Survey.

For the simulation, the horizontal grid resolution was 1 km × 1 km with a mesh size of 936 × 1248 and the vertical grid resolution of 0.25 km contained 70 levels, ranging from a near-surface

level at 50 m to the top level at 17.3 km. The vertical calculation was performed with a terrain-following coordinate as the terrain effect was also considered during the calculation, and the rainfall rate parameter was the instantaneous rainfall rate, which was obtained as one of the output parameters. It was calculated with the equation  $\rho V_t = (\frac{dq_l}{dz})$ . The duration of each time step was 10 min, similar to that of the radar data. The high range of the altitudes selected was due to the inclusion of the frozen precipitation at high altitudes since the scale of the typhoon was very large. A general rainfall field analysis with CReSS model data is shown in Appendix A. However, in the main manuscript, to compare the results obtained with the results of the multifractal analysis of the radar data, the same size of domains with mesh sizes of  $256 \times 256$  and  $64 \times 64$  covering the radar observation sites were selected.

### 3 Methodology

Multifractal tools are commonly used for studying rainfall fields and generalizations of fractal geometry. If the rainfall suits the fractality (Lovejoy and Mandelbrot, 1985; Olsson et al., 1993), the number  $N_\lambda$  of non-zero rainfall rates at resolution  $\lambda$  ( $\lambda = L/\ell$ ,  $L$  is the outer scale of the phenomenon and  $\ell$  is the observation scale) can be described in a scale-invariant notion as:

$$N_\lambda \approx \lambda^{D_F} \quad (1)$$

where  $D_F$  is the fractal dimension that characterizes how much space a geometrical set occupies. Fig. 3 shows the fractal dimensions of radar and CReSS simulations that were analyzed with the thresholds of 1, 5, and 10 mm/h at an altitude of 5 km to see the sparseness in the rainfall fields over the observation area with two different sizes of the domain. As it is shown in all datasets in both domain sizes, the values of the fractal dimension decrease as depicted by the slope of each graph, while the threshold values increase. Each graph shows a different fractal dimension depending on the thresholds, and when we see them in detail all the lines show linear fitting ( $R^2 > 0.9$  for all black, blue, and red lines). Also, the black and white figures show the rainfall occurrences changing with the different thresholds more visibly. The existence of rain is indicated in black.

In the multifractal framework,  $D_F$  is strongly dependent on the threshold defining the occurrence of rainfall. This shows that more than one fractal dimension is needed to characterize the rainfall field (Gires et al., 2013). Therefore, given a multifractal field  $\varepsilon_\lambda$  at a resolution  $\lambda$ , the probability of obtaining a singularity of order greater than or equal to  $\gamma$  is (Schertzer and Lovejoy, 1987):

$$\Pr(\varepsilon_\lambda \geq \lambda^\gamma) \approx \lambda^{-c(\gamma)} \quad (2)$$

where  $c(\gamma) = D - D_F(\gamma)$  is the codimension function and  $D$  is the dimension of the embedding space.

Also, multifractal fields can be described by their statistical moments of order  $q$ , following a power-law given by:

$$\langle \varepsilon_\lambda^q \rangle \approx \lambda^{K(q)} \quad (3)$$

$K(q)$  is the scaling moment function that characterizes the scaling variability of the process studied.

Furthermore, Parisi and Frisch (1985) indicated that the two functions  $c(\gamma)$  and  $K(q)$  have a one-to-one relationship by applying the Legendre transform:

$$K(q) = \max_{\gamma} \{q\gamma - c(\gamma)\} \leftrightarrow c(\gamma) = \max_q \{q\gamma - K(q)\} \quad (4)$$

These show the correspondence between the orders of moments and the singularities that can also be considered as evidence of the correspondence between high values of multifractal parameters and extreme events.

In the framework of universal multifractals (UM) (Schertzer and Lovejoy, 1987; Lovejoy and Schertzer, 2007; Schertzer and Lovejoy, 2011), the field can be described by only two “UM parameters” ( $\alpha$  and  $C_1$ ) when the field is conservative:

$$c(\gamma) = \begin{cases} C_1 \left( \frac{\gamma}{C_1 \alpha'} + \frac{1}{\alpha} \right)^{\alpha'}, & \alpha \neq 1 \\ C_1 e^{\frac{(\gamma-1)}{C_1}}, & \alpha = 1 \end{cases} \quad (5)$$

$$K(q) = \begin{cases} \frac{C_1}{\alpha-1} (q^\alpha - q), & \alpha \neq 1 \\ C_1 q \log(q), & \alpha = 1 \end{cases} \quad (6)$$

where  $\alpha$  is the Levy index and measures how fast the intermittency evolves when considering singularities that are slightly different from the average field singularity,  $C_1$  is the codimension of the singularity of the average field and can measure its concentration, and  $\alpha' = \frac{\alpha}{\alpha-1}$ .

In order to validate UM, the theoretical  $K(q)$  function should be compared with the one obtained from the observation, which is called the empirical  $K(q)$ . However, the theoretical  $K(q)$  can simulate the empirical one only up to a certain critical value of moment order. This critical value is related to what is called a multifractal phase transition (Schertzer et al. 1992). It is estimated as  $q_c = \min(q_s, q_D)$ , where  $q_s$  is the maximum-order moment estimated by a finite number of samples and  $q_D$  is the critical moment order of divergence.

The value of  $q_s$  is related to the maximal observable singularity  $\gamma_s$  using a Legendre transform, and it can be determined using the following equation:

$$q_s = \left( \frac{D+D_s}{C_1} \right)^{1/\alpha} \quad (7)$$

For example, in a 1-dimensional field ( $D = 1$  where  $D$  is the dimensional field) with only one data sample available ( $N_{sample} = 1$ , thus  $D_s = 0$  where  $D_s$  is the dimensional field with the number of samples), the critical value of moment order is usually  $q_c = q_s$ . This shows a linear behavior of the empirical  $K(q)$  for  $q \geq q_s$ .

Whereas, the moment order  $q_D$  represents the critical value of  $q$  for which extreme values of the field are becoming so dominant that the average statistical moment of order  $q \geq q_D$  approaches infinity:

$$\langle \varepsilon_\lambda^q \rangle = \infty, \quad q \geq q_D \quad (8)$$

The moment order  $q_D$  can be determined from the following equation:

$$K(q_D) = (q_D - 1)D \quad (9)$$

Determining the value of  $q_D$  can be graphically explained as the intersection between the theoretical  $K(q)$  function and the linear regression  $K(q) = (q-1)D$  that corresponds to the theoretical  $K(q)$  with  $C_1 = D$  and  $\alpha = 0$ . Therefore, when  $q_c = q_D$ , the empirical  $K(q)$  function starts approaching infinity for  $q \geq q_D$ .

Firstly, a spectral analysis was performed in order to identify the occurring physical processes, such as checking the scaling behavior of the data. A scaling field shows a power-law relationship between the power spectra  $E$  and the wave number  $\omega$  or frequency  $f$ :

$$E(f) = f^{-\beta} \quad (10)$$

where  $-\beta$  is the slope of the straight line that appears in the log-log plot of Eq. (10).

According to Tessier et al. (1993), if the spectrum behavior is linear with a spectral slope  $-\beta$ , the spectral exponent is linked to the degree of non-conservation  $H$  of the field:

$$\beta = 1 + 2H - K(2) \quad (11)$$

where  $H$  is the Hurst exponent and is 0 for a conservative field, and  $K(2)$  is the second-moment scaling function of the conservative part of the field. For a conservative field, the estimate of  $\beta$  is lower than the dimension  $D$  of the embedding space. From Nykanen (2008), if  $\beta > D$ , the field should be fractionally differentiated before implementing a multifractal analysis.

Once the scaling behavior and conservativeness of the rainfall field have been obtained, a multifractal analysis can be performed. Two different methods, which are widely used in geophysics, can be used to assess the UM parameters indirectly and directly: the Trace Moment (TM) (Schertzer and Lovejoy, 1987) and the Double Trace Moment (DTM) (Lavallée et al., 1993) methods, respectively.

The TM method is performed on a broad range of moments  $q$  to determine the scaling moment function  $K(q)$ , as shown in Eq. (3). It consists of taking the  $q^{th}$ -power of a multifractal field  $\varepsilon_\lambda$  at the highest resolution  $\lambda$  to repeatedly calculate the ensemble average at different scales and to represent the resulting averages  $\langle \varepsilon_\lambda^q \rangle$  in a log-log plot as a function of  $\lambda$ . Then, following Eq. (3), the slopes of the linear regressions give the values of  $K(q)$  for each  $q$ . Finally, using Eq. (6), the UM parameters can be estimated by:

$$C_1 = K'(q) \quad (12)$$

$$\alpha = K''(q)/C_1 \quad (13)$$

where  $K'(q)$  and  $K''(q)$  are the first and second derivatives of  $K(q)$ , respectively.

The DTM method was specifically developed in the framework of UM and is conducted to obtain more robust estimates of  $\alpha$  and  $C_1$  (Lavallée et al., 1993). It is a more reliable way of estimating UM parameters than the TM method. This technique is based on two steps. The first is to take the  $\eta^{th}$ -power of the conservative field  $\varepsilon_\lambda$  at the highest resolution  $\lambda$  and to normalize it:

$$\varepsilon_\lambda^{(\eta)} = \frac{\varepsilon_\lambda^\eta}{\langle \varepsilon_\lambda^\eta \rangle} \quad (14)$$

Then, the TM method is applied to the normalized field  $\varepsilon_\lambda^{(\eta)}$  to obtain the scaling moment function  $K(q, \eta)$  for each  $\eta$  value:

$$\langle (\varepsilon_\lambda^{(\eta)})^q \rangle \approx \lambda^{K(q, \eta)} \quad (15)$$

From Eq. (6) and Eq. (15):

$$K(q, \eta) = \eta^\alpha K(q) \quad (16)$$

Therefore, for a given  $q$  value,  $K(q, \eta)$  is plotted against  $\eta$  in a log-log plot and the slope of the curve gives an estimation of  $\alpha$ .  $C_1$  can also be estimated from the interception of the slope and the axis  $\log(\eta) = 0$ .

#### 4 Results

The multifractal analysis was conducted on the rainfall rate at three different altitudes (1 km, 2 km, and 5 km) retrieved from the radar data and from the CReSS model.

##### 4.1 Multifractal analysis on Radar data

The spectral and multifractal (TM and DTM) analyses were applied to the time ensemble average over the full rainfall event by considering each time step as an independent realization). For the analysis, two different sizes of domains were selected,  $256 \times 256$  and  $64 \times 64$ , because of the missing radar data at the lowest altitudes due to the minimum radar beam elevation angle of 0.5 degrees.

First of all, Fig. 4 shows the result of the spectral ( $\ln(E(k)) - \ln(k)$ ) analysis of rainfall rates at different altitudes that were retrieved from radar data of the larger domain ( $256 \times 256$ ). Table 1 shows all the values of the spectral exponent  $\beta$  and  $R^2$ . In this case,  $\beta$  varies from 1.61 to 2.64, while  $R^2$  is always close to 1 (it varies between 0.96 and 0.98), which shows no extreme scaling break. The graph shows that the scaling behaviors of the altitudes of 1 km and 2 km between  $\ln(k \geq 1)$  and  $\ln(k \leq 1.8)$  are not as linear as that of the altitude of 5 km. The TM analyses for the three altitudes with radar are presented in Fig. 5. On the left, the log-log plots of  $\langle \varepsilon_\lambda^q \rangle \approx \lambda^{K(q)}$  with the resolution  $\lambda$  (in this case, it is set from 1 to 256 increasing by powers of 2) and values of  $q$  that were freely chosen between 0.1 and 7.0. A scaling behavior was shown up to when  $q = 4.5$  at all altitudes. In Fig. 5(d, e, f), the estimated (or empirical) scaling moment functions  $K(q)$  (in black) are compared to the semi-theoretical functions that are the curves with the UM parameters  $\alpha$  and  $C_1$  retrieved from TM (red) and DTM (green) analyses. The empirical  $K(q)$  curves are relatively fitting with the semi-theoretical ones obtained by the TM method, where  $q = 0.5-2$  at every altitude, and with the semi-theoretical curves obtained by the DTM method, where  $q = 0.5-3$ . For  $q < 0.5$ , the altitudes of 1 km and 2 km present a more similar tendency between the two functions than the altitude of 5 km. However, for  $q > 3.0$ , the semi-theoretical function is more divergent from the empirical one at an altitude of 5 km than those at 1 km and 2 km. Moreover,  $q = 3.0$  can be considered as a multifractal phase transition point, as predicted by Mandelbrot (1974). This is caused mainly by one of two reasons: spatial integration or finite sample size (Schertzer and Lovejoy, 1987). A DTM analysis was performed and the result is shown in Fig. 6. A clear scaling behavior as depicted in Fig. 6(a, b, c) was retrieved, along with the result of the TM analysis. For each power  $\eta$ , with a fixed value of  $q$  ( $q = 1.5$ ), the slope of the linear regression gives an estimation of the scaling moment functions  $K(q, \eta)$ . Fig. 6(d, e, f) with S-shape curves are conditioned by the appearance of numerical limitations at smaller moments and the critical behavior of extremes at higher statistical moments. Both are characterized by the flattening of the DTM curves. The slope of the curve gives an estimation of  $\alpha$  and  $C_1$ . The value of  $\alpha$  increases with altitude while the value of  $C_1$  decreases, showing how concentrated the field is and how quickly the intermittency evolved. The values of  $\alpha$  ( $\alpha = 0.858, 1.072$ ) are close to 1 and the values of  $C_1$  ( $C_1 = 0.349, 0.255$ ) are higher at altitudes of 1 km and 2 km than at 5 km, which means they are sparse with high singularities (Biaou, 2004). On the contrary, at 5 km ( $\alpha = 1.421, C_1 =$

0.114),  $\alpha$  is larger and  $C_1$  is smaller than at 1 and 2 km, which means smaller singularities and a more homogeneous rainfall field.

As mentioned before, due to missing radar data at the lowest altitudes, the smaller domain was selected ( $64 \times 64$ ). This zero field bias results in a spurious estimation of the mean intermittency ( $C_1$ ) that decreases at higher altitudes when multifractality index estimates evolve in contrast. The results of spectral analysis at each altitude are shown in Fig. 7. The value of the spectral exponent  $\beta$  varies from 2.67 to 2.97,  $R^2$  is approximately 0.97 at lower altitudes but almost 1 at an altitude of 5 km (see Table 1). Regardless of the domain sizes, the graph shows that the rainfall field is the most conservative at 5 km. Fig. 8 shows the result of the TM analysis in the smaller domain. The  $q$  values selected were the same as those in the previous TM analysis (from 0.1 to 7.0). Each of the graphs shows the empirical (black)  $K(q)$  and semi-theoretical  $K(q)$  of the TM (red) and DTM (green) analyses. As  $\langle \varepsilon_\lambda^q \rangle \approx \lambda^{K(q)}$  approaches infinity as  $q \geq q_D$  and a finite value as  $q < q_D$  in Eq. (8), the moment order  $\langle \varepsilon_\lambda^q \rangle$  converges at the region  $q < q_D$ . From Fig. 8(e) it is observed that unlike the results from the larger domain, the empirical  $K(q)$  as a function of  $q$  has a smaller value than both the theoretical  $K(q)$  for the TM and DTM analyses, which means that the value of  $\alpha$  does not increase dramatically after  $q = 3$ , as in the larger domain. However, at 5 km, the empirical  $K(q)$  is better fitted than the semi-theoretical  $K(q)$  of the DTM analysis. Each value of the multifractality index from the different domains with the TM and DTM analyses are indicated in Table 2.

#### 4. 2 Multifractal analysis on CReSS model

The multifractal analysis of the CReSS model data was applied to the domain of the radar coverage with sizes of  $256 \times 256$  and  $64 \times 64$  (Figs. 10–12). The procedure was the same as the radar dataset, and the values of the result are also indicated in Table 2. More results of the multifractal analysis on the CReSS model simulation data in a larger domain ( $512 \times 512$ ) are described separately in App. A.

#### 4. 3 Comparison between radar data and CReSS

From the results of the TM and DTM analyses, the difference of the estimated  $\alpha$  values for the domain  $256 \times 256$  was obtained as 0.4, while it was 0.003 for the estimated  $C_1$  values, whereas for the domain  $64 \times 64$  the difference was 0.3 for  $\alpha$  and 0.003 for the estimated  $C_1$ . This shows that both domains present different degrees of multifractality and similar intermittencies of average intensity. Comparing the results of the estimated  $\alpha$  values from the DTM analysis, with the domain size of  $256 \times 256$  and an altitude of 5 km for the radar ( $\alpha = 1.421$ ), it fits considerably well with the DR for the CReSS model ( $\alpha = 1.416$ ). Also, regarding Eq. (6), if the  $\alpha$  values are considerably similar for two  $K(q)$  functions, these functions would be different from each other only by a ratio of  $C_1$  values, which would be, in this case,  $0.105/0.114 = 0.921$ . For the domain size of  $64 \times 64$ , the estimated  $\alpha$  value at an altitude of 5 km for the radar ( $\alpha = 1.356$ ) is smaller than the DR for the CReSS model ( $\alpha = 1.817$ ). However, the ratio of  $C_1$  values is  $0.092/0.089 = 1.034$ . This supports the fact that it fits better at an altitude of 5 km (the ratio of  $C_1$  values at 1 km = 0.301 and 2 km = 0.412 with the domain size of  $256 \times 256$ , and the ratio of  $C_1$  values at 1 km = 0.472 and 2 km = 0.532 with the domain size of  $64 \times 64$ ).

In order to obtain a more detailed comparison of linearity between the radar data and CReSS data, Fig. 13 compares each  $K(q)$  of the radar data at each altitude and  $K(q)$  of the CReSS model

data (Fig. 13(a, b, c) with the domain size of  $256 \times 256$  and Fig. 13(d, e, f) with the domain size of  $64 \times 64$ ). This comparison of ( $q$ ) functions shows that the consistency between the two different datasets is best at 5 km, because the curvature of blue dots at 5 km aligns straighter than at 1 km and 2 km, where there is a difference not only with  $C_1$  (departure from the bisectrix) but also with  $\alpha$  (presence of a curvature; departure from the linear regression fit).  $C_1$  describes the sparseness of the mean value of the field (mean intermittency) and  $\alpha$  describes how much it varies as it goes away from the mean value of the field (variability of intermittency). The sets of graphs on both domains demonstrate that departures from the bisectrix and linear regression fit diminish with increasing altitude.

$q_s$  and  $\gamma_s$  were calculated to see the maximal singularities, and they are illustrated in Fig. 14. It shows the tendency of each multifractality index and the consistency of the maximal singularity. It clearly shows that there is a decrease of the  $\alpha$  values from the TM analysis when comparing the two domains,  $256 \times 256$  and  $64 \times 64$ . It is due to the zero field at low altitudes. Although, the  $\gamma_s$  from the DTM analysis remains rather close with the same order between the two domains. TM and DTM were the independent method but with the same tendency that there is a decrease of  $\gamma_s$  at the higher altitude for the radar. Also, to see the difference in detail, the absolute values of difference of singularity  $\gamma_s$  were taken and respectively divided by  $C_1$  of the radar and CReSS (see Fig. 15). This demonstrates that the difference in singularities from the TM analysis with the  $64 \times 64$  domain is more than 1.5 times larger than the mean singularity. Fig. 15(b) shows that only the  $256 \times 256$  domain at an altitude of 5 km has a relatively similar result when the other values are much more than 1, which means the difference of singularities has become too strong.

## 5 Summary and Conclusion

Mesoscale observation data of Typhoon Bolaven were collected in Jeju Island, Korea as the strongest typhoon in a decade made landfall. An S-band radar recorded volume scans of reflectivity and Doppler velocity every 10 minutes and have been compared with CReSS model simulations. Detailed observational datasets from typhoons are rarely available for conducting multifractal analysis, and for the first time, a comparison of radar volume data and model simulations was performed. Despite the different analysis limitations, there is consistency in the multifractal intermittency.

For multifractal analysis, firstly, spectral analysis was performed to see the scaling behavior of the rainfall field. Then, TM and DTM analyses were performed in each case. From the results, regardless of the size of the domains, it is clear that there is a relatively good agreement of multifractality between radar at 5 km and CReSS in both domains ( $64 \times 64$  and  $256 \times 256$ ), but not at lower altitudes. This may be because many case studies of tropical cyclones have been performed at high altitude, e.g., 5 km, and used to tune the models, despite the possible presence of the bright band at these altitudes. To investigate this issue, the maximal singularities were compared between the radar and CReSS data. A comparison of the difference between singularities shows that maximal singularity tends to decrease at higher measurement altitude. These significant differences in singularities between the radar and CReSS show that the model simulates a much smoother field compared to the radar measurements at low altitudes.

This study is valuable as it was the first time a multifractal approach was applied to a large dataset for a typhoon case study. The multifractal parameters capture the vertical structure of the rainfall field in a typhoon in a simple way. Comparison of these parameters shows that the rainfall field obtained from a numerical model does not capture the detailed rainfall structure at

different altitudes. With model rainfall estimates at all levels, this technique could be applied to further compare model and observation rainfall structure to help define the range of applicability of model rainfall.

### Acknowledgment

We acknowledge financial support from the Chair “Hydrology for Resilient Cities” of Ecole des Ponts, endowed by Veolia.

This work is also supported by PHC STAR 2018 program in the framework of project 41606PG.

This research was supported by the International Cooperation Program of the National Research Foundation of Korea(NRF) funded by the Ministry of Science and ICT (Grant number: 2018K1A3A1A21044390)

## Appendix A

### Multifractal analysis of CReSS model simulation

For the multifractal analysis, the different domains were selected, and it is shown in figure A1. Similar to the radar data, in order to first identify the scaling behavior of the rainfall rate on CReSS model, spectral analysis was performed, as shown in Fig. A2 (a, f). In general, the analyses among D1 and D2 show the fact that as the rainfall rate is the average of all the levels of altitude, scaling behavior is more stable than when the analysis was performed separately on each altitude of radar data. The approximate values of  $\beta$  and  $R^2$  for D1 and D2 are, respectively,  $\beta=1.19$  and  $R^2=0.96$ ,  $\beta=1.39$  and  $R^2=0.98$ , with no apparent scaling break for both of the domains.

Afterward, TM analyses were also conducted with CReSS model for the three domains studied. On the left side of Fig. A2 (b, c, g, h), the scale invariance can be observed, with the resolution ranging from 1 to 512 for D1 and D2. The values of  $q$  are also freely set from 0.1 to 7 where the single scaling behaviors, with the imperfect but acceptable straight lines, are retrieved for all domains. On the right side of Fig. 14, the comparisons between empirical  $K(q)$  and semi-theoretical  $K(q)$  from TM and DTM are well-paired from  $q=0.5$  to  $q=2.5$  on both domains. The latter would be, therefore, the point of multifractal phase transition for the CReSS model data. Lastly, DTM analyses were performed also with CReSS model and, the graphs are shown in Fig. A2 (d, e, i, j). For each power  $\eta$ , the value of  $q$  was fixed to 1.5 as well as when analyzing radar data. Each  $\alpha$  and  $C_1$  retrieved from DTM analysis is indicated in Table A1. The  $\alpha$  values for both of the domains are not so different from each other which means the high singularities. The  $C_1$  values reflect the distribution of the rainfall. Thus, D1 is where the accumulated rainfall was distributed generally (lowest  $C_1$ ) while D2 has concentratedly high accumulated rainfall (highest  $C_1$ ).

Fig. A3 shows the  $\gamma_s$  of CReSS simulation depending on the size of the domain. The  $\alpha$  from TM and DTM analyses are decreasing along with the size of the domain when  $C_1$  is increasing. On the contrary, for the scales of 64 and 256, the estimate remains within the estimates of 512 for D2 domains. It also indicates that the bigger domain gives the estimates which are depending

on the position where it includes other estimations.

## References

- Biaou, A., 2004: De la méso-échelle à la micro-échelle: Désagrégationspatio-temporellemultifractale des précipitations. PhD thesis, Paris, ENMP.
- Chigirinskaya, Y., Schertzer, D., Lovejoy, S., Lazarev, A., and Ordanovich, A., 1994: Multifractal Analysis of Tropical Turbulence, part I: horizontal scaling and self-organized criticality, *Nonlinear Processes in Geophysics*, **1**, 105-114.
- Cho, N.S. and Lee, T.Y., 2006: A numerical study of multiple convection bands over the Korean peninsula. *J. Korean Meteorol. Soc.*, **42**, 87-105.
- Choi, H.Y., Ha, J.H., Lee, D.K., Kuo, Y.H., 2011: Analysis and simulation of mesoscale convective system accompanying heavy rainfall: the Goyang case. *Asia Pac. J. Atmos. Sci.*, **47**, 265-279.
- De Lima, M. I. P and Grasman, J., 1999: Multifractal analysis of 15-min and daily rainfall from a semi-arid region in Portugal. *J. Hydrol.*, **220**, 1-11.
- De Lima, M. I. P. and de Lima, J. L. M. P., 2009: Investigating the multifractality of point precipitation in the Madeira archipelago, *Nonlinear Processes in Geophysics*, **16**, 299-311.
- De Montera, L., Barth`es, L., Mallet, C. and Gol`e, P., 2009: The effect of rain–no rain intermittency on the estimation of the universal multifractals model parameters. *J. Hydrometeor.*, **10**(2), 493–506.
- Deidda, R., 2000: Rainfall downscaling in a space-time multifractal framework. *Water Resources Research*, **36**, 1779–1794.
- Gao, J., Xue, M., Shapiro, A., and Droege, K. K., 1999: A variational method for the analysis of three-dimensional wind fields from two Doppler radars. *Mon. Wea. Rev.*, **127**, 2128–2142.
- Gires, A., Onof, C., Maksimovic, C., Schertzer, D., Tchiguirinskaia, I., Simoes, N., 2012: Quantifying the impact of small scale unmeasured rainfall variability on urban runoff through multifractal downscaling: a case study. *J. Hydrol.*, 442-443, 117-128.
- Gires, A., Tchiguiringskaia, I., Schertzer, D. and Lovejoy, S., 2013: Development and analysis of a simple model to represent the zero rainfall in a universal multifractal framework. *Nonlinear Processes in Geophysics*, **20**, 343-356.
- Gupta, V. K., and Waymire, E. C., 1993: A statistical analysis of mesoscale rainfall as a random cascade. *J. Appl. Meteor.*, **32**(2):251–267.
- Harris, D., Menabde, M., Seed, A. and Austin G., 1996: Multifractal characterization of rain fields with a strong orographic influence. *Journal of Geophysical Research: Atmospheres*, **101**(D21):26405–26414.
- Harris, D., Seed, A., Menabde, M., and Austin, G., 1997: Factors affecting the multiscaling

- analysis of rainfall time series, *Nonlinear Processes in Geophysics*, **4**, 137-156.
- Hoang, C. T., Tchiguirinskaia, I., Schertzer D., and Lovejoy, S., 2014: Caractéristiques multifractales et extrêmes de la précipitation à haute résolution, application à la détection du changement climatique. *Revue des sciences de l'eau/Journal of Water Science*, **27**(3):205–216.
- Hong, S.Y. and Lee, J.W., 2009: Assessment of the WRF model in reproducing a flash-flood heavy rainfall event over Korea. *Atmos. Res.*, **93**, 818-831.
- Im, E.S., In, S.R. and Han, S.O., 2017: Numerical simulation of the heavy rainfall caused by a convection band over Korea: a case study on the comparison of WRF and CReSS. *Natural Hazards*, **69**, no.3, 1681-1695.
- Lavallée, D., Lovejoy, S., Schertzer, D. and Ladoy, P., 1993: Nonlinear variability and landscape topography: analysis and simulation. *Fractals in Geography*, edited by: De Cola, L., and Lam, N., Prentice-Hall, 171-205.
- Lazarev, A., Schertzer, D., Lovejoy, S. and Chiriginskaia, Y., 1994: Unified multifractal atmospheric dynamics tested in the tropics: Part II, vertical scaling, and generalized scale invariance. *Nonlinear Processes in Geophysics*. **1**, 115-123.
- Lee, K.O., Shimizu, S., Maki, M., You, C.H., Uyeda, H., Lee, D.I., 2010: Enhancement mechanism of the 30 June 2006 precipitation system observed over the north-western slope of Mt Halla, Jeju Island, Korea. *Atmos. Res.*, **97**, 348-358.
- Liu, J.C., Liou, Y.A., Wu, M.X., Lee, Y.J., Cheng, C.H., Kuei, C.P. and Hong, R.M., 2015: Analysis of interactions among two tropical depressions and typhoons Tembin and Bolaven (2012) in Pacific Ocean by using satellite cloud images. *IEEE Transactions on Geoscience and Remote sensing*, **53**, 1394-1402.
- Lovejoy, S. and Mandelbrot, B., 1985: Fractal properties of rain and a fractal model. *Tellus*, **37**, 209-232.
- Lovejoy, S. and Schertzer, D., 2007: Scale, scaling and multifractals in geophysics: Twenty years on. *Nonlinear Processes in Geophysics*, 311-337.
- Lovejoy, S., Schertzer, D., Silas, P., Tessier, Y. and Lavallee, D., 1993: The unified scaling model of the atmospheric dynamics and systematic analysis of scale invariance in cloud radiances. *Annales Geophysicae*, **11**, 119-127.
- Macor, J., Schertzer, D. and Lovejoy S., 2007: Multifractal methods applied to rain forecast using radar data. *La Houille Blanche-Revue internationale de l'eau*, **4**, 92–98.
- Mandelbrot, B. B., 1974: Intermittent turbulence in self-similar cascades: divergence of high moments and dimension of the carrier. *Journal of Fluid Mechanics*, **62**(2): 331–358.
- Marsan, D., Schertzer, D. and Lovejoy, S., 1996: Causal space-time multifractal processes: Predictability and forecasting of rainfields. *J. Geophys. Res.*, **101**, 26333-26346.
- Nogueira, M., Barros, A. P. 2015: Transient stochastic downscaling of quantitative precipitation estimates for hydrological applications. *J. Hydrol.*, **529** (3), 1407-1421.
- Nykanen, D. K., 2008: Linkages between orographic forcing and the scaling properties of convective rainfall in mountainous regions. *J. Hydrometeorol.*, **9**, 327-347.
- Olsson, J., Niemczynowicz, J., and Berndtsson, R., 1993: Fractal analysis of high-resolution

- rainfall time series. *J. Geophys. Res.*, **98**, 23265-23274.
- Ordanovich, A, Chigirinskaya, Y., 1993: Mathematical modeling of the inhomogeneous atmospheric boundary layer, *Dokladi Acad Nauk. UkrSSR*, A, in a press.
- Origuchi, S., Saito, K., Seko, H., Kuroda, T. and Mashiko, W., 2013: Triple eyewall experiment of the 2012 typhoon Bolaven using cloud-resolving ensemble forecast. *CAS/JSC WGNE Res. Activ. Atmos. Oceanic Modell.*, **43**, 5.09-5.10.
- Over, T. M., and V. K. Gupta, 1996: A space-time theory of mesoscale rainfall using random cascades, *J. Geophys. Res.*, **101**(D21), p. 26,319-26,331.
- Parisi, G. and Frish, U., 1985: A multifractal model of intermittency in: Turbulence and predictability in geophysical fluid dynamics, edited by: Ghill, M., Benzi, R., and Parisi, G., Elsevier North Holland, New-York, 111-114.
- Ryu, C.S. and Lee, D.S., 2012: A Comparative Study of Rain Intensities Retrieved from Radar and Satellite Observations: Two Cases of Heavy Rainfall Events by Changma and Bolaven (TY15). *J. Korean Earth Science Society*, **33**, no. 7, 569–582.
- Schertzer D., Lovejoy S., 2011: Multifractals, generalized scale invariance and complexity in geophysics. *Int. J. Bifurcat. Chaos*, **21**, 3417-3456.
- Schertzer, D., Lovejoy, S., 1983: Elliptical turbulence in the atmosphere, In proceedings of the forth symposium on turbulent shear flows, Karlshule, Germany, 11.1-11.8.
- Schertzer, D., Lovejoy, S., 1985: The dimension and intermittency of atmospheric dynamics, Turbulent shear flow. Ed. Launder, B., *Springer*, **4**, 7-33.
- Schertzer, D., Lovejoy, S., 1987: Physical modeling and analysis of rain and clouds by anisotropic scaling and multiplicative processes. *J. Geophys. Res.*, **92**, 9693-9714.
- Schertzer, D., Lovejoy, S., 1997: Universal multifractals do exist!: comments. *J. Appl. Meteorol.*, **36**, 1296-1303, 1997.
- Shimizu, S. and Maesaka, T., 2006: Multiple Doppler radar analysis using variational technique to retrieve three-dimensional wind field. Technical Report 70, National Research Institute for Earth Science and Disaster Prevention, Japan, 1-8.
- Shin, C.S. and Lee, T.Y., 2005: Development mechanisms for the heavy rainfalls of 6-7 August 2002 over the middle of the Korean Peninsula. *J. Meteorol. Soc. Jpn.*, **83**, 683-709.
- Sun, J. and Lee, T.Y., 2002: A numerical study of an intense quasi-stationary convection band over the Korean peninsula. *J. Meteorol. Soc. Jpn.*, **80**, 1221-1245.
- Sun, L., Dong, W., Yao, M., Zhu, D. and Li, Q., 2015: A diagnostic analysis of the causes of the torrential rain and precipitation asymmetric distribution of Typhoon Bolaven (2012), *Acta Meteorologica Sinica*, **73**, No. 01, 38-51.
- Tchiguirinskaia, I., Schertzer, D. Hoang, C. T. and Lovejoy S., 2011: Multifractal study of three storms with different dynamics over the Paris region. In Weather Radar and Hydrology Symposium. Exeter, UK: IAHS Red book.
- Tessier, Y., Lovejoy, S. and Schertzer, D., 1993: Universal Multifractals: theory and observations for rain and clouds. *J. Applied Meteorology*, **23**, 223-250.

- Tsuboki, K. and Sakakibara, A., 2002: Large-scale parallel computing of Cloud Resolving Storm Simulator. High Performance Computing: Proceedings of the Fourth International Symposium on High Performance Computing, H. P. Zima et al., Eds., *Springer*, 243–259.
- Tsuboki, K., 2004: High resolution modeling of multi-scale cloud and precipitation systems using a cloud resolving model. Annual report of the Earth Simulator Center, April 2003–March 2004, 21–26.
- Tsujino, S., Tsuboki, K., and Kuo, H., 2017: Structure and Maintenance Mechanism of Long-lived Concentric Eyewalls Associated with Simulated Typhoon Bolaven (2012). *J. Atmos. Sci.* doi:10.1175/JAS-D-16-0236, 1, in a press.
- Verrier, S., de Montera, L., Barths, L., Mallet, C., 2010. Multifractal analysis of African monsoon rain fields, taking into account the zero rain-rate problem. *J. Hydrol.*, **389** (12), 111-120.
- Yu, X. and Lee, T.Y., 2010: Role of convective parameterization in simulations of a convection band at grey-zone resolutions. *Tellus*, **62A**, 617-632.

**Table 1. The value of  $\beta$  and  $R^2$  from spectral analysis**

	Radar (256×256)			Radar (64×64)			CReSS	
	1 km	2 km	5 km	1 km	2 km	5 km	DR (256×256)	DR (64×64)
$\beta$	1.632	1.833	1.560	1.95	2.241	2.415	1.618	1.779
$R^2$	0.964	0.979	0.997	0.964	0.979	0.997	0.959	0.928

**Table 2. The multifractality index  $\alpha$  and  $C_1$** 

		Radar (256×256)			Radar (64×64)			CReSS	
		1 km	2 km	5 km	1 km	2 km	5 km	DR (256×256)	DR (64×64)
TM	$\alpha$	0.499	0.743	1.028	1.471	1.516	1.095	0.952	1.493
	$C_1$	0.358	0.261	0.117	0.206	0.185	0.092	0.113	0.095
DTM	$\alpha$	0.858	1.072	1.421	1.548	1.628	1.356	1.416	1.817
	$C_1$	0.349	0.255	0.114	0.195	0.173	0.089	0.105	0.092

**Table A1. Multifractal indexes on domain 1 and domain 2 with the size of 512×512.**

		D1		D2
TM	$\alpha$	0.68		0.582
	$C_1$	0.13		0.269
DTM	$\alpha$	1.109		0.928
	$C_1$	0.123		0.256

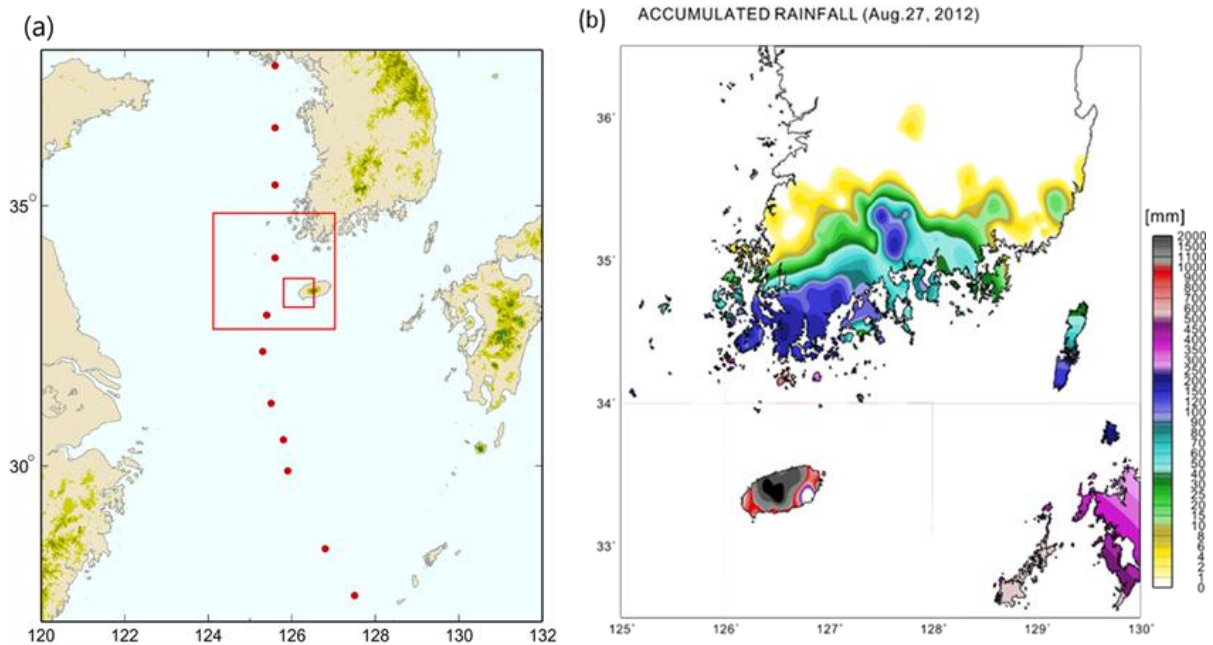


**Figure 1:** (a) The tracks of Typhoon Bolaven. The red dots indicate the center of the typhoon from 20 - 28 August 2012. (b) The daily accumulated rainfall on 27 August is shown. The maximum accumulated rainfall amount (mm) has occurred in Jeju Island. The squares in both figures indicate the selected domains for multifractal analysis.

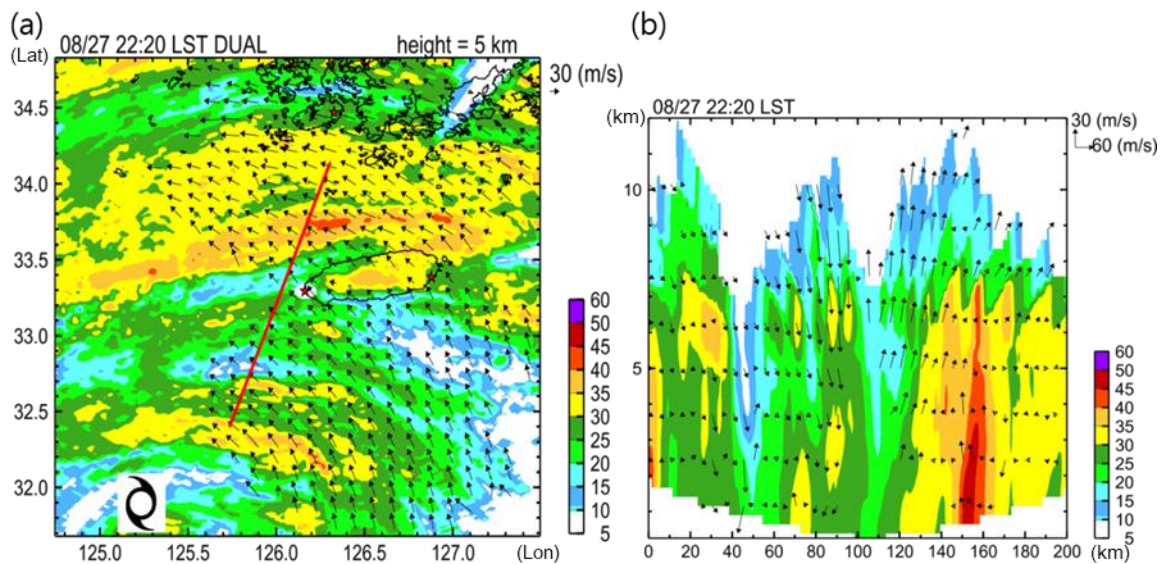
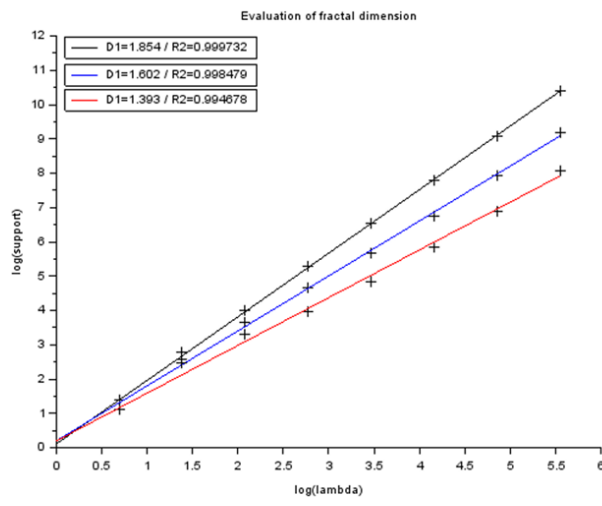


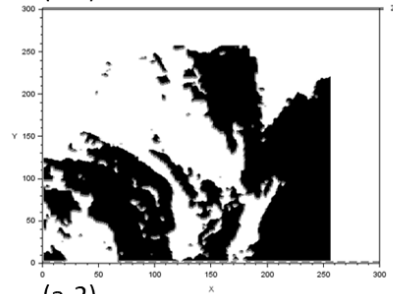
**Figure 2:** The wind field superimposed on the radar reflectivity (dBZ) on 5 km altitude on

**the left. The radar located in Gosan is shown as the red star in the middle of the figure. The vertical cross-section selected with a red line on the left is shown on the right. The updraft and downdraft are clearly shown in the vertical cross-section.**

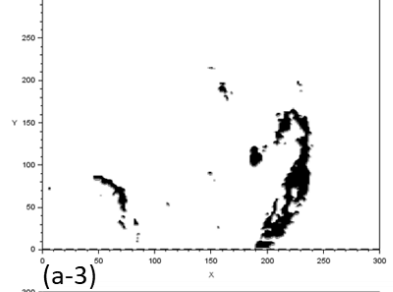
(a)



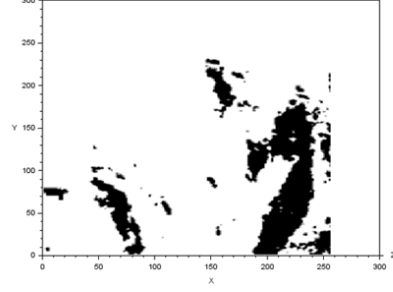
(a-1)



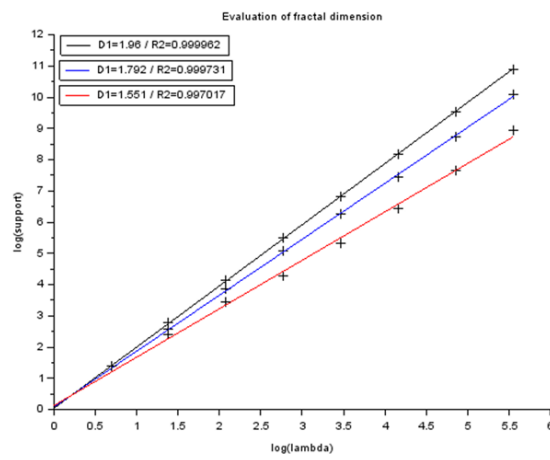
(a-2)



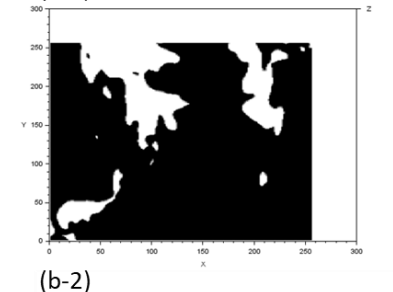
(a-3)



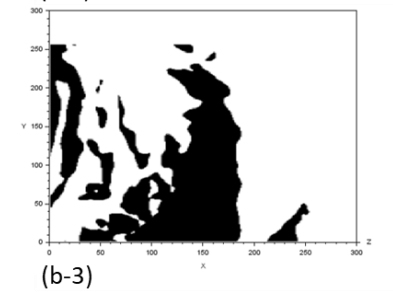
(b)



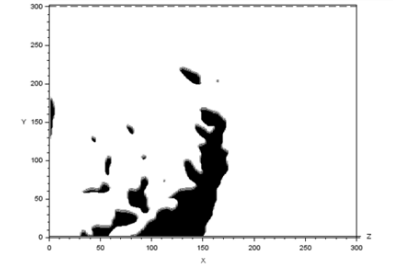
(b-1)



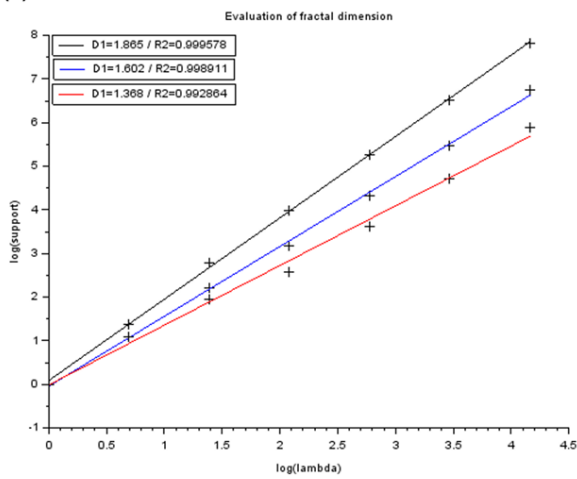
(b-2)



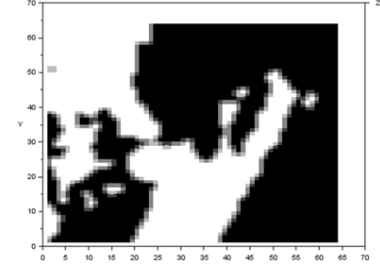
(b-3)



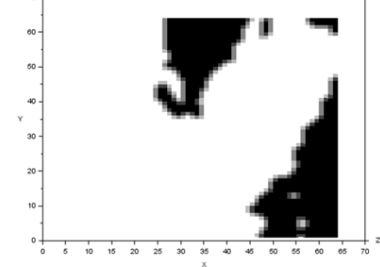
(c)



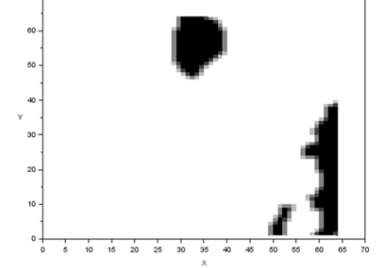
(c-1)



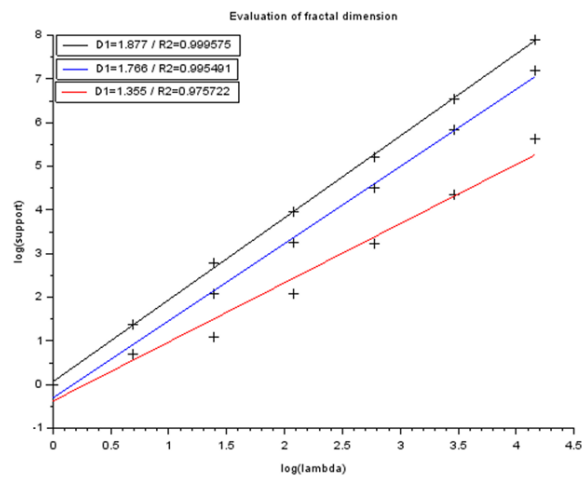
(c-2)



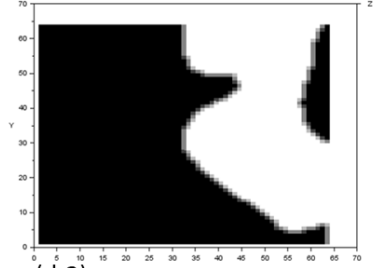
(c-3)



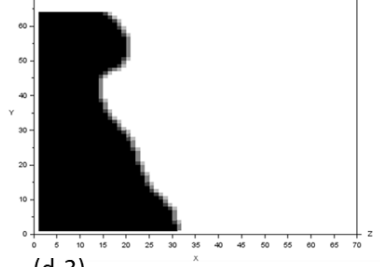
(d)



(d-1)



(d-2)



(d-3)

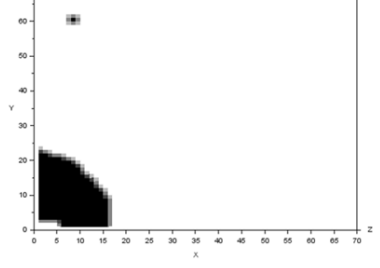


**Figure 3:** The fractal dimension calculated at 23:30 LST, Aug. 27<sup>th</sup> with (a) radar at 5 km and (b) CReSS in the domain size of  $256 \times 256$ . The fractal dimension with (c) radar at 5 km and (d) CReSS in the domain size of  $64 \times 64$ . The graph shows different slopes of fractal dimension depending on the threshold (with threshold 1 shows with the black, 5 with the blue and 10 shows with the red line). Also, the black and white figures (a-1,2,3, b-1,2,3, c-1,2,3, d-1,2,3) show the rainfall fields changing with the different thresholds more visually (the existence of the rain is indicated with black). (E.g.  $R^2$  is shown as R2 in the graphs)

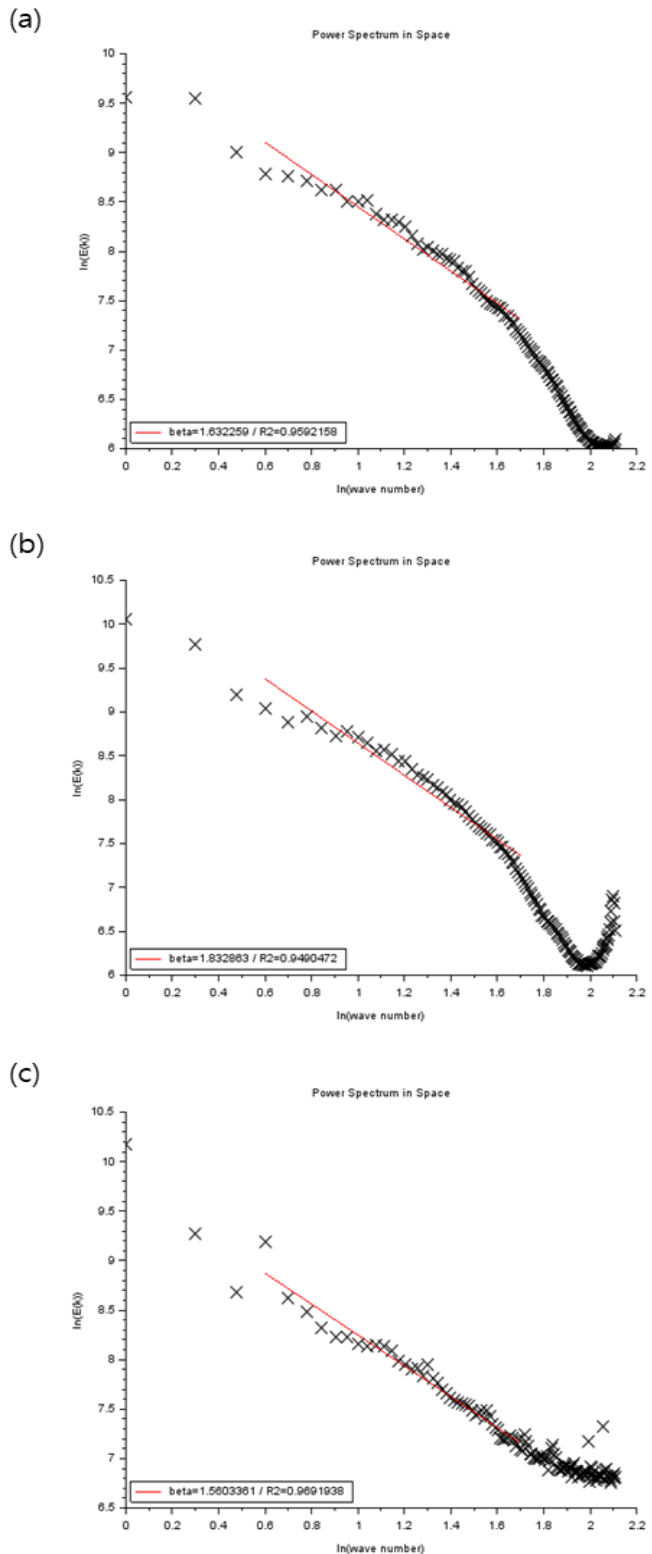
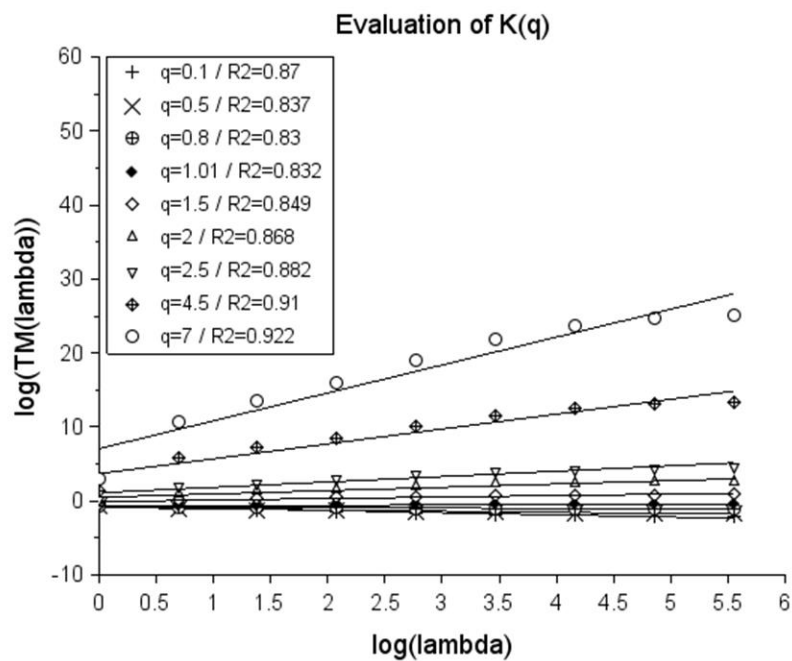


**Figure 4: The result of spectral ( $\ln(E(k))$ ) –  $\ln(k)$ ) analysis with the rainfall rate retrieved from radar data on every altitude (a) 1 km, (b) 2 km, and (c) 5 km in  $256 \times 256$  size of the**

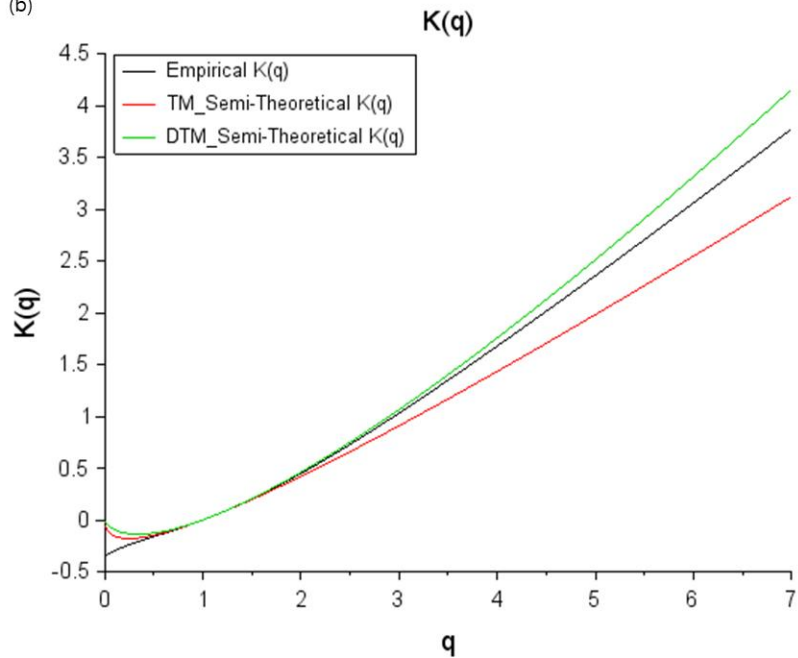
domain. (E.g.  $R^2$  is shown as R2 in the graphs)

1 km

(a)

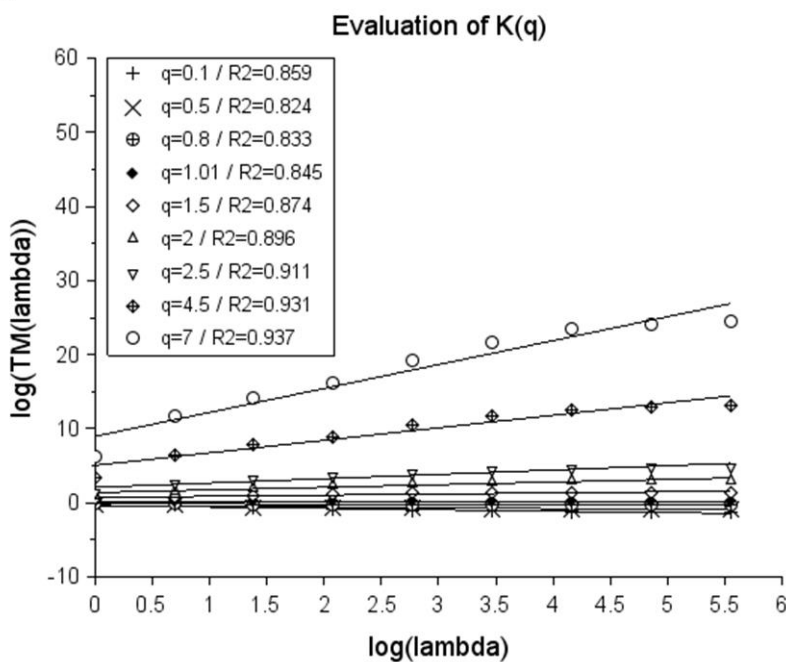


(b)

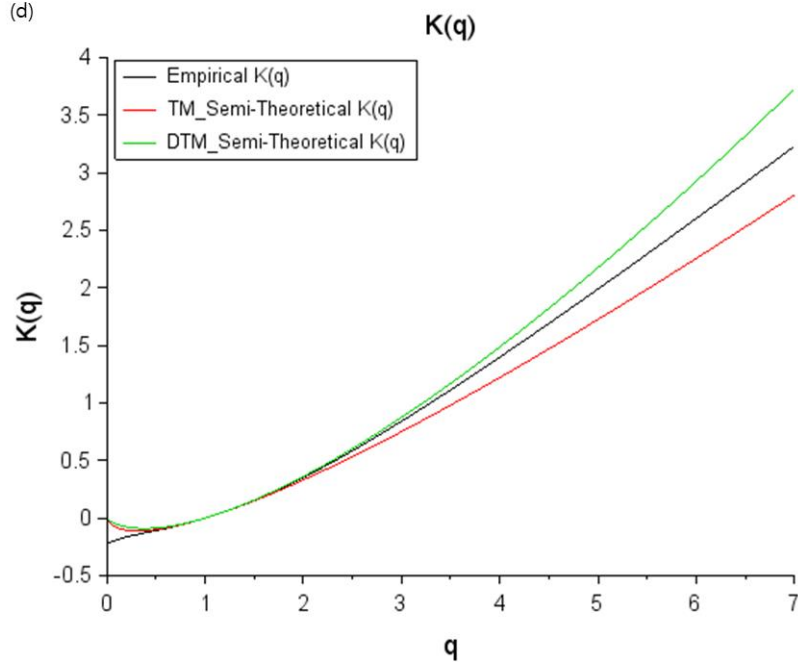


2 km

(c)

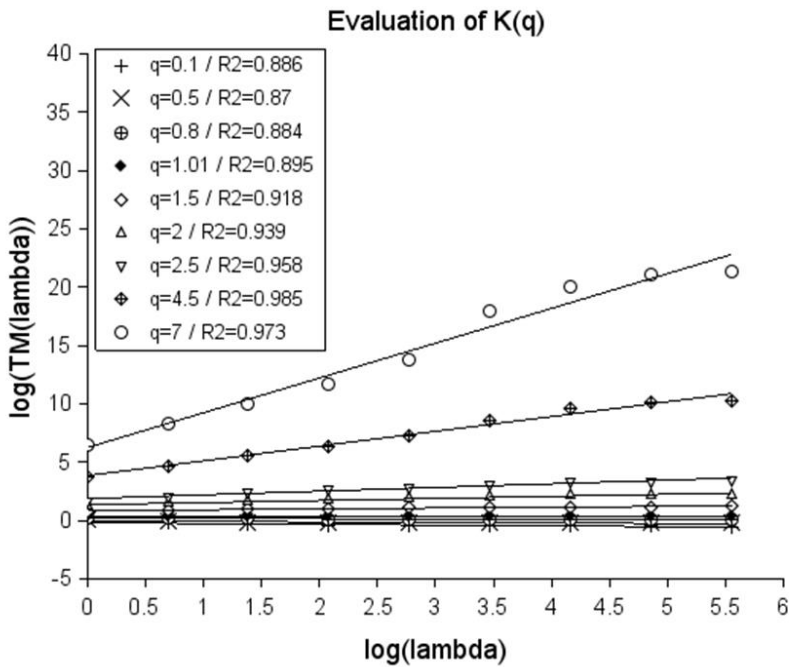


(d)



5 km

(e)



(f)

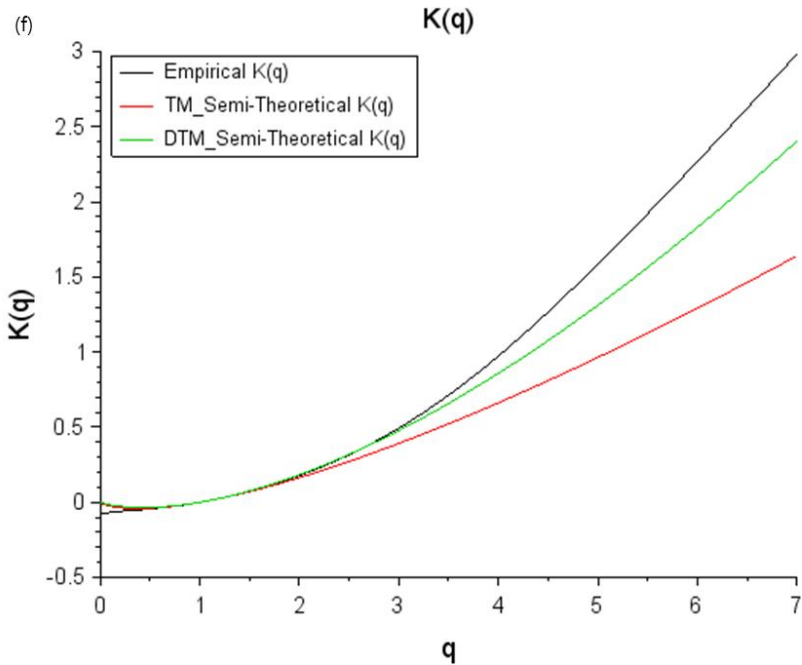
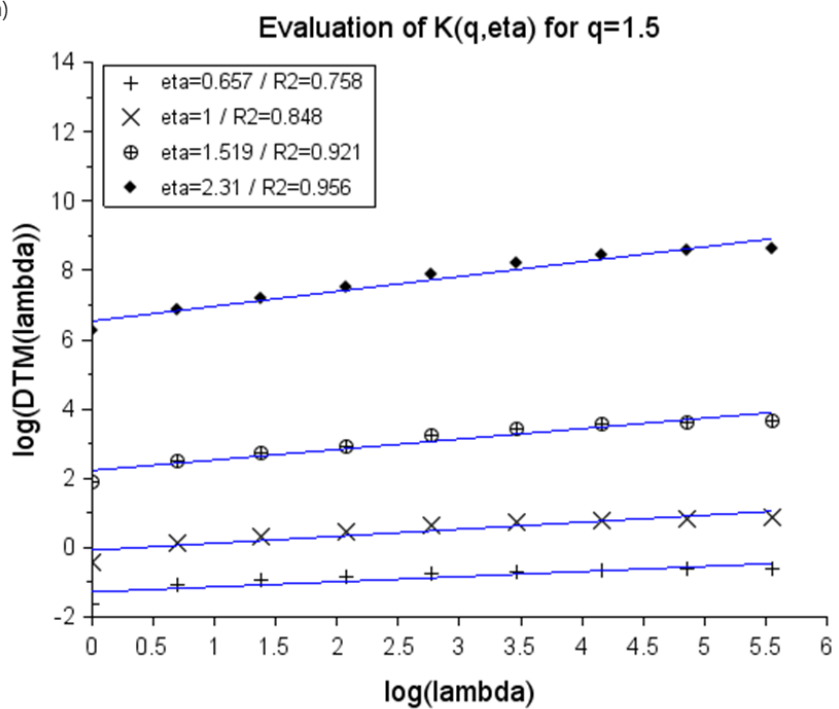


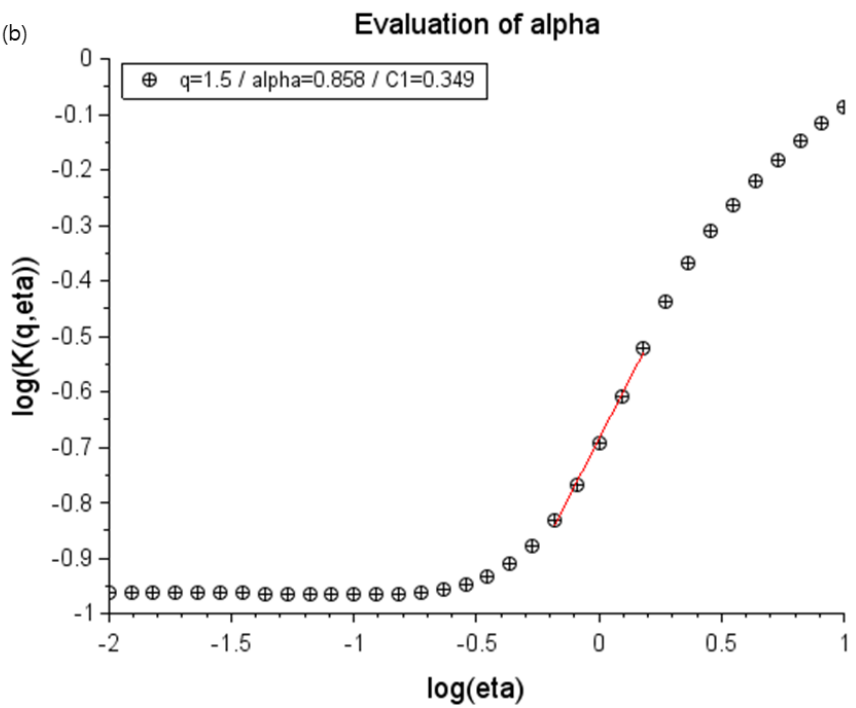
**Figure 5:** The result of TM analysis in  $256 \times 256$  domain. The scaling behavior with the value of different  $q$  from 0.1 to 7.0 at (a) 1 km, (c) at 2 km and (e) at 5 km. The empirical  $K(q)$  (black) is compared with theoretical  $K(q)$  with the multifractal parameters retrieved from TM analysis (red) and DTM analysis(green) (b, d, f). (E.g.  $R^2$  is shown as  $R2$  in the graphs)

1 km

(a)

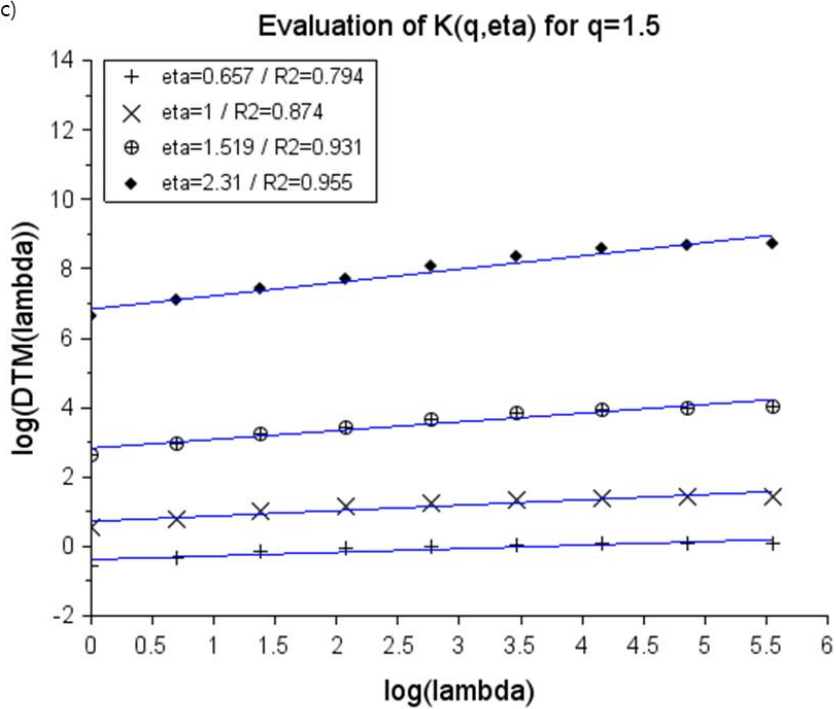


(b)

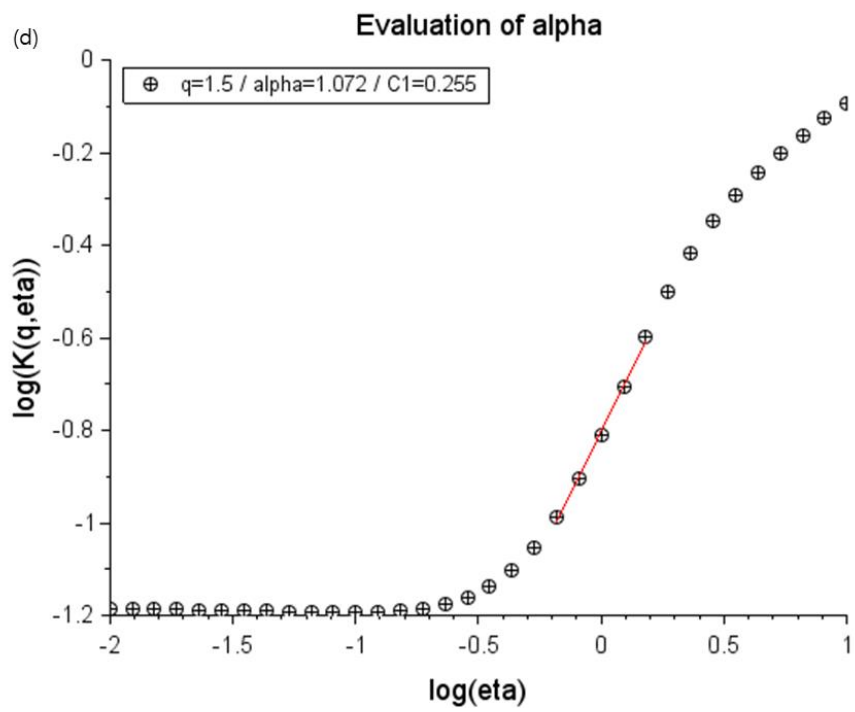


2 km

(c)



(d)



5 km

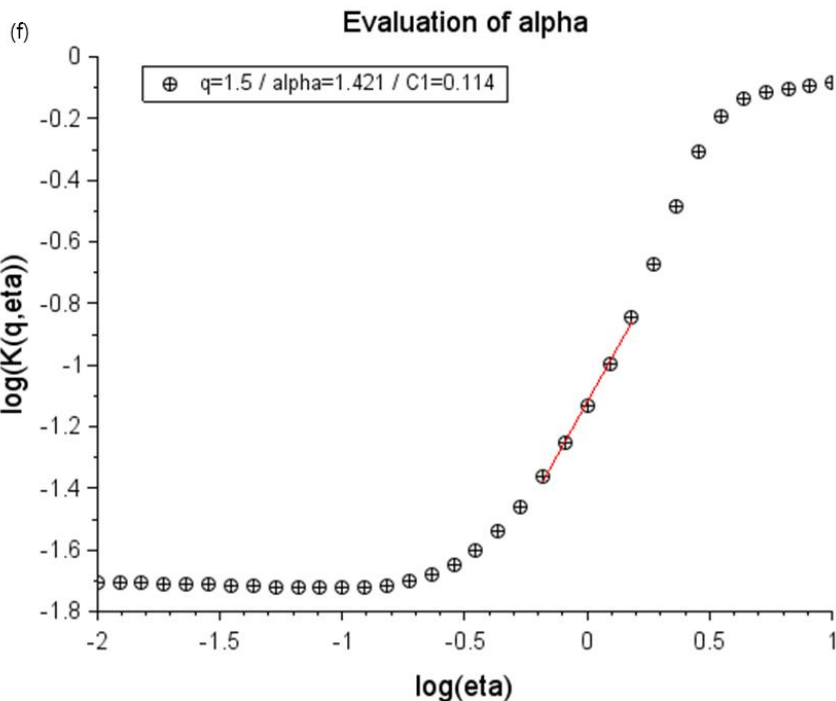
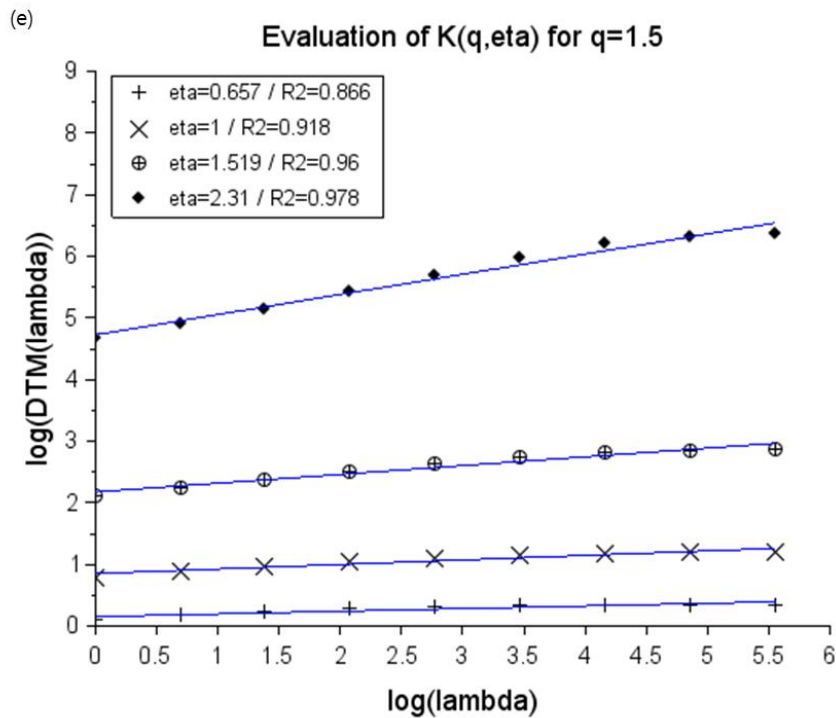
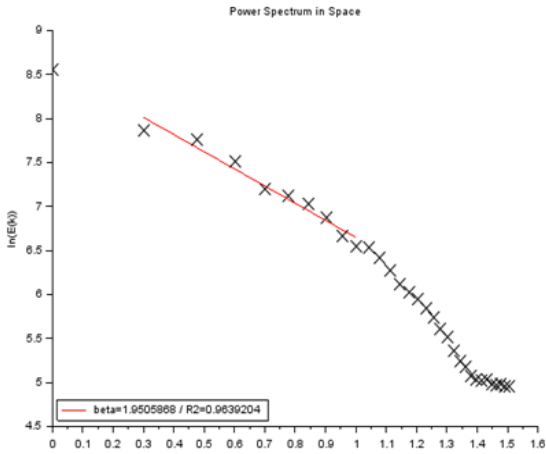
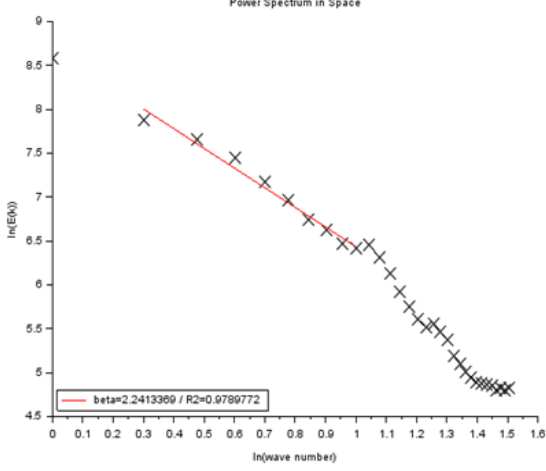


**Figure 6:** The DTM scaling behavior in  $256 \times 256$  size of the domain at each altitude; 1 km (a, b), 2 km (c, d) and 5 km (e, f) resulting double trace moment curve of S-band radar. (E.g.  $R^2$  is shown as R2 in the graphs)

(a)



(b)



(c)

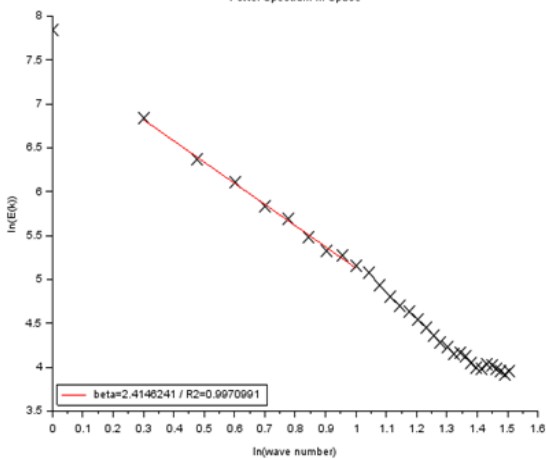
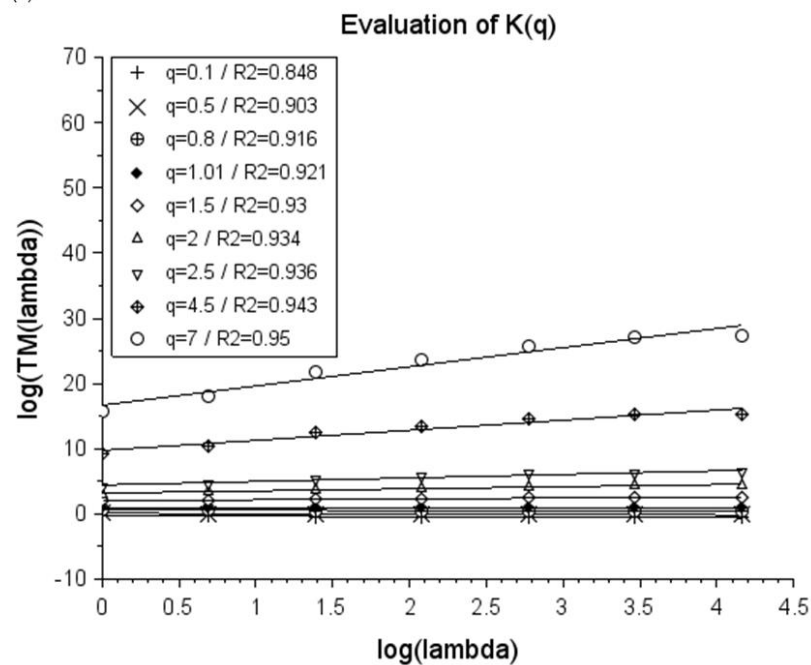


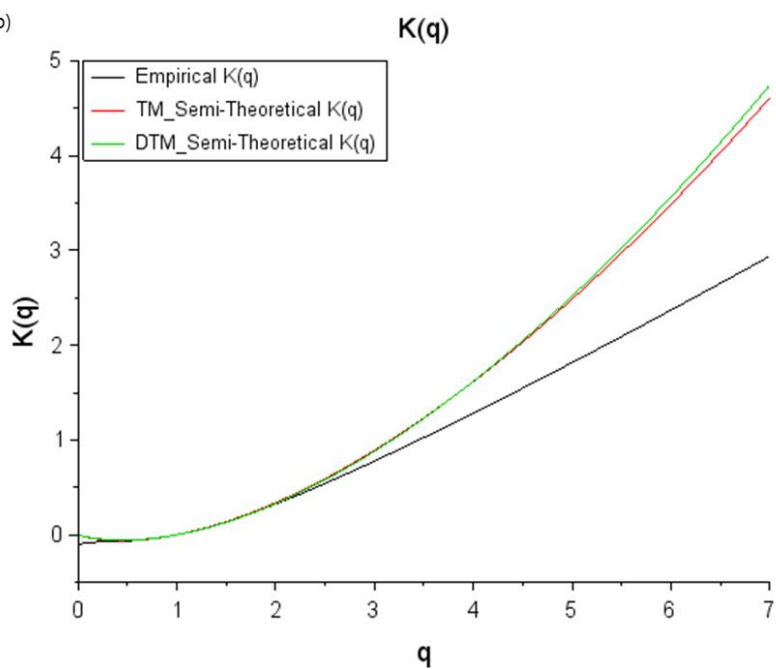
**Figure 7: Spectral analysis of the rainfall rate of Radar data on each level at (a) 1 km, (b) 2 km, and (c) 5 km in the  $64 \times 64$  size of the domain. (E.g.  $R^2$  is shown as R2 in the graphs)**

1 km

(a)

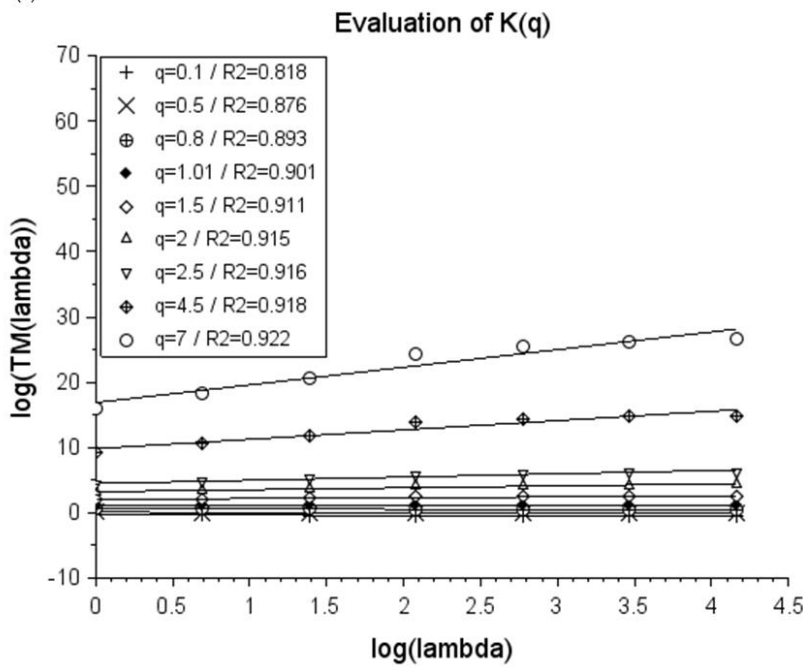


(b)

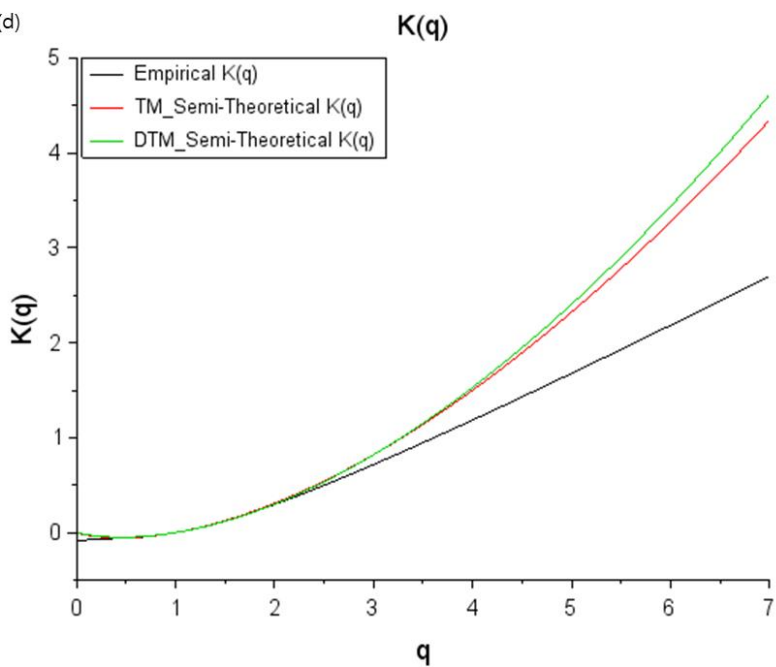


2 km

(c)

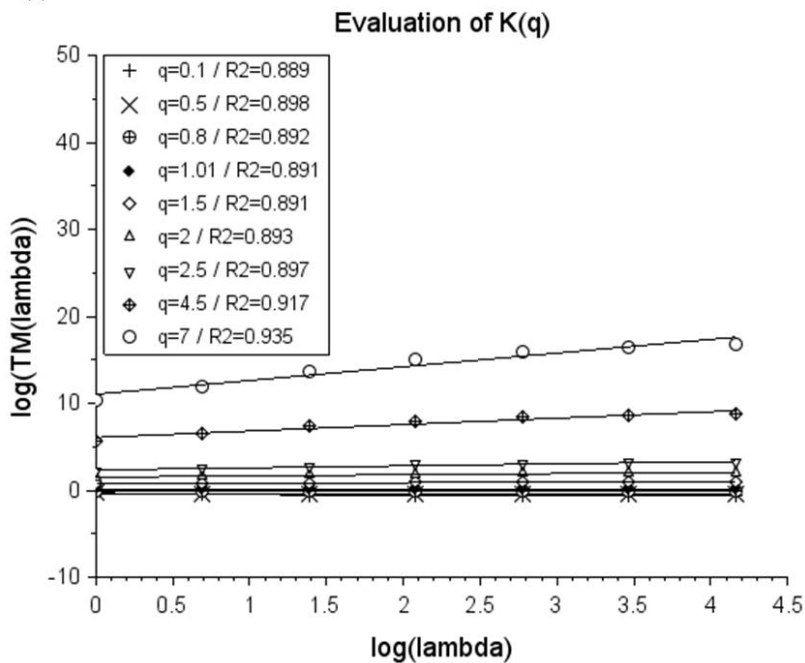


(d)



5 km

(e)



(f)

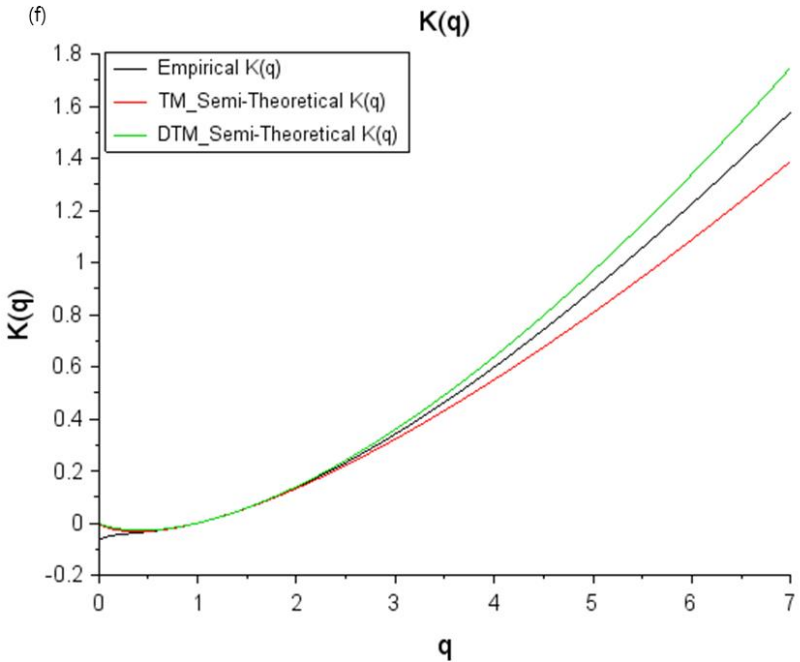
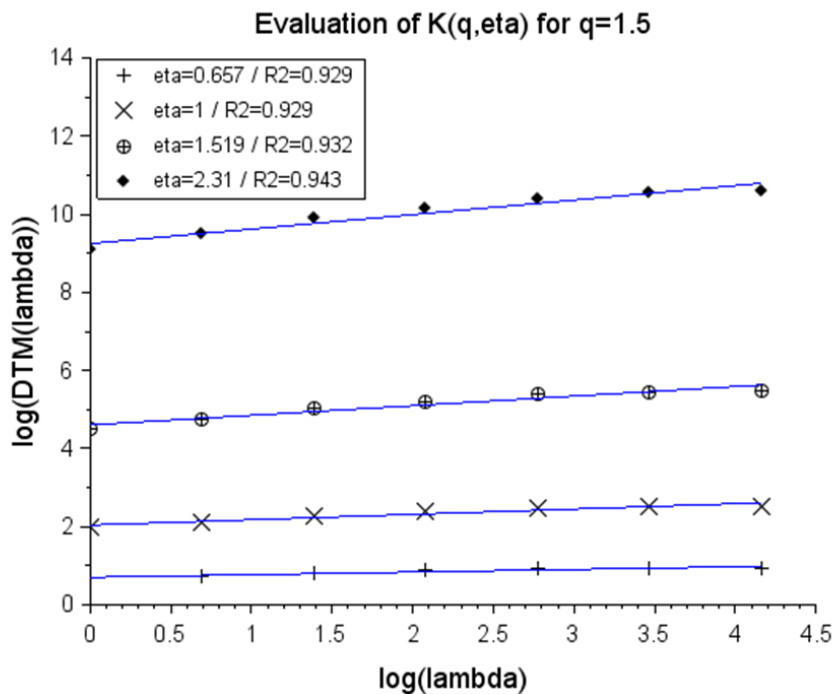


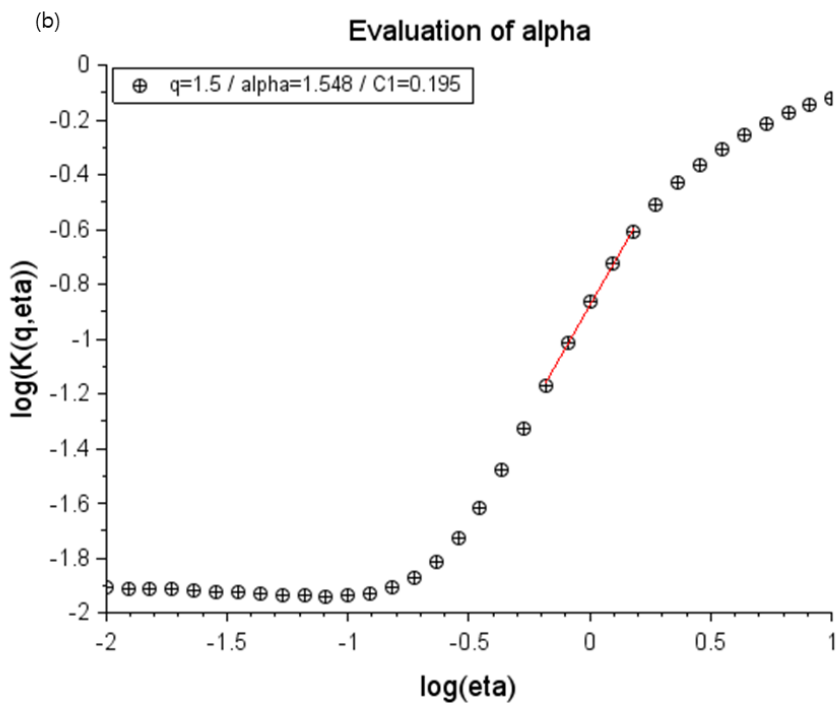
**Figure 8:** The result of TM analysis obtained from radar dataset in the  $64 \times 64$  size of the domain. The scaling behavior with the value of different  $q$  from 0.1 to 7.0 (a) at 1 km, (c) at 2 km and (e) at 5 km. The empirical  $K(q)$  (black) is compared with theoretical  $K(q)$  with the multifractal parameters retrieved from TM analysis (red) and DTM analysis(green) (b,d,f). (E.g.  $R^2$  is shown as  $R2$  in the graphs)

1 km

(a)



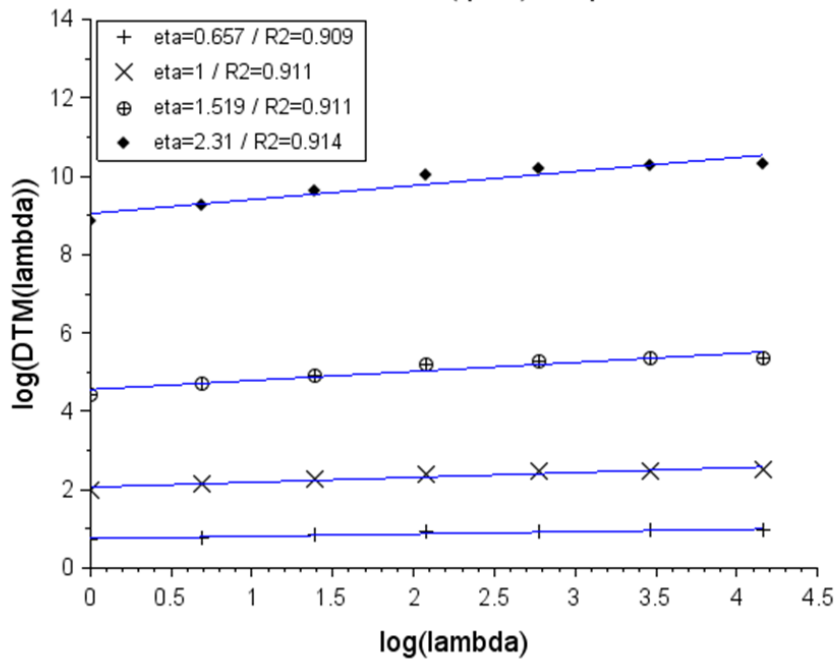
(b)



2 km

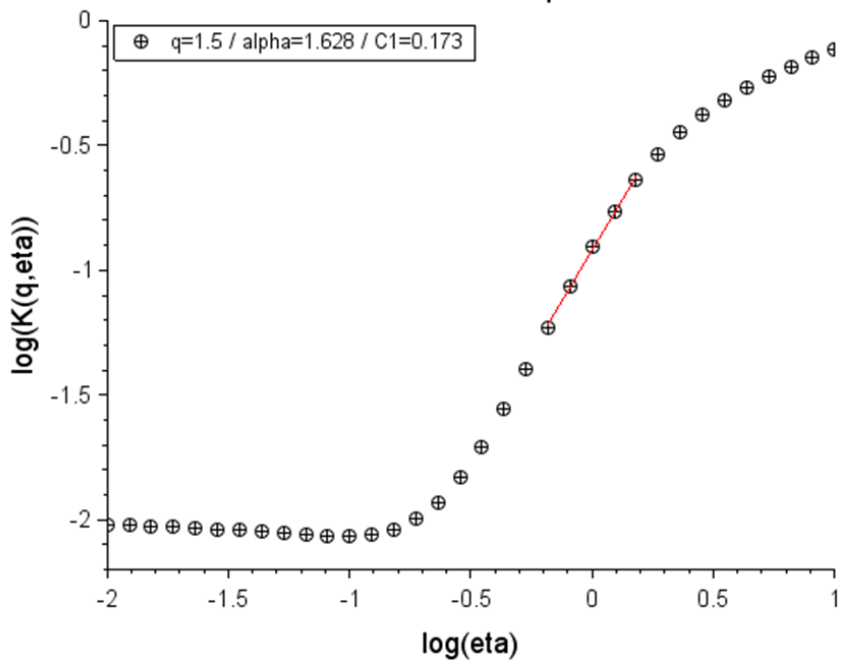
(c)

Evaluation of  $K(q,\eta)$  for  $q=1.5$



(d)

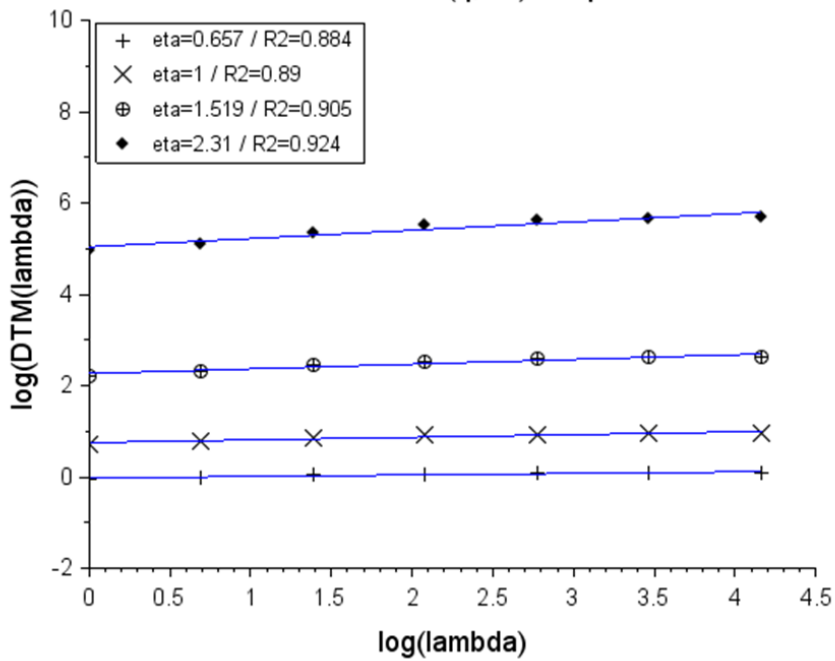
Evaluation of alpha



5 km

(e)

### Evaluation of $K(q,\eta)$ for $q=1.5$



(f)

### Evaluation of $\alpha$

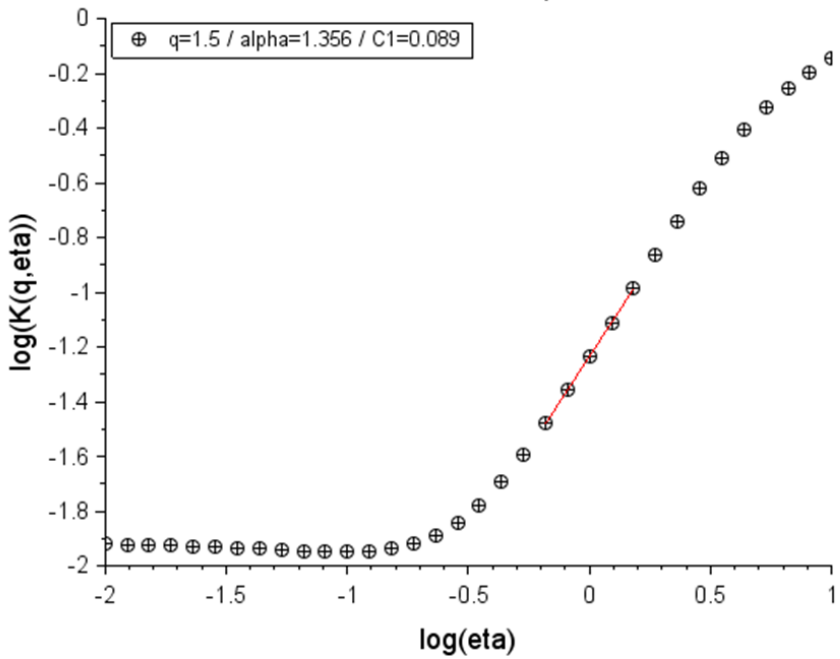
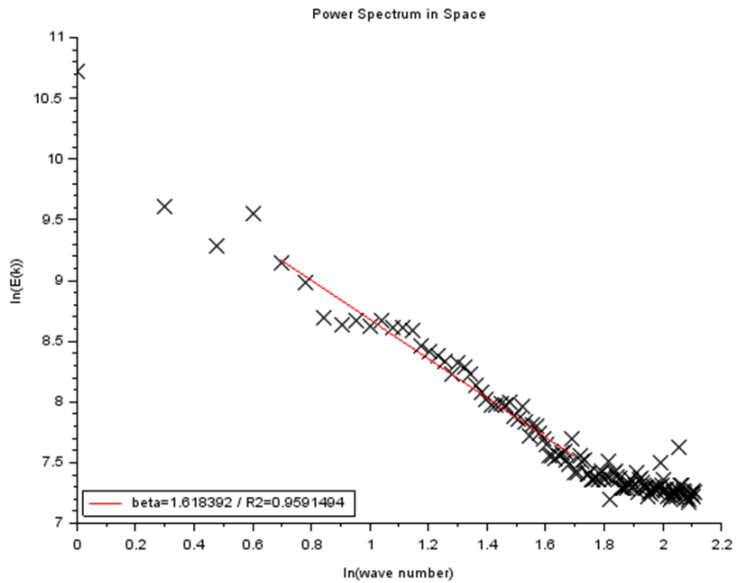
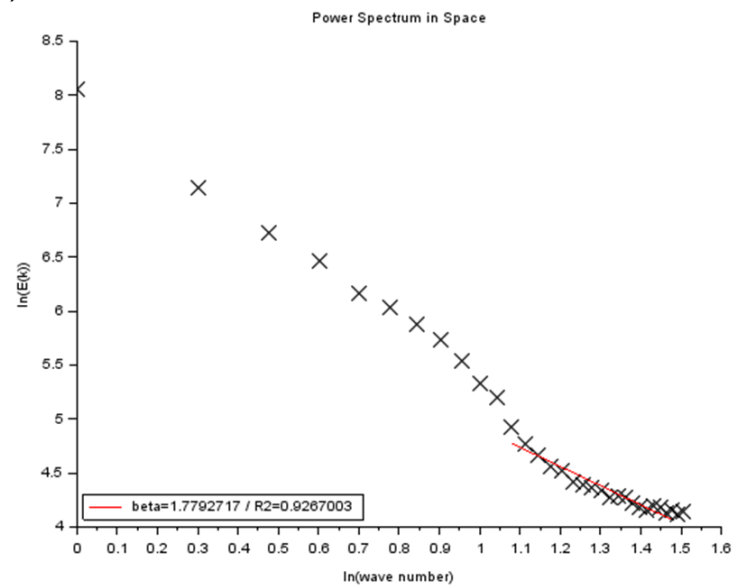


Figure 9: The DTM scaling behavior in  $256 \times 256$  size of the domain at each altitude; 1 km (a, b), 2 km (c, d) and 5 km (e, f) resulting double trace moment curve of S-band radar. (E.g.  $R^2$  is shown as R2 in the graphs)

(a)



(b)



**Figure 10: Spectral analysis of the rainfall rate of CReSS data on different domain size (a)  $256 \times 256$ , (b)  $64 \times 64$ . (E.g.  $R^2$  is shown as R2 in the graphs)**

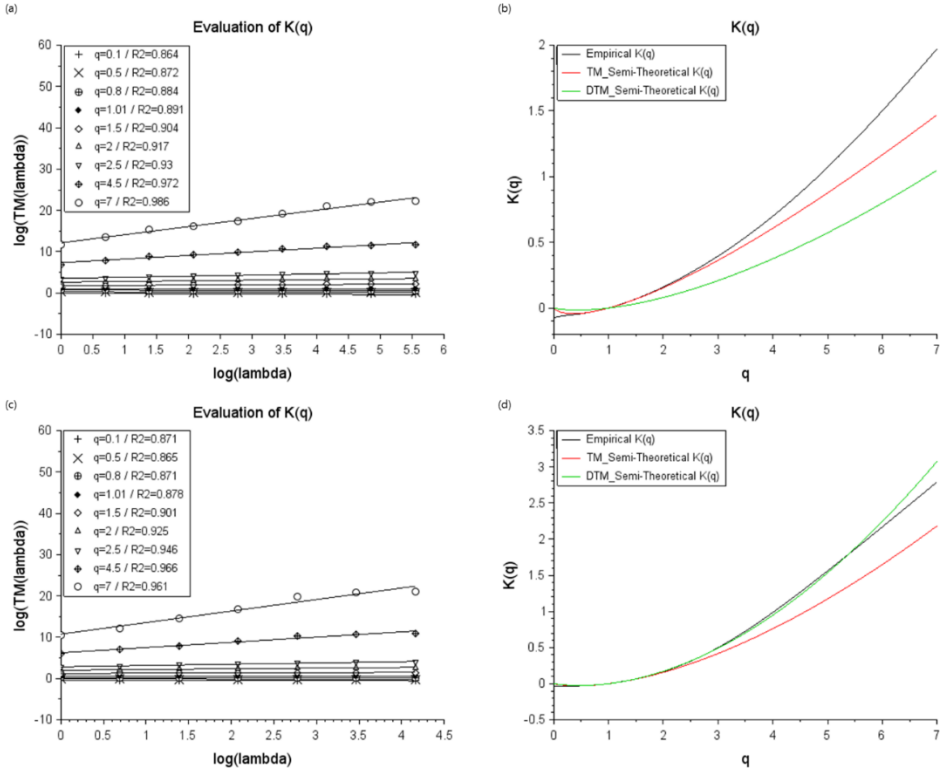


**Figure 11:** The result of TM analysis obtained from CReSS model dataset with each size of the domain,  $256 \times 256$  (a, b) and  $64 \times 64$  (c, d). The scaling behavior with the value of different  $q$  from 0.1 to 7.0 as same as the radar dataset (a,c). The empirical  $K(q)$  (black) is compared with theoretical  $K(q)$  with the multifractal parameters retrieved from TM analysis (red) and DTM analysis (green) (b, d). (E.g.  $R^2$  is shown as  $R2$  in the graphs)

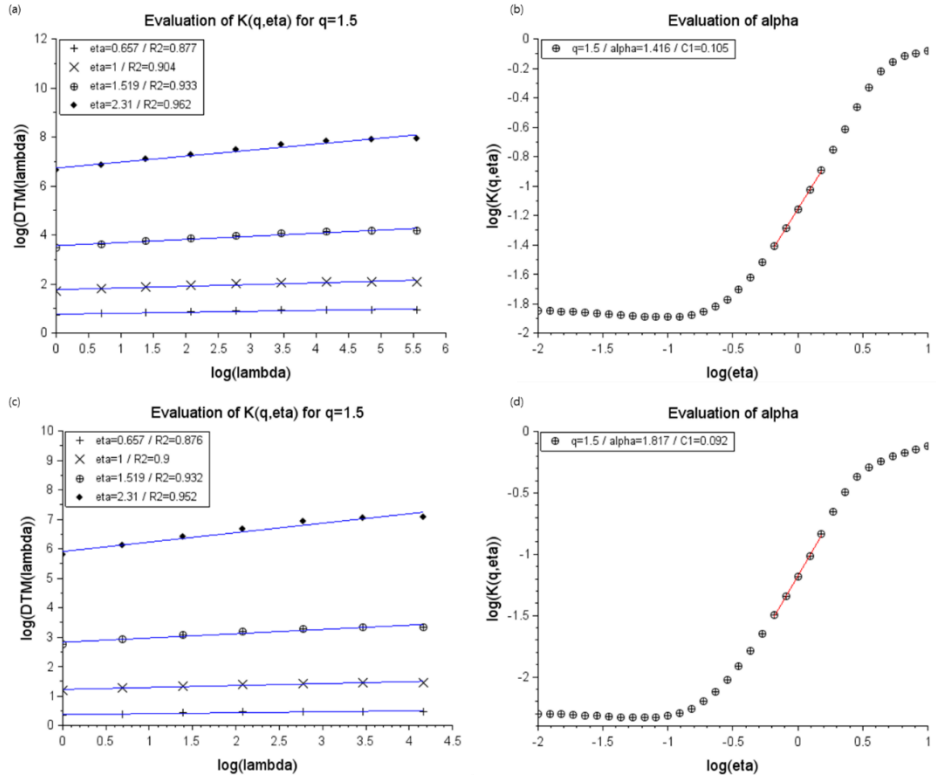
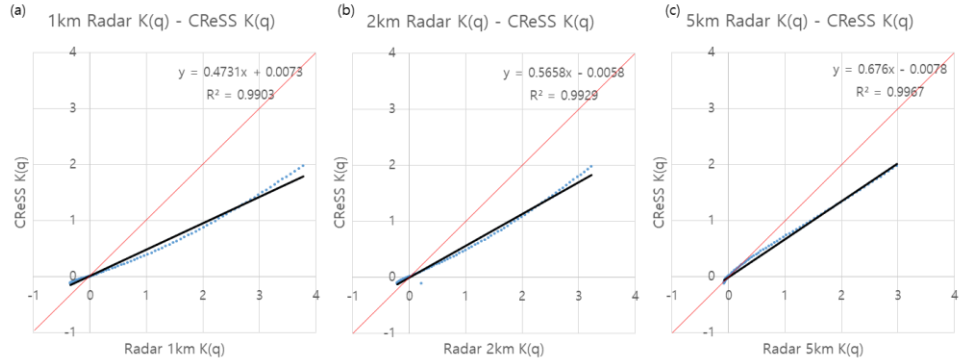


**Figure 12:** The DTM scaling behavior in each size of the domain,  $256 \times 256$  (a, b) and  $64 \times 64$  (c, d) and resulting double trace moment curve. (E.g.  $R^2$  is shown as R2 in the graphs)

256×256



64×64

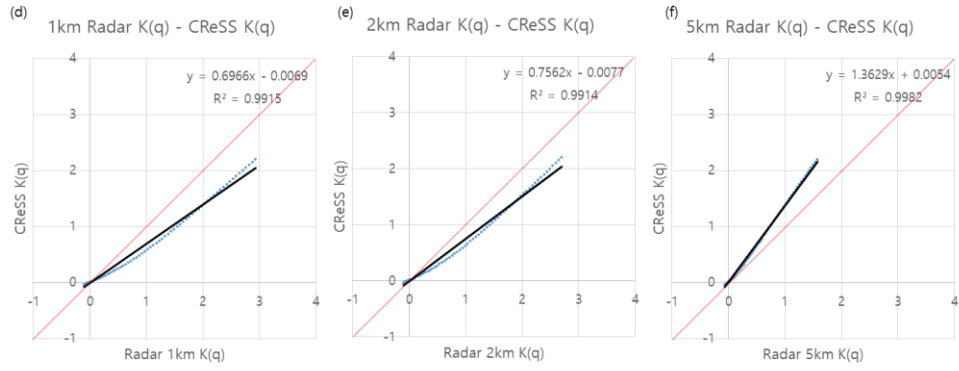


**Figure 13: Comparison between the empirical  $K(q)$  for each altitude of the radar data and for the CReSS model with domain sizes of  $256 \times 256$  (a, b, c) and  $64 \times 64$  (d, e, f). The blue dots correspond to the  $K(q)$  values for each  $q$  value; the black lines are the linear regression fits; and the red lines are the bisectrices.**

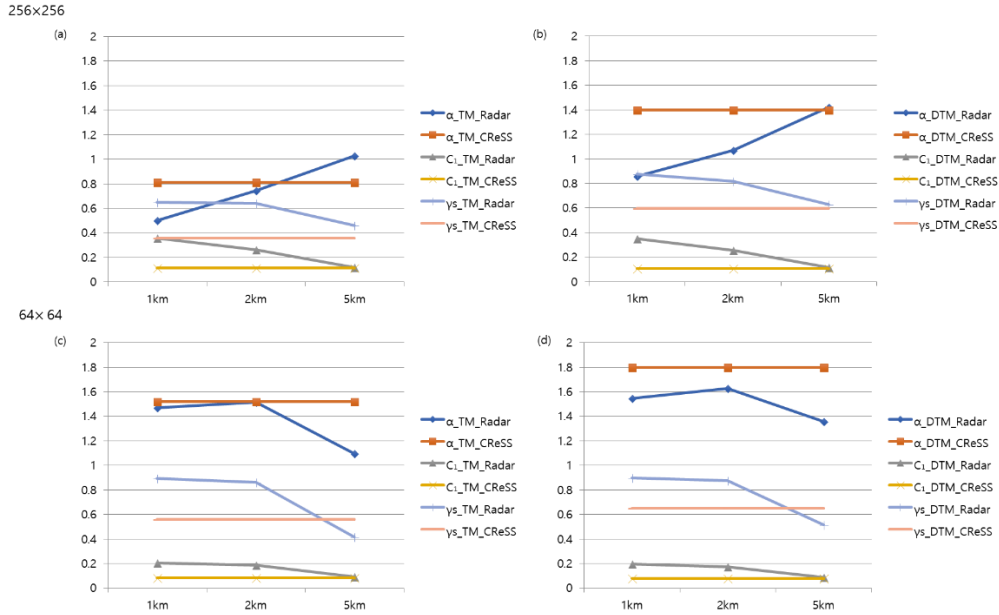


**Figure 14:** The graphs are showing the tendency of each multifractality index obtained from TM and DTM in different domain size of 256 × 256 (a, b) and 64 × 64 (c, d) as well as the maximal singularity  $\gamma_s$ .

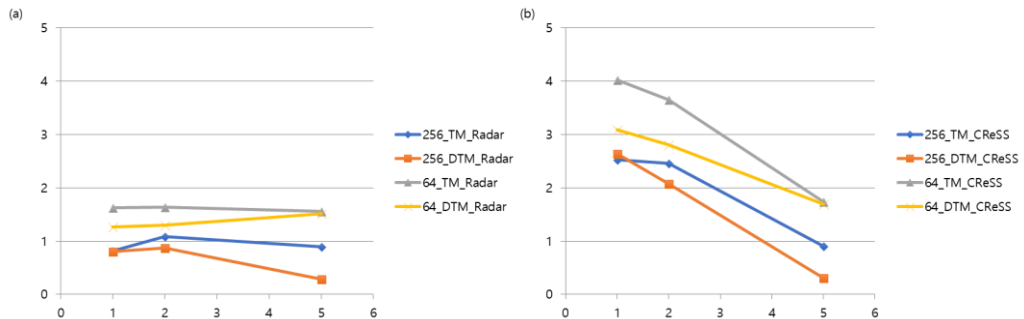


**Figure 15:** The absolute value of the difference between singularities  $\gamma_s$  of radar and CReSS normalized by  $C_1$ , respectively of the (a) radar and (b) CReSS.

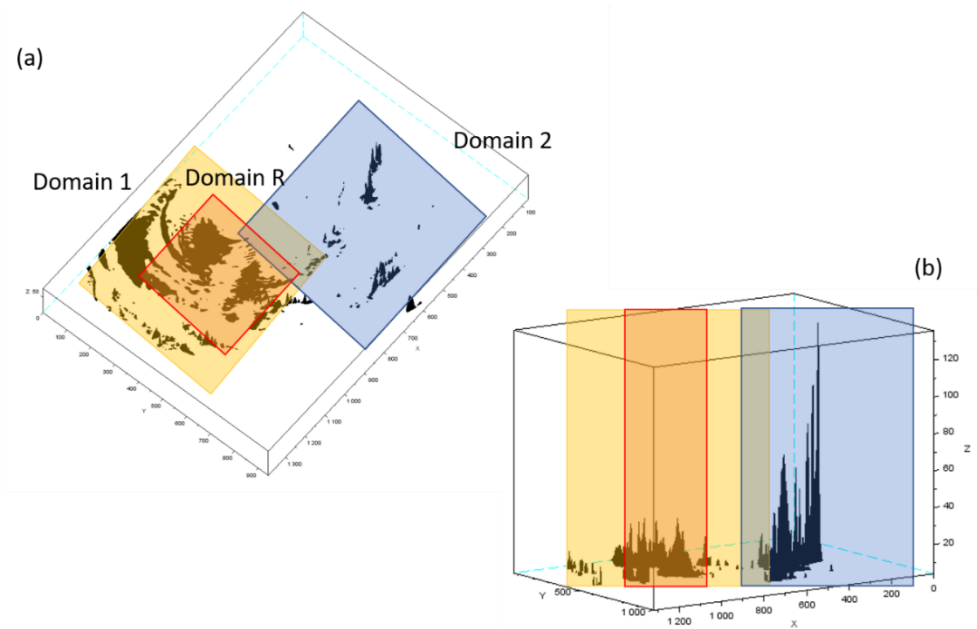


**Figure A1:** Three different domains selected for multifractal analysis with CReSS model. The yellow box is where the rainfall is spread around the whole area; the blue box is covering where there was the highest amount of accumulated rainfall and the red box is covering the same area as the radar domain.

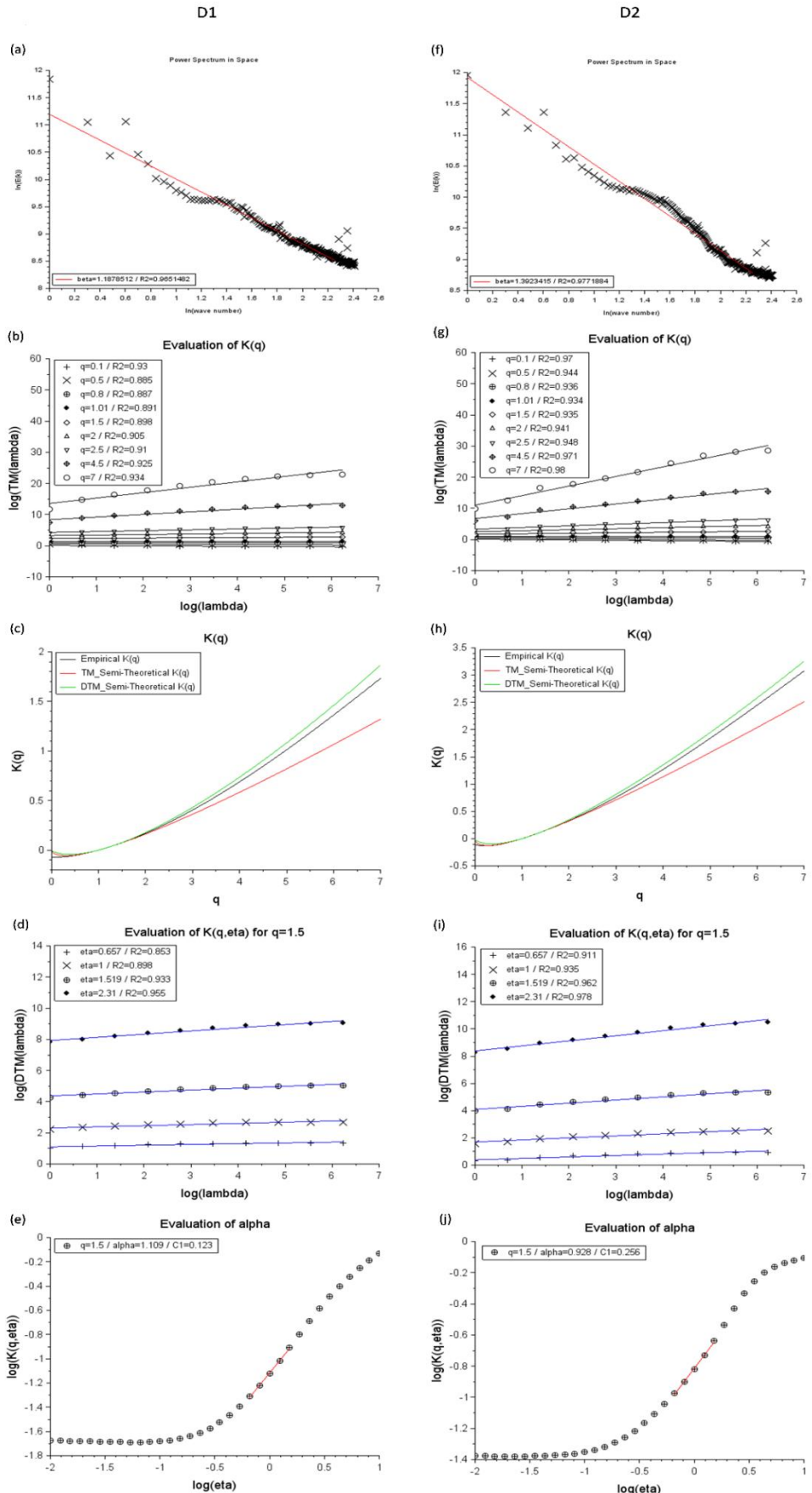


**Figure A2: Spectral analysis of the rainfall rate of CReSS model. ((a) D1 and (b) D2). The TM analysis on rainfall rate of CReSS model. (b, g) shows the scaling behavior with the value of different  $q$  from 0.1 to 7.0 as well as the result of the analysis with radar data. (c, h) also shows theoretical  $K(q)$  with the multifractal parameters retrieved from double trace moment analysis which is indicated with the red line has been compared with empirical  $K(q)$  that is shown in black line. The DTM scaling behavior (d, i) and resulting double trace moment curve of CReSS (e, j). (E.g.  $R^2$  is shown as R2 in the graphs)**

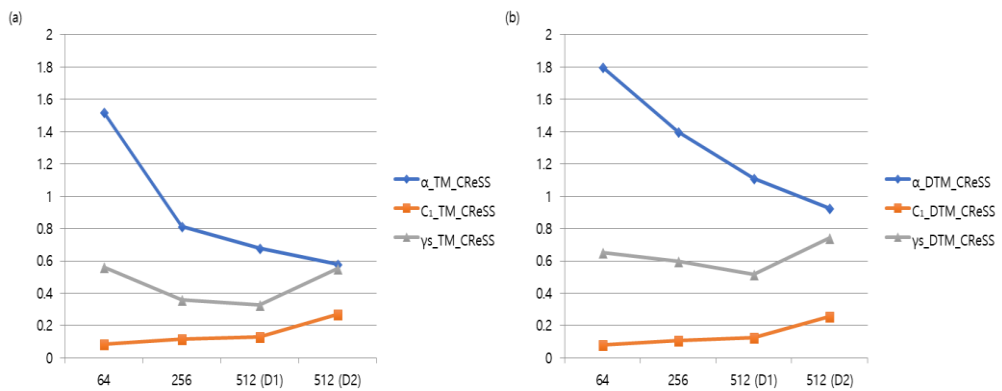


**Figure A3: The graph of multifractality index and  $\gamma_s$  of CReSS simulation depending on the size of the domain.**